

Mantle Pyroxenites: Deformation and Seismic Properties

by

Hadrien Henry

Australian Research Council Centre of Excellence for Core to Crust Fluid System (CCFS)
National Key Centre for Geochemical Evolution and Metallogeny of Continents (GEMOC)

Department of Earth and Planetary Sciences,
Faculty of Sciences and Engineering, Macquarie University, Australia

Géosciences Environnement Toulouse (GET), Observatoire Midi-Pyrénées,
Université Toulouse III Paul Sabatier, Toulouse, France

A thesis submitted for the degree of Doctor of Philosophy

March 2018



Bear Creek, Trinity, California, 2017



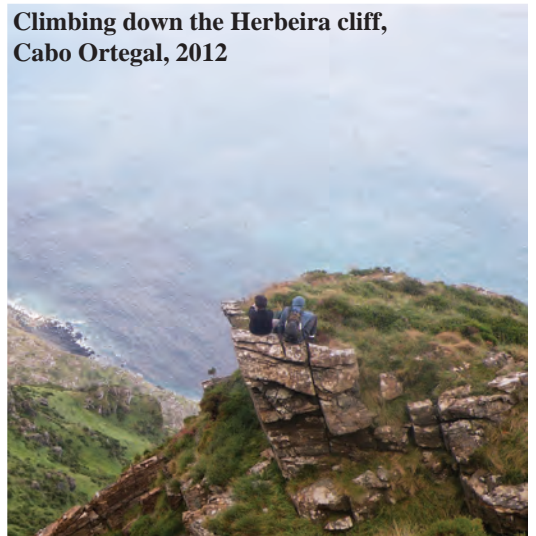
NE Herbeira cliff and view of Limo massif, Cabo Ortegal, 2012



Herbeira cliff, Cabo Ortegal, 2013



Climbing down the Herbeira cliff, Cabo Ortegal, 2012



The Trinity ophiolite and Mount Shasta, California, 2017



Table of Contents

Abstract	I
Résumé	V
Declaration	IX
Acknowledgements	XI
Chapter 1: General Introduction	1
<i>1.1 - What are pyroxenites and where to find them?</i>	<i>3</i>
<i>1.2 - Where do they come from?</i>	<i>3</i>
<i>1.3 - More than a chemical heterogeneity</i>	<i>4</i>
<i>1.4 - Pyroxenites and the structure of Earth mantle</i>	<i>4</i>
<i>1.5 - What needs to be done?</i>	<i>6</i>
Chapter 2: EBSD Methodology and Related Data Processing	11
<i>2.1 - Introduction to the EBSD technique and its history</i>	<i>13</i>
<i>2.2 - Preparation of geological samples for EBSD</i>	<i>14</i>
<i>2.3 - The analytical procedure at Macquarie University</i>	<i>15</i>
<i>2.4 - Data processing with MTEX</i>	<i>17</i>
<i>2.5 - Discussion of some of the axioms used</i>	<i>23</i>
<i>Grain reconstruction</i>	<i>23</i>
<i>Smoothing the grains</i>	<i>26</i>

2.6 - Some basic mineralogical information relevant to this work	27
<i>Olivine</i>	29
<i>Enstatite</i>	31
<i>Diopside</i>	32
<i>Hornblende</i>	34
 Chapter 3: The Microstructure of Cabo Ortegal Pyroxenites	 37
3.1 - A short introduction to the geology of NW Iberia	39
3.2 - The Cabo Ortegal Complex: A four-piece puzzle	39
<i>High-pressure gneisses</i>	40
<i>Eclogitic unit</i>	41
<i>High-pressure granulite unit</i>	41
<i>Peridotite units</i>	42
3.3 - What has been reported previously regarding the deformation?	44
3.4 - Previous microstructural studies in Limo and Herbeira massif	45
3.5 - What is observed in massifs analogous to Cabo Ortegal?	45
3.6 - What geodynamic scenario for the Cabo Ortegal complex?	46
3.7 - What can be done with Herbeira pyroxenites?	48
3.8 - Sample selection	49
3.9 - Microstructure of the Cabo Ortegal pyroxenites	51
3.10 - Fabrics and internal deformation from EBSD	56
3.11 - Conditions of deformation of the Cabo Ortegal pyroxenites	60
3.12 - Lithological constraints on the development of microstructures	64
3.13 - Investigation of the slip system activation	70
3.14 - Shear sense inferred from fabrics	73
3.15 - Tectonic and geodynamic implications	75

Chapter 4: The Microstructure of the Trinity Pyroxenites	79
<i>4.1 - Introduction to the Trinity ophiolite geology</i>	<i>81</i>
<i>4.2 - The four sampling localities</i>	<i>83</i>
<i>Corry Peak</i>	<i>83</i>
<i>Vicky Bluff</i>	<i>85</i>
<i>Layered Dunites</i>	<i>87</i>
<i>Bear Creek</i>	<i>88</i>
<i>4.3 - Why should the Trinity microstructures be studied?</i>	<i>93</i>
<i>4.4 - Textures and microstructures of the rocks from the 4 localities</i>	<i>94</i>
<i>Corry Peak</i>	<i>94</i>
<i>Vicky Bluff</i>	<i>96</i>
<i>Layered dunites</i>	<i>97</i>
<i>Bear Creek</i>	<i>99</i>
<i>4.5 - Mineral fabrics from EBSD</i>	<i>102</i>
<i>Corry Peak</i>	<i>103</i>
<i>Vicky Bluff</i>	<i>104</i>
<i>Layered dunites</i>	<i>107</i>
<i>Bear Creek</i>	<i>110</i>
<i>4.6 - Conditions of deformation of the Trinity rocks</i>	<i>120</i>
<i>Corry Peak</i>	<i>120</i>
<i>Vicky Bluff</i>	<i>122</i>
<i>Layered dunites</i>	<i>124</i>
<i>Bear Creek</i>	<i>125</i>
<i>4.7 - The case of opx</i>	<i>131</i>
<i>4.8 - The case of amphibole</i>	<i>132</i>
<i>4.9 - What did the microstructure reveal about the geology of the Trinity ophiolite?</i>	<i>132</i>

<i>4.10 - Trinity and Cabo Ortegal: microstructural links</i>	
<i>and the deformation of pyroxenes</i>	134
Chapter 5: The Seismic Properties of Layered Pyroxenite Media	137
<i>5.1 - The problem of interpreting seismic data</i>	139
<i>5.2 - What is the link between EBSD and seismic waves?</i>	141
<i>5.3 - The philosophy of the modelling</i>	142
<i>Elastic tensor correction</i>	142
<i>Density correction</i>	143
<i>ODF calculations</i>	143
<i>Definition of the different media</i>	144
<i>Calculation of the layered medium elastic tensor and seismic properties</i>	144
<i>5.4 - A Herbeira-like model</i>	144
<i>5.5 - Testing different fabrics</i>	150
<i>5.6 - Testing different abundances</i>	153
Chapter 6: Integrated Discussions and Perspectives	159
<i>6.1 - On the relative stability of the pyroxenite fabrics</i>	161
<i>6.2 - On the development of fabrics in pyroxenites</i>	162
<i>6.3 - On pyroxenites and shear instabilities</i>	163
<i>6.4 - On the seismic signature of layered pyroxenites</i>	163
<i>6.5 - Further perspectives</i>	165
Chapter 7: General Conclusions	169
References	175

APPENDICES	A-1
Appendix 1: Fabrics of Cabo Ortegal and Trinity samples	A-3
Appendix 2: Seismic Modelling Results	A-17
Appendix 3: Cabo Ortegal Sample Collection	A-23
Appendix 4: Trinity Sample Collection	A-41
Appendix 5: Publications	A-67

Abstract

The physical properties of peridotite are approximated by those of olivine for most mantle models. However, significant volumes of pyroxene-rich lithologies suggest a rheologically heterogeneous upper mantle, and thus interpretations of upper mantle properties that provide constraints to model large-scale processes, may be inaccurate. This study endeavours to better constrain the physical properties of pyroxenites by characterising their microstructure and by assessing different textural states at different stages of microstructural evolution in the “subduction factory”.

For that purpose and for consistency of methodology, I developed an automated script to process quantified microstructural data. I then applied this to two contrasting peridotite and ophiolite massifs bearing large volumes of pyroxenites.

In the Cabo Ortegal complex, Spain, dunites and layered pyroxenites crop out in what is interpreted as a preserved paleo-arc root that experienced deformation in the deep parts of a subducting slab. Investigation of pyroxenite microstructures reveals that they all reacted to deformation in a similar way, independent of composition. Petrofabrics suggest that layered pyroxenites can preserve structures and textures inherited from high-temperature deformation, could help to localize shearing, and may represent preferred pathways for later fluid percolation.

In the Trinity ophiolite, California, USA, well-preserved outcrops of mantle and crustal lithologies were studied. Microstructures from the mantle domains of the ophiolite reveal that peridotites and pyroxenites recorded high temperature plastic deformation involving melt percolation. In the crustal section, cumulate pyroxenites occur in the Bear Creek magma chamber. The microstructures of layered cumulate pyroxenites from the crustal section have a strong planar fabric with a weak linear component and likely formed by compaction and crystal-settling.

Microstructural data from the *Cabo Ortegal complex* and the *Trinity ophiolite* are then used to compute models of seismic properties for a layered pyroxenite-rich domain. The effect of compositional layering on seismic properties was incorporated into the models to produce the most geologically realistic results. The models suggest that layered pyroxenite-rich domains should induce distinctive signal deviations relative to peridotite domains devoid of pyroxenites. Using these data from Cabo Ortegal and Trinity, I investigated the relative influence of the textural state and the modal abundance on the seismic properties. The models suggest that plastically deformed and poorly-oriented pyroxenites have comparable seismic properties whereas pyroxenites affected by compaction would yield the most anisotropic seismic signal.

This quantification of pyroxenite microstructures with implications for the rheology and seismicity, is a novel step towards a better understanding of the role of heterogeneities in the geodynamic behaviour of the upper mantle.

Résumé

Dans la plupart des modèles rhéologiques, les propriétés physiques des péridotites mantellaires sont déduites de celles de l'olivine, leur constituant principal. Cette approximation a longtemps paru satisfaisante aux géophysiciens. Toutefois, dans les affleurements de roches du manteau, d'importants volumes de pyroxénites ont été observés, pouvant être la cause d'hétérogénéités rhéologiques. Par conséquent, les interprétations structurales du manteau supérieur et les processus qui en sont déduits souffrent d'un biais intrinsèque. Ce travail a pour objectif de contraindre les propriétés physiques des pyroxénites en caractérisant leur microstructure à différentes étapes du processus de subduction.

Dans un souci de cohérence durant le traitement des données, un script capable de traiter de manière consistante des données microstructurales acquises par Electron Back-Scattered Diffraction a été développé. Cette méthode a ensuite été appliquée sur des échantillons collectés sur deux massifs ophiolitiques renfermant d'importants volumes de pyroxénites.

Dans le complexe du Cap Ortegal (massif d'Herbeira) en Espagne, des dunites et pyroxénites litées affleurent dans ce qui est interprété comme une ancienne racine d'arc volcanique rentrée en subduction. Différentes catégories de pyroxénites y ont été distinguées sur des bases géochimiques. L'étude de leurs microstructures respectives révèle une réponse similaire à la déformation de toutes les pyroxénites. L'analyse des orientations préférentielles de réseau des pyroxènes suggère un épisode de déformation à haute température, possiblement dans le mantle wedge. La combinaison des données de terrain et des données microstructurales souligne l'influence des lits de pyroxénites sur le développement des zones de cisaillement et sur la percolation de fluides.

Dans l'ophiolite de Trinity, Californie, USA, des affleurements de roches mantelliques et crustales ont été échantillonnés. L'étude des microstructures de la section mantellaire de l'ophiolite suggère l'enregistrement, par les péridotites et pyroxénites, d'un épisode

de déformation à haute température en présence de fluide. Dans la section crustale, les pyroxénites cumulatives présentent une toute autre microstructure ne ressemblant en rien à celle décrite précédemment. Nos observations et nos données sont en accord avec un processus de compaction comme possible origine pour la microstructure résultant en une forte composante planaire et une faible composante linéaire.

Les données microstructurales des deux ophiolites ont par la suite été utilisées dans le but de modéliser les propriétés sismiques d'un domaine riche en pyroxénites litées. Afin d'obtenir les résultats les plus réalistes, l'effet du litage a été incorporé au protocole de modélisation. Les modèles suggèrent qu'un domaine riche en pyroxénites induirait, par rapport à un domaine pauvre en pyroxénites, une déviation particulière sur les ondes sismiques. De plus, les modèles indiquent que des pyroxénites déformées plastiquement et des pyroxénites avec une orientation aléatoire auraient des propriétés sismiques comparables. Les modèles présentant les plus forts taux d'anisotropie sont obtenus en utilisant les orientations préférentielles de réseau des pyroxénites cumulatives de la section crustale de Trinity.

En quantifiant l'impact de la microstructure des pyroxénites et de leur abondance sur la rhéologie et les propriétés sismiques du manteau, ce travail contribue à une meilleure compréhension du rôle des hétérogénéités sur la géodynamique terrestre.

Declaration

This thesis is based on the work carried out in the ARC Centre of Excellence for CCFS and GEMOC National Key Centre, Department of Earth and Planetary Sciences at Macquarie University, Australia and in the Géosciences Environnement Toulouse at Paul Sabatier University, France, over the period of March 2015 to March 2018. I hereby declare that all the data and interpretations presented in this thesis are from my own work, except for information cited from published sources, which has been explicitly indicated and acknowledged.

No part of this thesis has ever been submitted for any other degree in any university or education institute. This thesis is submitted to both Macquarie University, Australia and Paul Sabatier University, France under the conditions of a co-tutelle agreement between these two universities for this PhD program.

Sydney, March 09th 2018

Hadrien Henry

Acknowledgements

As the following pages are very likely to be the most-read section of this thesis, I am going to try to do this right!

I would like to first thank my supervisors who made this journey possible: Sue O'Reilly, Bill Griffin and Georges Ceuleneer. You provided me with the best work environment I could possibly think of, shielded me from turbulences, guided me through the long road that a PhD is and gave me a reason to get up every morning. For that I am very grateful to you all.

I would also like to thank my Master thesis supervisors Vincent Regard and Joseph Martinod who always supported me and were very helpful during the long years it took me to finally start a PhD.

In this adventure, several persons acted as unofficial supervisors and I would like to give them the recognition they deserve:

Takako and Mary-Alix, you guided me in the lab and turned a numerical modeller into a microstructure-enthusiastic lab-rat. This by itself, is already a great achievement!

Romain, you thought about the project, designed it and somehow made it real. You helped me tremendously with everything that is somehow related to a rock since 2006. If in this work there is something you like a bit more than the rest, it most likely comes from him. Thank you for everything work- and not work-related!

Michel, thank you for the time you gave me and all your support, before and during the PhD.

Norm, I wish I had exchanged more with you during my time at Macquarie. What happened to you is unfair and left the department deprived of one of its most brilliant minds.

This work was made possible thanks to the Australian Research Council grant for ARC Centre of Excellence for Core to Crust Fluid Systems (CCFS), a IMQRES scholarship, EPS postgraduate funds and funding from the Centre National de la Recherche Scientifique (CNRS). I used instrumentation founded by ARC LIEF, DEST Systematic Infrastructure, Macquarie University, NCRIS AuScope grants and industry partners.

Getting data out of the lab was not easy and a lot of cooperation was required. Manal Bebbington in Sydney and Fabienne de Parseval in Toulouse both provided, always ahead of schedule, the high quality thin sections needed for EBSD. My Scanning Electron Microscope skills resulted from very complex combination of interactions with David Adams, Liene Spruženiece, Sarah Gain and Tim Murphy. My programming skills were strongly challenged by Beñat Oliveira who helped me when I was in a dead end.

This work was strongly improved by the suggestions and comments from Patrick Launeau, Stéphane Guillot, Jacques Précigout, Pablo Puelles, Jean-Louis Bodinier, Peter Cawood and two anonymous reviewers.

Back in the office, the pleasant work atmosphere was only made possible thanks to all admins, fellow students, post-docs and researchers who surrounded me for the past 3 years. A big thank you to the whole BD family for dealing with my hyperactivity!

The French contingent at Macquarie composed of Yoann Gréau, Romain Tilhac, Bruno Colas, Mathieu Chassé, David Silva and Olivier Alard have to be acknowledged for all the comic relief they provided during or after work. A big thank you to the non-French contingent with whom I spent a lot of time with: Cait Stuart, Montgarri Castillo, Nicole McGowan, Tim Murphy, Nora Liptai, Sarah Gain, Rosanna Murphy... In Toulouse, regular coffee breaks with Baptiste Lemirre, Mathieu Rospabé and Paul Antonio were essential for a good day of work.

Outside the university, my mental sanity was kept in good condition mostly by my housemates. Cheers to James, Stewart, Helena, Steve, Bryant, Al, Scott and all the others with whom I shared a roof in the last 3 years. This whole experience would not have been as crazy if it was not for you all.

Depuis plus de dix ans une troupe des plus burlesques m'accompagne quotidiennement dans mes aventures. Un grand merci à Vincent, Raoul, Alexis, Cédric, Jean-Baptiste, Jeremy, Romain, Yannick, Thomas, Nicolas, Erwan, Nicolas, Stéphane, Robin, Sébastien, Romain et Maxime pour leur soutien.

Merci à Maël, Arthur, Jennifer, Vivien, Wilfried, Vincent, Marine, Marie, Frédéric, Marc, Bertrand et Lucille, ces amis d'enfance qui choisissent de partager la plupart de leurs temps libre avec moi depuis deux décennies.

Je finirai cette section en remerciant toute ma famille qui m'a soutenu et supporté depuis encore plus longtemps.

A mes parents, Sandrine et Fabrice, qui ont eu le courage et la patience de supporter mes fausses notes à la guitare mais aussi à l'école et ce pendant de trop longues années. A mon frère, Hugo, le meilleur compagnon qu'il soit quand il s'agit d'augmenter l'entropie dans le foyer familial. A mes grand parents, Gisèle, Monique, Raymond et Louis, qui se sont occupé de moi et m'ont accompagné depuis tout petit. Je ne serai pas celui que je suis aujourd'hui si vous n'aviez pas été là. Merci à tous!

Chapter 1:

General Introduction

1.1 - What are pyroxenites and where to find them?

Pyroxenes (from “pyro” and “xeno” meaning fire and stranger respectively in Greek) are, along with olivine, common minerals in mafic and ultramafic rock types and occur in two forms: clino- and orthopyroxenes (Morimoto, 1988). Pyroxenite refers to a lithology with a high proportion (>90%) of pyroxenes (clinopyroxenes, orthopyroxenes or both).

Pyroxenite is a common mantle-derived lithology found in mantle xenoliths, abyssal peridotites and in ophiolitic and orogenic peridotite massifs (e.g. DeBari and Coleman, 1989; Khan et al., 1989; Khan et al., 1993; Almqvist et al., 2013; O'Reilly and Griffin, 2013). Basalts from island arcs and mid-ocean ridges commonly show geochemical signatures indicating involvement of mantle pyroxenites in the partial melting process that formed their parent magmas (e.g. Sobolev et al., 2005; Lambart et al., 2012; Matzen et al., 2017). Such observations suggest that their abundance may be much higher than observed in most peridotite massifs. As of today, pyroxenites are mostly considered to be the crystallisation products of melts that did not reach the surface and remained trapped in the upper mantle (e.g. Müntener and Ulmer, 2006; Downes, 2007).

1.2 - Where do they come from?

Pyroxenites are part of the compositional heterogeneities of Earth's mantle and are thus important in understanding mantle, and especially lithospheric mantle structure, processes and properties. Their formation is widely debated and multiple hypotheses have been proposed to explain their genesis. Amongst them, the recycling of oceanic lithosphere in subduction zones (e.g. Allègre and Turcotte, 1986) or the partial melting of a host peridotite (e.g. Van Calsteren, 1978) have been first suggested. Recently, pyroxenites are more commonly interpreted as mineral segregates or cumulates from upwelling melts in magmatic conduits (e.g. Kornprobst, 1969; Bodinier et al., 1987; Ceuleneer and Le Sueur, 2008; Tilhac et al., 2016).

In supra-subduction zones, where large volumes of pyroxenite may occur, the most accepted process of formation of pyroxenite starts with the release of water by the slab, due among other factors, to the breakdown of amphibole. This water will contribute to lowering the solidus of the hanging wall peridotites eventually causing them to partially melt.

Pyroxenites are interpreted as the crystallisation product of such melts. As a consequence, they encapsulate a complex crystallised association of slab-derived fluid and mantle-wedge material; their relative contributions are still debated (e.g. Matzen et al., 2017).

1.3 - More than a chemical heterogeneity

Because of its difference in mineralogical composition from the surrounding peridotites, pyroxenite also constitutes a rheological heterogeneity (e.g. Girardeau et al., 1989; Girardeau and Gil Ibarra, 1991). Depending on the pressure, temperature and water content, pyroxenites may end up more, less or equally viscous compared to the surrounding peridotites (Avé Lallemant, 1978). In a volume where large proportions of pyroxenites are present, that viscosity differential may govern the way the whole domain will deform by localising, directly or indirectly, the development of shear zones (e.g. De Bresser et al., 1998; De Bresser et al., 2000; Chen et al., 2001; Toy et al., 2010).

1.4 - Pyroxenites and the structure of Earth mantle

The mantle is the thickest of Earth's compositional layers and is made up of two distinct sub-layers, the upper and the lower mantle, separated by the D' seismic discontinuity at a depth of about 670 km. The Earth mantle and crust are where most of the geodynamic processes originate and the relative contribution of each to plate tectonics is still debated. Solving this problem requires the estimation of the respective contribution of basal heating (heat flux from the core) and internal heating (due to radioactive decay). According to classical fluid dynamics, if basal heating dominates, the convective pattern will be conditioned by upwelling currents rooted in the lower thermal boundary layer. Conversely, if internal heating dominates, it will be conditioned by cooling and eventual sinking of the upper thermal boundary layer. Given the complex (non-newtonian, among other) nature of the "geological fluid", it is critical to better constrain the rheology of mantle and crustal rocks to have a robust understanding of the Earth's convective dynamic.

The rheology of Earth's upper mantle is highly influenced by the evolution of its mineralogical composition with changing pressure and temperature conditions (Fig.1.1). Olivine ($(\text{Fe,Mg})_2\text{SiO}_4$), the main upper mantle mineral, undergoes several phase transitions:

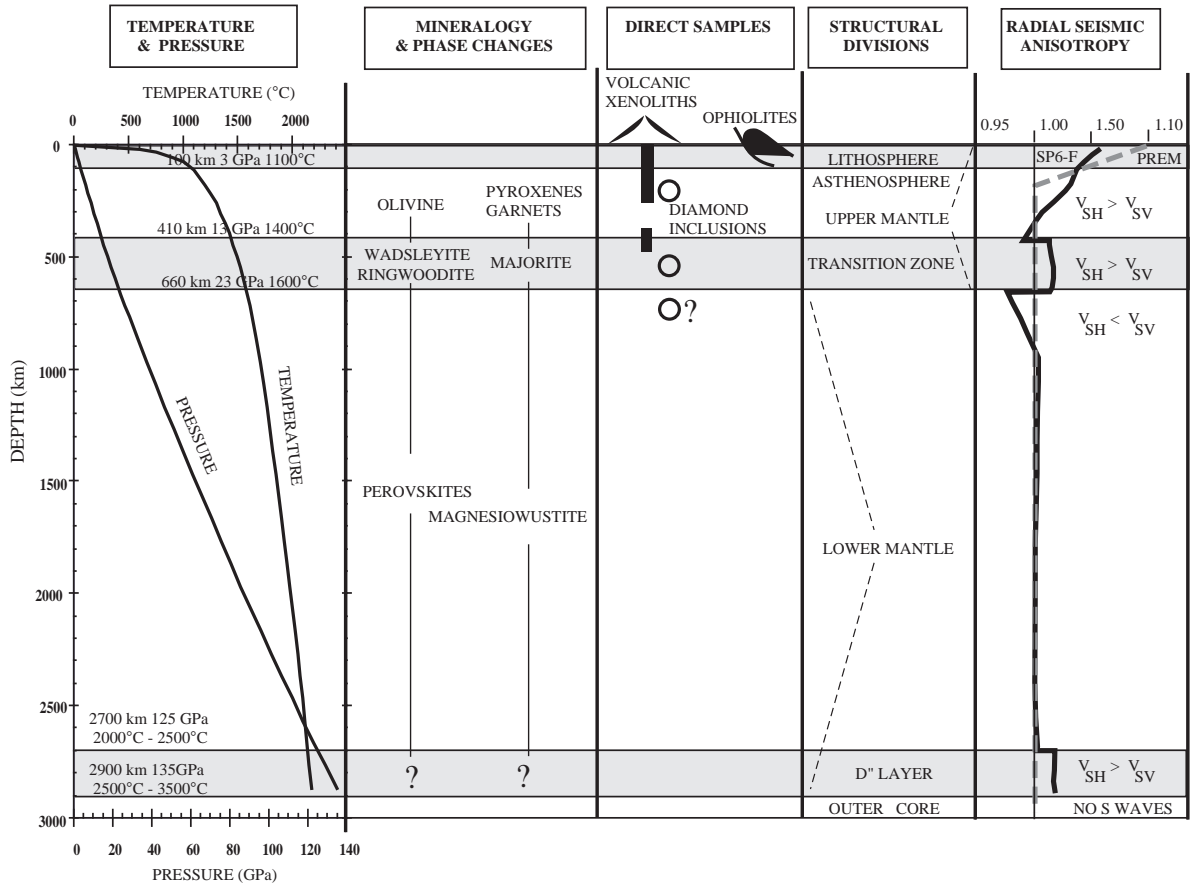


Fig.1.1: Schematic structure of the Earth: P/T conditions, stratification and phase transitions as functions of depth, after Mainprice et al. (2013). Ophiolitic rocks, which are the subject of this study, sample a very shallow part of the Earth.

first to wadsleyite at 410 km depth, then to ringwoodite at about 515 km. Clino- and orthopyroxenes ($(\text{Mg,Fe})\text{Ca}(\text{Si})_2\text{O}_6$ and $(\text{Mg,Fe})\text{SiO}_3$ respectively) coexist in the upper mantle until the orthopyroxene reacts out at 275 km. From 300 to 500 km, clinopyroxene and garnet ($(\text{Mg,Fe,Ca})_3\text{Al}_2\text{Si}_3\text{O}_{12}$) slowly decline in proportion and their elements are accommodated in the phase transition towards majorite (Mainprice, 2007; Mainprice et al., 2013). Deeper, the Transition Zone between the upper and lower mantle is reached. It corresponds to the phase transition from ringwoodite ($(\text{Fe,Mg})_2\text{SiO}_4$) to bridgmanite (magnesio-perovskite) + magnesio-wustite ($(\text{Fe,Mg})_2\text{SiO}_3 + (\text{Fe,Mg})_2\text{O}$) and from majorite to calcium-bearing perovskite (Agee, 1993; Helffrich and Wood, 2001). This transition occurs from 410 to 660 km; this layer is considered to be particularly rich in ringwoodite and could host an important amount of water, averaging up to an end-member of 1 weight percent of the bulk rock (Schmandt et al., 2014). The 670km discontinuity at the bottom of the transition zone is marked by an important jump of 10^2 to 10^3 in viscosity, probably related to the phase transition and is visualized in seismic as the D' discontinuity. This jump in viscosity is likely

to be responsible for the slab anchor phenomenon observed when slabs are in contact with the discontinuity (Uyeda and Kanamori, 1979).

Fig.1.1 shows the clear relationship between each mineral assemblage and the behavior of seismic waves. Consequently, a correct understanding of the inner Earth structures and the associated dynamics through the studies of seismic data can only be achieved with better constraint on the different lithologies composing it, including pyroxenites.

1.5 - What needs to be done?

This study aims to better characterise the deformational behaviour of pyroxenites in the upper mantle, by exploring two different aspects of the problem. Full characterisation of the deformational behaviour of a rock requires the investigation of its microstructure before and after deformation and when possible, combining the results with information gathered in the field (Mercier and Nicolas, 1975; Girardeau and Mercier, 1988). Here, two pyroxenite-rich domains have been targeted, each potentially providing a piece of the puzzle.

The Cabo Ortegal complex, Spain, offers the opportunity to sample strongly deformed pyroxenites which underwent a complex tectono-metamorphic evolution involving delamination from an arc root, travel through a mantle wedge and introduction into a subduction channel (Jamaa, 1988; Girardeau et al., 1989; Ábalos et al., 2003; Puellas et al., 2012; Tilhac et al., 2016). These specific pyroxenites were the topic of several other works in the past decades, making them a very well characterised set of samples. However, since the pioneering microstructural work on the Cabo Ortegal peridotites of Ben Jamaa, Girardeau and Gil Ibarguchi in the late 1980's, no study has reported microstructural data from that locality with modern tools (i.e. Electron Back-Scattered Diffraction).

The Trinity ophiolite, California, USA hosts large quantities of obducted ultramafic material intruded by several gabbroic plutons (e.g. Hamilton, 1969; Lindsley-Griffin, 1977; Ceuleneer and Le Sueur, 2008). The history of Trinity, in contrast to Cabo Ortegal, does not involve significant plastic deformation in specific outcrops and can give access to a textural panel that potentially reflects the initial textural state for Cabo Ortegal, when only a magmatic fabric was present.

This work is structured as follows:

Chapter 2 provides a review of the current technique used to acquire microstructural data, known as Electron Back-Scattered Diffraction (EBSD). The protocol required to get the most information out of a sample is reviewed. Sample collection, preparation and the analytical procedure are discussed. An automated and adaptive code to process EBSD data, developed within the frame of this PhD, is presented. Along with the code, examples of results as well as discussion of specific axioms are covered.

Chapter 3 presents the Cabo Ortegal pyroxenites. After a review of the regional geology, the microstructures of the different types of pyroxenites cropping out in the Herbeira massif are investigated. Deformation conditions are explored and the impact of the presence of pyroxenite layering in a supra subduction domain is discussed. Using microstructural and structural data, the history of the Cabo Ortegal pyroxenites is submitted to the test and regional implications are drawn.

Chapter 4 reports modern microstructural data from the Trinity ophiolite. Several localities were sampled for this work and include both mantle- and crust-derived material. After a description of the different localities, the microstructural investigation and interpretation of each lithology is presented. This chapter provides a strong emphasis on the Bear Creek magma chamber, which contains abundant pyroxenite-rich cumulates. In the light of the results, the nature of each locality is then discussed and put back into a larger context.

Chapter 5 links all the previous chapters with seismic modelling that uses the microstructural data presented earlier. A modelling protocol designed to handle layered media is presented. Various models of layered pyroxenites embedded in dunites were run using the modelling protocol and are presented in this chapter. The effect of both the mineral fabrics and their relative modal abundance on the seismic properties is explored through the prism of layered pyroxenites, and the consequences for the seismicity of subduction zones and their interpretation are discussed.

Chapter 1

Chapter 6 summarizes and discusses the major results obtained in the study of the Cabo Ortegal and Trinity pyroxenites and of the seismic modelling. Potential implications and perspectives are discussed.

Chapter 7 is a conclusive chapter where the most significant findings are summarized.

Chapter 2:

EBSD Methodology and Related Data Processing

2.1 - Introduction to the EBSD technique and its history

Electron Back-Scattered Diffraction (i.e. EBSD) aims at gathering crystallographic information from crystalline material using a scanning electron microscope (SEM). During EBSD analysis, a beam of electrons is projected on to a sample tilted at 70° . In reaction to the incoming beam and because of the particule-wave duality nature of the electrons, the sample lattice will diffract a fraction of the electrons and form a divergent source of electrons close to the surface of the sample. This divergent source, when used to form an image on the EBSD detector (i.e. a phosphor screen, Fig.2.1), forms characteristic band-shaped patterns (i.e. regions with greater electron density) called Kikuchi bands. These patterns are directly a function of the lattice itself (i.e. chemical composition and structure) and its orientation relative to the experimental setup. By setting up a user-defined grid, it is possible to collect a series of measurements to form a map of the sample, resulting in a mapping of the phases and their spatial orientation at every point of the grid.

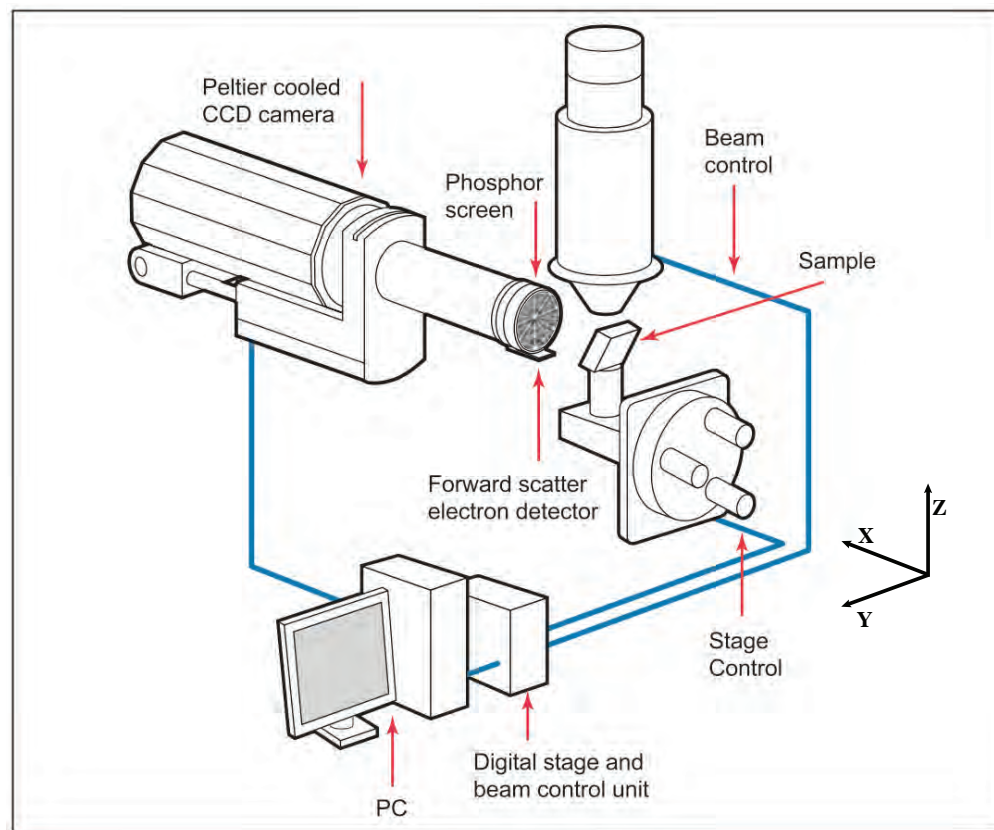


Fig.2.1: Sketch of the EBSD configuration at Macquarie University modified after Oxford instrument documentation. The SEM directions X, Y and Z are shown.

After being initially developed for the material sciences, the work of Prior et al. (1999) brought EBSD into Earth Sciences. In Geology, EBSD is now used as replacement for the universal stage and provides, quickly and relatively easily, high-quality quantitative data on the mineral content, texture and microstructure of a sample. The mineral fabrics and the grains' internal structures are therefore quantified and provide insights on the mechanisms that caused this fabric (i.e. crystallization and / or deformation). The strong inter-dependency of chemical / physical instability makes the combination of EBSD data with advanced *in situ* analytical techniques an essential tool to understand the processes at work in geological samples.

2.2 - Preparation of geological samples for EBSD

A specific protocol of sampling and sample preparation has to be respected to collect and interpret correctly EBSD data. Knowledge of the orientation of the sample relative to the structural framework is crucial to define a shear sense, a fabric and the potential slip system activated. Accordingly, during fieldwork, most of the samples collected have been annotated with the foliation plane, the mineral lineation, the upward direction and the magnetic north direction. These annotations are used to create the thin-section in a known “XZ” plane which is determined based on macroscopic minerals shape preferred orientation. Because the XZ plane is perpendicular to the foliation plane and includes the mineral stretching lineation (Fig.2.2), this framework is pertinent for structural observation for multiple reasons: (1) there is a direct relationship between the macroscale deformation markers (i.e. schistosity and lineation) and the azimuth of the crystallographic axis involved during plastic deformation thus allowing a more straight forward interpretation of the dominant slip system activated in the dislocation creep regime; (2) shear senses are observable in this plane and (3) deformation markers such as kink bands or subgrain rotation are more visible and easier to interpret. If no lineation or foliation is visible and the sample still presents a strong fabric, possible work-around exists to determine the correct orientation using subgrain analysis, or the coincidence of maximum-point of the fabrics. In this study, the structural framework was available for most of the samples collected. For samples from Tilhac (2017) that were not oriented, rotations of the dataset have been performed using a combination of both methods as well as field / lab pictures of the samples.

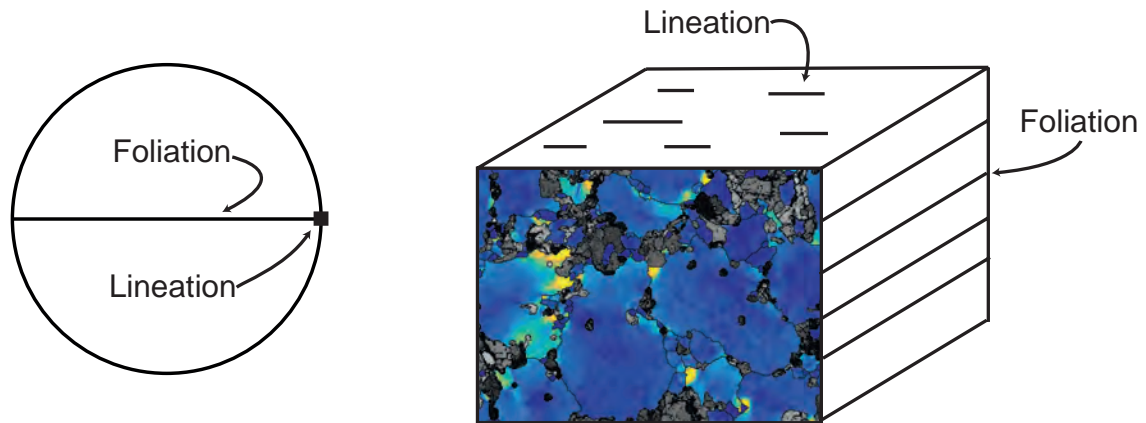


Fig.2.2: Position of the structural reference frame in both pole-figures and EBSD-derived maps.

In order to maximise the data collection, the sample surface has to be as flat as possible. Thin-sections were subject to a series of different polishing to get to a satisfactory result. The process includes impregnation of the sample at every stage, 30 minutes of polishing on a tin lap with a 3 μ m diamond paste; 30 minutes on a thin nap cloth with a 1 μ m diamond paste and 2 minutes on a silk, thicker-nap cloth with a 1 μ m diamond paste. An additional chemical polishing was carried out for 5 minutes with a colloidal silica-water solution (mixed in 70 / 30 proportion) to reduce any surface damage produced by the previous steps. As the analysis were performed in high-vacuum, a carbon coating of 25 angstroms thick was finally applied to the sample to prevent charge build-up during analysis.

2.3 - The analytical procedure at Macquarie University

In the Geochemical Analytical Unit, Macquarie University, a HKL NordlysNano EBSD detector is attached to a Zeiss EVO MA15 scanning electron microscope, forming a setup similar to the sketch in Fig.2.1. Despite being very versatile, this setup has a limitation intrinsic to its geometry. The sample has to be irradiated at a relatively small working distance (i.e. the electrons beam focal distance; < 22 mm) to obtain reliable results. To satisfy this condition, EBSD analysis is restricted to a limited range of Z values (vertical direction in the SEM reference frame, cf. Fig.2.1). Consequently, analyses could be performed, at best, on half of the thin-section closest to the electron gun.

Calibration and optimisation of the electron beam is required before analysis. This step was usually carried out before the sample insertion. All the work presented in this thesis was done using a 20kV accelerating voltage.

A routine EBSD analysis in the GAU would start with the following steps:

- (1) The sample is inserted into the SEM vacuum chamber and the carbon coating is tested.
- (2) The sample is then tilted at 70° to the electron beam (Fig.2.1).
- (3) The EBSD and EDS (Energy-Dispersive X-ray Spectroscopy) detectors are inserted in the chamber.
- (4) The phases present in the sample are input in AZTec settings. Inputting the phase list will have two consequences: it reduces significantly the time needed to index a measurement and gives much more consistent and realistic results.
- (5) A background measurement is made to subtract the background noise. It is performed at maximum scan speed and at a lower magnification in order to remove any potential local bias (e.g. large grains, tape, glue, etc...).
- (6) The number of frames per measurement during analysis and the exposure time of each frame are set to get a signal strength greater than 30% (i.e. quality of the Kikuchi bands after processing). When the polishing or the carbon coating has failed, no realistic compromise can be reached and the sample preparation has to be restarted from scratch.
- (7) If the signal is satisfactory, the area that needs to be analysed is defined and the step size (distance between each measurement on the user-defined grid) specified. For the analyses presented in this study, the typical step size is $15\text{ }\mu\text{m}$. This is small enough to observe, with great accuracy, most of the criteria for internal deformation. Generally, the analysis step size will be subject to variation according to the resolution desired or simply because of time constraints determined by the instrument availability.
- (8) The analysis is then carried out by the AZTec software, which pilots the SEM stage and receives the raw data. For each measurement, the Kikuchi pattern is compared to the AZTec library and the most statistically viable combination of orientation and phase is deduced and stored.

The total time needed to perform the analysis is a function of several factors such as the size of the surface analysed, the step size and the beam conditions, which may vary significantly depending on the analysis.

In this study, large maps (quarter to half of the thin-section) were routinely made. Because the surface analysed was always bigger than the minimal magnification of the SEM, the raw data are made up of several single frames that, put together, constitute the whole analysed surface (i.e. a mosaic). Stitching of the different frames is made easier by a 15% forced overlap of the frames during acquisition and is performed using the band contrast canal, as this is the parameter that best represents the microstructure.

After the stitching operation and the creation of a single file for the analysis, Channel 5 software was routinely used to perform a standard noise reduction (remove isolated analyses) as well as to interpolate the missing data with at least 8, 7, 6 and then 5 identical neighbours with the same orientation. Grains with an equivalent diameter smaller than 4 times the step size are then deleted from the data set in order to avoid any indexing errors. The now “cleaned” dataset was then saved and processed using the MTEX toolbox for Matlab.

2.4 - Data processing with MTEX

In order to take full advantage of the EBSD datasets, the choice to use MTEX and Matlab (Bachmann et al., 2010b, 2011) instead of the Channel 5 software has been made. This is because of its greater versatility and the possibility to use MTEX for seismic modelling later in the project. So far, no user-friendly script has been provided to easily and routinely produce EBSD-derived figures. Part of this project was dedicated to this. All the functions and a comprehensive guide on how to use them is provided in the electronic appendix.

This work benefited greatly from the previous work of David Mainprice and several other contributors from the [MTEx](#) and [Matlab](#) community forums. The following has been optimised and debugged using version 4.1.4 and 4.5.0 of MTEX and R2015b of Matlab. Results were benchmarked against David Mainprice’s Unicef Careware Fortran program and Channel 5 software.

Mtex provides a user-friendly graphic user interface that reads the EBSD data file (here, our “cleaned” dataset) and detects the phases that were chosen during the acquisition. Once the data have been read and the phases defined, a rotation tool, capable of rotating the dataset to the reference frame needed by the user is available. It was used to put the data back into the field / structural reference frame in order to allow the determinations of the mineral fabrics. Consequently, every map and pole-figure presented in this work respects a specific convention presented in Fig.2.2. After this preliminary work, MTEX creates a “.m” file that is used to load the EBSD data into Matlab memory.

To accurately compare samples and easily produce a wide range of figures, an automated protocol was designed. The protocol uses several functions each designed to solve a specific problem. Here, a brief description of the philosophy of the algorithm is carried out.

Firstly, measurements with a mean angular deviation (i.e. MAD) value greater than 1.3 are discarded as they are not reliable enough to be included. A first grain calculation is then performed. In MTEX, a grain is a region in which the misorientation of neighbour measurements is less than a given threshold. In this study, 10° was used as threshold. More detail is provided on this protocol in this chapter. To get the most realistic and reliable results possible, grains smaller than 10 pixels are discarded, and smoothing of the dataset and eventual extrapolation of some missing values inside grains are performed by default.

Once the grains are defined, pole-figure calculations start for each phase. According to the crystallography of the target mineral, the axes that need to be observed may vary. If the symmetry of the phase is not included in the script’s database, results will be plotted by default along the [100], [010] and [001] axis.

In order to compare different samples microstructure, pole-figures are classically calculated and plotted using 1 point per grain (i.e. the mean orientation of the grains is used) and therefore this form of plotting was set as the default plotting method. However, depending on the user input, different ways to handle the dataset can emerge:

(1) When twin detection is requested, the script will search all the grain boundaries between two grains of the same phase and extract the misorientation angle. If the

misorientation at a grain boundary corresponds to the mineral twinning angle modulo an error, the grain boundary will be flagged as a twin boundary and the grains on both parts of the grain boundary will be merged together. In the case of a dataset with twins, the pole-figures will be computed with all the measurements as using one point per grain is not adapted.

(2) If the current phase matches a phase that was requested in all measurements by the user, the given phase pole-figure will be computed using all the data instead of the default one point per grain. This feature is particularly useful for serpentized olivine in abyssal peridotite and ophiolites as pole-figures in all measurement have been shown to yield comparable results than the standard one point per grain model (Achenbach et al., 2011). In this study a more conservative approach is taken: pole-figure drawn with all the measurements will be used only if the fabric is clear, obvious and the grain size prior serpentization is close to coarse or bigger (sensus Mercier and Nicolas, 1975). That choice is motivated by the fact that a pervasive serpentization will result in artefacts in a weak fabric by simply removing data and creating artificially lower and greater concentration in the ODF.

If the number of data points in the chosen dataset is less than 100, the mean orientation of each grain is plotted. If it is greater than 100, an orientation density function (ODF) is calculated using a de la Valee Poussin kernel density estimation with a 10° halfwidth and pole-figures are drawn. The 10° of halfwidth is a good compromise and is not too large to over-smooth the ODF and not too small to prevent single measurements to appear.

For consistency of comparison between samples, the contours in the pole-figures are drawn at a rounded number of multiples of uniform distribution. Concretely, if the maximum density of a pole-figure is 4.5, the contours plotted will be 1, 2, 3, 4 and 5 multiple of uniform distribution.

Integration of David Mainprice's function "PFs_Texture_Index_MTEX4" into the program allows the extraction of statistical values for the pole-figures, such as the M and J indexes (Bunge, 1982; Skemer et al., 2005). The J-index is commonly used in both material and geological sciences and is defined as the second moment of an ODF and ranges from 1 for a randomly oriented material to infinity, in theory, for a single crystal. As the J-index is sensitive to both the number of data and the smoothing parameters used, the M-index was also

computed. The M-index is based on the distribution of uncorrelated misorientation angles, is not sensitive to parameters used for its calculation and is reliable for dataset larger than 150 data. In this work, both indexes will be used to better quantify the fabric strength.

Quantitative descriptions of the fabrics shapes are presented using eigenvalues. Orientation tensors are calculated for each crystallographic axis of interest using Bachmann et al., 2010a method. The 3 eigenvalues are extracted and used to define a normalized point maximum, girdle and random distribution affinity for the orientation dataset.

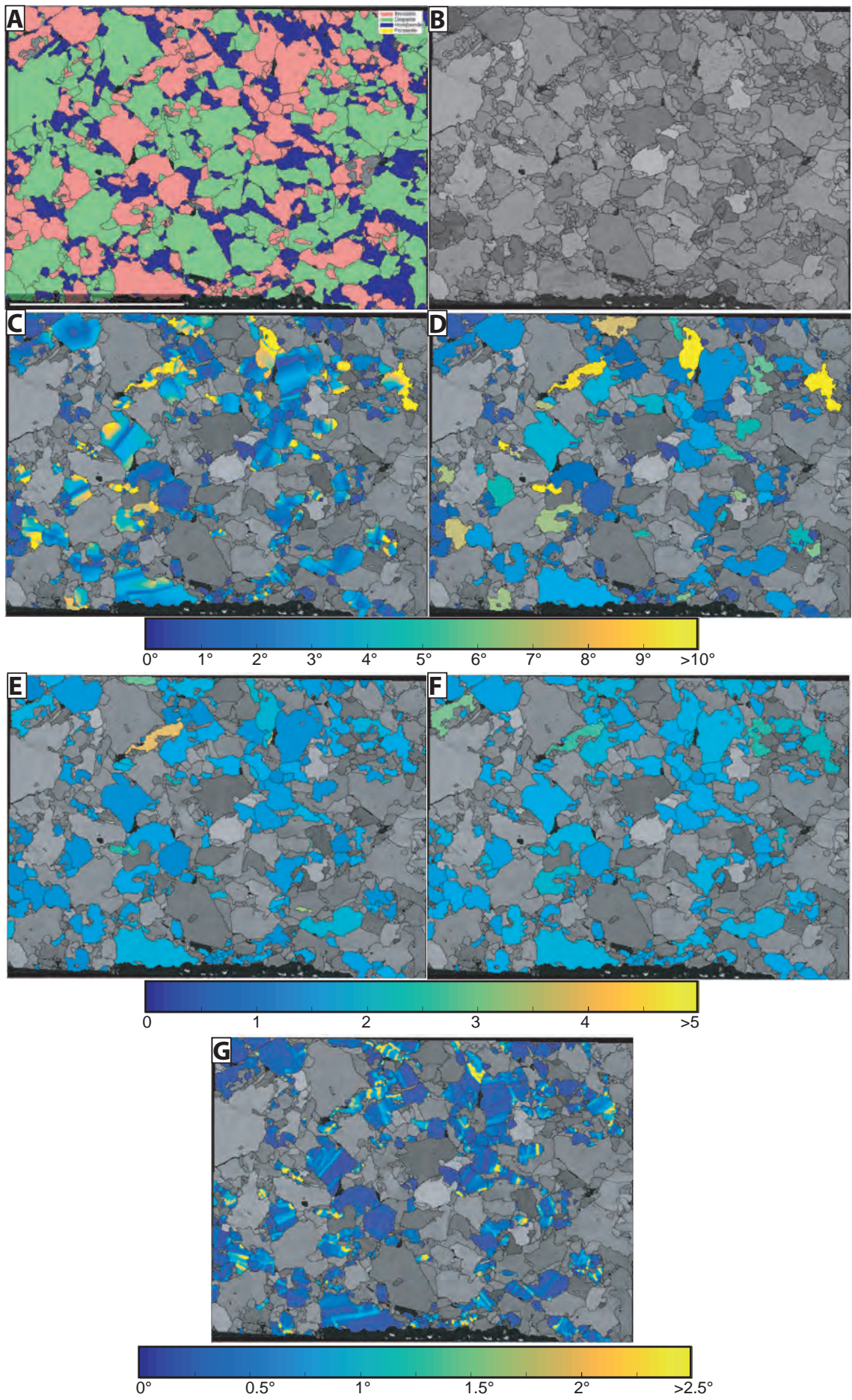
Other statistical values are also extracted such as the percentage of grains with at least one twins, the modal percentage, the number of grains, the number of data and the area weighted grains size, aspect ratio and shape factor.

Along with pole-figures, maps derived from EBSD data are produced for each phase and reveal different information such as the lattice deformation at each point of space, its absolute orientation and other microstructural parameters, all of which are useful to understand the sample microstructure. Below, a concise description of each parameter is provided. Selected examples of results are provided in Fig.2.3. As all of the figures are automatically generated and saved, a consistent labelling protocol was used for each parameter plotted. All of the results provided in these thesis (and in the electronic appendices) follow this rationale and thus the acronyms corresponding to each parameters are given below.

Phase map (Fig.2.3-A; MAP_Phase_Grains_GB):

In this map, grains are represented with a colour defined by the user during the data importation that indicates its phase. Colours can be modified to fit any needs. In this work, a colour code consistent with the one used by Tilhac et al. (2017) has been used: Olivine is yellow, orthopyroxene (i.e. opx) is light red, clinopyroxene (i.e. cpx) is light green, chromite is grey, garnet is magenta and hornblende is blue.

Fig.2.3: Opposite page, examples of maps created routinely using data from sample CO-97-A. (A) Phase map; (B) Band contrast map; (C) Misorientation relative to mean orientation map for opx. Scale is in degrees and every value greater than 10 or 5° (depending on the parameter) has been brought down to 10 or 5 to allow a clearer observation; (D) Grain orientation spread maps; (E) Aspect ratio map; (F) Shape factor map and (G) Kernel average misorientation map.



Band contrast (Fig.2.3-B; Band_Contrast_GB):

Calculated from the Kikuchi patterns. It is an indicator of the quality of the data, the whiter (i.e. stronger values and therefore better contrast) the better. It allows a good visualization of the grain- and subgrain boundaries. It is used to check the grain computation and as a background for some plots to display the underlying textural information. The function “freezeColors.m” by J. Iversen, from the package with the same name, is required to properly plot this parameter as a background.

Misorientation to mean orientation (Fig.2.3-C; indexed / phase_indexed_Mis2mean_BC_BG):

This parameter represents the angular difference between each measurement and the mean orientation of the grain they belong to. It is a straight forward and powerful way to observe internal imperfection of the mineral lattice of each grain.

Grain Orientation Spread (Fig.2.3-D; indexed / phase_GOS_BC_BG):

The grain orientation spread is the average deviation in orientation between each point in a grain and the average orientation of the grain. It is used to easily spot porphyroclasts and grains with a non-equilibrated lattice (Wright et al., 2011).

Aspect ratio (Fig.2.3-E; indexed / phase_AR_BC_BG):

The aspect ratio is calculated as the length of the longest axis divided by that of the smallest. It indicates and quantifies grain elongation. This parameter is plotted for the whole sample and individually for each phase.

Shape factor (Fig.2.3-F; indexed / phase_SF_BC_BG):

The shape factor of a grain is defined as the perimeter of the grain divided by the perimeter of a circular grain with an equivalent surface. It is indicative of the complexity of the grain boundaries.

Kernel average misorientation (Fig.2.3-G; indexed / phase_KAM_BC_BG):

The kernel average misorientation reflects the intergranular average misorientation angle per orientation calculated on a 1st order kernel. This microstructural parameter is useful for revealing subgrains.

Inverse Pole-figures:

This script produces color-coded orientation maps (*IPF_Map_Phase_Lineation / Foliation / TheOtherOne*) and inverse pole-figures (*IPF_Phase*) of a specified phase using 3 directions in the SEM framework SEM directions. For this work, rotation of the dataset before/after loading of the data into Matlab memory allows two of them to coincide with the lineation and the foliation of the sample. As all of the samples obey the same convention, the program automatically retrieves the correct axis and label the figures accordingly.

Misorientation angle distribution (generic name: Angle_distrib_Phase):

This histogram displays the normalized frequency of the misorientation angle between a given phase and the other phases in contact with it in the sample. The two solid lines represent the theoretical curve for a random distribution of misorientation angle at the phase/phase boundaries and the same line for the analysis.

2.5 - Discussion of some of the axioms used

Grain reconstruction

Depending on the material, the angle used to separate one grain from another may change. In material science the threshold is sometimes fixed at 15° while in geology, a 10° value has been classically used (e.g. Mainprice et al., 2015). For EBSD and relevant data processing, the angle threshold values dictates where grain boundaries will be drawn. This threshold is therefore critical as it may influence every microstructural parameter that is based on the number of grains and the grain shape (e.g. mean grain orientation, shape factor, aspect ratio, fabrics and their strength). Other representations like the Kernel Average Misorientation and color-coded maps relative to the SEM (i.e. inverse pole-figures maps as described above) are by definition not sensitive to this value and are reliable in every case. To evaluate the sensitivity to the threshold of the pole-figures and fabric-derived parameters, two series of calculations were made. The J-index, M-index and the number of grains of Cpx and Opx were calculated with a grain-defining threshold angle changing from 1 to 20° for sample T3BC1 and CO-97-A.

The results of the calculations are shown in Fig.2.4. Fig.2.5 displays 3 examples of maps of the same sample (CO-97-A) using a 5°, 10° and 15° angle for grain reconstruction. Fig.2.6 shows enstatite pole-figures (one point per grain of the same sample for 5, 10 and 15° threshold angle). It suggests that the sensitivity to the angle threshold of the J and M-indexes and the number of grains becomes negligible past the 3-4° limit. From a map- and pole-

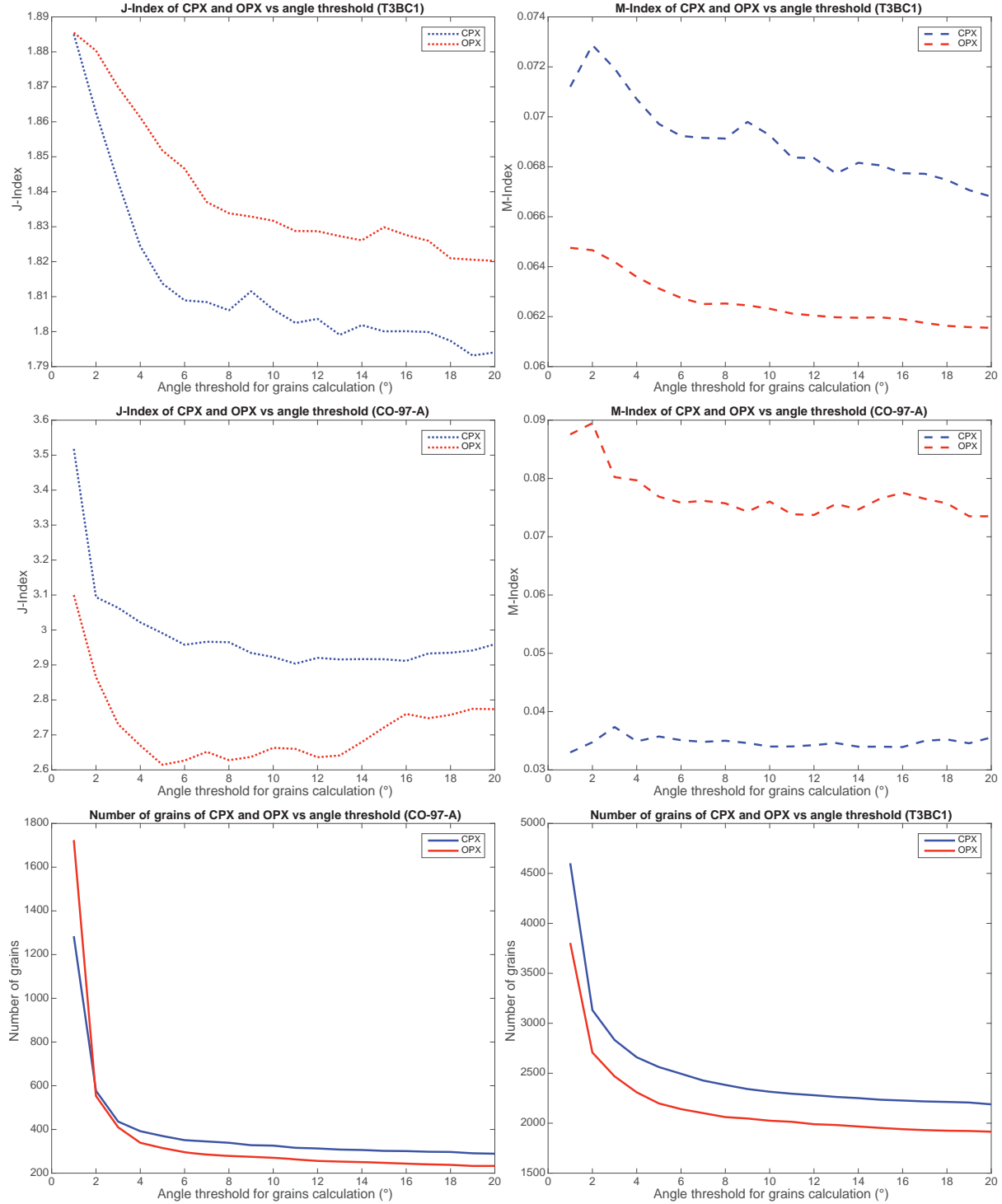


Fig.2.4: J-indices; M-indices and number of grains as a function of the angle threshold for grain calculation for cpx (left) and opx (right) in sample CO-97-A and T3BC1.

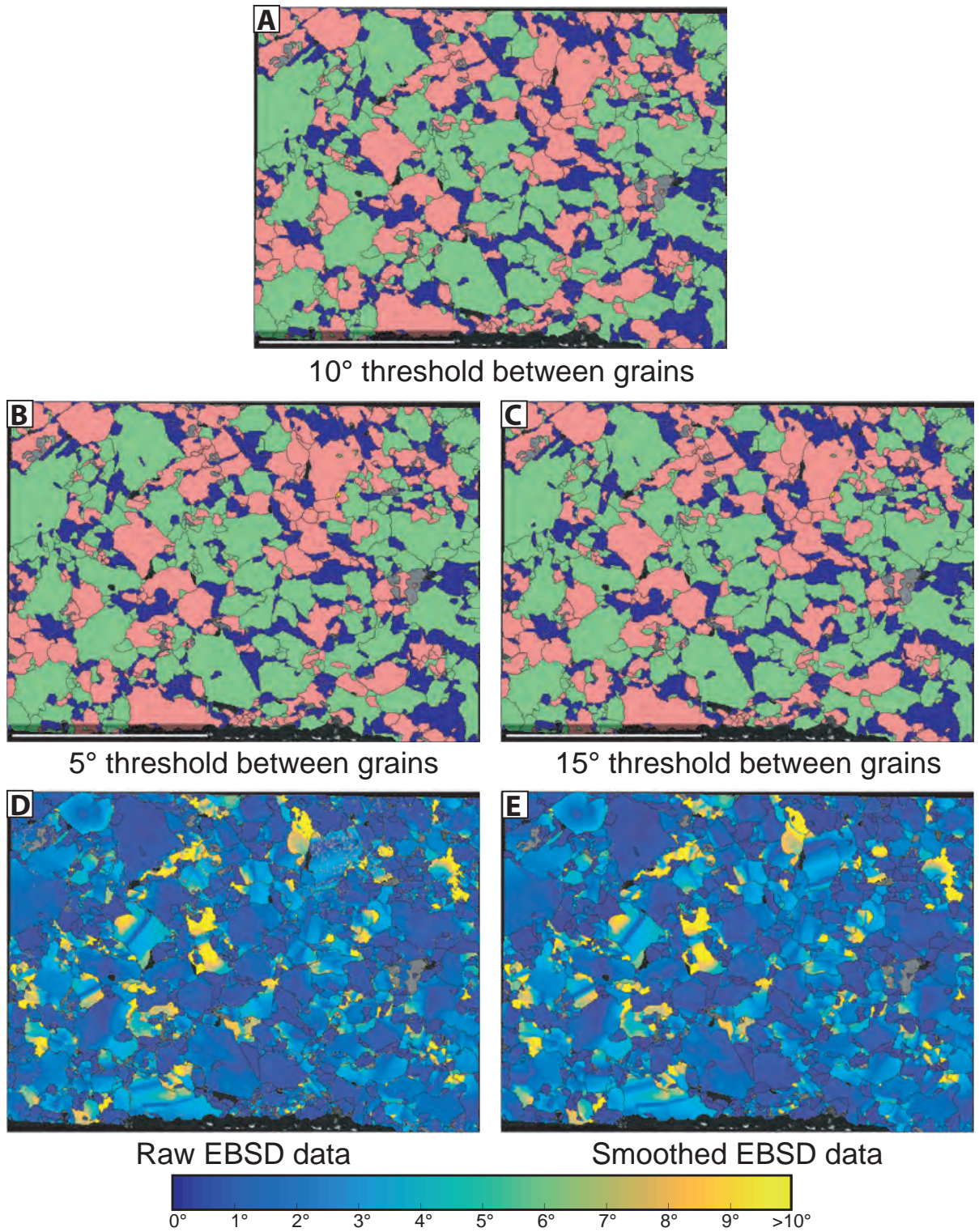


Fig.2.5: Example of different thresholds for grain determination for 10 (A), 5 (B) and 15° (C) impact on phase maps for the same sample (CO-97-A); (D) and (E) display the difference between a raw EBSD dataset and one smoothed using a median filter on the misorientation to mean grain orientation in the same sample.

figure point of view, Fig.2.5 and Fig.2.6 do suggest that the threshold does not change the general texture and interpretation of fabrics if the angle threshold is set above 5° . One can then conclude that using 10° as threshold to reconstruct grains is relevant, for several reasons: (1) it allows for an accurate comparison with previously published studies which uses 10° and (2) it does not introduce any bias from a statistical point of view, thus making it the most appropriate value to use in our case.

Smoothing the grains

In this work, EBSD datasets are smoothed. The choice to smooth was motivated by several reasons: (1) to reduce the noise, (2) to interpolate missing data and (3) to give a more realistic aspect to the results. An example of raw and smoothed data is provided in Fig.2.5. The smoothing can be performed using different filters. The mean filter takes the orientation mean within a certain neighbourhood. It works well with Bingham noise but will smooth away some sub-grain boundaries. The median filter works better for removing outliers but tends to underestimate the local texture gradient. The spline filter automatically calibrates

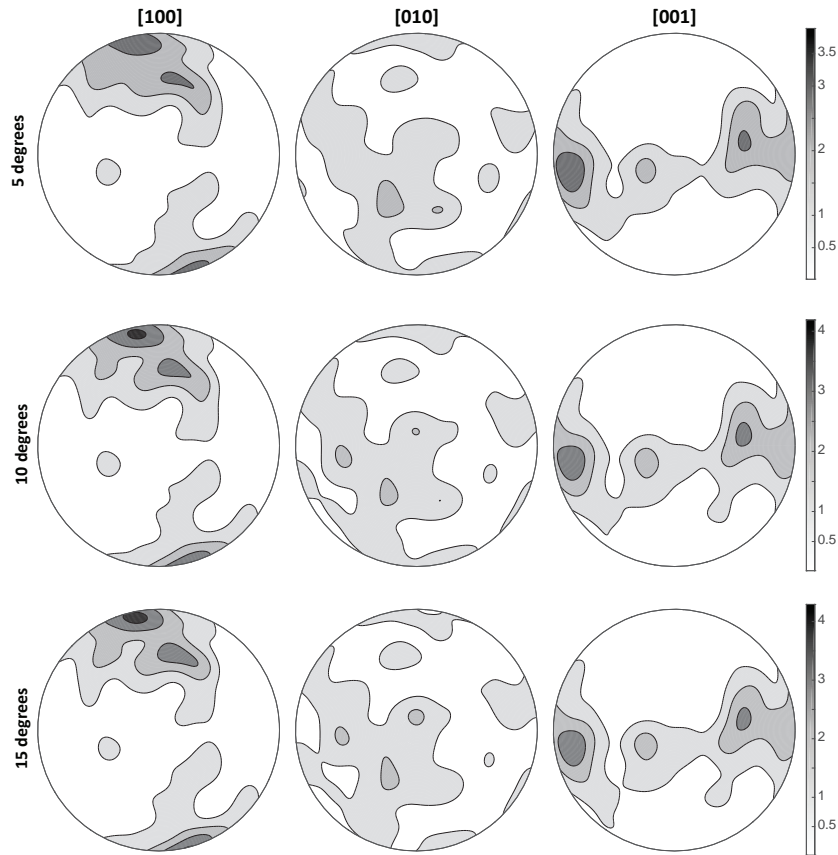


Fig.2.6: One-point-per-grain pole-figures of enstatite in sample CO-97-A calculated with a 5-, 10- and 15-degree threshold for grain differentiation.

the smoothing parameter; it is straightforward and easy for the end user but sometimes may smooth away subgrain boundaries and could result in errors if MTEX cannot calibrate the smoothing parameter. The halfquadratic filter differs from the spline in that it better preserves subgrain boundaries but requires the input of a smoothing parameter. In this work, the median filter was used as no possible computation error or convergence failure could occur using this filter.

2.6 - Some basic mineralogical information relevant to this work

In this work, four main minerals of interest will appear: clinopyroxene, orthopyroxene, olivine and amphibole. From a crystallographic point of view, each of these minerals is described by multiple crystallographic axes (denoted by $[\]$) and the angle between them. The combination of the lengths of the axes and their relative angles will then determine each mineral symmetry (Fig.2.7). The crystal symmetry plays an important role in determining the crystal properties and their behaviour during deformation.

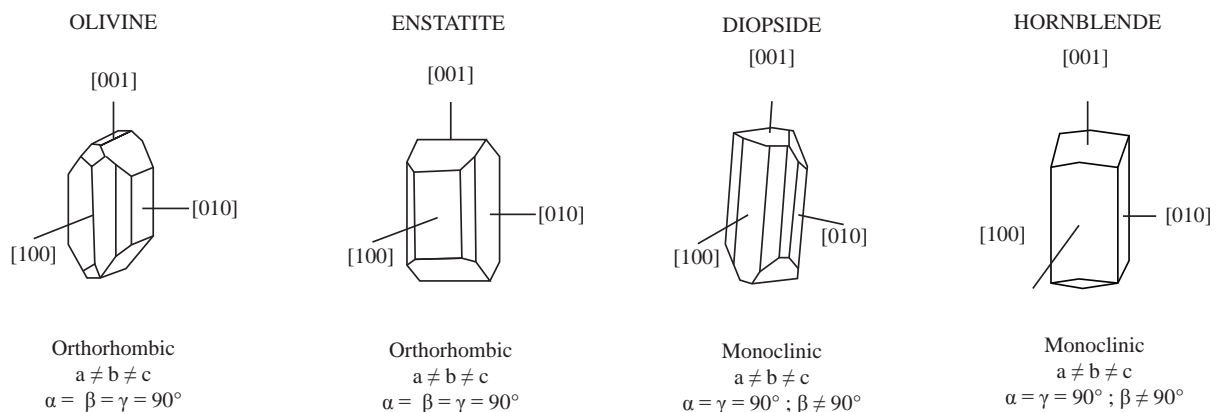


Fig.2.7: Sketches of the 4 minerals of interest in this work. Their respective symmetry, relative axis lengths and angle relationships are displayed.

In a rock, the crystallographic axes of the minerals may not be randomly distributed in space but rather arranged in a certain way. In this case, the mineral is said to have a Crystallographic-Preferred Orientation (i.e. CPO). CPO has traditionally been linked to deformation occurring in the dislocation-creep regime of a mineral. This regime is entered when deformation of the crystal is mainly accommodated by the displacement of imperfections (i.e. dislocations) through the lattice. The couple formed by the plane and the direction in which the dislocation moves relative to the crystal lattice is called a slip system and is denoted [direction](plane) by convention.

In previous studies of microstructures, an obliquity between the XZ plane and the mineral fabric is observed. In this study, we use the fabric obliquity to determine the shear sense by following the principles presented in Bouchez et al. (1983).

During deformation by dislocation creep, several slip systems are activated, but mainly, one will dominate and can be inferred from the analysis of pole-figures. Experimental studies tend to show that the activation of a slip system is a function of several parameters such as the phase symmetry, the pressure, the temperature, the water content or even the intensity of the stress field. Consequently, determination of the activated slip system may help reconstruct the deformation conditions and even reveal a part of a rock's history that is not accessible through geochemistry (e.g. Satsukawa et al., 2015; Henry et al., 2017; Xiong et al., 2017). It is still important to keep in mind that other factors may influence a CPO and care has to be taken when it comes to interpretation of fabrics.

Besides dislocation creep, diffusion creep and sometimes cataclastic flow have been regarded as responsible for the formation or preservation of CPO (e.g. Passchier and Trouw, 1996; Díaz Aspiroz et al., 2007; Skemer and Karato, 2008; Miyazaki et al., 2013). Karato and Ping (1992) interpreted the disappearance of seismic anisotropy at a depth of 200 km as a possible switch from dislocation to diffusion creep as main deformation mechanism thus implying that the shallow part of the upper mantle would be dominated by the dislocation creep. Additionally, efficient deformation by diffusion creep requires temperatures high enough to provide mobility to the atoms thus making diffusion creep not the best candidate to account for plastic deformation of the shallow upper mantle. In this study, as the temperature is either not high enough for efficient diffusion creep to operate or not low enough to produce cataclastic flow and as deformation markers implying deformation in the dislocation creep regime are observed, we will also consider dislocation creep as the main CPO-forming mechanism.

In this section, a brief overview is given of what is known about the deformation behaviour of the four main minerals involved in this study in the framework of the conditions relevant to this work.

Olivine

Easily deformable under mantle conditions, olivine is considered to accommodate most of the deformation in the upper mantle. Dislocation creep (and to a lower extent, diffusion creep, see Miyazaki et al., 2013) is considered to be the dominant fabric-forming mechanism for the shallower upper mantle olivine. The resulting fabrics have been widely used to interpret deformation conditions (Fig.2.8). The most commonly activated slip system in upper mantle olivine is $[100](010)$, which leads the so-called A-type fabric. It was related by several studies to a low-deviatoric stress, high-temperature ($>1000^{\circ}\text{C}$) environment of deformation (Nicolas and Christensen, 1987; Ismaïl and Mainprice, 1998). The B-type fabric, which is attributed to the activity of $[001](100)$ slip, is produced in different contexts: (1) during the A- to B-type transition upon a decrease in temperature and/or an increase in stress (Carter and Avé Lallemant, 1970); (2) at high temperatures with increase in the olivine water content and a possible increase of stress (Jung and Karato, 2001); (3) at pressures greater than 3 GPa in a dry environment (e.g. Jung et al., 2009; Ohuchi et al., 2011); (4) between 5 and 8 GPa with a relatively low proportion of opx (Soustelle and Manthilake, 2017). The A- to B-type transition in olivine has been proposed as an explanation for the switch in the direction of the fast seismic velocity direction from trench-normal to trench-parallel at the volcanic front in subduction zones. Besides A- and B-type olivine, other less frequent fabrics such as C-, D- and E-type olivine have been reported (see Michibayashi and Oohara, 2013 and Fig.2.8). C-type was observed to form (1) at low temperature and high strain rate (Carter and Avé Lallemant, 1970); (2) at higher water content than A-type in the A-type stability field (i.e. >800 ppm H/Si, Jung and Karato, 2001) or (3) during high pressure flow where the water solubility is enough to keep $[001](100)$ slip active (Couvry et al. 2004). D-type was observed in several environments and could be indicative of (1) deformation at low/moderate stress and temperatures $\sim 900^{\circ}\text{C}$ (Michibayashi and Oohara, 2013); (2) deformation at low temperatures (750°C) under high-stress conditions such as in lithospheric shear zones (Park and Jung, 2017) or (3) in similar conditions as A-type but in a deformation regime involving intense simple shear, forcing the dislocations to move on both (010) and (001) planes. E-type olivine fabric remains still unclear today. It was reported during (1) deformation at high stress and temperatures $\sim 900^{\circ}\text{C}$ (Michibayashi and Oohara, 2013); (2) high-temperature deformation with a high melt content (Tommasi et al. 2006) and (3) at low temperature during the mechanical weakening of a pre-existing anisotropy (Michibayashi and Mainprice, 2004).

010-fibre fabric may develop under a range of conditions. Experimental studies reproduced this fabric (with a strong linear component for [001]) by performing axial compression at low temperature and activation of (110)[001] (e.g. Carter and Avé Lallemant, 1970). At high

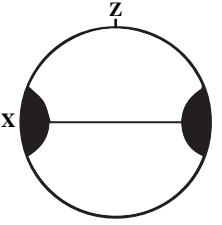
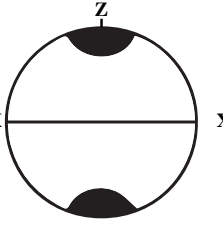
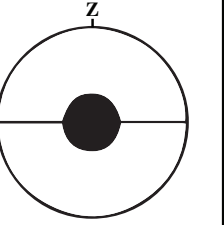
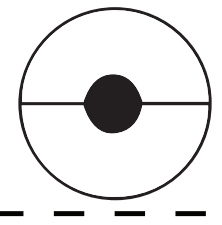
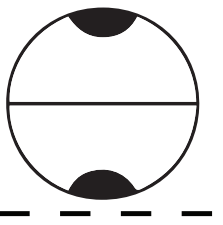
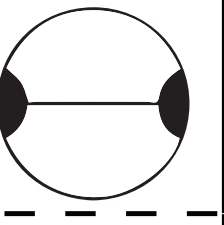
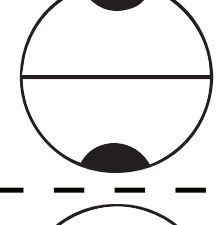
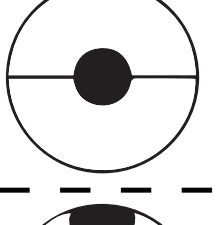
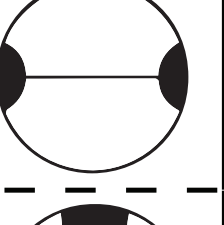
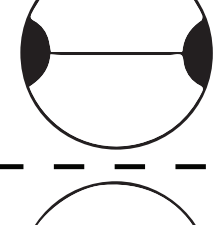
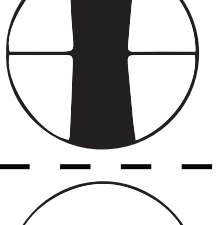
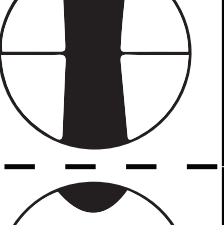
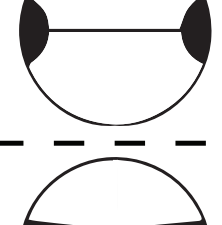
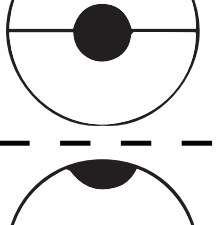
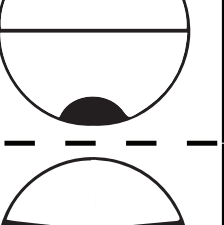
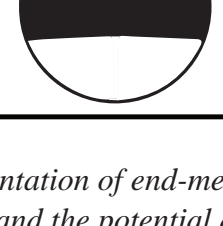
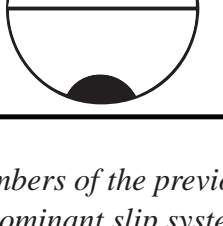

Olivine Fabric type	Pole figure in the XZ plane			Slip system
	[100]	[010]	[001]	
A-type				[100](010)
B-type				[001](010)
C-type				[001](100)
D-type				[100](0kl)
E-type				[100](001)
010-fibre				[h0l](010) [001](110)

Fig.2.8: Representation of end-members of the previously reported fabrics of olivine in the XZ reference frame and the potential dominant slip system responsible for it.

temperature, axial compression or transpression are likely mechanism to create 010-fibre (i.e. Tommasi et al., 1999). Transition between A- and B-type fabric are also likely to result in 010-fibre when slip direction change over between [100] and [001], this includes deformation with interstitial melt, change of pressure or both (e.g. Holzmann et al., 2003, Vauchez et al., 2005; Mainprice et al., 2005).

Enstatite

In peridotites, high-temperature deformation of opx is typically accommodated by slip along [001](100), forming an AC-fabric sensu Jung et al. (2010) (Fig.2.9). The commonly observed glide along the [001] axis can be understood from the crystal structure, as [001] is the shortest Burgers vector in the orthopyroxene. The appearance of [001](010) (BC-Type fabric, Fig.2.9) has been observed in natural specimens as well as in experimental studies and was suggested to be potentially related to a strain rate greater than 40% (i.e. Mercier and Nicolas, 1975; Ross and Nielsen, 1978; Nicolas and Christensen, 1987; Soustelle et al., 2010; Frets et al., 2012). Simple kinking has been described in natural enstatite crystals and

OPX Fabric type	Pole figure in the XZ plane			Slip system
AC-type				[001](100)
BC-type				[001](010)
ABC-type				[001](hk0)

Fig.2.9: Representation of end-members of the previously reported fabrics of enstatite in the XZ reference frame and the potential dominant slip system responsible for it.

because of the orthorhombic symmetry, the gliding is two-sided so that conjugate kink-bands have to be expected (Starkey, 1968). Manthilake et al. (2013) showed that a change in Al_2O_3 and H_2O content leads to a change in crystallographic preferred orientation: (010) replaces (100) as the active gliding plane when aluminum is incorporated into the crystallographic structure. However, on the introduction of H_2O in an aluminum-rich orthopyroxene, the (010) activity decreases and (100) again becomes the dominant slip system. ABC-type fabric sensu Jung et al. (2010) is characterised by a weak concentration of both [100] and [010] next to the foliation pole and [001] along the lineation direction. It is still poorly understood and no hypothesis on the activated slip system or the environment of formation were formulated yet.

Diopside

The pioneering study of Avé Lallemant (1978) was amongst the first to explore deformation processes in natural websterites and more particularly, in clinopyroxene. He showed that under high-temperature conditions (above 1050°C), the deformation of the volumetrically dominant clinopyroxene is mostly accommodated by dislocation creep through non-selective translation gliding, polygonization and syntectonic recrystallization; at lower temperature, mechanical twinning is activated. Similar conclusions were reached by Kirby and Kronenberg (1984), who observed the activation of kink bands and twinning at low temperature as well as a switch to subgrain rotation and recrystallization at temperatures higher than 1000°C . Because of the similar lattice geometry of omphacite and diopside, the numerous studies on eclogites may be extrapolated to understand diopside deformation (Bascou et al., 2002). Consequently, omphacite fabrics characterized by Helmstaedt et al. (1972) and Zhang et al. (2006) can therefore be used to understand mantle cpx and provide insights on the deformation regime. The L-type fabric (Fig.2.10) displays [001] axes clustered next to the lineation while the [010] axes form a girdle in the plane normal to the lineation; the S-type fabric is characterized by [010] clustering next to the foliation pole and [001] forming a girdle in the foliation plane, and the SL-type fabric is similar to a [001](010) fabric. These three types of fabric respectively testify to either axial compression, shear or both. A strong [010] cluster next to the foliation pole was identified as the consequence of slip along {110} planes at high temperature ($>1000^\circ\text{C}$) where [001]{110}, and $1/2 \langle 110 \rangle$ {110} are particularly active (Bascou et al., 2002; Amiguet et al., 2010). Dominance of the $1/2 \langle 110 \rangle$ {110} duplex during plastic deformation at shallow depth will result in a clustering of [100] axis along the foliation

CPX Fabric type	Pole figure in the XZ plane			Slip system
S-type	[100]	[010]	[001]	$1/2\langle 110 \rangle\{110\}$ and / or $[001]\{110\}$
L-type				$1/2\langle 110 \rangle\{110\}$ and / or $[001]\{110\}$
SL-type				$1/2\langle 110 \rangle\{110\}$ and / or $[001]\{110\}$
ABC-type				$1/2\langle 110 \rangle\{110\}$
AC-type				$[001](100)$

Fig.2.10: Representation of end-members of the previously reported fabrics of diopside in the XZ reference frame and the associated dominant slip system responsible for it.

pole and form what can be called a ABC-fabric (Fig.2.10). At lower temperatures ranging from 900 to 1000°C, $[001](100)$ slip was shown to be activated and dominant thus resulting in what can be referred to as a AC-type fabric (Fig.2.10, Raterron et al., 1994). Diopside rheological law of clinopyroxenes aggregate suggest that deformation by dislocation creep below 700°C requires unreasonable stress and/or low strain rates making diopside fabrics a powerful indicator of high-temperature deformation events.

Rooney et al. (1975) performed plastic deformation experiments on hornblende and observed that mechanical twinning on (-101) is the major deformation mechanism at low temperature. At high temperature and/or low stress, several slip systems are activated: [001](hk0), [001](100), [100](010) and $\langle 110 \rangle_{1/2} \langle -110 \rangle$ (e.g. Dollinger and Blacic, 1975; Rooney et al., 1975; Biermann and Van Roermund, 1983). Twinning deformation in naturally deformed hornblende is uncommon because of the inherent strength of the mineral and the relatively high stress required for twinning. Translation gliding operates on [001](100) at a temperature $< 800^\circ\text{C}$ and pressure of 0.5 to 2 GPa (e.g. Dollinger and Blacic, 1975; Rooney et al., 1975; Berger and Stünitz, 1996). Recently, Ko and Jung (2015) showed the dependence of the amphibole CPO to the temperature and differential stress and highlighted their relationships with [001](100), [010](100) and [0kl](100).

Summary of Chapter 2

*The **EBSD** experimental protocol used for this study was given in detail.*

*The choice to work with **MText** was explained and a script for **routine plotting of EBSD data** was described.*

*The choice of using a minimum **misorientation angle of 10°** to define grain boundaries during data processing was discussed and tested. The results suggest that **10° is consistent both from a petrological and statistical perspective.***

Chapter 3:
The Microstructure of
Cabo Ortegal Pyroxenites

3.1 - A short introduction to the geology of NW Iberia

Galicia and northern Portugal host a remarkable assemblage of ancient subducted oceanic and continental lithosphere in what is known as the “allochthonous complexes of North-West Iberia” (e.g. Ábalos et al., 2003). The different complexes make up a large portion of the region and are scattered over several hundred square kilometres. The whole Allochthonous Complex is composed of three main slices: the upper allochthonous unit, the ophiolitic unit and the lower allochthonous unit.

Paleo map-reconstructions by Stampfli and Borel (2002) illustrate the evolution of the NW Iberian terranes, before their emplacement during the Variscan orogenesis, relative to the Gondwana-Laurussia reference frame (Fig.3.1). A regional geodynamic reconstruction proposed by Martínez Catalán et al. (2009) suggests that today’s structure and the emplacement of the allochthonous complexes are well explained by a series of subduction zones coupled with the openings and closing of different paleo-oceans (Fig.3.2). Separation of the Upper Allochthonous Units (i.e. UAU) from the Gondwana margin around 490 My is consistent with the opening of the Rheic ocean. Expansion of the Rheic ocean lead to the accretion of the UAU against the margin of Baltica, and eventually the accretion of Baltica itself to the Laurussia continent. Between 400 and 385 Ma, the opening of the Rheic ocean ceased and an intra-oceanic, west-dipping, subduction started. This new context eventually led to the collision of Gondwana and Laurussia and to the creation of the Variscan orogen. The collision of these continental masses is considered to be responsible for the accretion of the 3 main allochthonous units together and their subsequent preservation from recycling due to their obduction on to the margin of Gondwana (Martínez Catalán et al., 2009; Weil et al., 2013).

3.2 - The Cabo Ortegal Complex: A four-piece puzzle

Amongst the upper allochthonous unit, which is mainly composed of island-arc-related material, the Cabo Ortegal complex crops out at the most south-western point of the Bay of Biscay. This large complex is composed of four units (Ábalos et al., 2003), each made of different lithologies: gneiss, eclogite, granulite and peridotite. In this section, a description of the four units is given with an emphasis on the peridotitic section (Fig.3.3).

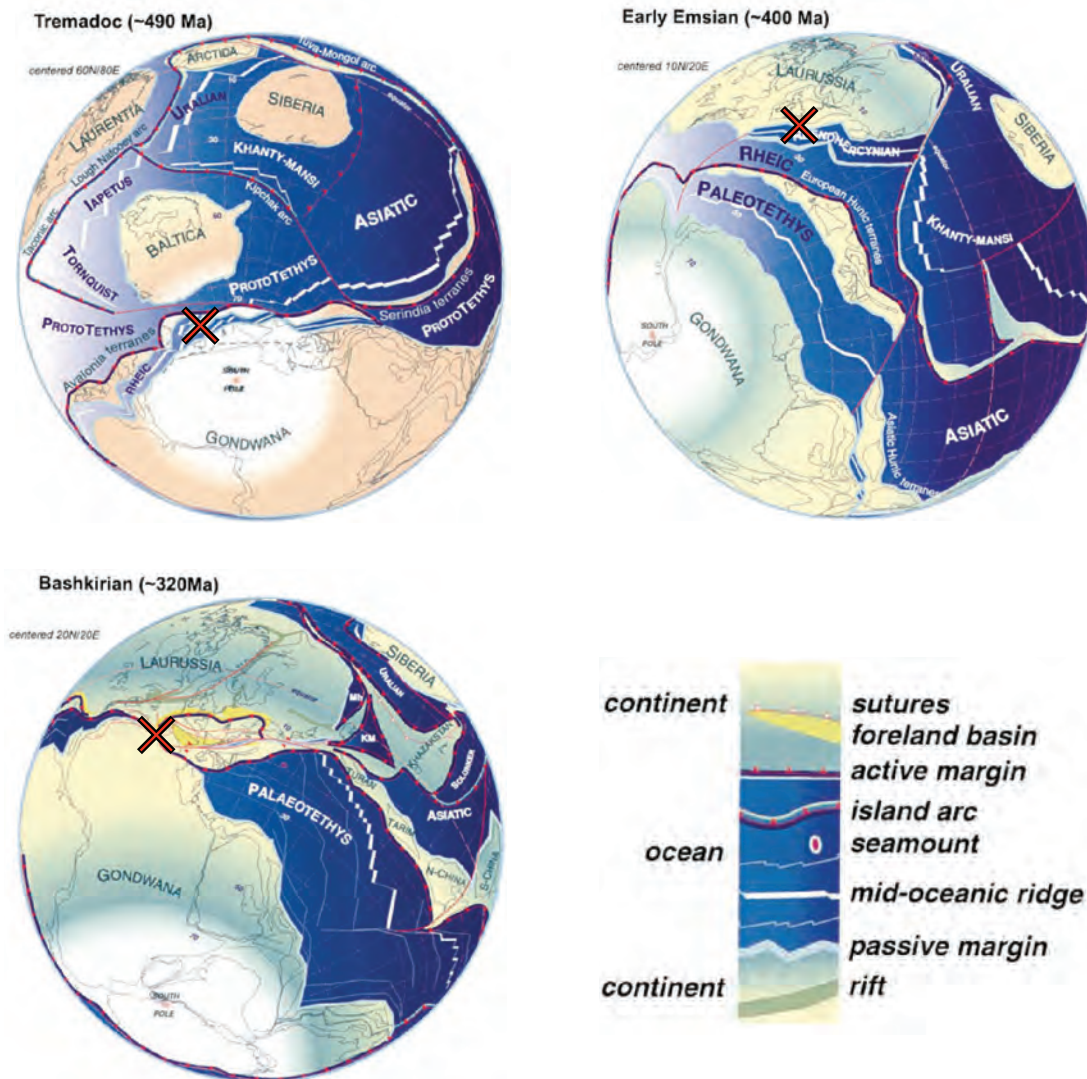


Fig.3.1: Paleo map reconstruction showing the Gondwana-Laurussia evolution and collision where the Cabo Ortegal complex originated, after Stampfli and Borel (2002). The red cross is a speculative position of the Upper Allochthonous complex at each time step.

High-pressure gneisses

The underlying unit of the Cabo Ortegal complex, first described by Vogel (1967), is composed of three high-pressure gneiss formations (i.e. Chimparra, Carino and the Banded Gneisses), each displaying various intercalations of mafic rocks interpreted as former dykes or sills. Calculated thermo-barometric conditions of peak metamorphism are 715°C and 1.6 GPa. Intercalations of plagioclase granulite are estimated to have formed at 695°C-755°C and 1.45-1.55 GPa. The age of HP metamorphism is estimated at 392 ± 27 Ma (Ordóñez Casado et al., 2001) and 382 ± 3 Ma (Vaquero and Fernández, 1996). Crustal detrital components derived from Gondwanan sources (2.5 Ga and 515 ± 15 Ma) were also found by these authors (Ábalos et al., 2003).

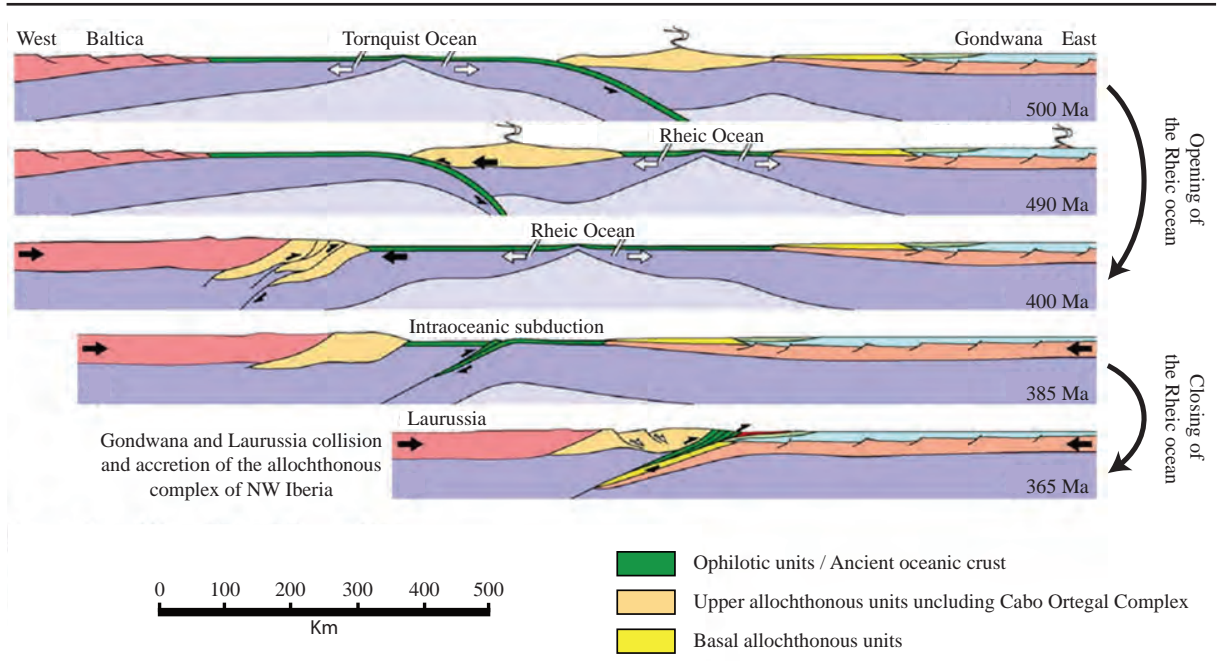


Fig.3.2: Geodynamic evolution of the Cabo Ortegal complex, modified after Martínez Catalán et al. (2009).

Eclogitic unit

Eclogites crop out as a 100-700m-thick slab. They are interpreted as ancient oceanic basalts affected by high-temperature and high-pressure metamorphism (ca 790°C, 17 kbar Gil Ibarguchi et al., 1990). Undeformed and deformed eclogites are the two facies encountered in this unit (Ábalos et al., 2011). U-Pb dating of magmatic zircons from massive and deformed eclogite gave ages of 507 ± 17 Ma and 473 ± 9 Ma respectively (Ordóñez Casado et al., 2001). The metamorphism of the MORB-like protolith has been dated circa the same era of ~480 Ma (Peucat et al., 1990).

High-pressure granulite unit

Granulites crop out in the southern part of the complex and in the surroundings of the peridotites massifs. Contacts with the overlying peridotites are marked by strong mylonitisation. Several facies are observed: granulitic orthogneiss, ultramafic granulites, Mg-rich granulites, intermediate and mafic granulites (Ábalos et al., 2011). This unit is considered by Peucat et al. (1990) and Gil Ibarguchi et al. (1990) to be the metamorphic product of supra subduction material (possibly a volcanic arc) close to a continental margin that formed 482-490 My ago. The HP-HT metamorphic event (ca 800°C, 13,5 kbar Girardeau et al., 1990)

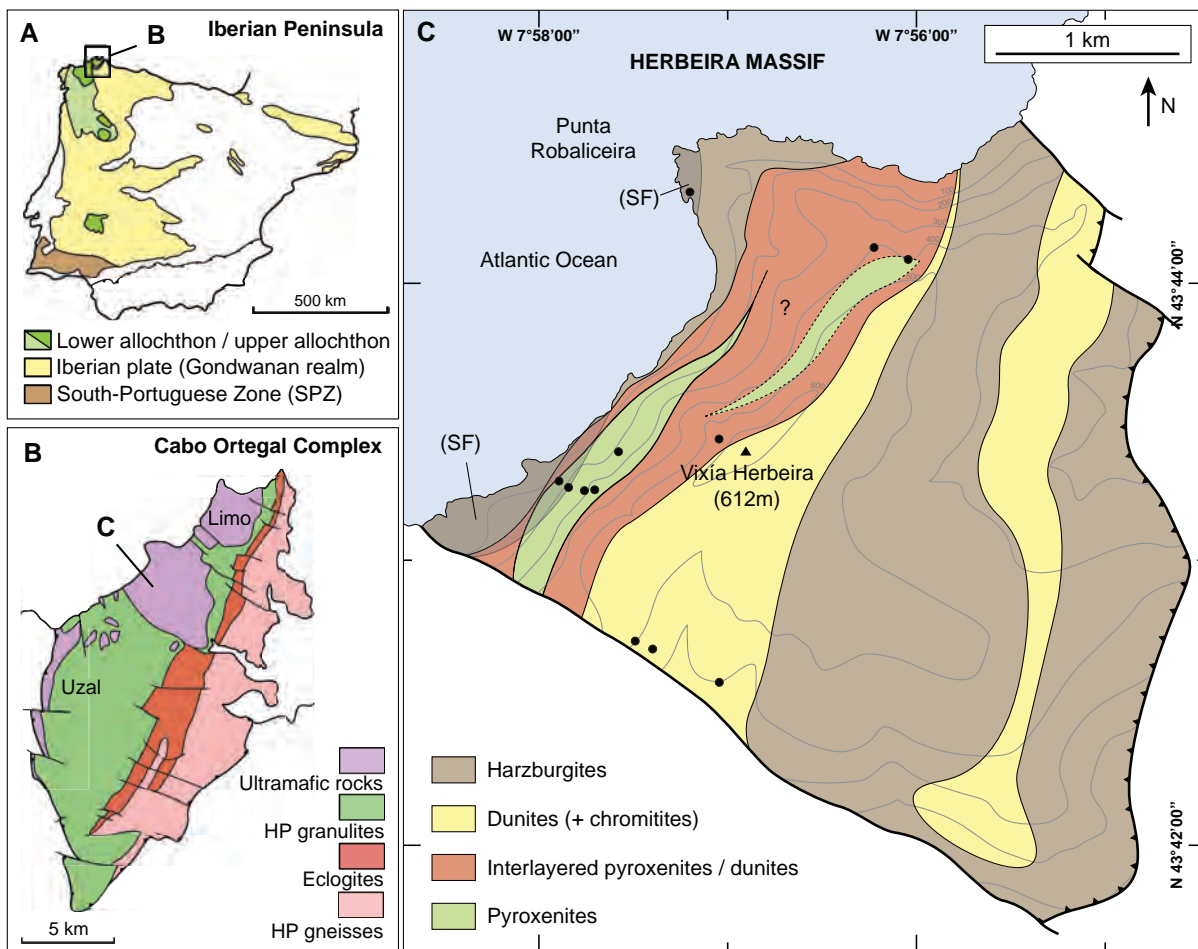


Fig.3.3: (A): location of the Cabo Ortegal Complex on the Iberian Peninsula (after Puelles et al., 2012); (B): simplified map of the high-pressure units of the Upper Allochthon (after Llana-Fúnez et al., 2004); C: geological map of the Herbeira massif (modified after Tilhac et al., 2016). SF indicates the areas where sheath folds have been observed. Selected samples locations are indicated by the black dots. The black triangle indicates the Herbeira massif highest point. Outline of the eastern dunite body after Puelles et al. (2012).

forming the granulites is estimated to have occurred 470-480 My ago (U-Pb on zircon and monazite Peucat et al., 1990).

Peridotite units

Ultramafic rocks extend over 25 km² and lie on top of the three units described above. Peridotites are found in three separate massifs (from south to north: Uzal, Herbeira and Limo, Fig.3.3-B); all of them are in contact with granulites. Mantle rocks are harzburgite and dunite, with frequent pyroxenite layering. We will focus the description on the two largest massifs: Limo and Herbeira.

The Limo massif extends over 6.6 km² and is composed of harzburgite with rare pyroxenite layering. It has been initially described as a rather homogenous harzburgite from both petrological and structural point of view (Jamaa, 1988; Girardeau et al., 1990). However, recent studies using mineral fabrics showed that the Limo peridotites underwent a complex deformation history, and retain evidence of high-temperature - low-stress deformation and low-temperature - high-stress with high shear-strain deformation in the form of sheath folds (Puelles et al., 2012). Retrograde metamorphism in the amphibolite facies was dated between 430 and 390 My (Van Calsteren et al., 1979; Peucat et al., 1990).

The Herbeira massif is by far the most spectacular massif. It extends over 15.5 km² and its morphology exposes a cross section through the ~N30°/30°SE foliated structure of the unit. Our measurements of foliations and lineations, despite some strong and very local variations, lie within the range of previously published orientations of ~N25°/30SE (Girardeau and Gil Ibarguchi, 1991; Ábalos et al., 2003).

At the top of the massif, on the Herbeira plateau, *the first unit of harzburgites* with low volumes of pyroxenites crops out with some minor dunite (Fig.3.3). Sub-spherical, 5-10 mm opx (10-30% modal) and some very rare cpx are observed inside the strongly serpentinized olivine matrix. Rarely, chromite-rich/chromitite can be observed (Tilhac, 2017).

The second unit crops out sequentially lower in the cliff. It can be divided into 3 subunits. The first and last subunit consists of a dunite-dominated domain in diffuse contact with the uppermost and lowermost harzburgite from the first unit and presenting more frequent pyroxenite layers (Fig.3.3). They both sandwich an approximately 300- to 400m-thick subunit of pyroxenites with minor dunites. This subunit includes a lens-shaped pyroxenite-rich body. It extends over 3 km in length with a variable thickness between 50 to 300 meters (Fig.3.3, Girardeau and Gil Ibarguchi, 1991). Field observations from this study support formation as a combination of multiple smaller bodies rather than a single homogeneous lens.

The third unit of the Herbeira massif is located at the base of the Herbeira cliff where harzburgite with pyroxenites crops out. Sheath folding and mylonites are common and amphibole are more abundant than in the overlying layers.

In the Herbeira massif, pyroxenite layers display sharp contacts with their host rock. They very commonly show boudinage and isoclinal folds. In the third unit, sheath folds are clearly delineated by the pyroxenite layers. Despite the strong deformational overprint, the lateral extent of some pyroxenite layers can exceed 100 m (Girardeau et al., 1989). The pyroxenites are mostly clinopyroxenites and websterites with some minor orthopyroxenites (Tilhac, 2017). Amphibole is always present in pyroxenites with different proportions that may depend on the sample location in the massif. Overall, the estimated volume of pyroxenites (20% opx, 80% cpx) accounts for 35 to 40% of the volume the whole massif.

3.3 - What has been reported previously regarding the deformation?

Microstructures observed in the high-grade metamorphic and mantle rocks cropping out at Cabo Ortegal are strongly affected by the successive deformation episodes. Ábalos et al. (2003) reported a series of deformation events that led to the present-day state of the Cabo Ortegal peridotite. It includes high-pressure deformation events ($D1_{HP}$ and $D2_{HP}$) and exhumation-related deformation (D_3 and D_4) visible in the granulites, gneiss, peridotites and eclogites of the Cabo Ortegal complex. In addition, the ultramafic massifs underwent an extra high- temperature deformation episode (D_{HT}) before recording the common Cabo Ortegal high-pressure history (Fig.3.4). Below, a description of the deformation is presented, with emphasis on the ultramafic unit.

D_{HT} deformation was recorded in the harzburgite, dunites and pyroxenites. This high-temperature ($>1000^{\circ}\text{C}$) shear deformation led to the formation of a tectonic foliation parallel to the compositional layering of the ultramafic massif (spinel and orthopyroxene stretching lineation trending $N10^{\circ}-30^{\circ}$), a porphyroclastic microstructure with an olivine and pyroxene preferred orientation, isoclinal folding and boudinage of the compositional layering (Girardeau and Gil Ibarguchi, 1991).

$D1_{HP}$ deformation is visible near the contacts with structurally underlying granulites and is recorded by mylonitic bands. Sheath folding is associated with this deformation episode. In the pyroxenite sheet, $D1_{HP}$ is recorded by pyroxenite and garnet-rich dykes injected into fractures either parallel or oblique to the D_{HT} layering. Microstructural and petrofabric data indicate that this deformation occurred at $\sim 800^{\circ}\text{C}$ (Ábalos et al., 2003).

$D2_{HP}$ deformation is represented by the isoclinal folding of the Uzal Peridotites. This deformation episode is likely to be related to early stages of the exhumation processes.

Later deformations, recorded by the whole complex, occurred first under amphibolite-facies conditions (D3) and later in the greenschist-facies (D4). However, these deformations are outside the scope of this study.

3.4 - Previous microstructural studies in Limo and Herbeira massif

The structure and microstructures of the Limo massif were examined by Puelles et al. (2012). Unlike Herbeira, Limo does not display meter-scale pyroxenite-rich layers. Field evidence of high-temperature and high-pressure deformation were reported (e.g. sheath folds, boudinage). Petrofabric analysis displayed A- and B -type fabrics for olivine (Jung and Karato, 2001), an L-type fabric for Cpx (Helmstaedt et al., 1972) and an AC-type fabric for Opx (Jung et al., 2010). Puelles et al. (2012) reported a mimicking of the Cpx fabric by the amphibole, suggesting epitaxial growth of amphibole during static replacement of the primary Cpx.

In the Herbeira massif, similar high-temperature and high-pressure deformation markers (i.e. boudinage, isoclinal folds and sheath folds) have been reported and are common in the Herbeira cliffs (Jamaa, 1988; Girardeau and Gil Ibarguchi, 1991). Fabrics of olivine from harzburgite analysed by Jamaa (1988) reveal a [100](010) fabric in olivine, suggesting the activation of [100](010) slip. The same study also reported a [100](001) fabric for olivine in mylonitic samples.

3.5 - What is observed in massifs analogous to Cabo Ortegal?

So far, only few microstructural studies of natural pyroxenites have been carried out. Frets et al. (2012) observed in the Beni Boussera massif, Morocco, that dynamic recrystallization by subgrain rotation, grain-boundary migration and recovery plays a major role in the deformation of websterites at high-temperatures (1100-1150°C and 1.8 GPa). Their observations also suggest that [001]{110} slip in cpx and both [001](100) and [001](010) in opx were activated. Muramoto et al. (2011) studied garnet pyroxenites from the Higashi-akaishi peridotite, Japan, and showed that [001](100) was dominant at 700-800°C and 3 GPa and was consistent with minor activation of [100](010) and $\langle 110 \rangle$ {110} (Bascou et al., 2002).

3.6 - What geodynamic scenario for the Cabo Ortegal complex?

Ábalos et al. (2003) provided comprehensive pressure-temperature-time paths of the different units of the Cabo Ortegal complex (Fig.3.4). The gneiss, granulite and eclogite units were subject to a prograde metamorphic episode followed then by a retrograde metamorphism with a peak at ~1.8 GPa and ~800°C at 390 My (Tilhac et al., 2017).

The scenario proposed by Ábalos et al. (2003), Martínez Catalán et al. (1996) and Martínez Catalán et al. (2009) explains the P-T-t paths and the field and microstructure observations by suggesting the dragging of the granulite, eclogite and gneiss units in a subduction zone and more specifically in a subduction conduit. The subduction conduit is a region, above the subduction channel and below the undeformed lithosphere, in which material slowly accumulates by tectonic underplating (Fig.3.5, Beaumont et al., 1999). This idea is consistent with the steady increase in P/T conditions reported in the prograde metamorphism.

What happened to the peridotite massifs during that period is unclear. Tilhac et al. (2016) using geochemical data, proposed that the increase in pressure recorded in the Herbeira massif might have been triggered by delamination of the massif from an arc root because of the density anomaly produced by the enrichment in pyroxenites. However, additional constraints on that period are needed to better understand the processes at work during the D_{HT} phase.

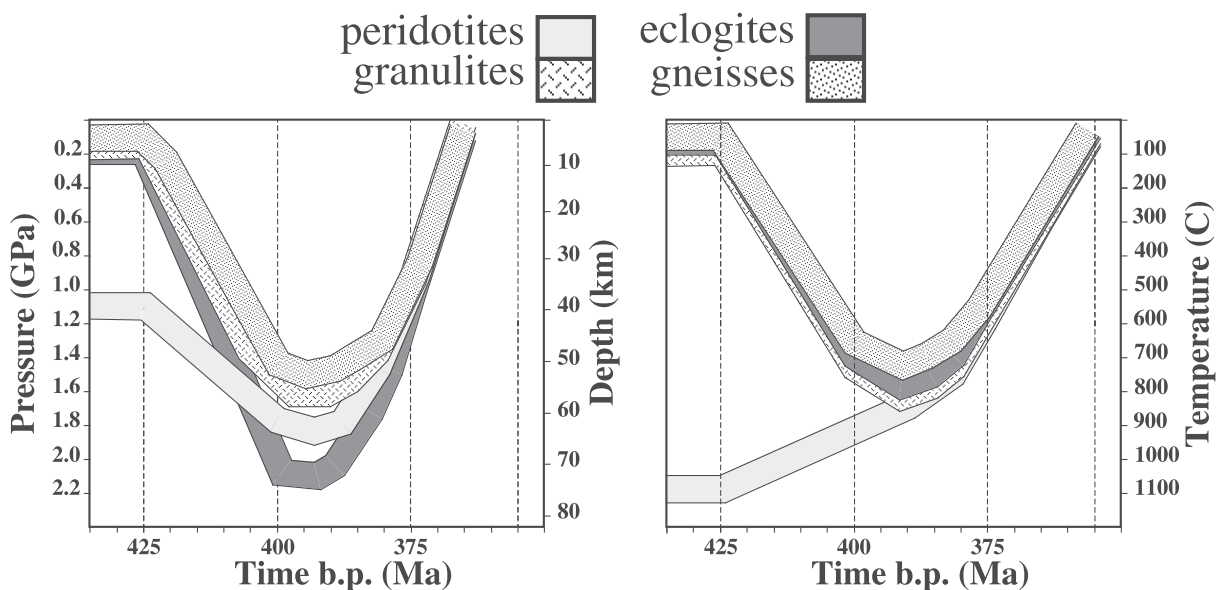


Fig.3.4: Pressure, temperature and time path of the Cabo Ortegal units reconstructed by Ábalos et al. (2003).

Once merged in the subduction conduit ($D1_{HP}$), the exhumation of the whole complex is hypothesised to have been driven by a combination of two processes: a subduction return flow followed by an orogenic event.

In a subduction channel, the hydration of the hanging wall of the mantle wedge and of the top part of the oceanic crust result in the crystallisation of serpentine. Because of (1) its relative low density and softness in regards to the rigid slab and mantle wedge and (2) its triangle shaped geometry related to the hydration front, the material in the channel is forced upward (Fig.3.5, Gerya and Stöckhert, 2002; Gerya et al., 2002; Nakajima et al., 2006). Abalos et al. (2003), based on the nature of the tectonic melange in the Cabo Ortegal complex, proposed that the complex first experienced exhumation upon introduction in a subduction return flow in the subduction channel. This process would have been active until the subduction stopped and a collision and orogenic event took over as suggested by the extensional features observed in the field that would suggest syn-orogenic extension and uplift of the province.

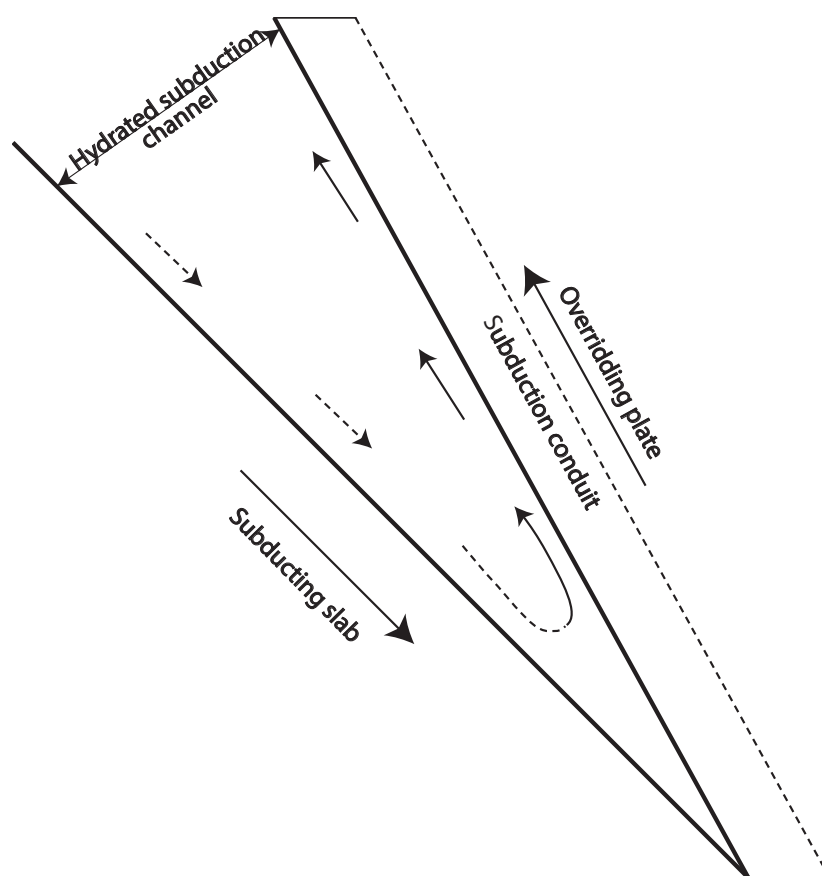


Fig.3.5: Sketch of a subduction return flow principle. The geometry of the hydrated subduction channel and the associated viscosity drop allow for an upward material flow between the subduction plate and the over-riding plate.

3.7 - What can be done with Herbeira pyroxenites?

Studying the Cabo Ortegal pyroxenites (more specifically the Herbeira pyroxenites) will provide several interesting outcomes:

(1) The Herbeira massif is an exceptional opportunity to understand how a pyroxene-dominated domain has accommodated deformation in several environments (i.e. upper mantle, mantle wedge and subduction channel).

(2) The microstructure of the Cabo Ortegal pyroxenites can be used to model the seismic properties of the samples. In Chapter 5, the fabrics will be used to model a pyroxenite-rich domain in order to better constrain the contribution of lithological heterogeneities to the seismic signal arising from the upper mantle.

3.8 - Sample selection

Pyroxenite layers were sampled along two cross sections: one along the Punta Robaliceira and another along the Vixia Herbeira. Sampling was focused on the contacts between dunite and pyroxenites to observe the two lithologies and shear senses more easily. The rock samples were oriented and treated according to the principles explained in Chapter 1 regarding the collection of oriented samples.

28 samples were selected for EBSD analysis and a set of 16 samples was selected for very detailed study. They are representative of the work of Tilhac et al. (2016) and provide geochemically well-characterised samples, comprising 10 from the pyroxenite-rich area and 6 chosen from different parts around the massif (Fig.3.3). Due to their very high degree of serpentinization, dunites and harzburgites were not included in this study. Pyroxenites are less affected by low-temperature alteration and offer excellent material for textural and EBSD studies. Each selected sample satisfies the petrological requirement to belong in one of the pyroxenite type defined by Tilhac (2017) and Tilhac et al. (2016) described below:

(1) *Type-1* pyroxenites include olivine-clinopyroxenites and websterites with dunitic lenses observable at both outcrop and thin-section scales (Fig.3.6-A and D).

(2) Massive olivine-free websterites (i.e. with higher opx/cpx ratios) and devoid of dunite lenses are classified as *type-2* pyroxenites (Fig.3.6-B and E).

(3) *Type-3* pyroxenites include foliated clinopyroxenites and few websterites, commonly strongly amphibolitized (Fig.3.6-C and F).

(4) *Type-4* pyroxenites represent uncommon orthopyroxene-rich websterites and orthopyroxenites.

Pictures of the samples, thin-sections, processed EBSD (including number of grains, J and M-index and other statistical values) and field data are provided as appendices and in the electronic appendices.

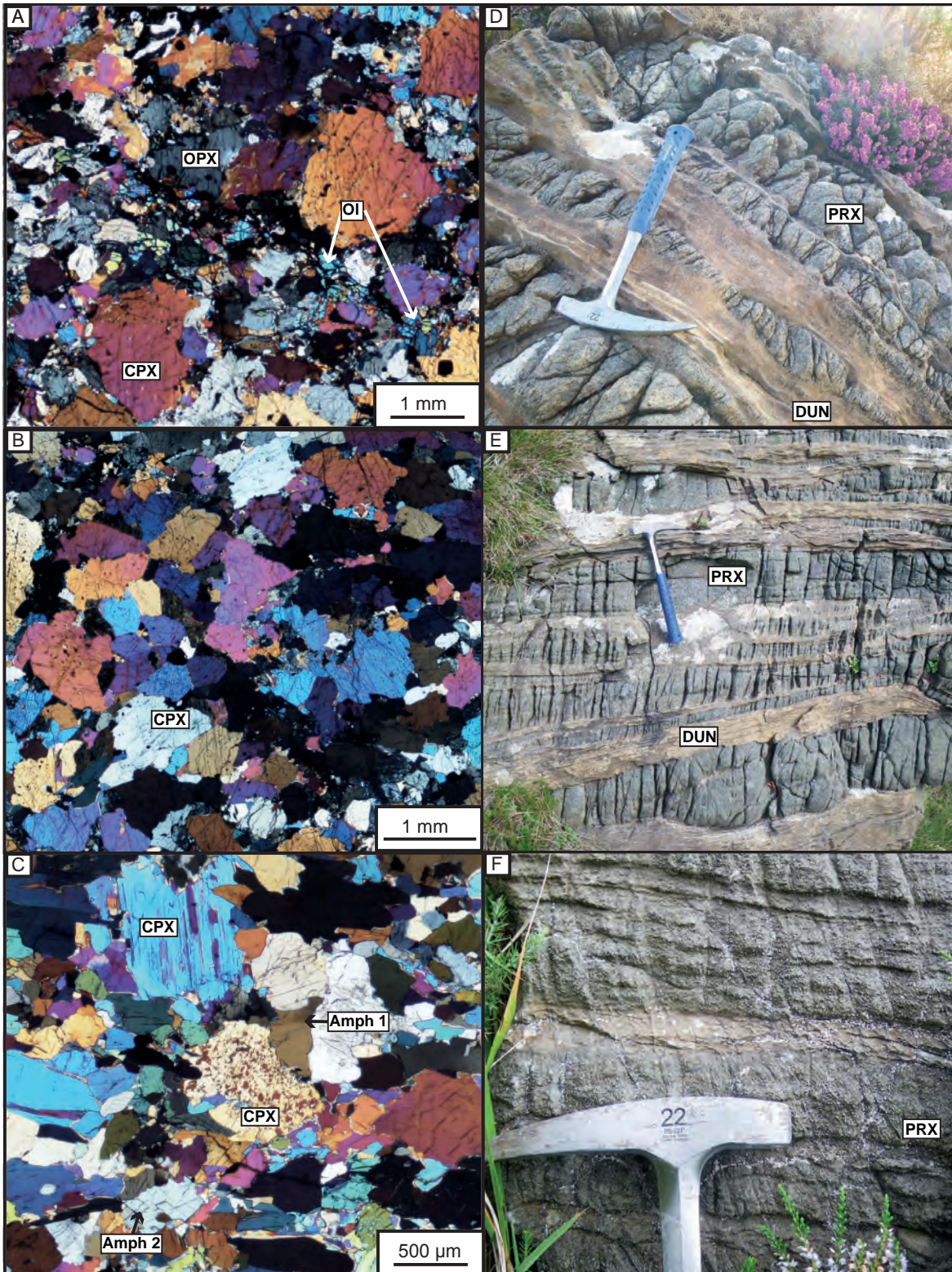


Fig.3.6: Photomicrograph illustrating (A) the dominant porphyroclastic texture in a type-1 pyroxenite (sample CO-096-A/B); (B): an equigranular texture in sample 701BA; (C): two textural relationships between amphibole and pyroxenes in a type-3 pyroxenite with xenomorphic (Amph 1) and idiomorphic to sub-idiomorphic (Amph 2) grains. Field photographs illustrating the occurrence of (D) type-1 pyroxenites, with interstitial dunite (note the boudinage of the pyroxenite layers); (E) type-2 massive pyroxenites with massive appearance and (F) type-3 pyroxenites, exhibiting a characteristic thinly foliated aspect.

3.9 - Microstructure of the Cabo Ortegal pyroxenites

A detailed description of the textures, microstructures and chemical compositions of the different types of pyroxenite has been provided by Tilhac et al. (2016) and Tilhac (2017) where further details can be found. For simplicity, I present here a concise description of the microstructure of the four types of pyroxenites as well as a description of the dominant phases forming the Cabo Ortegal pyroxenites: opx, cpx, olivine and amphibole. Phases such as spinel and sulfide, and minerals related to low-temperature alteration, such as serpentine, were not studied here because this study is focused on the pyroxenites, and also because it is not feasible to achieve EBSD analyses for minerals with very different hardness on a single thin-section. Garnet also is not considered here as it is present in only a few samples.

In the field, the different types of pyroxenites have a rather random occurrence. *Type-3* pyroxenites are an exception and are found more commonly near the sheath fold close to the contact with the underlying harzburgite (i.e. *third unit* described previously).

Type-1 pyroxenites (clinopyroxene-rich websterites and clinopyroxenites, Fig.3.6-A, Fig.3.6-D and Fig.3.7-B) have a dominantly porphyroclastic texture, except for sample 701BA which displays an equigranular texture (Fig.3.6-B). The grain-size distribution is thus bimodal and large grains make up ~50% of the rock surface area. In *type-1* pyroxenites, cpx makes up most of the surface area. It is associated with amphibole, which constitutes on average 10% of the surface area; olivine (and less commonly opx) may also be present in similar proportions.

In *type-2* pyroxenites (olivine-free websterites, Fig.3.6-E) the modal abundance of opx is higher than in *type-1* pyroxenites (20 to 30% of surface area); olivine is absent and amphibole makes up ~20% of the surface area (Fig.3.8-B and Fig.3.8-C). The grain-size distribution in *type-2* is similar to that in *type-1* pyroxenites. Coarse cpx and opx grains make up 55% of the rock surface area. The texture is mostly porphyroclastic and the grain boundaries of porphyroclasts indicate an absence of textural equilibrium between pyroxenes, either due to dynamic recrystallization or to the presence of amphibole neoblasts.

Type-3 pyroxenites (foliated clinopyroxenites and websterites, Fig.3.6-F and Fig.3.10) are strongly amphibolitized (up to 55% of the surface area) and locally become a quasi-bimineralic assemblage of cpx and amphibole (Fig.3.6-C). Intervals of large and unstrained

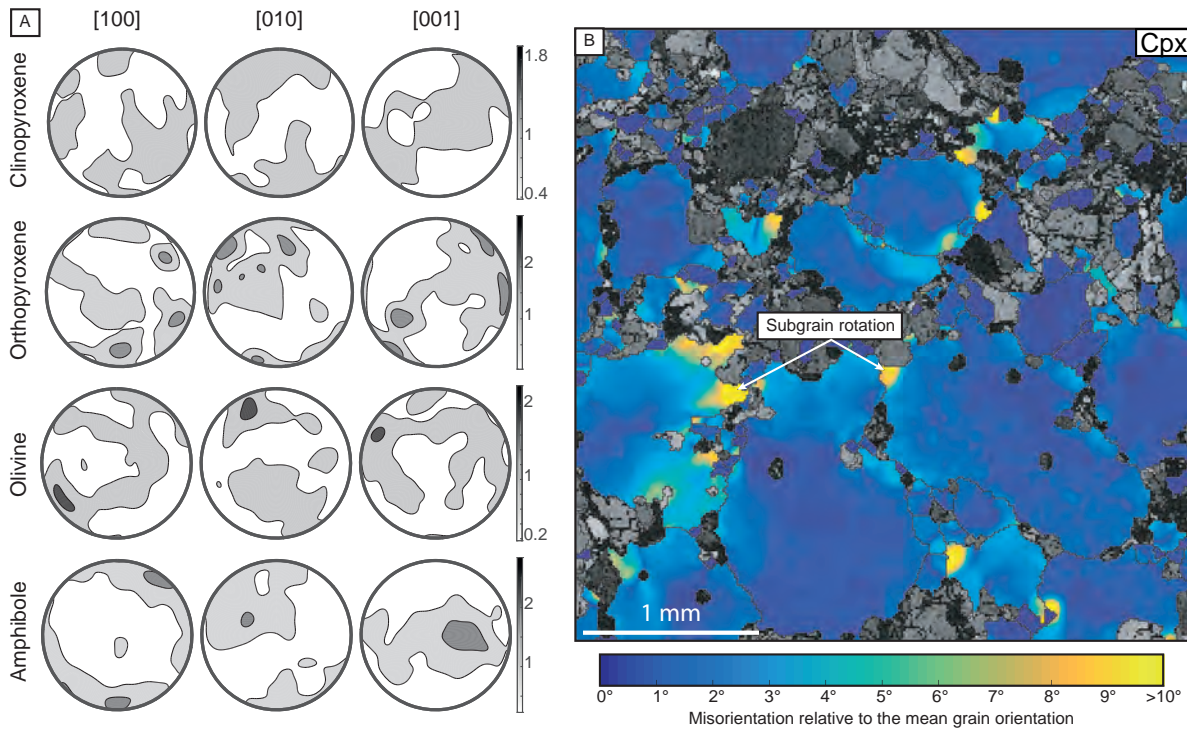


Fig.3.7: (A) CPO of cpx, opx, olivine and amphibole and (B) color-coded EBSD map of a type-1 pyroxenite (CO-096-A/B) showing for cpx the misorientation to the mean grain orientation for each measurement (i.e. pixel). Yellow color indicates a deviation of 10° or more from the mean grain orientation while dark blue indicates a value close to the mean grain orientation.

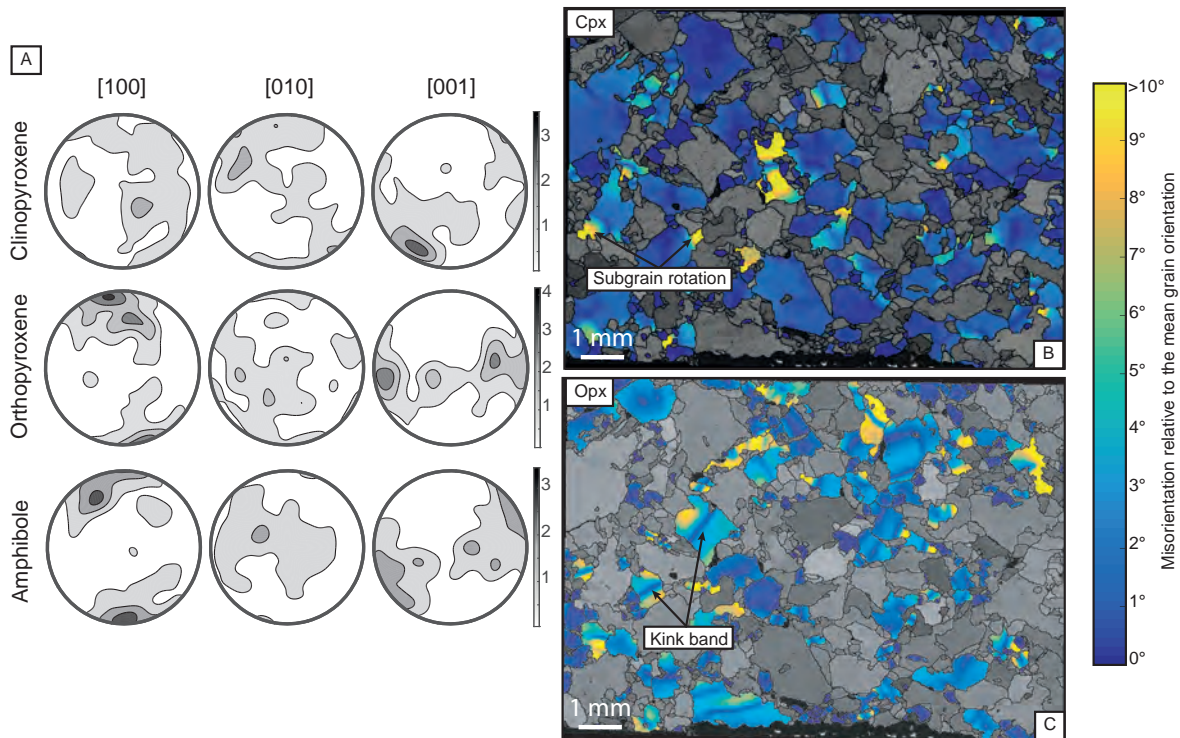


Fig.3.8: (A) CPO of cpx, opx and amphibole of a type-2 pyroxenite (CO-097-A); (B) and (C) show the misorientation to the mean grain orientation for cpx and opx in the same sample respectively. Note the difference in microstructure and deformation behavior between opx and cpx.

grains of amphibole can be observed parallel to the tectonic foliation (Fig.3.9). In contrast to *type-1* and *-2* pyroxenites, the grain-size is dominantly equigranular with a grain equivalent diameter of $\sim 800\mu\text{m}$. Such a grain-size distribution probably results from the growth and/or the static recrystallization of amphibole along pyroxene grain boundaries and among matrix minerals, as described by Tilhac et al. (2016) and Tilhac (2017).

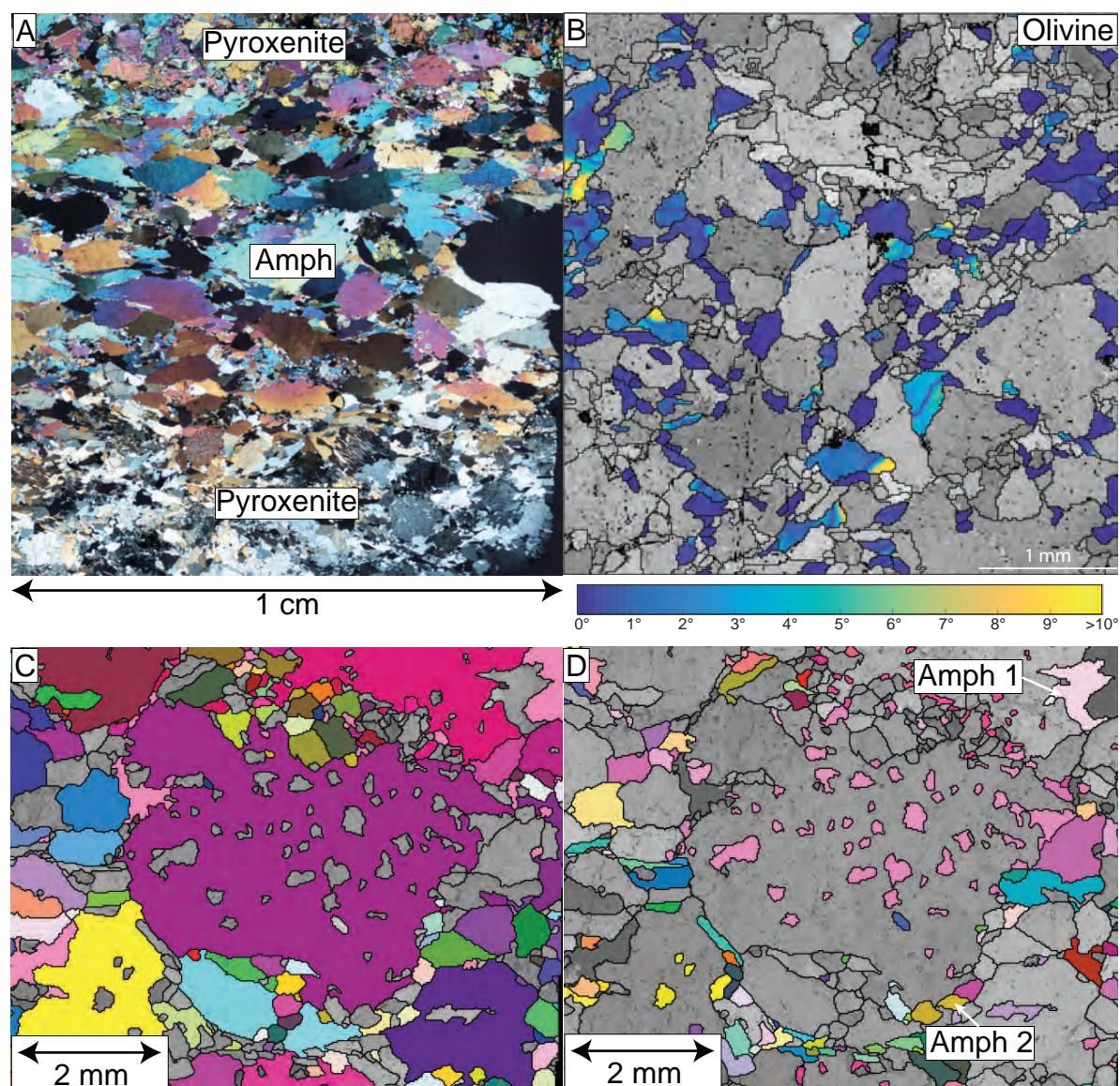


Fig.3.9: (A) Photomicrograph of a type-3 pyroxenite (CO-067-A) displaying amphibole-rich level with sub-euhedral to euhedral in a zone aligned with the tectonic foliation and lineation; (B) color-coded EBSD map showing the misorientation of each measurement to the mean orientation of the grain for olivine in sample 704A. Note that the olivine appears mainly as interstitial mineral and most grains are mainly free of lattice misorientation; (C) and (D) EBSD-derived color coded maps of the same region of sample 604B. The relationship between the cpx grains mean orientation (C) and the amphibole mean grain orientation (D) is visible. Euhedral and anhedral amphiboles with no sign of internal deformation (Amph 1), or with a high degree of deformation (Amph 2) growing over the cpx are visible as well as amphibole growing along the large Cpx.

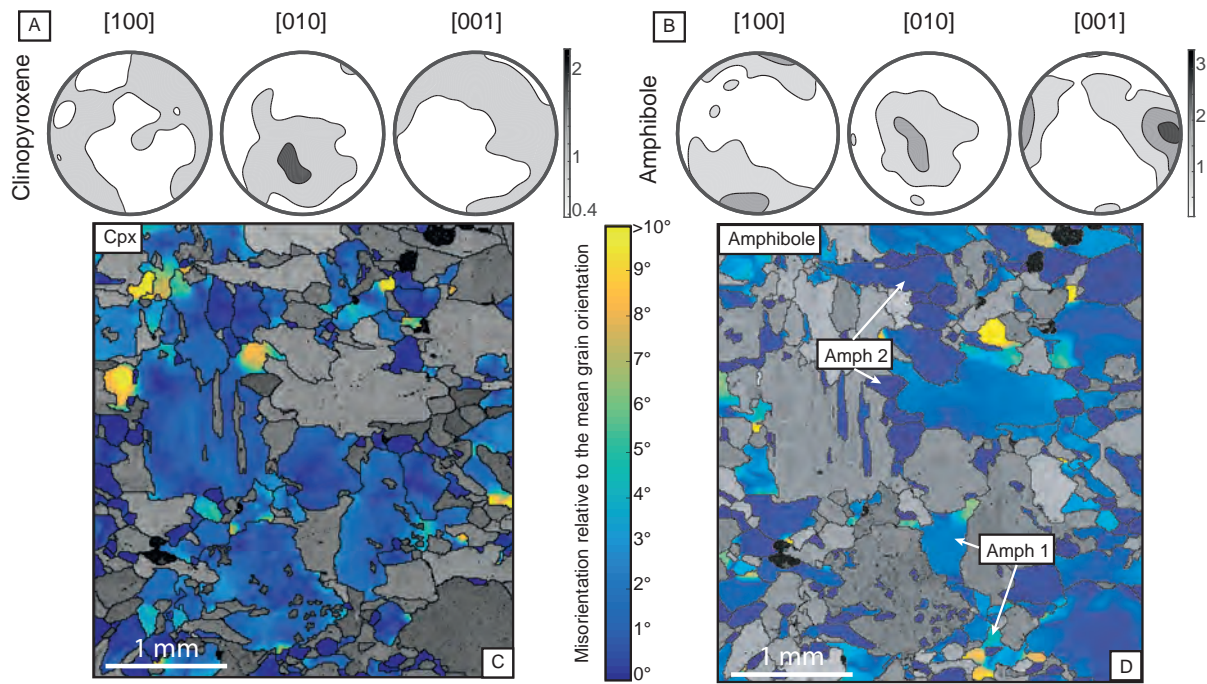


Fig.3.10: CPO and color-coded EBSD map of a type-3 pyroxenite (CO-101-C) showing the misorientation of each measurement to the mean grain orientation for (A) cpx and (B) amphibole. Idiomorphic (Amph 2) and xenomorphic (Amph 1) grains are clearly visible here.

Type-4 pyroxenites (opx-rich websterites and orthopyroxenites) contain more than 70% of opx. The modal proportion of olivine ranges from 5% to 20% in some samples, amphibole occurs in a proportion similar to that in *type-1* pyroxenites and rare cpx may be observed. The grain-size distribution is also bimodal but is here dominated by porphyroclasts; opx accounts for the coarse fraction while opx, cpx and/or amphibole constitute the fine-grained parts.

In all types of pyroxenites, opx (enstatite) occurs as porphyroclasts (500 μm to 3 mm) displaying undulose extinction and kink bands highlighted by exsolved spinel and/or cpx (Fig.3.8-C). Grain boundaries are complex, irregular and shaped by various equilibrated neoblasts ($\sim 175 \mu\text{m}$) grown at the expense of the unrecovered porphyroclasts and accounting for a smaller proportion of the surface area (Fig.3.11-B). Similarly, cpx (diopside) occurs as porphyroclasts hosting exsolved spinel along cleavages and exhibits a range of grain sizes similar to that of opx. It also displays complex and irregular grain boundaries. Subgrain boundaries near the contacts with surrounding grains, and sometimes undulose extinction, can be observed in most grains. Cpx also occurs as misorientation-free neoblasts comparable in size to the opx neoblasts (Fig.3.7-B and Fig.3.8-A). Olivine (Fo_{86-89}) may occur as relics of larger grains that have been serpentinized (i.e. mesh texture) forming bands in *type-1* pyroxenites, as inclusions in pyroxenes but most commonly as elongated and recovered

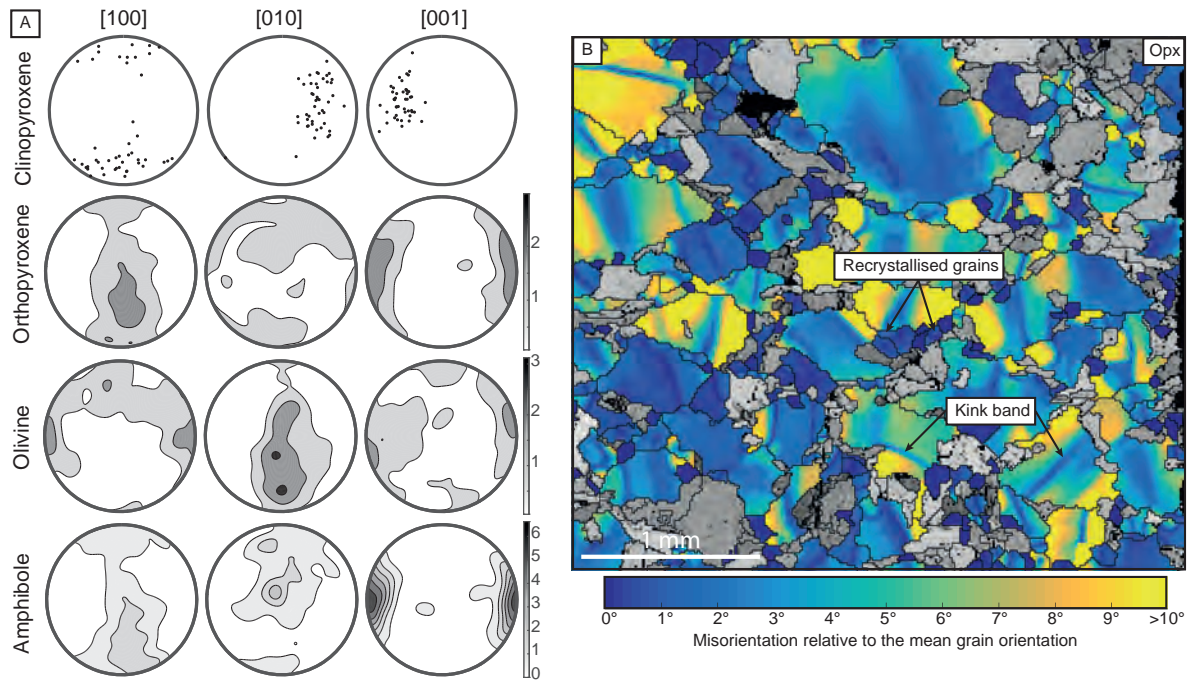


Fig.3.11: (A) CPO of cpx, opx, olivine and amphibole and (B) color-coded EBSD map of type-4 pyroxenite (704A) showing for opx the misorientation of each measurement to mean grain orientation map.

interstitial grains in type-1 and -4 pyroxenites (Fig.3.9-B). Their grain size is relatively homogeneous with a mean equivalent grain diameter (i.e. the diameter of a perfectly rounded grain with a similar surface area) of ~160 μm .

Amphibole (magnesio-hornblende in all samples) is observed as lamellae, replacing exsolved cpx and/or locally associated with spinel opx and cpx or as interstitial grains between the pyroxenes, resulting in sutured grain boundaries of cpx porphyroclasts. When occurring within pyroxenes, idiomorphic to sub-idiomorphic grains occurring preferentially along the pyroxenes cleavage can be observed. These observations suggest that some of the amphibole has grown at the expense of clinopyroxene (Fig.3.6-C, Fig.3.10 and Fig.3.9). The growth habit of amphibole depends on its modal abundance and on the type of pyroxenite, resulting in various textural overprints, notably responsible for the co-existence of porphyroclasts in otherwise equigranular samples. Based on the grain shape and on the internal deformation, two populations of amphibole grains can be distinguished: (1) idiomorphic to sub-idiomorphic grains (Amph 1 in Fig.3.6-C and Fig.3.9), with no sign of internal deformation; (2) xenomorphic grains (Amph 2 in Fig.3.6-C) with a higher degree of lattice misorientation, in the form of undulose extinction or subgrain boundaries, especially in grains squeezed between two pyroxene grains. These grains are xenomorphic and have more irregular boundaries. Both populations have comparable major and trace-element

Chapter 3

compositions within a given sample Tilhac et al. (2016) and may cover the whole range of the amphibole grain sizes, which has a mean value of $\sim 180 \mu\text{m}$ (Table.3.1).

Sample	Grain equivalent diameter (micro meters)						Cpx differential stress (Mpa)	Opx differential stress (Mpa)
	Opx		Cpx		Amphibole	Olivine		
	Neoblasts	Porphyroclasts	Neoblasts	Porphyroclasts				
Type-1 pyroxenites								
CO-096-A/A	117	595	111	900	113	115	50	34
CO-096-A/B	170	652	149	903	161	149	36	22
CO-100-A	268	668	235	803	256	240	22	13
CO-100-B	197	651	211	772	201	205	25	18
401A	45	X	59	920	52	50	101	103
701BA	208	571	227	816	167	193	23	17
702A	185	543	184	676	156	152	29	20
Type-2 pyroxenites								
706AA	164	756	178	712	153	X	30	23
CO-024	160	898	173	782	166	X	31	23
CO-097-A	237	792	208	862	239	X	25	15
CO-099-A	196	831	192	810	96	X	27	18
Type-3 pyroxenites								
CO-067-A	X	X	191	634	386	X	28	X
CO-067-B	168	853	170	805	198	X	31	22
CO-101-C	193	806	190	681	200	X	28	19
Type-4 pyroxenites								
602C	185	660	155	X	138	180	35	20
704A	147	692	132	X	139	130	42	26

Table.3.1: Grain size of the pyroxenes, amphibole and olivine derived from the EBSD analysis and Differential stress calculated from Avé Lallemant 1978 and Ross and Nielsen 1978.

The field data and petrographic observations do not allow definition of any systematic relationship between the deformation markers in pyroxenes, the different types of pyroxenite, their location or the thickness of the layer. On the contrary, and with the exception of the sheath-folded areas, macro and micro-scale deformation markers, as well as the different textures, are randomly distributed in the massif.

3.10 - Fabrics and internal deformation from EBSD

EBSD analysis of intracrystalline deformation in *type-1* pyroxenites reveals a relatively low degree of lattice misorientation (Fig.3.7-B). Rare concentrations of misorientations occur in the tips of large cpx grains at contacts with other cpx porphyroclasts and along subgrain boundaries. With the exception of sample 701BA, both M- and J-indices are low (0.01 for M- and 1.6 for J-index; Table.3.2), indicating a rather weak CPO for cpx. CPO also suggests weak cpx fabrics but a [001](010) pattern (SL-fabric) is nevertheless observable in half of the samples (Table.3.3 and Appendix 1.1). Either a random distribution or the presence of [001](100), as in the case of sample CO-096-A/A, makes up the other half of the samples. Rare opx grains may define either a weak [001](100) fabric or a random distribution (Fig.3.7-A). Olivine CPO is weak and mostly random but still allows the recognition of a [001](010)

The Microstructure of Cabo Ortegal Pyroxenites

Sample	Cpx			Opx			Amphibole			Olivine		
	J-index	M-index	n	J-index	M-index	n	J-index	M-index	n	J-index	M-index	n
Type-1 pyroxenite												
CO-096-A/A	1.4	0.010	2077	1.6	0.020	687	1.9	0.030	1612	1.3	0.010	1282
CO-096-A/B	1.6	0.020	1032	2.6	0.030	164	2.2	0.030	473	1.8	0.010	332
CO-100-A	1.7	0.010	828	4.0	0.040	149	3.8	0.090	416	3.4	0.040	181
CO-100-B	1.6	0.010	828	1.5	0.020	550	3.1	0.080	740	1.4	0.010	921
401A	1.6	0.010	695	1.4	0.010	583	2.4	0.060	790	1.4	0.000	1120
701BA	11.1	0.130	465	-	-	51	8.4	0.130	94	-	-	21
702A	1.7	0.040	1705	2.9	0.030	151	2.9	0.060	469	3.2	0.060	123
Type-2 pyroxenite												
706AA	2.3	0.050	886	2.0	0.030	377	2.1	0.030	764	-	-	-
CO-024	2.1	0.030	638	1.9	0.030	603	1.8	0.030	1402	-	-	-
CO-097-A	2.9	0.030	259	2.7	0.080	227	3.0	0.050	333	-	-	1
CO-099-A	1.8	0.050	1511	1.7	0.040	612	1.8	0.040	1298	-	-	-
Type-3 pyroxenite												
CO-067-A	2.4	0.070	541	-	-	-	4.9	0.120	933	-	-	-
CO-067-B	1.6	0.030	1653	2.5	0.030	192	2.0	0.040	2459	-	-	-
CO-101C	1.6	0.020	1348	4.1	0.080	199	2.2	0.040	2110	-	-	-
Type-4 pyroxenite												
602C	-	-	48	2.3	0.100	783	4.7	0.100	204	-	-	27
704A	-	-	46	1.8	0.050	791	4.8	0.100	258	2.2	0.060	458

Table.3.2: Fabric-strength indexes (*J* and *M*) and number (*n*) of grains analysed for *opx*, *cpx*, *amphibole* and *olivine* for Cabo Ortegal pyroxenites.

Sample	Fabric type				Texture
	Cpx	Opx	Olivine	Amphibole	
Type-1 pyroxenite					
CO-096-A/A	[001](100); [001](010)	[001](100)	Random	[001](100)	Porphyroclastic
CO-096-A/B	[001](010)	Random	Random	[001](100); [001](010)	Porphyroclastic
CO-100-A	Random	Random	Random	[001](100)	Porphyroclastic
CO-100-B	Random	[001](100)	Random	[001](100); [010](100)	Porphyroclastic
401A	Random	Random	[001](010)	[010](100)	Porphyroclastic
701BA	[001](010); [100](010)	Random	[001](010)	Random	Granoblastic
702A	[001](010)	Random	[100](010)	[001](100); [001](010)	Porphyroclastic
Type-2 pyroxenite					
706AA	[001](100); [001](010)	[001](100)	-	[001](100)	Porphyroclastic
CO-024	[001](010)	[001](100)	-	[100](010); [001](010)	Porphyroclastic
CO-097-A	[001](010)	[001](100)	-	[001](100)	Porphyroclastic
CO-099-A	[001](010); [100](010)	[001](100)	-	[001](010)	Porphyroclastic
Type-3 pyroxenite					
CO-067-A	[001](010)	-	-	[001](100)	Equigranular
CO-067-B	[001](010)	Random	-	[001](100); [001](010)	Equigranular
CO-101C	[001](010)	Random	-	[001](100)	Equigranular
Type-4 pyroxenite					
602C	[010](100) or [001](100)	[001](100)	-	[001](100)	Equigranular
704A	[010](100) or [001](100)	[001](100)	[100](010)	[001](100)	Porphyroclastic

Table.3.3: Fabric for each phase and texture of Cabo Ortegal pyroxenites.

fabric in 3 samples and of a [100](010) fabric in another (Fig.3.7-A). A [001](100) fabric of amphibole seems to dominate in *type-1* pyroxenites (Fig.3.7-A). This fabric is consistently stronger than the fabrics of pyroxenes and olivine (0.05 for *M*- and 2.7 for *J*-index) and may display a point maximum, girdles or a random distribution depending on the sample and the axis considered. Beside [001](100), amphibole from samples 401A (Fig.3.12) and 100B display a [010](100) fabric and [001](010) is found in sample CO-96-A/B and 702A.

Optically, the intracrystalline deformation recorded in *type-2* pyroxenites (olivine-free massive websterites) appears to be stronger than in *type-1* pyroxenites (Fig.3.8). However, a probability-density function of the grain orientation spread (GOS) of the volumetrically dominant cpx reveals that the two types are very similar from an internal-deformation point of view (Fig.3.13-A). In *type-2* pyroxenites, cpx fabrics are dominated by [001](010) (i.e. SL-

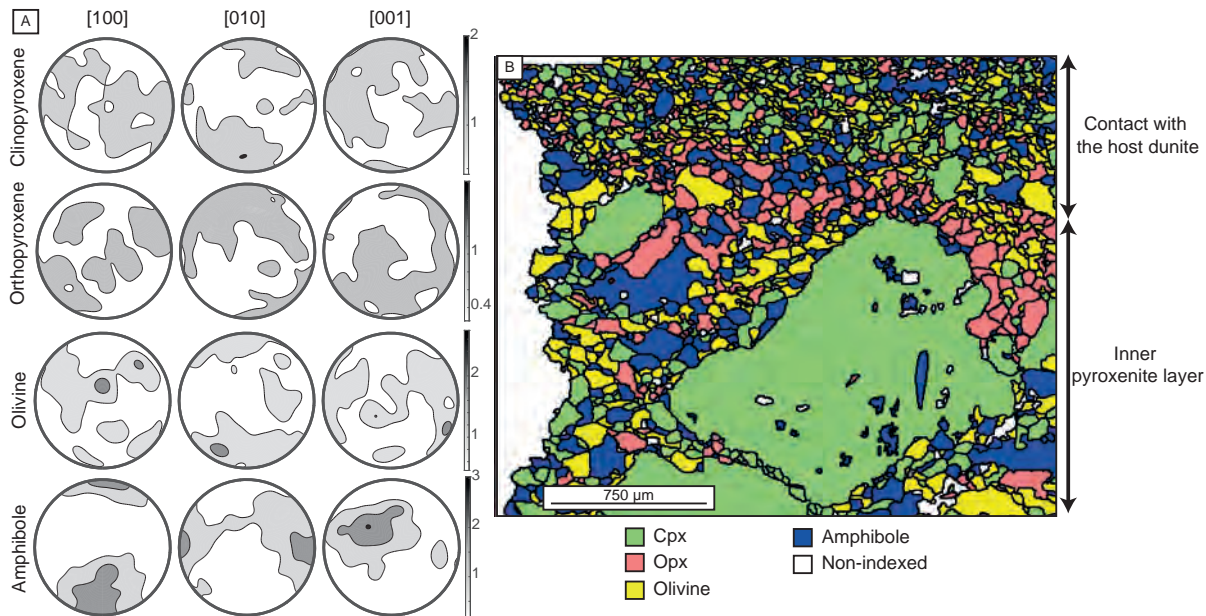


Fig.3.12: (A) CPO of cpx, opx, olivine and amphibole in a type-1 pyroxenite (sample 401A) and phase map (B) of the same sample at the contact between host dunite and pyroxenite, where grain size reduction occurs. Note how the amphibole fabric differs from the commonly observed [001](100) and the rather weak fabrics of the pyroxenes and olivine.

type fabric) except for sample CO-099-A, which displays a S-type fabric (Appendix 1.2). Opx has a very homogenous [001](100) fabric. Although the M- and J-indexes of pyroxenes are slightly greater than in *type-1* pyroxenites (Fig.3.13-C and -D), the limited number of samples does not support a meaningful statistical interpretation. Amphibole fabrics display the same variability as observed in *type-1* pyroxenite with [001](100), [001](010) or even (010) with two girdles formed by [100] and [001] axes (Fig.3.8-A, Table.3.3 and Appendix 1.2).

In type-3 pyroxenites, the internal energy seems optically similar to that of type-1 (i.e. misorientations restricted to grain and subgrain boundaries; Fig.3.10), but this is mainly due to the lack or low abundance of opx. Subgrain rotation can be observed in large cpx grains and strong lattice misorientations appear in some amphibole grains (Fig.3.10-B). Cpx fabrics are [001](010) and can be both of S- or L-type (Appendix 1.3 and Table.3.3). Because of the high modal abundance of amphibole, the two different populations described above are here easily recognized. Amphibole shows a striking [001](100) fabric; in sample CO-067-B, a girdle is formed by [100] along the plane normal to the lineation. Large idiomorphic amphiboles with shapes matching the foliation and lineation reference frame can be observed in sample CO-067-A (Fig.3.9-A).

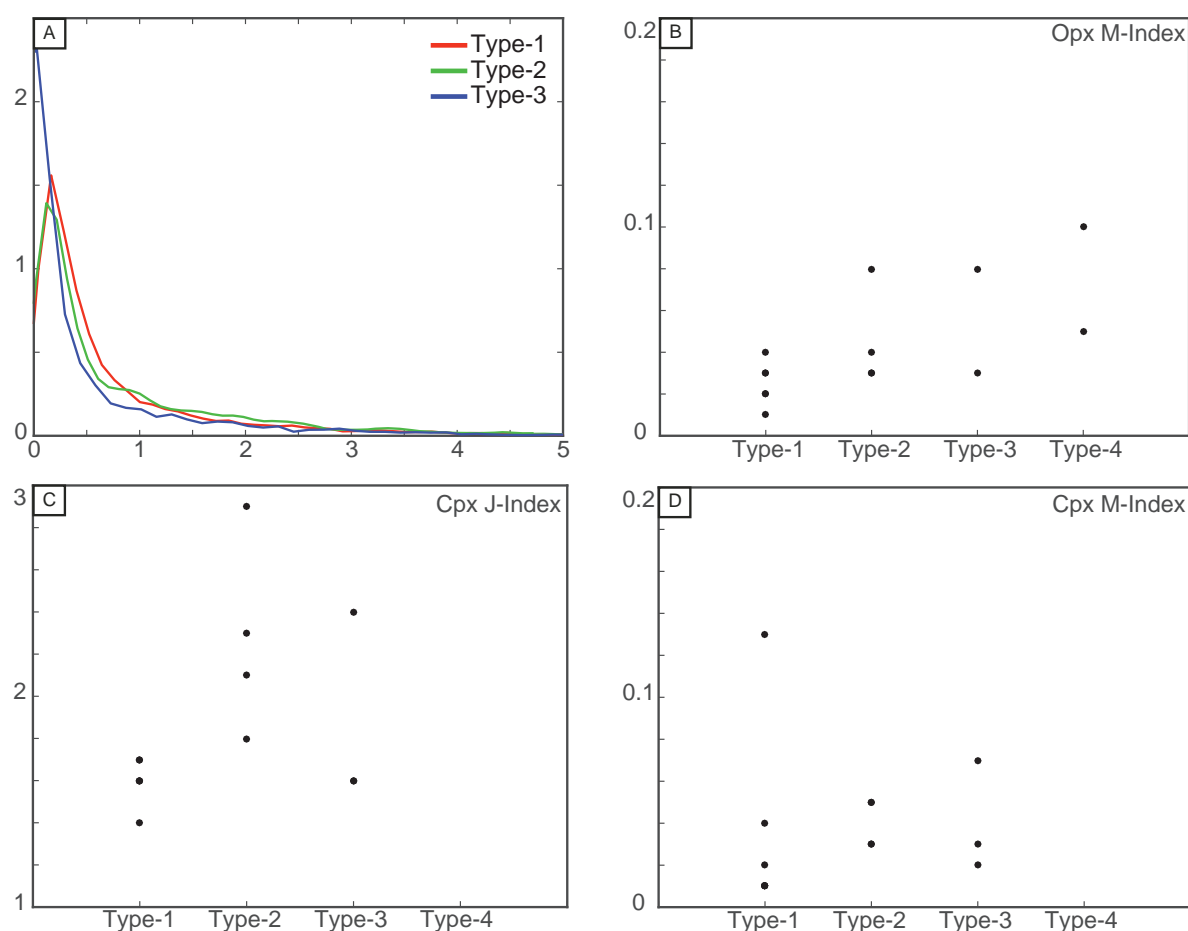


Fig.3.13: Trends observed in the CPO data from Cabo Ortegal pyroxenites. (A) Probability-density function of the Grain Orientation Scattering (GOS) for all cpx grains in type-1, 2 and -3 pyroxenites (i.e. the average deviation in orientation between each point in a grain and the mean grain orientation). While the distinction between type-1 and type-2 is subtle, indicating a similar level of internal deformation, type-3 pyroxenites clearly have more equilibrated cpx than the other two types; (B) and (D): M-index of opx and cpx CPO for each type of pyroxenite; (C) J-index of cpx for each type of pyroxenite. Sample 701BA has been excluded from the plots because of its anomalously high J- and M- indices compared to the other type-1 pyroxenites.

In type-4 pyroxenites, internal deformation is particularly striking. Kink bands are abundant and their axes are sub-normal to normal relative to the main foliation (Fig.3.11-B and Appendix 1.4). Finer grains (of all phases) are well-equilibrated internally compared to the large porphyroclasts, and only rarely display evidence of misorientation. Opx displays a strong [001](100) fabric, which also occurs in amphibole with a notably strong linear component (Fig.3.11-A). The combination of [100](010) and [001](010) fabrics for olivine is suggested in sample 704A. Due to the limited number of grains (i.e. <100), the contours of the cpx ODF have not been drawn and the J- and M- indices are excluded. However, both selected type-4 pyroxenites show a strong concentration of the three cpx crystallographic axes ± 90 -degree rotation around the [100] axis (Fig.3.11-A).

Sample	Opx	Cpx	Amphibole	Olivine	Other (e.g. garnet, spinel...)	Grains > 500 µm of equivalent diameter	% of amphibole with a GOS > 2 degree
Type-1 pyroxenites							
CO-096-A/A	7.64	65.17	16.4	9.44	1.35	52	19.58
CO-096-A/B	5.01	77.25	11.32	5.62	0.8	61	20.98
CO-100-A	3.57	82.79	10.37	3.06	0.21	69	6.75
CO-100-B	15.5	45.52	20.87	17.65	0.46	39	20.59
401A	11.02	44.44	21.87	22.62	0.05	16	19
7018A	4.06	91.17	3.13	0.74	0.9	72	16.26
702A	3.27	87.38	7.01	1.52	0.82	47	16.57
Type-2 pyroxenites							
706AA	17.9	60.68	21.42	0	0	36	17.28
CO-024	36.71	27.94	32.71	0	2.64	48	23.9
CO-097-A	31.83	47.73	20.42	0	0.02	72	19.85
CO-099-A	22.72	61.31	15.87	0	0.1	64	29.16
Type-3 pyroxenites							
CO-067-A	0	17.5	82.5	0	0	74	13.53
CO-067-B	4.95	51.29	43.73	0	0.03	40	26.22
CO-101-C	5.6	44.5	49.9	0	0	51	21.2
Type-4 pyroxenites							
602C	87.89	2.29	8.89	0.84	0.09	37	35.37
704A	69.93	1.96	11.4	16.66	0.05	32	25.27

Table.3.4: Area fraction (%) of opx, cpx, amphibole and olivine in Cabo Ortegal pyroxenites derived from indexed EBSD data.

3.11 - Conditions of deformation of the Cabo Ortegal pyroxenites

The average grain size of cpx neoblasts computed from EBSD data (Table.3.1) was used to estimate the differential stress following the relation of Avé Lallemant (1978). Results are relatively homogenous, exhibiting a mean value of 30.8 ± 7.6 MPa (Table.3.1). Sample 401A, which represents the contact between a pyroxenite layer and its host dunite, displays a much higher differential stress of 101 MPa. The [001](010) fabric in cpx is visible in most samples and does not seem to be correlated with a specific type of pyroxenite. Such fabric, possibly related to slip along $[001]\{110\}$ and $1/2\langle 110 \rangle\{110\}$, was described as the main deformation mechanism at temperatures $>1000^\circ\text{C}$ (Bascou et al., 2002; Amiguet et al., 2010). Additional clustering of [100] axes next to the foliation pole on top of the [001](010) fabric, as observed in samples CO-096-A/A, 706AA and CO-097-A/A (Appendix 1.1 and Appendix 1.2) may indicate the activation of [001](100) and/or the relative domination of $1/2\langle 110 \rangle\{110\}$ (Raterron et al., 1994; Amiguet et al., 2010). Considering that the formation of the [100] cluster by $1/2\langle 110 \rangle\{110\}$ would require an axial compression at high-temperature, an S-type fabric would be expected in these cases, but this is not observed. The activation of [001](100) at lower temperatures (900 to 1000°C) is therefore more consistent with our observations and could explain the [100] clustering next to the foliation pole. This clustering of cpx [100] axes next to the foliation pole in *type-4* pyroxenites may be regarded as evidence for the latter deformation, although it alternatively could be interpreted as reflecting an effect of modal composition on the cpx fabric. Considering that no mechanical twins or kinks are observed, clinopyroxene did not record deformation at lower temperatures (i.e. $< 900^\circ\text{C}$). S-, L- and SL-type fabrics are unrelated to the different types of pyroxenite, and therefore it is inferred that

deformation regimes may potentially reflect the initial orientation of the pyroxenite layers/dykes relative to the paleo-stress field.

Based on these results, it is suggested that cpx in Cabo Ortegal pyroxenites records deformation at temperatures greater than 900°C, and mostly higher than 1000°C. This high-temperature deformation event included either a shear component, an axial compression component or both depending on the sample.

The grain size of opx neoblasts has been used to estimate the differential stress following the relation of Ross and Nielsen (1978). This shows results consistent with those observed in cpx, yielding a mean value of 20.3 ± 5.1 MPa (Table.3.1). Again, sample 401A records a greater differential stress than the other samples with an estimated stress of 103 MPa. In most pyroxenites of all types, opx fabrics seem to indicate the activation of [001](100) glide (i.e. AC-type fabric *sensu* Jung et al., 2010) which has been widely reported in upper-mantle samples (Nicolas and Christensen, 1987). In contrast to the results of Jung et al. (2010), we observe an increasing CPO strength with increasing opx content and an [001] (100) type regardless of the modal proportion (Table.3.2 and Table.3.4). Assuming a water-rich environment and a strain rate of 10^{-13} s^{-1} (Ábalos et al., 1996; Ábalos et al., 2003; Puelles et al., 2009; Tilhac et al., 2016), deformation by transformation to clino-enstatite can be estimated to occur below ~800°C (Ross and Nielsen, 1978). The absence of observed clino-enstatite may thus suggest that opx recorded deformation at temperatures greater than 800°C. However, although clino-enstatite has never been reported in the Cabo Ortegal pyroxenites, its presence cannot be ruled out altogether and a more conservative interpretation has to be retained.

Even if the opx fabric, kink bands and undulose extinction are consistent with deformation at mantle conditions, we will consider the opx to be inconclusive when it comes to defining a temperature field for that deformation event.

The A- and B-type olivine fabrics observed in *type-1* and *type-4* pyroxenites suggest the activation of [100](010) and [001](010) slips respectively. The A-type fabric is commonly found in upper-mantle peridotites and has been observed in high-temperature, low-stress environments in a wide variety of xenoliths (Nicolas and Christensen, 1987; Ismaïl and Mainprice, 1998). B-type fabric is produced (1) during the A- to B-type transition upon a

decrease in temperature and/or an increase in stress (Carter and Avé Lallemant, 1970); (2) at high temperature upon an increase in the olivine water content and a possible increase of stress (Jung and Karato, 2001); (3) at pressures greater than 3 GPa in a dry environment (e.g. Jung et al., 2009; Ohuchi et al., 2011); (4) between 5 and 8 GPa with a relatively low proportion of opx (Soustelle and Manthilake, 2017). In the Cabo Ortegal Complex, the peak metamorphism reached a pressure of ~1.7 GPa (i.e. Ábalos et al., 2003), excluding the possibility of a pressure- triggered B-type fabric. The heterogeneous distribution of the phases (i.e. the layering), the lack of cpx and the different pressure ranges at which the experiments were carried out make it difficult to use the results of Soustelle and Manthilake (2017) to understand the fabrics of Cabo Ortegal pyroxenites. Consequently, the origin of B-type fabrics in the Cabo Ortegal pyroxenites is likely to be the result of variations in stress, temperature and/or water content. B-type fabrics have been documented in the harzburgites of the neighbouring Limo massif (Puelles et al., 2012) and were interpreted as a result of decreasing temperature and an increasing stress. In the Cabo Ortegal pyroxenites, stress triggering of the A- to B-type fabric transition is not consistent with our differential stress calculations: while the B-type fabric is found in the most stressed sample (i.e. sample 401A, Fig.3.12), it is also found in other samples exhibiting the same range of stress as the A-type fabric (Table.3.3). The lack of lattice misorientation in the olivine grains of the Cabo Ortegal pyroxenites also suggests a re-equilibration of the lattice (Fig.3.9-B) at temperatures sufficient for efficient diffusion to operate. This thus excludes a simple temperature decrease as a cause of the B-type fabric. An alternative way to understand the B-type fabric would be to hypothesise the presence of melt in the Cabo Ortegal pyroxenites during deformation as suggested by experimental work on melt-bearing peridotites (e.g. Kohlstedt and Holtzman, 2009).

Therefore, it is inferred that the olivine found in Cabo Ortegal pyroxenites recorded deformation at temperatures greater than 1000°C and possibly provides evidence for a hydrous / melt-bearing environment.

Among the main rock-forming phases in the Cabo Ortegal pyroxenites, amphibole has the strongest fabric, with [001](100) appearing in most samples (Fig.3.7-A, Fig.3.8-A, Fig.3.10-A and Table.3.3). This fabric has been observed in deformation experiments and natural samples at temperatures between ~ 500°C and 800°C (Dollinger and Blacic, 1975; Getsinger and Hirth, 2014; Ko and Jung, 2015). Along the contacts between pyroxenite and dunite (i.e.

sample 401A), a fabric switch to [010](100) is observed (Fig.3.12). This switch in fabric has also been observed experimentally and was linked to a potential increase in stress (Ko and Jung, 2015). Amphibole CPOs display values of mean uniform distribution that could be interpreted as the result of a cataclastic process (Díaz Aspiroz et al., 2007). However, such interpretations are not consistent with the textural and petrographic observations on the Cabo Ortegal pyroxenites, suggesting that only little deformation was recorded by most amphiboles. The greater strength of amphibole fabrics may be interpreted as the result of an oriented growth taking place in a stronger stress field than the one that is related to the pyroxenes and olivine fabrics. The mimicking of cpx CPO by amphibole, which is observed in some of our samples, indicates that some proportion of the amphibole has grown after cpx and inherited its crystal orientation. This is consistent with the close textural relationships shared by amphibole and cpx (Tilhac et al., 2016; Tilhac, 2017), their mutual isotopic equilibrium (Tilhac et al., 2017) and similar observations made in the Limo massif (Puelles et al., 2012), supporting the idea of a metamorphic origin for at least part of the amphibole grains. The alignment of amphibole fabrics with the structural framework and its abundance in Cabo Ortegal pyroxenites suggest that the lineation observed at macroscopic scale is mostly defined by amphibole grains. Only in *type-4* pyroxenite, which is relatively poor in amphibole, is the lineation dominated by elongated and well-aligned opx grains.

On the basis of the textural observations and fabrics, it is concluded that amphibole mainly records a low-stress plastic deformation at temperatures ranging from ~800°C to a minimum of 500°C, after the higher-temperature episode recorded by the pyroxenes and olivine.

Mineral fabrics in the Cabo Ortegal pyroxenites reveal two distinct deformation events: opx, cpx and olivine provide evidence for deformation at high temperatures and low stress, compatible with an upper mantle setting (>1000°C), possibly in a hydrated / melt-bearing environment, while amphibole records a lower-temperature deformation (~ 800°C to a minimum of 500°C) probably mainly accommodated by strongly sheared and serpentinized harzburgitic or dunitic hosts. The results also indicate that Cabo Ortegal pyroxenites were deformed under relatively low-stress conditions during both episodes. The consistency of opx [001](100) and cpx [001](010) fabrics and their close spatial coincidence suggest that all Cabo Ortegal pyroxenites recorded the same high-temperature deformation, overprinting any microstructural differences possibly acquired previously.

3.12 - Lithological constraints on the development of microstructures

In addition to the fabrics, the degree of internal deformation for each type of pyroxenite is here quantified in order to assess the lithological constraints imposed on the development of microstructures. For that purpose, GOS probability-density functions for the volumetrically dominant cpx was calculated (Fig.3.13-A). Results suggest that cpx in both *type-1* and *-2* pyroxenites shows quite similar internal deformation. Therefore, any subjective estimate of a deformation difference in thin section is likely to be the result of the modal composition, notably the higher abundance of opx, best illustrated in *type-4* pyroxenites. However, the cpx GOS of *type-3* pyroxenites is different from the other types and indicates a generally lower internal energy, consistent with petrographic observations.

As described above, EBSD maps and petrographic observations consistently indicate two populations of amphibole grains: one of idiomorphic and unstrained grains (Amph 1, Fig.3.6-F) and another of xenomorphic and un-equilibrated grains (Amph 2 in Fig.3.6-C, Fig.3.10-B and Fig.3.9). EBSD data allow the estimation of the mean surface area for each population. Using a petrographically realistic GOS threshold of 2 degrees to separate the two populations (Wright et al., 2011), one can estimate that ~20% of the amphibole surface area in the Cabo Ortegal pyroxenites is represented by xenomorphic amphibole (Table.3.4). This value is roughly constant regardless of the pyroxenite type and therefore amphibole deformation cannot be used as a criterion to differentiate between the pyroxenite types. Nonetheless, it can be interpreted as evidence for a mostly post-kinematic amphibolitisation. Assuming a melt-bearing pyroxenite, as possibly suggested by the B-type olivine, syn-kinematic amphibole could be interpreted as the product of the crystallization of that possible interstitial melt.

Tilhac et al. (2016) suggested, based on the low modal proportion of opx and their foliated aspect outlined by dunitic intercalations, that *type-3* pyroxenites may represent the deformation of a protolith similar to the one that formed *type-1* pyroxenites (Fig.3.14). Such a process would have several consequences for the microstructures and thus can be tested. One would require the pyroxenites to be mechanically stronger than the host dunite, so that the deformation would be localized in the dunitic lenses. As observed in sample 401A, grain-size reduction and the relatively high-stress amphibole fabric suggest that the deformation is

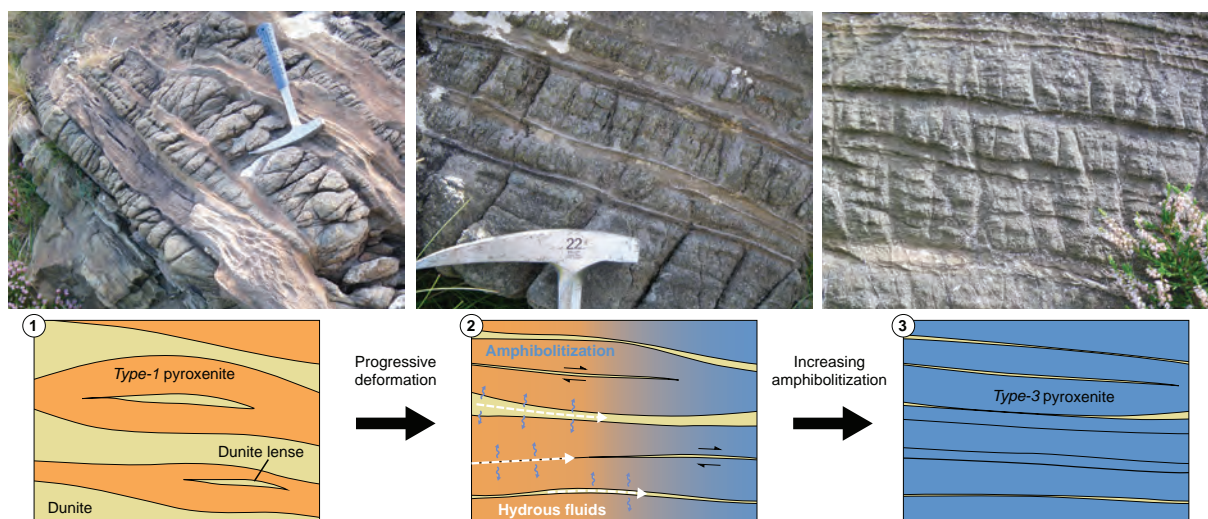


Fig.3.14: Sketch depicting the model proposed by Tilhac (2017) for the formation of type-3 pyroxenites from on a protolith similar to those of type-1 pyroxenites; increasing deformation by axial compression and shear eventually stacks pyroxenite layers (1 and 2) creating preferential pathways for fluid percolation and amphibolitization (3).

mainly accommodated by the host rock. In addition, flow laws for deformation of websterites and dunites in a hydrated environment under upper mantle conditions (0.5 to 1.5 GPa of confining pressure) predict a high viscosity contrast between websterites and dunites, which would tend to localize the deformation in the dunites (Avé Lallemant, 1978). Accordingly, the deformation mechanism needed to produce the lamination of the dunitic lenses in *type-1* pyroxenites is evidenced by the S- and SL- cpx fabrics in the pyroxenites. A corollary of this process, and especially of the grain size reduction, is the development of preferential paths for subsequent fluid percolation in the dunitic lenses. The lower GOS in the cpx of *type-3* pyroxenite, which may be interpreted as the result of a lattice re-equilibration in the presence of a fluid, and the high abundance of amphibole, are both compatible with this process.

A continuous profile along two continuous thin-sections from sample CO-010 has been established. The profile features several layers of clinopyroxenite with minor olivine and amphibole alternating with olivine-rich layers bearing clinopyroxenes and amphibole. More information about the profile location and sample CO-010 can be found in Tilhac et al. (2016) and Tilhac (2017). Tilhac (2017) recorded a high- resolution profile using EMP and LA-ICP-MS and revealed that one end of the profile fits the chemical characteristics of *type-1* pyroxenites while the other end fits the *type-3* pyroxenites. In this section the results of the EBSD analysis along the same profile are presented and interpreted in the framework of the previously discussed *type-1* to *type-3* model.

The sections used by Tilhac (2017) were cut perpendicular to the foliation. During sample preparation, the lineation direction was not taken into account as they were prepared for chemical and not for structural analysis. In order to respect the plotting convention detailed in Chapter 2 and interpret the fabrics correctly, a rotation of the dataset of 90° around to foliation pole was performed. This rotation yield consistent fabrics with that of other Cabo Ortegal pyroxenites for the 3 phases of interest that are cpx, olivine and amphibole.

Along the profile, two different types of layers alternate with each other. The dominant type is a clinopyroxenite (~80% of cpx) with minor amphibole (~15%) and olivine (~5%) as interstitial minerals (Fig.3.15). The texture is porphyroclastic and may show strong enrichment in amphibole in some layers (Fig.3.15). Rare orthopyroxene occurs as less than 10% of the mode. The other type of layer is fine-grained and shows a significant increase in olivine modal proportion (~30%), and sheared serpentine is present. In a few layers, some porphyroclasts have been preserved but represent only a small percentage of the surface area. EBSD-derived modal compositions have been computed for each layer and are presented in Fig.3.16. As observed by Tilhac (2017), progression from *type-1* to *type-3* pyroxenite show a general increase in the mode of amphibole at the expense of clinopyroxene.

Cpx fabrics are similar to the those of the main Cabo Ortegal trend where they are overall weak but present an S-, L- or SL- fabric. However, no correlation can be drawn between the Cpx fabrics, fabric strength and mode along the profile (Fig.3.17 and Fig.3.16)

The olivine fabric is more complex (Fig.3.18). Throughout the profile, olivine [010] and [001] both display a point maximum fitting the foliation pole and the lineation respectively. The concentration of [100] axes varies along the profile and may display either a girdle, a maximum fitting the lineation or a maximum at 90° to the lineation direction. A maximum of olivine [100] fitting the lineation direction is only observed in the pyroxenite-rich layers and does not seem to appear in the fine-grained olivine-rich layer. Regarding fabric strength, the olivine J-index shows a perfect anti-correlation with the olivine mode (Fig.3.16). In contrast, the M-index is correlated with the olivine mode when close to the *type-1* end and becomes anti-correlated when approaching the *type-3* end. This dichotomy may be the result of the limited number of grains in some layers, especially on the third layer starting from the *type-1* end which yields only 133 grains, and thus not enough for the M-index to be reliable. This

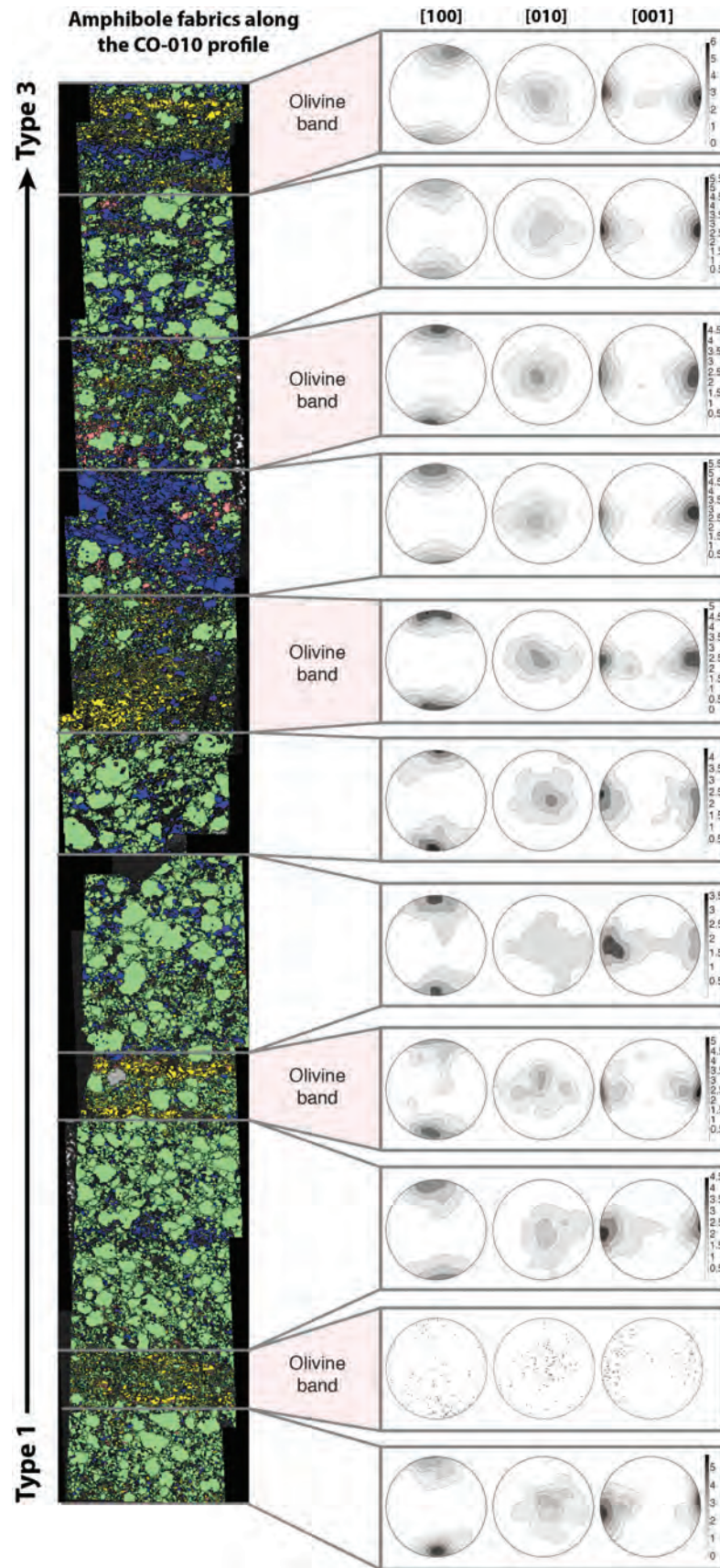


Fig.3.15: Fabrics of amphibole along sample CO-010 profile. Phase map displaying the pole-figure location is shown with a similar color code to that of Fig.3.12-B. The whole transition from type-1 to type-3 pyroxenite presented here is 9 cm long.

demonstrates the limitations and difficulty of using either index to clearly quantify a fabric strength. Both indices show an anti-correlation of the olivine fabric strength with mode in the *type-3* end of the profile.

As observed before, the amphibole mode increases toward the *type-3* end of the profile (Fig.3.15). The [001](100) fabric is consistent all the way through the profile but its intensity seems to be related to the type of layer (i.e. olivine-rich or pyroxene-rich): When in a olivine-rich (and therefore fine-grained) layer, the fabric intensity of amphibole is greater than it is in a pyroxene-rich layer. It potentially reflects the shear localization while in the amphibole stability field.

The texture of the pyroxene-rich layers indicates that the internal deformation was limited in contrast to that in the olivine-rich layers that show a highly deformed texture close to mylonitic. The cpx fabric strength is also an indicator of the low degree of deformation of the pyroxene-rich layer along the whole profile. Olivine fabrics show an interesting distribution with both [100](010) and [001](010) present within the pyroxene-rich layers and [001](010) clearly dominating in the olivine-rich layers. These observations, coupled with the lattice equilibrium of the interstitial olivine in the pyroxene-rich layers, provide a strong argument supporting the concept that the interstitial olivine is shielded by the pyroxenite layer, and therefore preserves an ancient physical state that probably originated at high temperature (as discussed above for the olivine fabrics). The variation in olivine fabric strength along the profile is also unexpected: the fabric strength decreases as the olivine mode increases.

Amphibole does not show any variation in the fabric type along the profile but variations in the fabric strength which follows the opposite trend to the olivine one and increases in the olivine-rich layers (Fig.3.15 and Fig.3.16).

Considering these observations, we can conclude that a deformation event occurred in the stability field of amphibole and was relatively stronger in the olivine-rich layers. The decrease in olivine fabric strength is consistent with deformation progressing outside the plastic-deformation field of olivine and therefore at lower temperature (i.e. in the plasticity field of amphibole). Therefore, and considering the arguments above, it is possible to hypothesize that before this late deformation event, the fabric of the fine-grained olivine-rich layers was at least as strong as the fabric preserved in the pyroxene-rich layers.

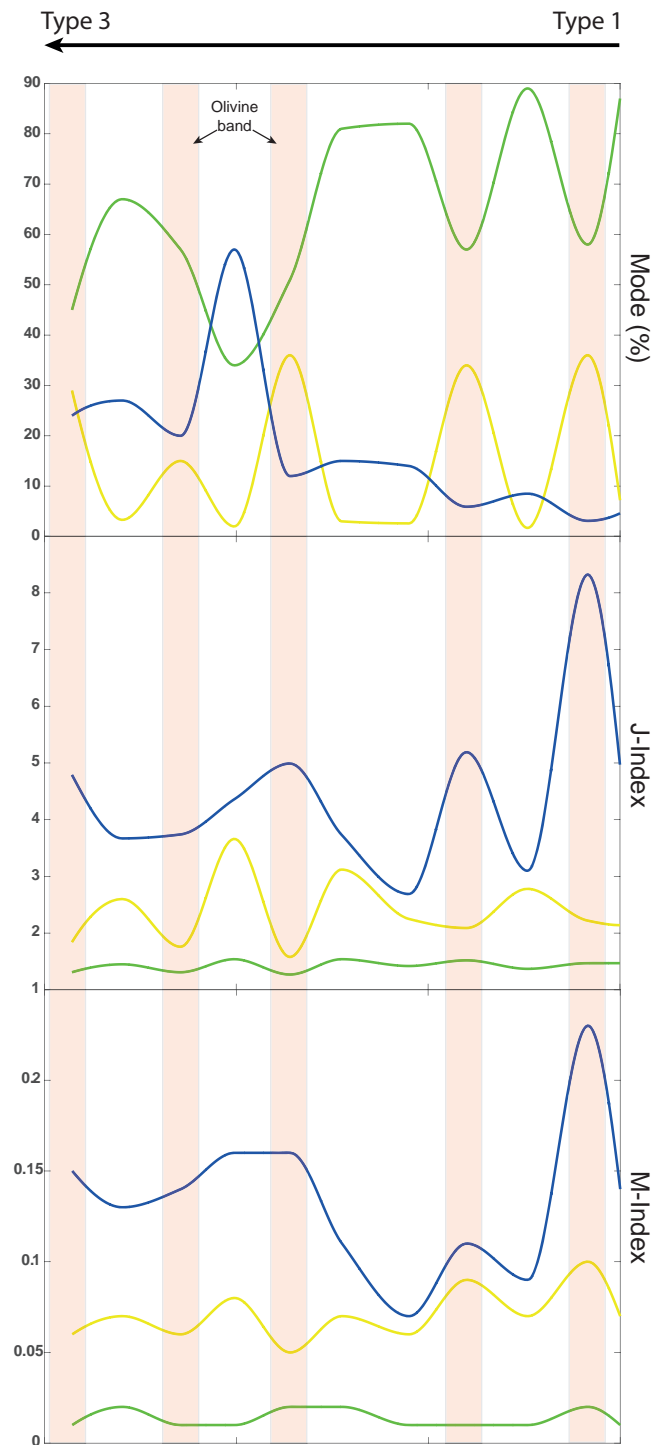


Fig.3.16: Mode, J- and M-indices of cpx (green), olivine (yellow) and amphibole (blue) along the profile across sample CO-010. Locations of olivine bands are indicated by red stripes.

Despite the lack of a striking deformational trend in a *type-1* to *type-3* transition, the profile in sample CO-010 reveals that: (1) the pyroxene-rich layers were deformed but to a lesser extent than the olivine-rich layers; (2) the interstitial olivine fabrics within the clinopyroxenite layers seem to have a different pattern (stronger contribution of [100](010)) from that of the olivine rich layers (B-type) suggesting that the pyroxenites may have preserved a previously acquired fabric; (3) a late deformation event occurred in the amphibole stability field and was preferentially localised in the olivine-rich intervals, probably overprinting the previous fabrics that are still preserved in the olivine-poor layers.

Our results show that the internal deformation of minerals allows a distinction between *type-1* and -2 pyroxenites *versus type-3* pyroxenites, and *type-4* pyroxenites. This correlation between pyroxenite type and internal deformation is most likely an effect of modal proportions (i.e. presence of opx in *type-2* pyroxenites). Microstructural features are especially consistent with a process that may produce Cabo Ortegal *type-3* pyroxenites from the deformation and hydration of a protolith similar to the *type-1* pyroxenites. The implications of this are two-fold and potentially have a global significance for the evolution of mantle domains: (1) during deformation, pyroxenites formed by original mantle wall-rock replacement such as *type-1* pyroxenites may represent preferential locations for fluid infiltration and the development of shear zones; (2) as a corollary, their presence in recycled mantle domains is likely to be commonly obscured (and thus underestimated) because of the overprint of metasomatic reactions, producing deformed pyroxenites and hornblendites. A similar process, in which deformation controls pyroxenite formation, was suggested by Chen et al. (2001) based on xenolith studies. By bringing statistical quantification of the mineral deformation with the use of the GOS and mineral fabrics on both *type-1* and 3 as well as on a transitional sample, the present study is thus the first to provide robust microstructural evidence to test (and in this case, support) this hypothesis.

3.13 - Investigation of the slip system activation

Fabrics are a good indicator of slip system activation but can be sometimes misleading, especially in crystals with complex symmetry. For example in cpx, [001](010) does not represent activation of [001](010) slip, but results from activation of [001]{110} and $\frac{1}{2}\langle 110 \rangle\{110\}$ that control the position of (010) along the foliation plane (Bascou et al.,

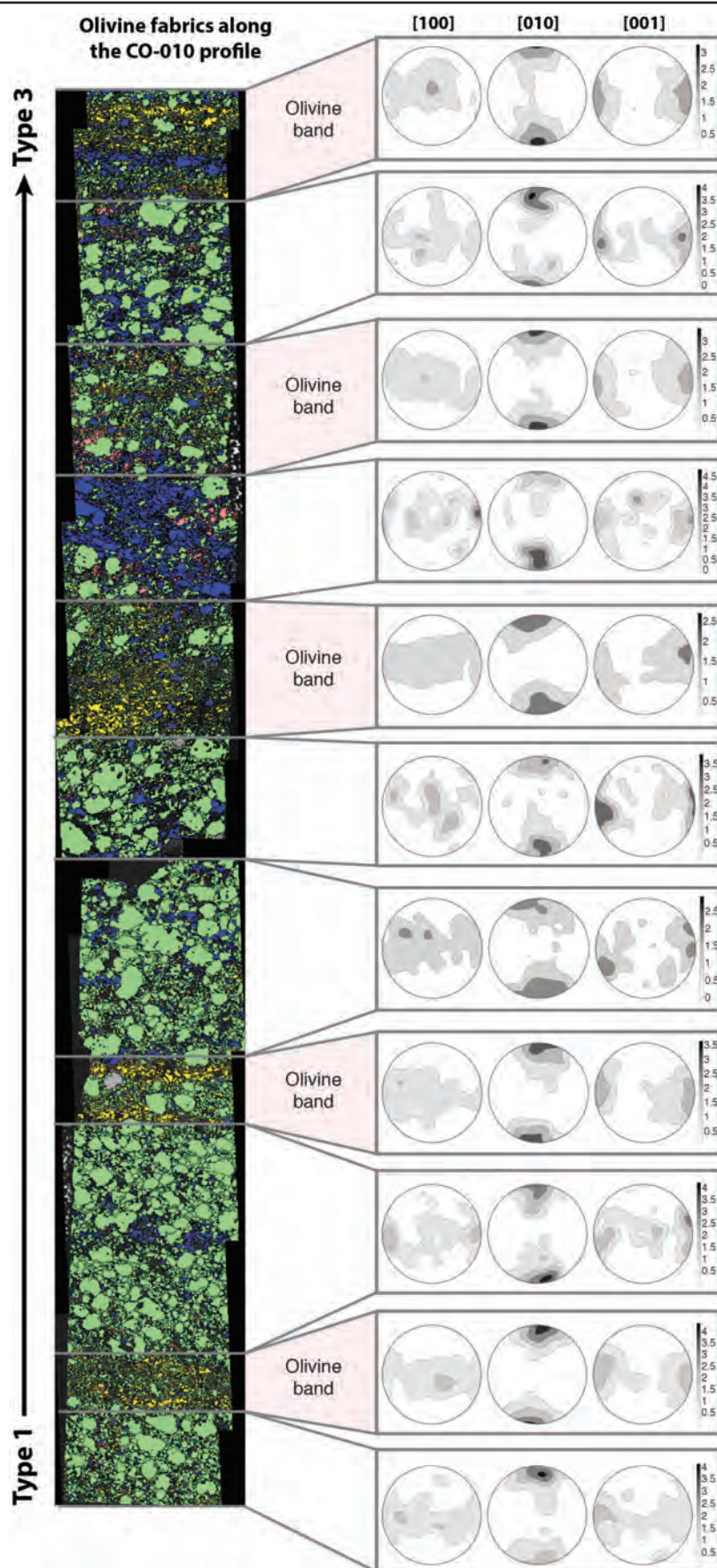


Fig.3.18: Fabrics of olivine along sample CO-010 profile. Phase map displaying the pole-figure location is shown with a similar color code to that of Fig.3.12-B.

2002). One way to verify the activation of a slip system using EBSD data is by subgrain analysis. In a subgrain analysis, the spread of crystallographic axes next to a subgrain is examined. Based on the spread of the axis, a slip plane and slip direction can be determined (Fig.3.19, Satsukawa and Michibayashi, 2009).

In Cabo Ortegal pyroxenites, subgrain analysis is possible but difficult in most cases. In every sample analysed, no cpx or amphibole subgrain could provide evidence of a clear slip system activation. This result is predictable because of the low symmetry of both phases and the multiple slip systems activated during deformation. Olivine did not provide a good support for subgrain analysis for three reasons: (1) the olivine is mostly re-equilibrated and shows only few clear subgrains; (2) the grain size of the un-equilibrated olivine grains is too small to perform the analysis or (3) the mesh alteration texture of the large olivine prevents subgrain analysis by sometimes removing the subgrains.

Opx is the only mineral in our samples where subgrain analysis is viable. The abundance of porphyroclasts with kink bands makes it easy to investigate the slip system activated. As the fabric suggests, subgrain analysis of opx confirms the activation of $[001](100)$ slip (Fig.3.19) in multiple samples.

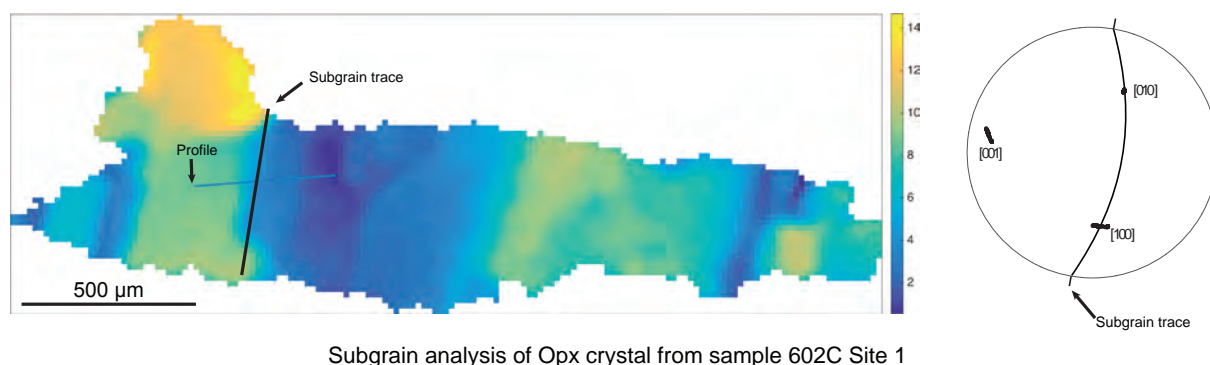


Fig.3.19: Subgrain analysis on a kinked opx from sample 602C. A misorientation to the mean grain orientation map of the grain and a pole-figure are shown. The spatial repartition of the axis in regard to the subgrain trace is indicative of migration of the dislocation on the plane (100) in the (001) direction thus suggesting activation of $[001](100)$ slip.

3.14 - Shear sense inferred from fabrics

The analyses were performed in the XZ plane, thus allowing the use of the EBSD-derived fabrics to quantify the shear sense (Bouchez et al., 1983; Simpson and Schmid, 1983). The fabrics were put in context using the vertical polarity of the sample, so the structural

framework and a shear sense was determined. When the obliquity was too small, or the fabric strength too weak, or if there was a doubt on the XZ plane determination, the shear sense was not investigated.

Results are presented in Table.3.5. Correlations are elusive, but two trends may be noticed: both shear senses are found in all types and pyroxenes have recorded more top-to-north shearing than amphibole, which recorded more top-to-south shearing. Based on more sample and a more exhaustive structural study of the massif, Girardeau and Gil Ibarguchi (1991) observed a lens shape for the pyroxenite-rich outcrop distribution in Herbeira and related this shape to a top to the north shearing direction observed in thin sections. The fact that amphibole mostly records the opposite motion, sometimes even in the same sample, may suggest a different deformation regime during the plastic-deformation event recorded by amphibole. This is consistent with the introduction of the ultramafic massif in a subduction channel and a shear sense inversion during the late history of the massif that is the exhumation. However, the amount of shear sense determined is not statistically significant and therefore any interpretation based on this has to be taken with care.

Sample	Shear direction			
	Orthopyroxene	Clinopyroxene	Amphibole	Olivine
Type-1 pyroxenites				
CO-096-A/A	-	Top to the South	Top to the North	-
CO-096-A/B	-	Top to the South	-	-
CO-100-A	-	-	Top to the South	Top to the South
CO-100-B	Top to the South	-	-	-
401A	-	-	-	-
701BA	-	-	-	-
702A	-	Top to the South	-	-
Type-2 pyroxenites				
706AA	Top to the North	-	Top to the North	-
CO-024	Top to the South	Top to the North	Top to the North	-
CO-097-A	Top to the South	Top to the South	Top to the South	-
CO-099-A	Top to the North	Top to the North	Top to the North	-
Type-3 pyroxenites				
CO-067-A	-	-	-	-
CO-067-B	-	Top to the South	-	-
CO-101-C	-	-	Top to the North	-
Type-4 pyroxenites				
602C	-	-	Top to the South	-
704A	-	-	-	-
Other samples				
204A	-	Top to the South	-	-
604A	Top to the South	Top to the South	-	-
604B	-	Top to the South	-	-
605BA	-	-	-	-
703A	-	-	-	-

Table.3.5: Shear direction inferred from fabric obliquity following the principle of Bouchez et al. 1983. Only obvious obliquity are reported in this table.

3.15 - Tectonic and geodynamic implications

Isoclinal folds (which indicate a low viscosity differential between the two lithologies involved) and boudinage, (related to a higher viscosity differential, e.g. Passchier and Trouw, 1996), are both observed in the field. This combination could result from a succession of two deformation events that occurred under different conditions, leading to different viscosity contrasts. However, field observations instead suggest that both deformation markers developed at the same time (Jamaa, 1988; Girardeau and Gil Ibarguchi, 1991; Ábalos et al., 2003). In a dry and shallow mantle (0.5 to 1.5 GPa and up to 1100°C), flow laws predict that dunite would have a viscosity similar to websterites and that the websterite would be more viscous under a hydrated and shallow upper mantle conditions (Avé Lallemant, 1978). The addition of a hydrous fluid during deformation in a dry environment, or the presence of an interstitial fluid in the websterites, as possibly suggested by the B-type olivine, could bring the viscosity contrast to a tipping point where boudinage and isoclinal folding could develop simultaneously (Avé Lallemant, 1978). Considering that the Cabo Ortegal pyroxenite most likely originated in a sub-arc mantle regime (Tilhac et al., 2016), both scenarios are possible and not mutually exclusive.

The CPO maxima of pyroxenes and olivine differs significantly from that of amphibole in some samples, suggesting that amphibole recorded a different deformation episode, as illustrated by sample CO-101-C (Fig.3.10). Cpx clearly exhibits an S-type fabric while amphibole shows point maxima fitting both the foliation and lineation reference frames. Sample CO-101C is from an area containing sheath folds, suggesting that amphibole was still recording plastic deformation during their growth subsequent to the high-temperature event recorded by the pyroxenes and olivine. However, it is difficult to determine whether the deformation regime recorded by the amphiboles is a continuation of the high-temperature event or a separate one.

It has been suggested by several authors that some of the high-pressure allochthonous units of the Cabo Ortegal Complex originated in an arc region (Ordóñez-Casado et al., 1996; Albert et al., 2014; Arenas et al., 2014) and that their exhumation and emplacement occurred after they became part of a subduction return flow associated with an orogenic episode. Tilhac et al. (2016) confirmed the arc-related origin for the Cabo Ortegal pyroxenites and suggested that their introduction into the subduction channel was the result of delamination of the relatively

dense pyroxenite-rich domain from a harzburgite sub-arc mantle. The relatively low-stress, high-temperature and potentially hydrous environment, suggested by cpx and olivine fabrics, is consistent with such a scenario where deformation of the Cabo Ortegal pyroxenites occurred in a supra-subduction, arc-root environment.

In agreement with the petrological constraints, EBSD data support the coexistence of syn- and post-kinematic amphibole formation. The lack of initial Sr-Nd isotopic equilibrium between cpx and amphibole suggests percolation of a hydrous fluid during amphibole growth but cannot rule out the possibility of a magmatic origin for the amphibole (Tilhac et al., 2016; Tilhac, 2017). However, the textural relationship of amphibole and cpx and the volumetric dominance of undeformed amphibole suggest that a metamorphic origin for the amphibole is more likely even if no intracrystalline magnetite were observed. The homogeneity of the amphibole fabrics and the probable low-stress environment (although greater than the stress during high-temperature deformation) in which the deformation occurred are further indicators that the deformation was relatively limited once the amphibole stability field was reached. The common similarity of the maximum points of fabrics associated with the high-temperature and low -temperature events may be explained by two scenarios that are not mutually exclusive:

- (1) the deformation was continuous and in an almost spatially constant stress field.
- (2) a re-orientation of the structure occurred due to late mylonitisation that would be difficult to observe in the field.

Nonetheless, the petrological, geochemical and microstructural evidence is consistent with the introduction of a relatively competent, pyroxenite-rich mantle domain into a relatively softer subduction channel.

Summary of Chapter 3

*The Cabo Ortegal **pyroxenites** all display a **similar response to deformation (fabrics and deformation markers)**.*

*Deformation features of **olivine and pyroxenes** are consistent with **deformation at high temperature**.*

***Amphibole** fabric and texture are consistent with a **lower temperature deformation**.*

*Microstructural and geochemical data are in agreement with a scenario where **deformation of the dunite bearing type-1 pyroxenites** would result in **type-3 pyroxenites**, thus creating a **preferred path for later fluid percolation**.*

*Our data are all consistent with a deformation in a **mantle wedge setting** followed by introduction into a **subduction return flow**.*

Chapter 4:
The Microstructure of the
Trinity Pyroxenites

4.1 - Introduction to the Trinity ophiolite geology

Located in the Klamath Mountains, the Trinity ophiolite is the largest mafic-ultramafic body (3000 km²) outcropping in California, USA (Fig.4.1). It forms part of the Paleozoic Terranes that were accreted to the North American Cordillera in Devonian time (Lanphere et al., 1968; Hamilton, 1969; Irwin and Mankinen, 1998).

The first geological studies of the complex interpreted it as an ultramafic pluton intruded by younger gabbroic and granitic batholiths (e.g. Lipman, 1964). It was only after the demonstration of its sheet-like geometry by combined structural and geophysical studies that its allochthonous origin was suggested (Irwin, 1966; Hamilton, 1969) and that the association of ultramafic and mafic units were considered as the co-genetic components of an ophiolitic assemblage (Lindsley-Griffin, 1977).

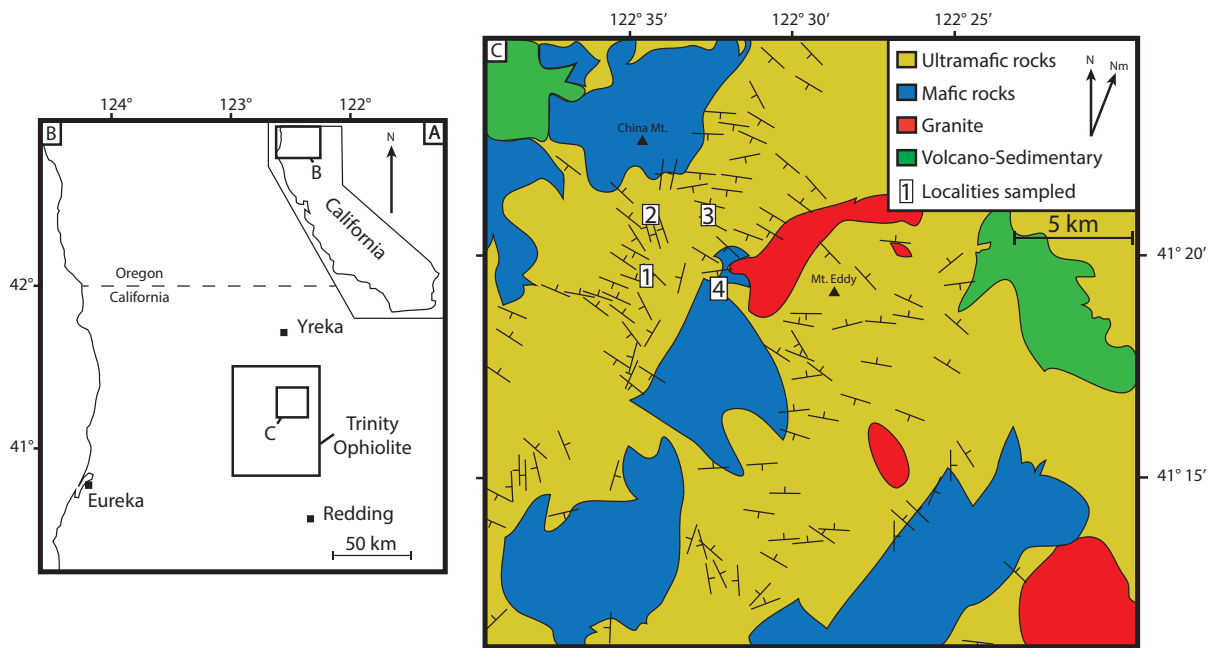


Fig.4.1: Location and geology of the Trinity ophiolite. A- Map of the state of California, USA; B- location of the Trinity ophiolite and C- region of interest of the study. The main lithological units, dip and foliation direction are after Boudier et al. (1989). White boxes represent the location of the four localities sampled: 1, Corry Peak, 2, Vicky Bluff, 3, Layered Dunites and 4, Bear Creek.

Based on geochemical evidence from extrusive rocks associated with the ophiolite, Brouxel and Lapierre (1988) and Brouxel et al. (1988) proposed that the Trinity terranes originated and evolved in an arc-related oceanic basin. More recently, Mankinen et al. (2002) showed that the oceanic basin in which the Trinity ophiolite evolved could have lain between Rodinia and Laurentia. They further suggested that the emplacement of the Trinity ophiolite may have resulted from the closure of that basin during the Ordovician and its obduction onto the North America continent.

Several geochronology analyses have dated the last partial melting event experienced by plagioclase lherzolites at 470 ± 40 My using Sm-Nd (Jacobsen et al., 1984). Peridotites from the Toad lake area provided a Sm-Nd age of 420 ± 50 My (Gruau et al., 1991). Crustal rocks of the Toad Lake and China mountain area have U/Pb zircon ages ranging from 405 to 430 My (Wallin et al., 1995; Wallin and Metcalf, 1998).

Boudier and Nicolas (1985) declared Trinity as the archetype of what is defined as the “Lherzolite Ophiolite Type”, interpreted as the equivalent of the mantle beneath present-day slow spreading mid-ocean ridges. Their main argument was the association of relatively fertile lherzolites with a poorly developed magmatic crust in Trinity, contrasting with the association of highly depleted harzburgites with a thick magmatic crust in what they defined as the “Harzburgite Ophiolite Type”, interpreted as the remnants of fast-spreading ridges, like Oman. However, Ceuleneer and Le Sueur (2008) demonstrated that the crustal section of Trinity crystallized from a boninitic melt ultra-depleted in HFSE and could not be considered as derived from the associated fertile lherzolites, thus calling into question the Boudier and Nicolas (1985) argument that the poorly developed crust is not a consequence of the low degree of melting of the associated lherzolites.

Overlying a basal metamorphosed crust, a typical section of the Trinity ophiolite starts with the deepest part of the mantle section that it hosts: plastically-deformed plagioclase lherzolite. 2 km below the top of the mantle section of the ophiolite, dunite and harzburgite become abundant and can locally become the dominant lithology. The mantle section shows a steep dipping foliation and a sub-horizontal lineation in regard to the overlying crustal section and the paleo-surface (Le Sueur et al., 1984; Boudier et al., 1989). The crustal section is 2-3 km thick and is made up of differentiated plutons. The structure of the plutons shows gradual

transitions from layered cumulates rich in olivine (~300m in thickness) towards cumulates rich in pyroxenes (~500m) and eventually transitioning towards gabbro-diorite where the magmatic layering is poorly developed and the magmatic breccias quite frequent (~500m in thickness, Ceuleneer and Le Sueur, 2008).

4.2 - The four sampling localities

Four localities were targeted for this study (Fig.4.1 and Fig.4.2) and provide insight on the mantle and crustal sections of the ophiolite. Following the paleo-structural order, each locality is presented below. As a significant shift between the geographic and magnetic North is observed in north California, it is important to note that every measurement presented here and in the electronic appendices is relative to the magnetic North.

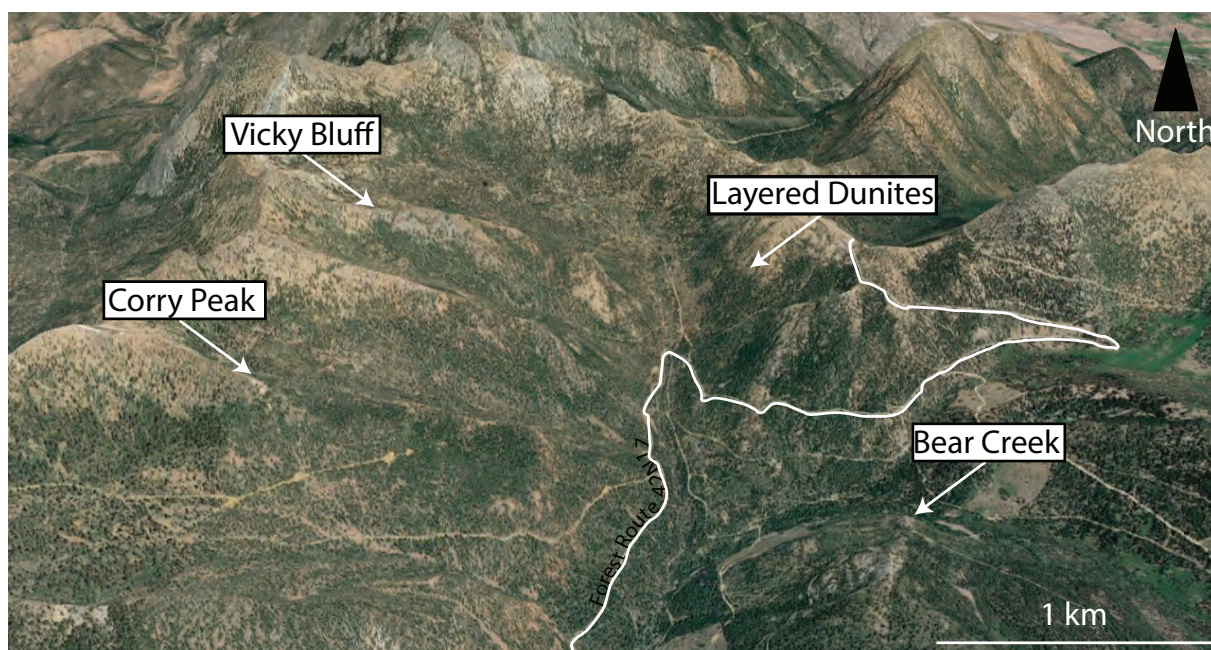


Fig.4.2: Satellite view of the 4 localities sampled: Corry Peak, Vicky bluff and the Layered dunites are located along the Pacific crest trail. Bear Creek is separated from the other localities by the Trinity River fault following the Forest route highlighted in white.

Corry Peak

Corry peak is located in the deepest part of the mantle section where fieldwork was undertaken (Fig.4.2). The location of sample T5CP1A is characterized by fresh and massive lherzolites (Fig.4.3-A). They show a consistent lineation (N120, horizontal) and a foliation

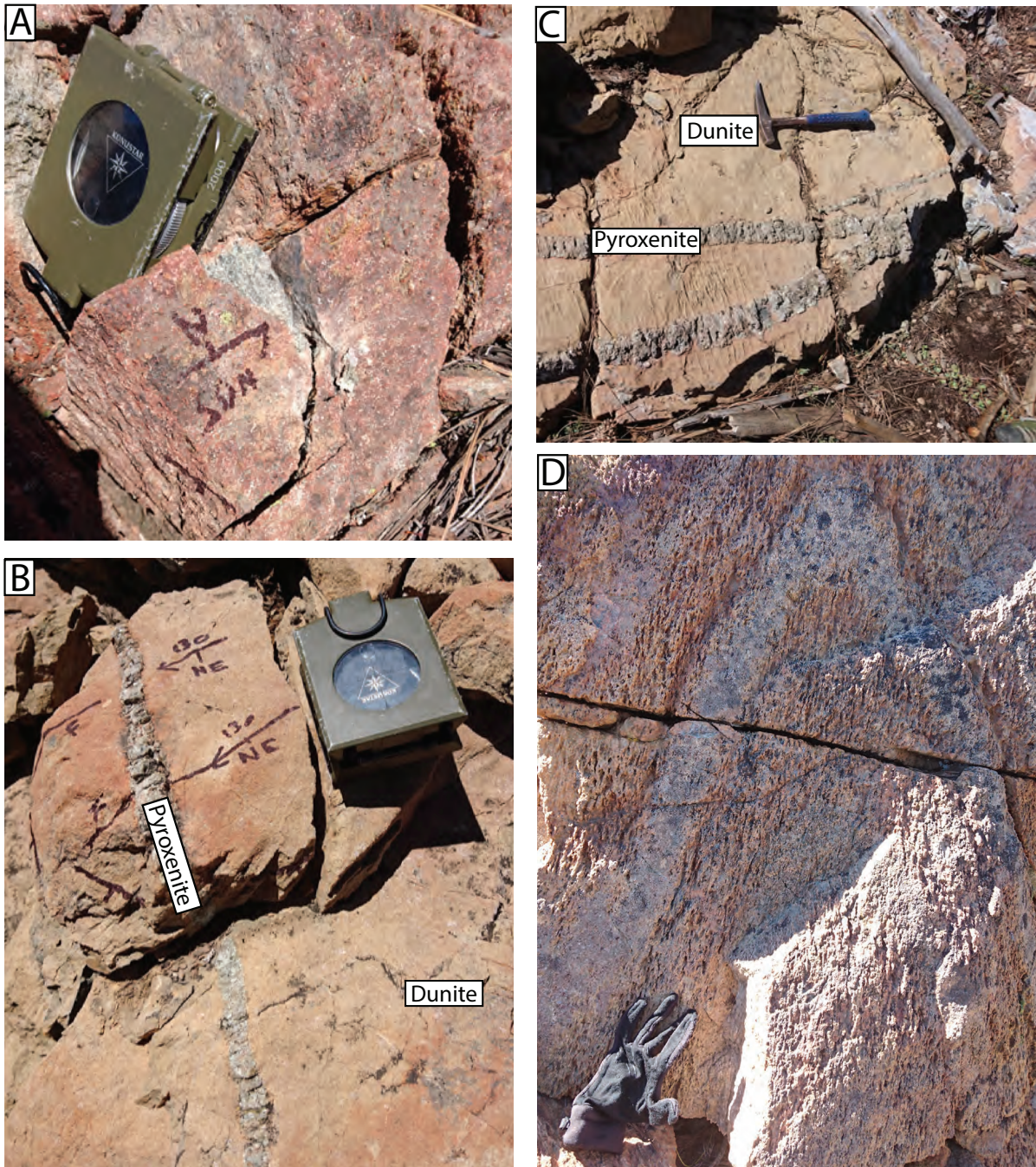


Fig.4.3: Field pictures from Corry peak. (A) outcrop of plagioclase-bearing lherzolite (T5CP1); (B) and (C) dunite bodies cross-cut by a pyroxenite layer at lower altitude (T5CP2), and (D) isoclinal fold in lherzolite on the Pacific Crest trail (sample T5CP4 location).

with a N120 azimuth and variable dip. Cross-cutting of the plagioclase lherzolite by pyroxenite veins can be seen and both deformed and undeformed pyroxenite veins can be distinguished, suggesting different timing of intrusions relative to the plastic deformation history.

A dunite body occurs downslope; its contact with the overlying plagioclase lherzolite is masked by rubble (Fig.4.3-B and -C). This domain does not show a clear foliation but the elongation of the spinel grains defines a lineation in the N130 direction. Numerous crosscutting pyroxenites and melt-rock interaction structures are exposed in this dunite (Fig.4.3-B and -C). Pyroxenite veins show very variable internal structures and they can (1) be continuous and made of pure pyroxenite; (2) have a continuous or discontinuous olivine-rich core and pyroxene-rich rim or (3) have a dashed-line aspect. These different types could be interpreted as representing either different degrees of dissolution of a continuous pyroxenite layer or previously zoned veins resulting from crystal segregation. Further downslope, plagioclase lherzolite occurs again, showing evidence of isoclinal folding (Fig.4.3-D, sample T5CP4).

Vicky Bluff

Vicky Bluff lies 2 km north of Corry Peak, a few hundred metres below the gabbros of the China Mountain pluton (Fig.4.1 and Fig.4.2). In this locality, harzburgite, lherzolite, dunite and pyroxenite coexist and display spectacular features of melt-rock interaction. In Vicky bluff, sharp and complex contacts between lherzolites and other lithologies occur at relatively small scales (few centimetres to few decimetres, Fig.4.4-A and Fig.4.4-B).

Peridotites (i.e. lherzolite or harzburgite depending on the sample considered, Fig.4.4-C) are the most abundant host rock at this site and within it, pyroxene-rich layers with diffuse contacts are visible, along with late pyroxenite pegmatites that crosscut all other lithologies (Fig.4.4-D). The plastic-deformation structures of the peridotites are poorly developed: elongated spinels hint at a lineation (~N130), while the foliation is poorly defined and its dip is difficult to identify with certainty. Sheath folds in harzburgite were observed in the immediate vicinity of Vicky Bluff, making the identification of a foliation that is not related to this shear fold event at the scale of the outcrop, even more tricky.

The dunite (Fig.4.4-B) domains can be either channel-shaped with or without dendritic terminations, or simply pocket shaped; they are always enclosed in peridotite. In some outcrops, dunite bodies can be interconnected and discordant with the primary plastic deformation structures of the peridotite. In this particular outcrop, the geometry of the

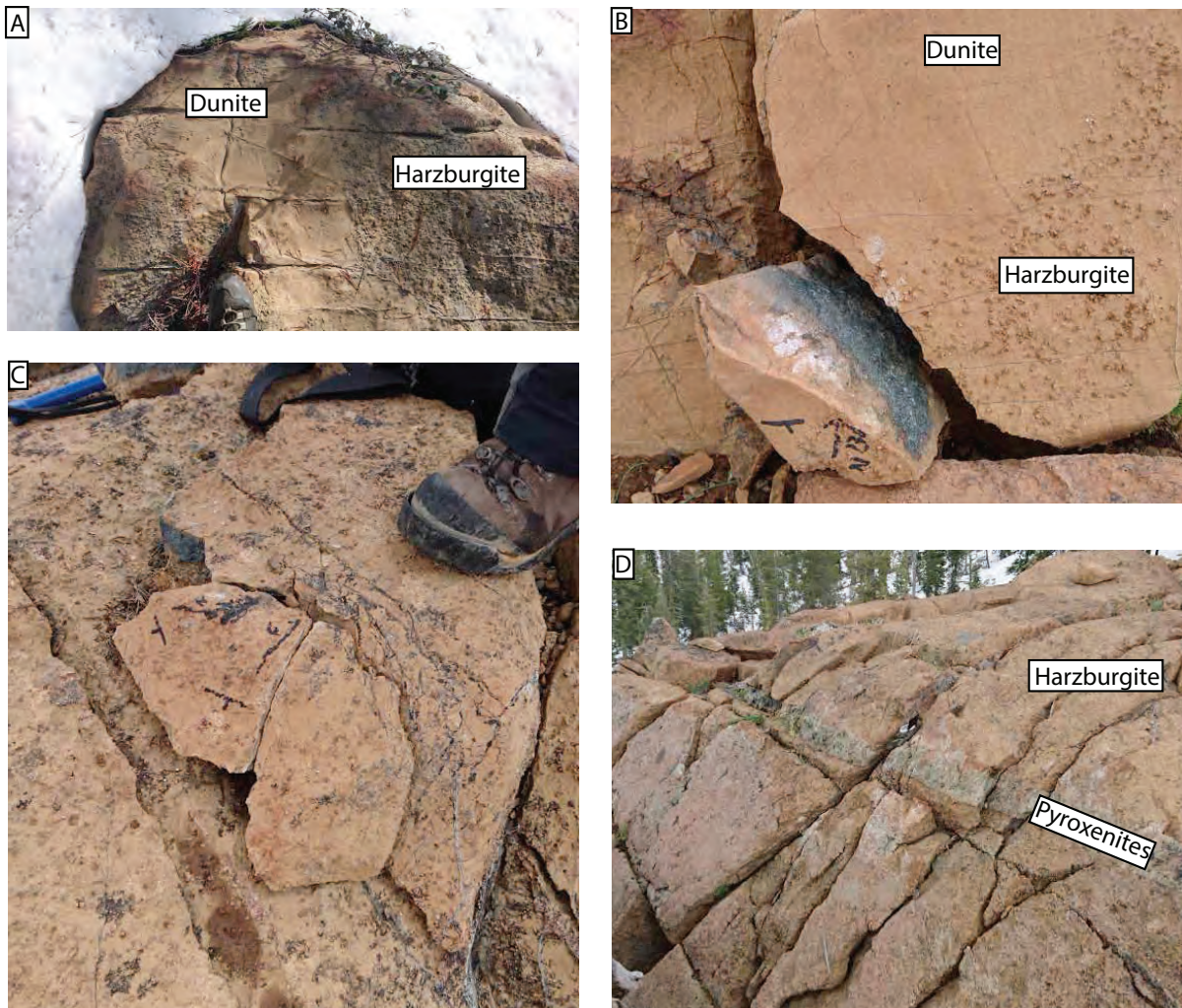


Fig.4.4: Field pictures from Vicky Bluff. (A) Dunite and harzburgite displaying an example of melt-rock interaction; (B) contact between dunite and harzburgite. Note the sharp contact between the lithologies (T2VB3); (C) massive harzburgite (T2VB2), and (D) pegmatitic pyroxenite layer within harzburgite.

dunitic channels is not randomly oriented relative to the structural features of the peridotite (i.e. the presence or absence of pyroxene-rich layers). Dunitic bodies are connected to dunitic channels which are deflected when crosscutting diffuse pyroxenite-rich layers in the lherzolite. The cores of some dunite channels preserve relict pyroxenes, suggesting the melt involved in the formation of the dunite was undersaturated in pyroxene.

Layered Dunites

This site is located in the upper parts of the mantle section and hosts two major facies. At the top of the section, layered dunites crop out. Their layered aspect is marked by serpentine-filled joints. Layers have thicknesses varying between a few centimetres and one metre (Fig.4.5-A). The geometry of the contacts is not regular and most of the layer boundaries have plano-convex shapes (planar feature measurement: ~N130, 30N). In the dunite, elongation of spinels defines a relatively clear lineation (~N130) but, as at Vicky Bluff, the foliation is not clearly expressed.



Fig.4.5: Field picture of the Layered Dunites locality. (A) Typical dunite outcrop (sample T1LD2). The plano-convex serpentine levels are labelled as layer boundary with white dashed-line. (B) massive harzburgite outcrop; the trace of the foliation is visible here. (C) Zoomed out picture of (A) and (B) showing the diffuse contact and the proximity of the two samples. Sample T1LD1 and T1LD2 are next to the Harzburgite and Dunite tags respectively.

The origin of this type of facies is still debated and no clear answer has been provided yet. Mineral compositions reported by Ceuleneer and Le Sueur (2008) plot in the trend of the overlying ultramafic cumulates of the Bear Creek pluton. Among other, the very low TiO_2 content of Cpx and Cr-spinel suggest a common origin from fractional crystallization or re-equilibration with a melt ultra-depleted in HFSE. The complex compositional trends shown by Cr-spinel and their local decoupling with the composition of silicates especially in the lower part of the unit could indicate a reactional origin for the lower part of the layered dunites and a cumulative origin for the upper part as suggested for the dunitic transition zone of the Oman ophiolite (Abily and Ceuleneer, 2013).

Upsection, harzburgite is first found interlayered with dunite before becoming the main facies outcropping at the location of sample T1LD1 (Fig.4.5-B and Fig.4.5-C). Structural relationships between dunite and harzburgite suggest that dunite postdates the formation of harzburgite and even the small pyroxenite layers that can be found in the harzburgite. Foliation ($\sim\text{N}140$, 25N) and lineation ($\sim\text{N}140$, horizontal) are visible because of aligned spinels and opx representing both the elongation direction and the foliation plane.

Bear Creek

The Bear Creek locality is the shallowest section of the Trinity ophiolite that was investigated and may correspond to the upper structural part of the layered dunite unit described above, separated from one another by the Trinity River Fault (Fig.4.2, Ceuleneer and Le Sueur, 2008). The Bear Creek hosts one of the 12 gabbroic intrusions in the Trinity Ophiolite. It was emplaced at relatively shallow depth in the lithosphere as evidenced by a well-developed pegmatitic aureole in the host peridotites and to the occurrence of swarms of diabase dykes, probably the roots of a sheeted dyke complex, several hundred meters upsection. The crystallization sequence and the mineral compositions suggest that the Bear Creek pluton crystallized after injection of a single batch of boninitic-andesitic melt (high silica and water content, low HFSE and Al_2O_3 Ceuleneer and Le Sueur, 2008).

The Bear Creek magma chamber displays a complete and structurally consistent cumulate sequence starting from olivine-bearing cumulates and ending in magmatic breccia at the summit above Toad Lake. The overall structure of the Bear Creek locality from the structural

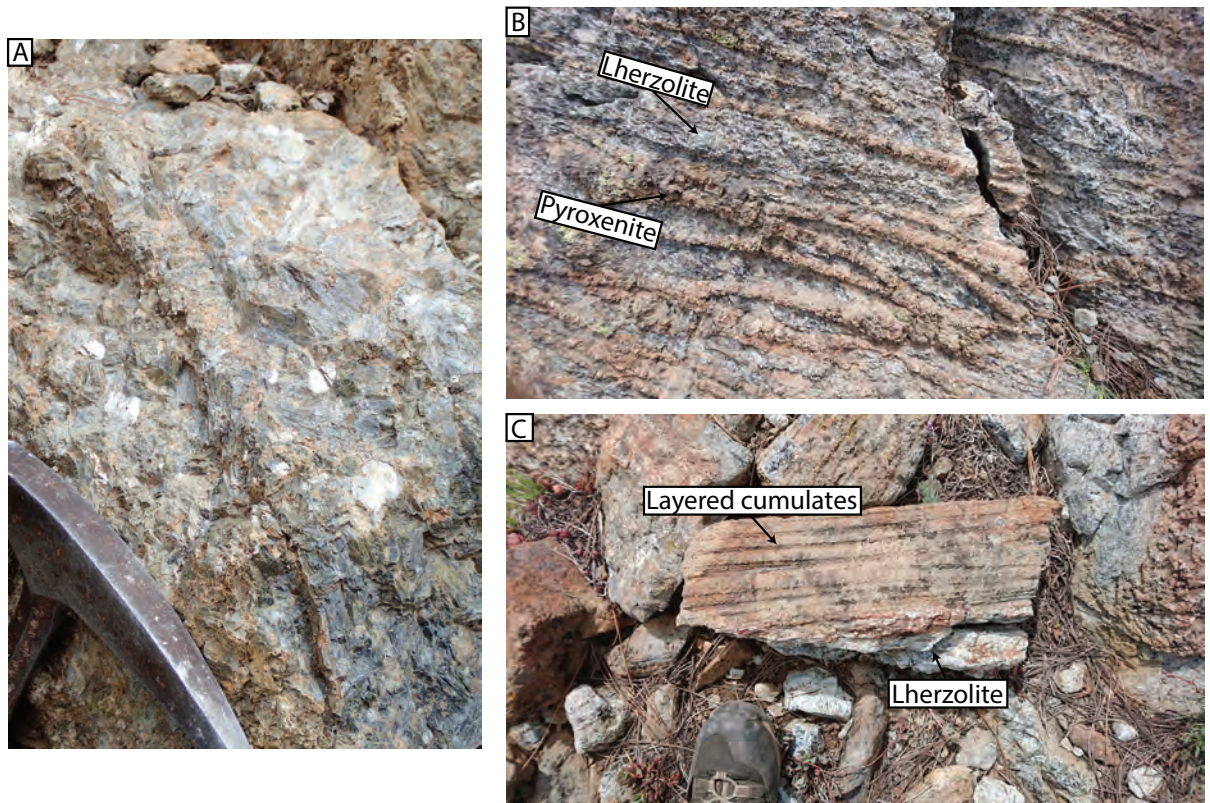


Fig.4.6: Field pictures of the basal portion of the Bear Creek section. (A) pegmatitic cpx in lherzolite; (B) serpentinized lherzolite with numerous pyroxenite layers (sample T4BC3) and (C) contact between the serpentinized lherzolite and the overlying finely layered cumulates, found on a loose block.

bottom to the top, as reported by Ceuleneer and Le Sueur (2008), starts with alternating finely-layered olivine-rich and olivine-free cumulates over ~200m. Above this, olivine disappears and clinopyroxenite with larger grain size and a more massive aspect (where the compositional layering is more difficult to observe) crops out for another ~ 200m. Higher up, plagioclase segregations in massive pyroxenites become visible. Plagioclase content within the cumulates continues to increase with altitude, eventually leaving gabbro-diorites as the only remaining lithology. The end of the section is located close to the summit and features a magmatic breccia and the diabase dyke complex.

As the emphasis of this work is on the massive pyroxenites and the finely-layered cumulates, a more detailed description of this section is provided below.

The layered pyroxenites structurally rest on serpentinized lherzolite invaded by fine-grained and coarse-grained pyroxenites (Fig.4.6-B). Large volumes of pegmatites were observed and reveal a link with the coarse-grained pyroxenites; the latter are dendritic

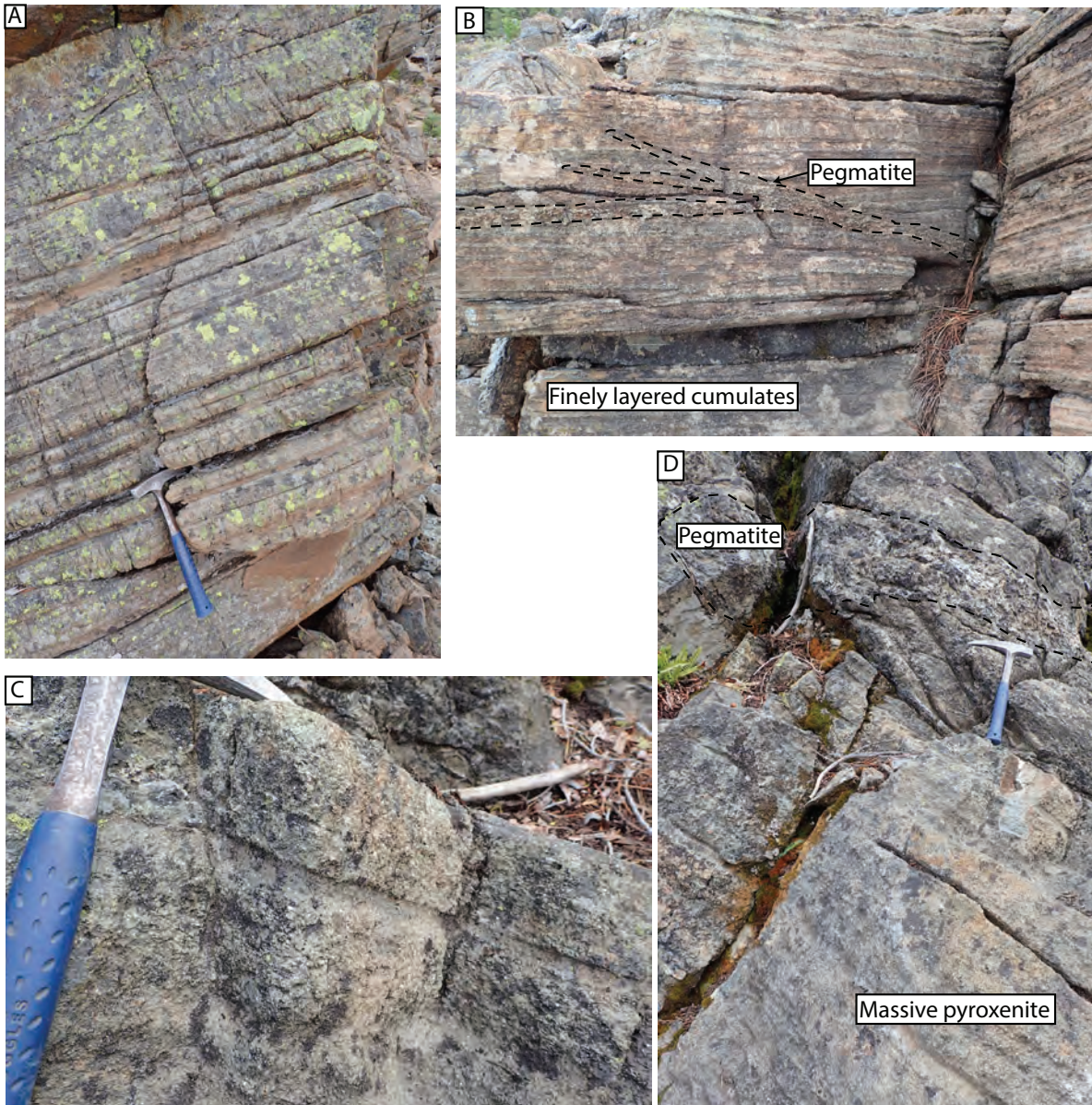


Fig.4.7: Field picture of the Bear Creek cumulates. (A) Typical outcrop of finely layered cumulates; (B) Finely layered cumulates intruded by pegmatite (dashed lines) following and/or discordant to the compositional layering; (C) Outcrop of massive pyroxenite higher up in the section. In the field, the grain size is coarse and contrasts with the fine-grained and finely-layered cumulates; (D) pegmatite intrusion within massive pyroxenites (dashed lines).

intrusions in the lherzolite that are connected to larger pockets of pegmatite (Fig.4.6-A). The contact between the lherzolite and the layered cumulates was only found on one loose block (Fig.4.6-C) suggesting a possibly complex shape for the lithological contact.

Above the lherzolite, which shows clear sign of plastic deformation in the field, finely layered cumulates crop out (Fig.4.7-A and Fig.4.7-B). Olivine-free cumulates are mainly clinopyroxenite and websterite (with a high cpx / opx ratio) and alternate with dunite, harzburgite or lherzolite. Depending on the sample, the three phases (olivine, cpx and opx)

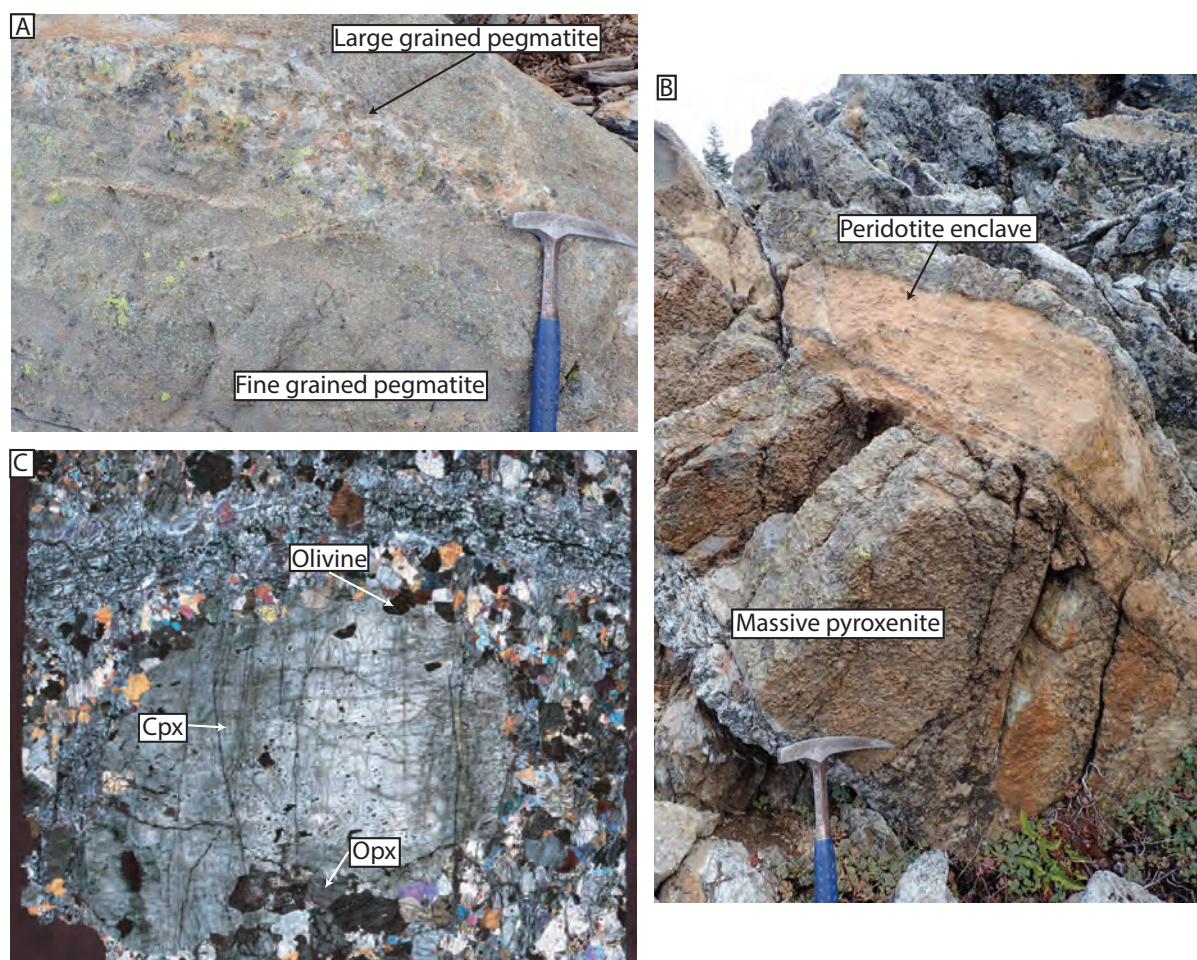


Fig.4.8: Important and noteworthy features from the Bear Creek locality. (A) diffuse grain size reduction from large to finer grain at the extremities of some pegmatites; (B) example of a peridotitic enclave (sample T4BC6) embedded within massive pyroxenites; (C) cross-polarised image of a thin section of a finely layered cumulate exhibiting a macrocrystal perturbing the layering above it. Width of the section is 2cm

can be homogeneously mixed and no bedding can be seen, or clear contacts can be seen between the compositional layers with no sign of graded bedding. The layering frequency can range from millimetric (i.e. close to that of the grain size) to centimetric; the lateral extension of the layers is great and their terminations are rarely observed. From a structural point of view, the foliation (i.e. magmatic layering) is well defined but no obvious lineation could be observed.

Higher up, the thin compositional layering disappears, potentially suggesting a decrease in the frequency of olivine-rich layers and a transition towards the massive pyroxenite facies. A foliation is still visible but the frequency at which olivine-rich levels appear becomes decimetric to metric. The observation of a lineation in that facies is still very difficult. The grain size increases with the shift toward that “massive” clinopyroxene-rich facies (Fig.4.7-C

and Fig.4.7-D). Above the massive pyroxenite unit, outcrops are rarer due to the denser vegetal cover. Despite this, clinopyroxene-rich pegmatite pods several meters thick, similar to those found in the Iherzolite, are visible on the way up.

All along the cross section of the Bear Creek magma chamber, two features disrupt the pyroxenite layering: (1) clinopyroxenite-pegmatite segregations and (2) peridotitic xenoliths or megacrysts.

Pegmatite segregations postdate the pyroxenite layering and can either follow the compositional layering or crosscut it (Fig.4.7-B and Fig.4.7-D). In the dendritic extremities of the pegmatites, the grain size is reduced to nearly the grain size of that of the massive pyroxenite (Fig.4.8-A). It is noteworthy to mention that in the larger-grained fraction, euhedral grain shape can be seen. In this chapter, the large-grained fraction of the pegmatitic outbursts will be referred to as coarse-grained pegmatite.

Peridotitic xenoliths or macrocrysts are two other causes of perturbations in the compositional layering (Fig.4.8-B and Fig.4.8-C) and appear throughout the whole section. In some cases, pegmatite segregations originated next to enclaves, suggesting different possible origins for both features. On one side, the peridotite enclaves may represent blocks detached from the roof of the magma chamber. This would imply that the surrounding pegmatite could reflect either (1) a sudden expulsion of residual magma after the impact between the mush and the falling enclave; (2) a quick crystallisation of the liquid surrounding the enclave because of its temperature difference relative to crystal mush or (3) veining processes that could lead to the fall of wall-rock into the crystal mush. An alternative interpretation could be to consider them as pieces of the country rock isolated due to the complex shape for the intrusion.

4.3 - Why should the Trinity microstructures be studied?

The sampling of the Trinity rocks represents a wide range of lithologies that can be split in two large groups: (1) the mantle section of the ophiolite and (2) the mafic-ultramafic plutons. Trinity thus represents an ideal opportunity to compare the textural and the deformational state of pyroxenites and associated rocks that evolved in the asthenosphere on one hand, and as layered cumulates in a differentiated intrusion on the other hand.

Furthermore, the comparison between the microstructure of the Trinity and the Cabo Ortegal pyroxenites may bring more insights on the deformation processes of pyroxene-rich lithologies in the subduction channel. In that respect, Trinity can be viewed as some sort of initial state of pyroxenites before their processing in the subduction factory.

This chapter will try to clarify the following:

- (1) What were conditions and history of deformation at the 4 localities?
- (2) Are the mantle and crustal intrusions consistent in terms of deformation and what does it mean in terms of possible geodynamic scenario?
- (3) What are the microstructures of the pyroxenes in a gabbroic intrusion and to what extent can they be used as a pre-deformation analogue for Cabo Ortegal pyroxenites?

4.4 - Textures and microstructures of the rocks from the 4 localities

This section provides a microstructural description of each lithology from every locality. EBSD data are then presented. As this work is focused on pyroxenites, the descriptions will be focused on the following phases; olivine, cpx, opx and when present and not fully altered, plagioclase and amphibole. Field data, fabrics statistics, ebsd maps as well as selected reconstructed outcrops from the Trinity campaign are provided in the electronic appendices.

Corry Peak

Corry Peak hosts two major lithologies: plagioclase lherzolite and pyroxenite-bearing dunite.

Plagioclase lherzolites are mainly composed of olivine with opx aggregates, together with rare aggregates of smaller cpx and altered feldspars (Fig.4.9-A). No compositional layering is observed but a shape-preferred orientation of the minerals defining the lineation/foliation reference frame is visible. Textures are close to equigranular with olivine and opx having similar grain size (~1mm of equivalent diameter) and cpx being smaller (~300µm). Pyroxenes occur as interstitial grains interstitial to the volumetrically dominant olivine. Grain boundaries are curvilinear, and 120° angles at triple contacts are very common. Subgrains and rare kink bands are observed in large olivine grains. No deformation markers are clearly expressed in the other phases.

The dunite microstructure is partially obscured by serpentine. A consistent shape-preferred orientation is not obvious. The texture is recrystallized and close to textural equilibrium with a coarse grain size (Mercier and Nicolas, 1975): ~3-4mm olivine grains coexist with rarer smaller ones (~300µm). The grain boundaries are curvilinear and 120° contacts are found, but less frequently than in the plagioclase-bearing lherzolite. Kink bands and undulose extinction are observed in the larger grains (Fig.4.9-B).

The sampling allows the investigation of a pyroxenite layer embedded in the dunite body. The pyroxenite sampled did not seem to show any evidence of dissolution by a latter melt and has a clear contact with the host rock. It is composed of cpx and opx in equal proportions. Amphibole can also be seen along cpx grain boundaries. Despite the strong serpentinization

overprint on the pyroxenite, a bimodal distribution for the pyroxenes is visible: a ~1mm grain size for the large grains and ~300 μ m grain size for the smaller fraction (Fig.4.9-C). The smaller-grain population shows a slight undulose extinction and 120° contacts. In the coarse-grain population, opx does not display any deformation markers and has complex, yet relatively straight grain boundaries. Cpx also displays complex grain boundaries along with kink bands.

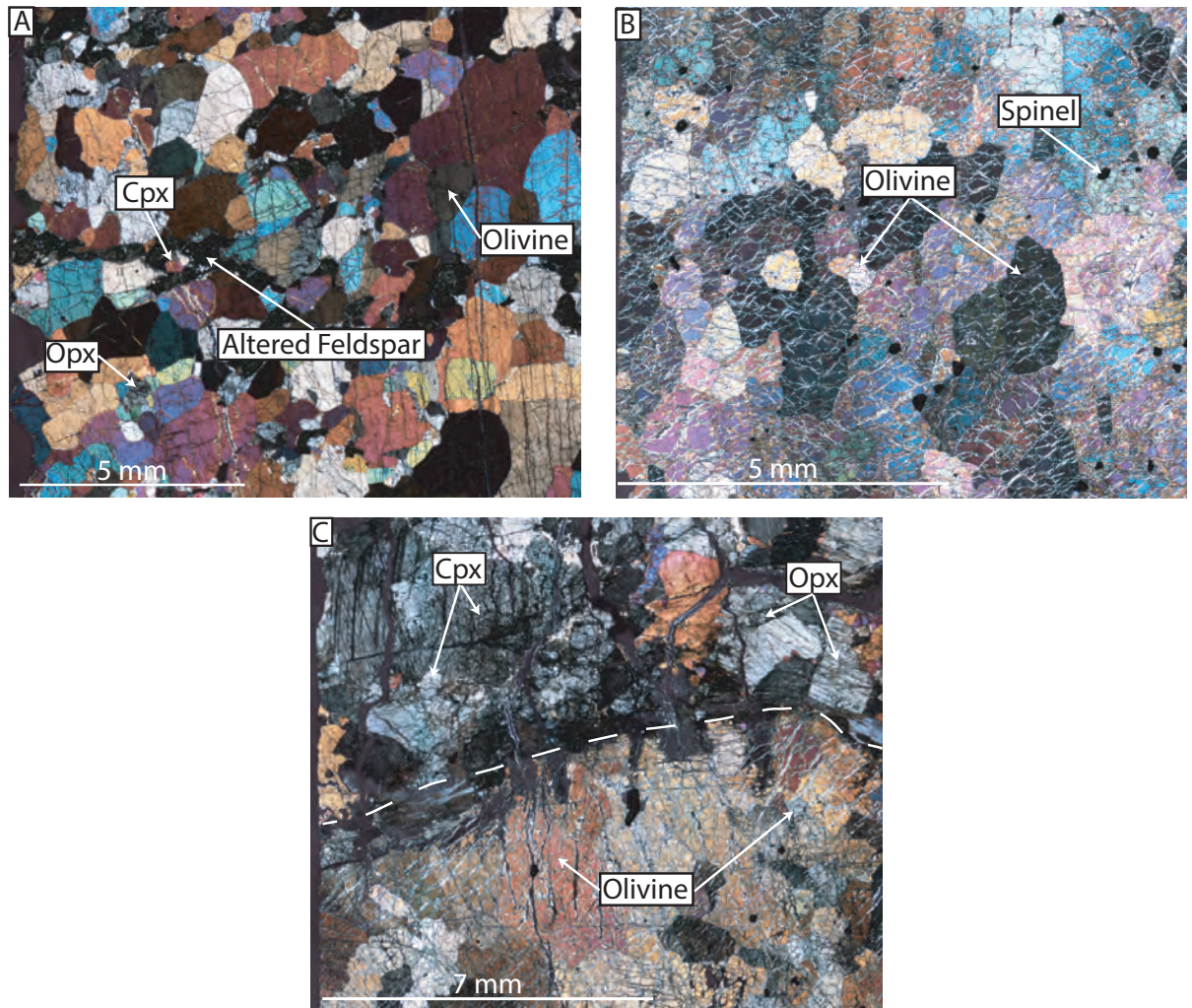


Fig.4.9: Cross-polarized photomicrographs of the microstructure of lherzolite, dunite and pyroxenite from the Corry Peak. (A) Plagioclase-bearing lherzolite from Corry Peak. Plagioclase grains are altered and are aligned along the lineation direction (sample T1CP1A); (B) Microstructure of Corry Peak's dunite: large olivine grains coexist with a smaller-sized fraction (sample 17T25E-A); (C) Contact (dashed line) between a pyroxenite layer and the host dunite in Corry Peak's dunitic body (T5CP2A). Serpentine veins crosscut the pyroxenite layer and fade in the host dunite, thus indicating a higher viscosity of the pyroxenite during the serpentine stability field.

In Vicky Bluff, 2 main lithologies were identified: peridotites and pyroxenites.

Peridotite (includes harzburgite and lherzolite) is the dominant facies by volume. Aggregates of opx (3-4mm) are found in an olivine and the heavily serpentinized matrix (Fig.4.10-A). Cpx is either associated with the opx aggregates or occurs as interstitial minerals in the olivine matrix. Overall, the texture displays a bimodal grain size distribution. For opx and olivine, coarse grains are $\sim 500\mu\text{m}$ while the smaller ones are around $\sim 50\mu\text{m}$. Depending on the sample, cpx only appears as small grains or possibly as aggregates, similar to opx,

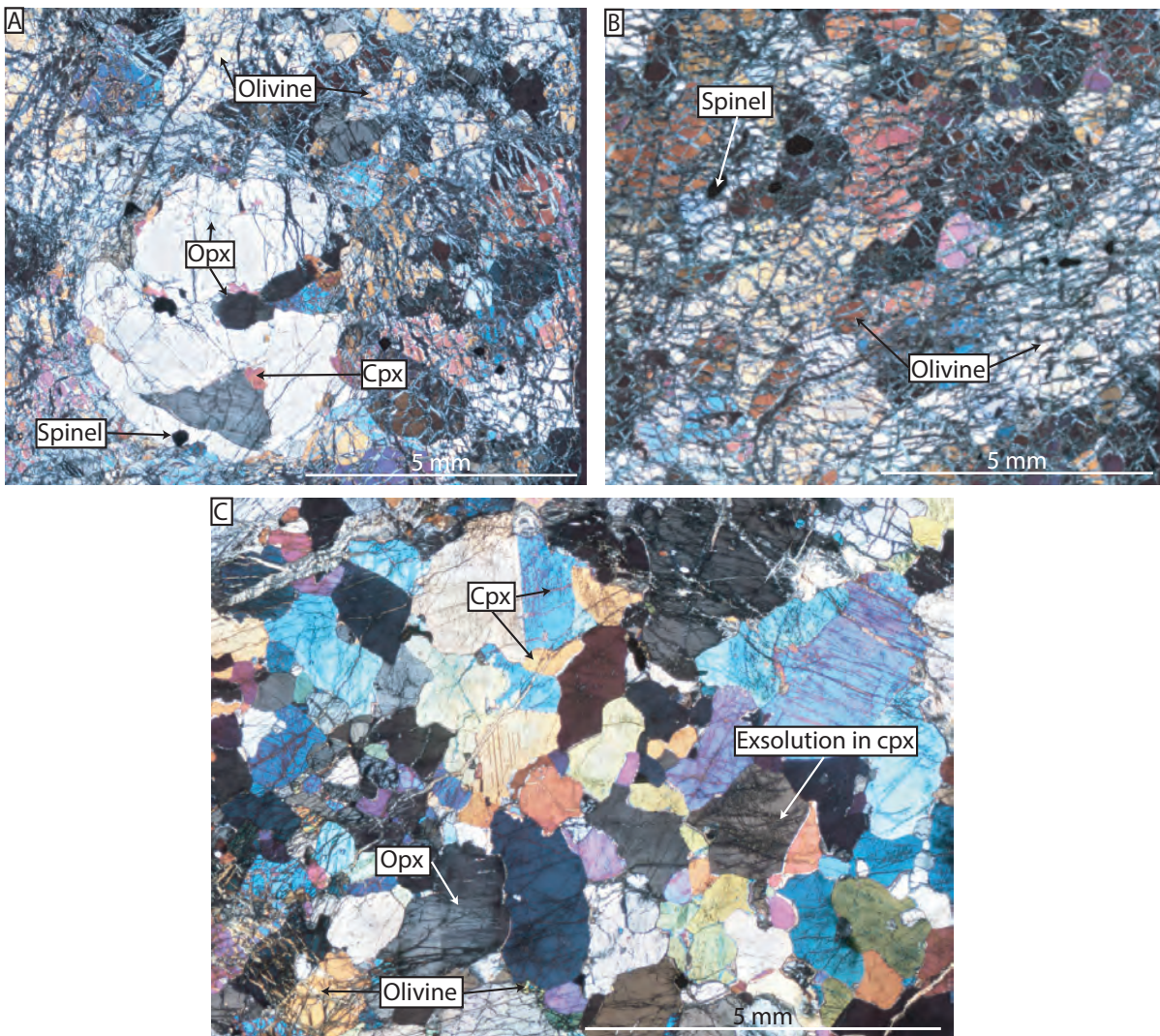


Fig.4.10: Photomicrographs of Vicky Bluff dunite, peridotite and pyroxenite. (A) Dunite (17T4A-A) and (B) the host peridotite (T2VB3A). Note the presence of opx aggregate in the peridotite; (C) pyroxenite layer in sharp contact with the dunite. Twinning in cpx is visible. Complex exsolution patterns are also visible, possibly indicating an annealing event.

therefore changing the rock type from harzburgite to lherzolite. Grain boundaries of olivine are mostly lobate and curvilinear. Pyroxene grain boundaries are complex and can be straight or curved. 120° contacts are visible in the smaller-grained fraction of the pyroxenes. The strong serpentinization of the olivine makes the identification of deformation markers difficult but subgrains can still be observed. Deformation markers in opx are striking and kink bands and undulose extinction coexist in opx aggregates.

Because of the high degree of serpentinization, the investigation of the shape-preferred orientation of olivine in the Vicky Bluff dunite is difficult (Fig.4.10-B). The grain size distribution is bimodal; large grains coexist with smaller ones with dimensions similar to the olivine grains in the surrounding harzburgite/lherzolite. The grain boundaries between olivine crystals are curvilinear in most cases. Deformation markers are unclear as the olivine has been dislocated into the characteristic mesh texture.

Two late pyroxenite veins were sampled at Vicky Bluff. Both pyroxenites are composed of opx and cpx in equal amounts, with minor amphibole at grain boundaries between pyroxenes. No shape-preferred orientation is observable for any phase. Grain-size distribution is bimodal; large cpx and opx (~3-4mm) coexist with smaller grains (~700µm) representing most of the volume. Pyroxenes are not homogeneously distributed and aggregates of opx occur within a cpx matrix. Grain boundaries can be either curvilinear or straight. 120° contacts are dominant and sometimes, small opx grains are found in the triple junction between cpx grains. Cpx deformation markers are very subtle and rare subgrain rotations at high- angle contacts are visible. Opx can show undulose extinction but is mostly recovered. Spinel exsolution in cpx may hint at an annealing event (Fig.4.10-C).

Layered dunites

The layered-dunite locality hosts two main types of lithologies: layered dunites are found close to the summit while harzburgites crop out at lower altitude.

The microstructure of the harzburgite is illustrated by two samples; one is part of the massive harzburgites at the bottom of the section and the other represents a dunite/harzburgite contact higher up. In both sections, olivine and opx make up most of the rock volume

(Fig.4.11-A) and minor cpx and chromite make up the remaining volume. A slight flattening and elongation fitting the possible lineation/foliation reference frame is visible in some olivine grains but not in pyroxenes. Grain-size distribution is bimodal: the olivine matrix is mainly

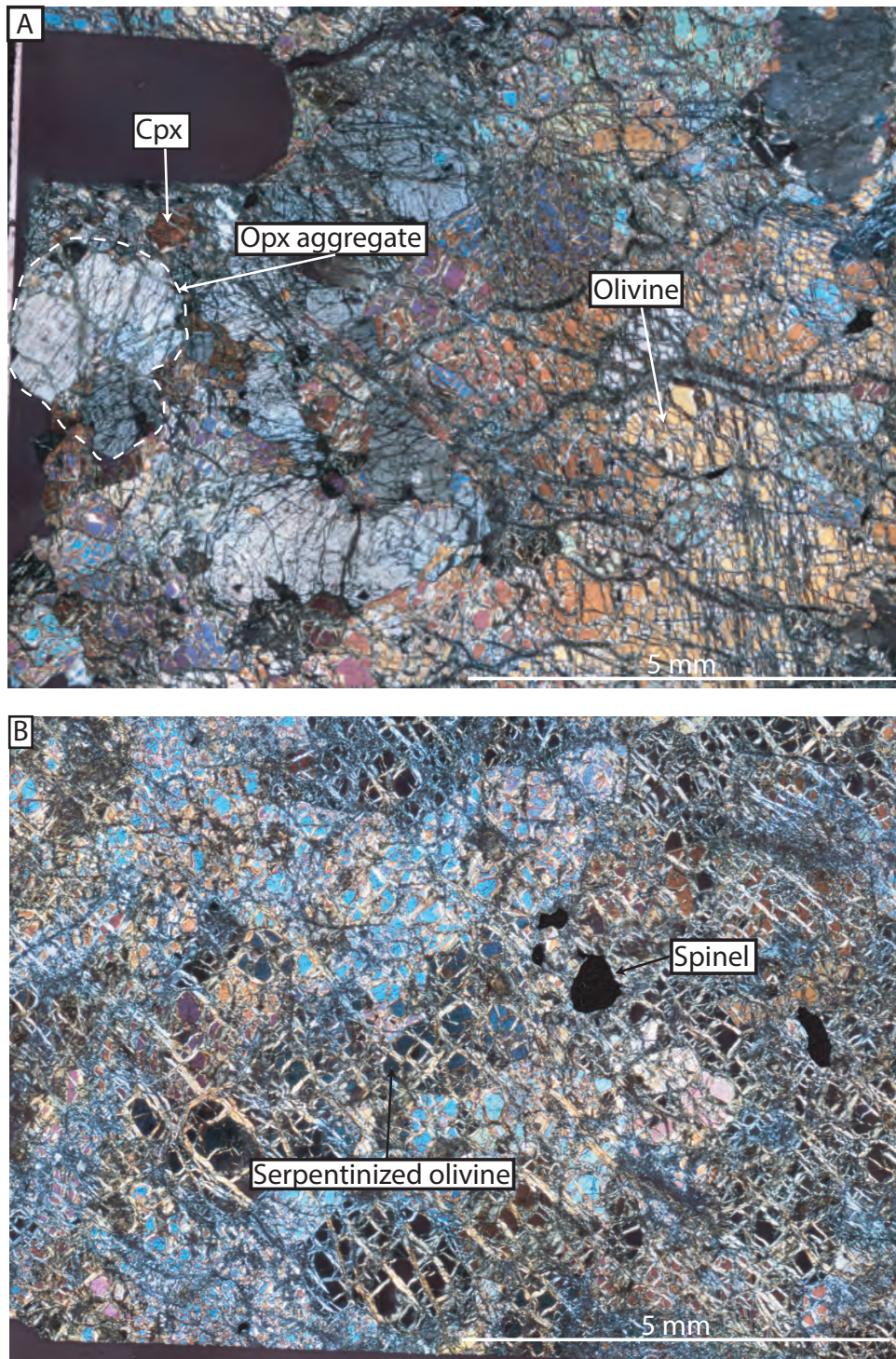


Fig.4.11: Photomicrographs of harzburgite and dunite from the layered dunite locality. (A) Harzburgite displaying large serpentinized olivine, opx aggregate and rarer interstitial cpx and opx (T1LD1A); (B) Strongly serpentinized dunite with coarse olivine grains and interstitial spinel (T1LD2A).

coarse-grained (~1mm) with minor smaller grains (50µm) and a greater concentration of smaller grain is found near the opx aggregates. Pyroxenes occur either as large porphyroclasts (~3mm) or smaller (~200µm) grains surrounding the porphyroclasts. Cpx always appears as small grains (~50 to 100µm). Pyroxenes are commonly found as clusters where cpx grains are associated with opx. Grains of amphibole are present in the pyroxene aggregates. Grain boundaries are curvilinear in olivine and complex for cpx; no straight grain boundaries or 120° contacts are visible for any phase. Subgrains are found in olivine and opx while undulose extinction is visible in all the phases.

In the dunite, the only accessory mineral is chrome spinel (Fig.4.11-B). No obvious shape-preferred orientation is visible for the olivine grains. The grain size is generally ~3-4mm across, but some smaller grains (300µm) are present. Because of the relative abundance of the two grain populations, the dunite texture is better described as protogranular (*sensu* Mercier and Nicolas, 1975) rather than porphyroclastic. Grain boundaries are best described as curvilinear and rare 120° contacts can be found between grains belonging to the smaller grain-size fraction. The strong serpentinization makes the investigation of deformation markers in olivine very difficult and none were found.

Bear Creek

In the Bear Creek locality, 5 different lithologies were observed: (1) the basal lherzolites, (2) the finely-layered cumulates, (3) the massive pyroxenites, (4) the peridotitic enclaves and (5) the pegmatitic segregations.

The basal lherzolites are highly serpentinized and only portions where pyroxenes are abundant were preserved (Fig.4.12-A). Aggregates of opx with interstitial olivine are observed in the serpentinized matrix. Cpx is visible in the aggregates and as exsolution lamellae parallel to the opx cleavages. Aside from the cpx aligned in the opx cleavage, no clear shape-preferred orientation of any mineral is visible. The grain-size distribution of olivine is bimodal and the olivine-rich parts are coarse grained (~3mm) while the olivine around the opx aggregates is finer grained (~50µm). Opx aggregates typically host one large porphyroclast (~2mm) surrounded by smaller grains of opx, cpx and olivine (~50µm). Grain-boundary geometry is difficult to observe in the olivine-rich part of the samples because

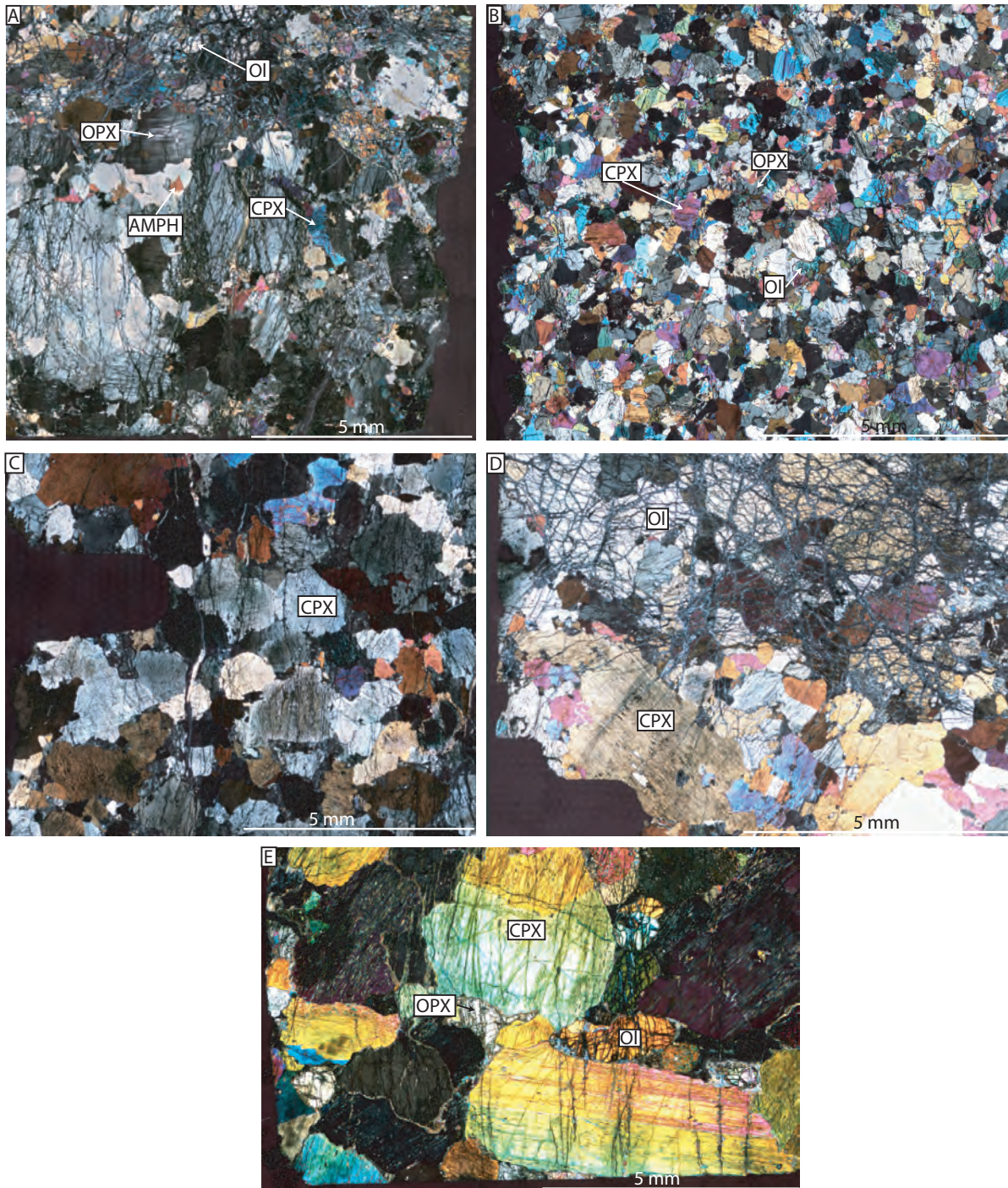


Fig.4.12: Photomicrographs of the five lithologies found in Bear Creek. (A) Example of the lherzolite microstructure showing the strong serpentinization of the rock (T4BC2A); (B) Typical microstructure of the finely-layered cumulates (T3BC1A). The homogeneous grain size and homogeneous distribution of the grains is visible; (C) Representative microstructure of massive pyroxenites (T3BC4A). The difference in grain size and grain-boundary shapes from the finely-layered cumulates is striking; (D) Microstructure of the peridotitic enclave with a pyroxenite layer (T4BC6A). The bimodal grain-size distribution of the cpx in the pyroxenite is visible as well as the coarse olivine grain in the peridotite; (E) Coarse-grained pegmatite with typical twinned cpx and interstitial opx and olivine (03T16A).

of serpentinization. Near the aggregates, the grain boundaries of all phases are complex. Undulose extinction and the formation of subgrains are visible in opx porphyroclasts. The smaller-grained fraction of opx and cpx does not show any deformation markers; this is also true of olivine whether it is associated with pyroxene aggregates or in olivine-rich regions.

In the finely-layered cumulates olivine-poor layers are composed of ~1/3 of olivine, opx and cpx homogeneously distributed. No shape-preferred orientation is clearly visible in this facies. Grain-size distribution is simple with a mean grain size of ~400µm for all phases. Grain boundaries are curved/lobate, and appear magmatic (Mercier and Nicolas, 1975); 120° contacts are common and only few deformation markers can be observed (i.e. kinking in olivine).

Massive pyroxenites are distinguished from the finely-layered cumulates by their modal composition, which is almost purely clinopyroxenitic, and by their larger grain size (Fig.4.12-C). Only rare olivine-rich layers are visible. A subtle shape-preferred orientation is visible in the pyroxenes and some grains are flattened in the foliation plane (sample T4BC4). Grain-size distribution is bimodal and coarser grains (~500 µm to 1mm) coexist with a finer fraction (~50 µm) that makes up a limited percentage of the rock volume. In their rare occurrences, olivine and opx are associated with each other and their grain boundaries are lobate/curved. Cpx, on the other hand, comprises all of the large grain fraction and display complex to straight grain boundaries between cpx grains. 120° triple junctions between cpx grains indicate a certain degree of textural equilibrium. Deformation markers are visible in the olivine with subgrains. Cpx also shows rare subgrains, mostly at contacts with other grains.

Sample collection includes a peridotitic enclaves crosscut by a pyroxenite-rich layer (reported by Ceuleneer and Le Sueur, 2008, Fig.4.12-D and Fig.4.8-C). The peridotitic part is of lherzolithic composition and does not show any shape-preferred orientation. Large olivine grains (5-10 mm) coexist with a smaller fraction of olivine, opx and cpx (~500 µm). Pyroxenes occur in aggregates or as interstitial minerals in the olivine-dominated matrix. Grain boundaries of olivine are best described as curvilinear, while the pyroxenes have more linear grain boundaries with some 120° contacts in aggregates. Deformation markers such as undulose extinction and kink bands are visible in large olivine grains.

The pyroxenite section of the sample is composed mostly of cpx with opx, hornblende and olivine grains as interstitial minerals. Grain size is distinctly bimodal with coarse cpx grains (1mm) coexisting with a finer fraction (100-500 μm) of cpx, opx, hornblende and olivine. Olivine, opx and hornblende are mostly associated in now-serpentinized aggregates between coarse cpx grains. Boundaries between large cpx grains can be complex or linear and often form 120° contacts. Grain boundaries between olivine and cpx are mostly curved/lobate. Some large cpx show evidence of lattice distortion at contacts with others grains.

The pegmatite lithology was not collected as an oriented sample during this field trip. However, non-oriented thin sections still provide valuable information (Fig.4.12-E). They are composed dominantly of coarse-grained cpx in subhedral to euhedral grains (mm to cm in diameter). Olivine, opx and hornblende grains are also visible, commonly together and as interstitial minerals between coarser cpx ($\sim 500\mu\text{m}$ to 2mm). Grain boundaries appear linear for the large cpx but still show a non-negligible sutured component. In contrast to the cpx, olivine and opx grain boundaries are mostly lobate and curvilinear. As in the previous facies, the coarse cpx fraction commonly has 120° contacts. Other phases and fractions do not show this type of triple junction as often. Deformation markers are absent and only twinning can be seen in large euhedral cpx grains (Ceuleneer and Le Sueur, 2008).

4.5 - Mineral fabrics from EBSD

In this section, the fabrics of the minerals are reported. It is important to note that, when the lineation was not visible in the field and in hand specimen, the thin sections were systematically cut in the plane normal to the foliation with the N130 direction on the lineation (see Fig.2.2). This direction was chosen based on the much larger and more complete structural study by Le Sueur et al. (1984) and Boudier et al. (1989). It corresponds to the regional stretching direction in the mantle peridotite and also to the strike of the sheeted dyke complex. This adds a layer of complexity to the determination of the fabrics and requires the investigation of the spatial coincidence of the crystallographic-axis directions of different phases to make a reliable interpretation of the data.

Corry Peak

Fabrics in Corry Peak's lherzolite were investigated using sample T5CP1A. The olivine fabric is consistent with $[100](001)$. Determination of the fabrics of other minerals is difficult. The EBSD map clearly shows the presence of kink bands in olivine grains and confirms the optical observation that pyroxenes are internally equilibrated (Fig.4.13-A and Fig.4.13-B).

The presence of a strong fabric in olivine, which would typically be paired with several deformation markers, contrasts with the equilibrated texture of the rock. It may suggest a possible annealing/recovery episode which allowed a selection of previously plastically-oriented grains to grow and form this fabric. This process is consistent with the mostly equigranular texture of the sample, which could reflect a recovery process. The presence of kink bands in some olivine grains may be interpreted as marker of a later deformation that is now superimposed on the relict one preserved in the fabrics, or alternatively as non-recovered deformation markers.

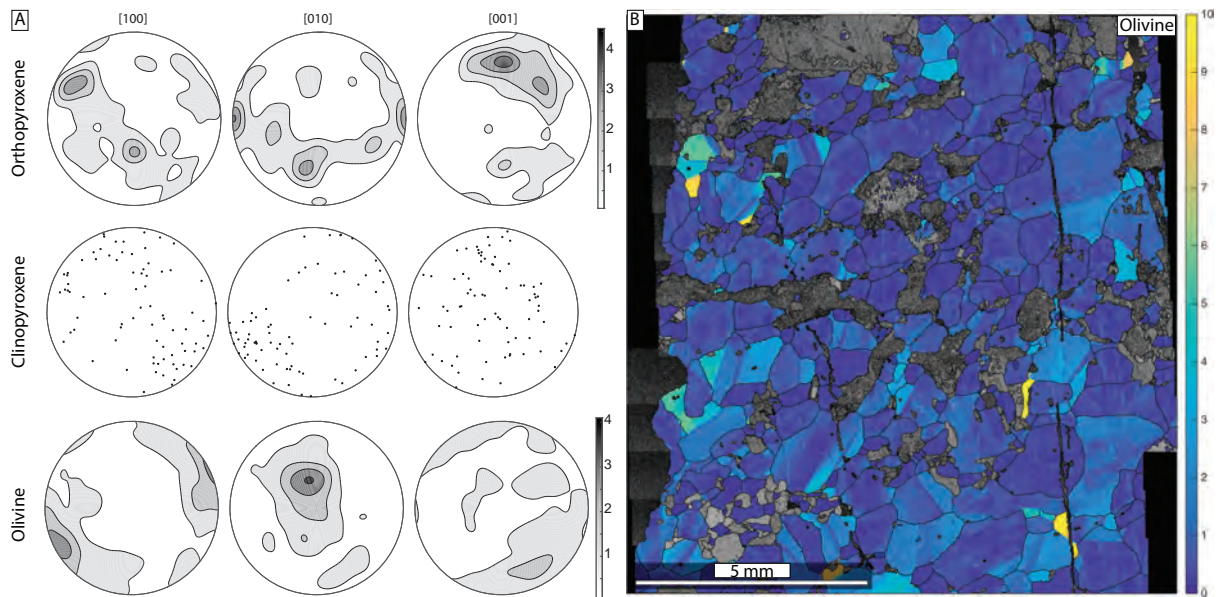


Fig.4.13: (A) CPO of opx, cpx and olivine and (B) colour-coded EBSD map of a plagioclase bearing lherzolite (T5CP1A) showing the misorientation to the mean grain orientation for olivine. The coexistence of kink bands in some grains and the equilibrated grains showing a 120° contact is clearly visible. The sample was prepared in the XZ reference frame.

The dunite section of Corry Peak is best represented by samples T5CP2A and 17T25EA. They show similar microstructures with the $[100]$ of olivine aligned parallel to the N130

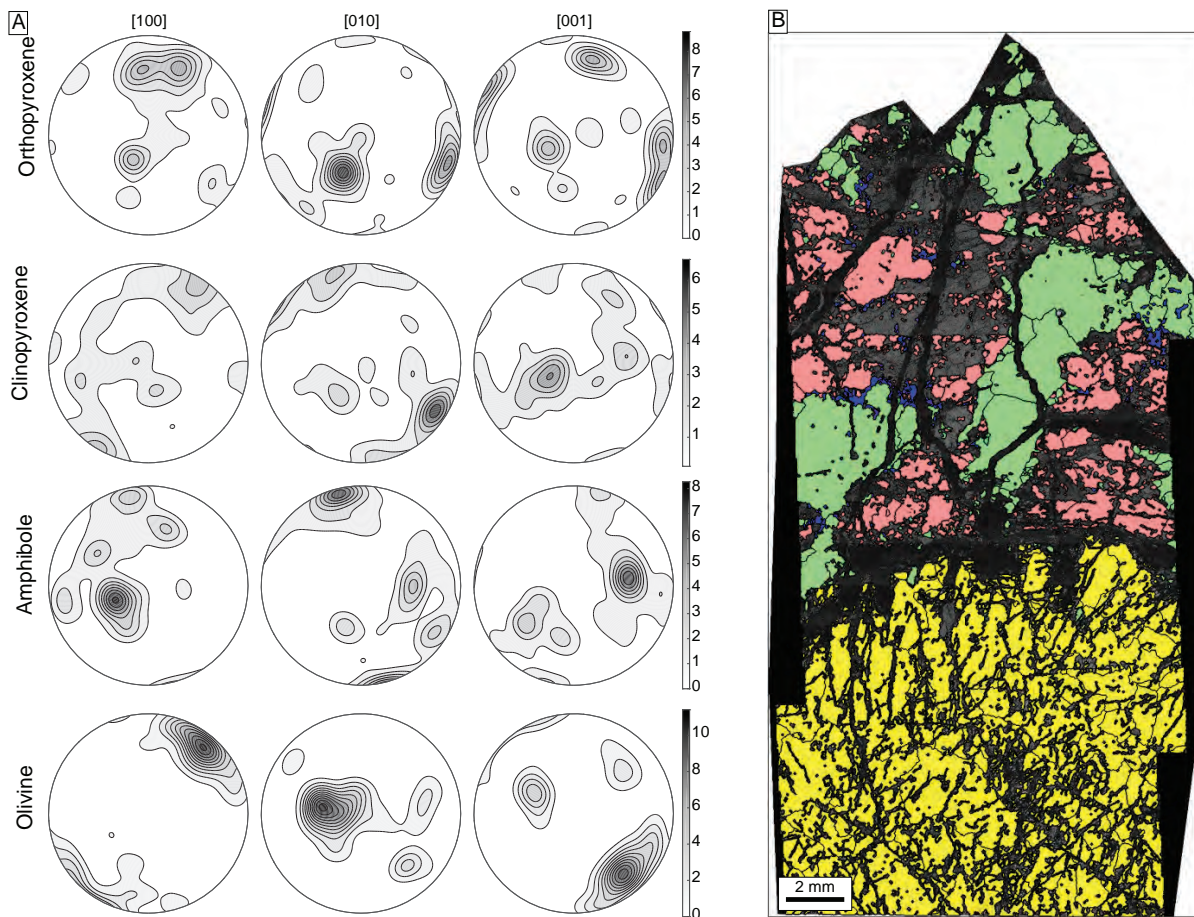


Fig.4.14: (A) CPO of opx, cpx, amphibole and olivine and (B) colour-coded EBSD map of pyroxenite-bearing dunite (T5CP2A) showing the phase distribution. Cpx is pictured in green, opx in red, amphibole in blue and olivine in yellow. The sample was prepared in the XZ reference frame.

direction. In sample T5CP2A, the most likely fabric is [100](001) for olivine along with a weak [001](010) for cpx (Fig.4.14-A and Fig.4.14-B). Amphibole fabrics show some similarity with that of cpx and display a (010) orientation next to that of cpx (Fig.4.14-A). Sample 17T25EA has a similar direction for olivine [100] axis but displays two girdles for [010] and [001]. In both samples, kink bands and undulose extinction are visible in some olivine grains, as in the plagioclase lherzolite.

Vicky Bluff

In Vicky Bluff, three different lithologies have been analysed: the host peridotite, the dunite and the pyroxenite layers.

In the field, the structural framework was very difficult to determine. While a N130 lineation defined by aligned spinels was often visible, the determination of a foliation plane

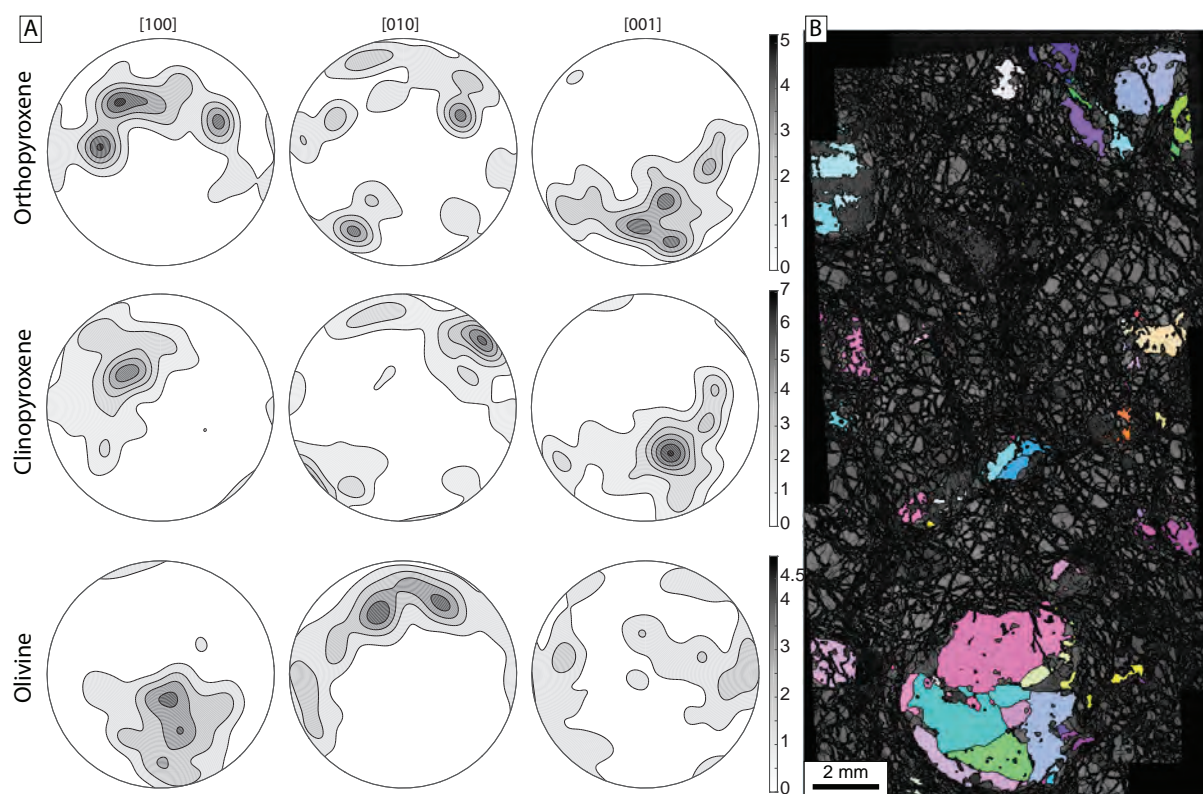


Fig.4.15: (A) CPO of opx, cpx and olivine and (B) colour-coded EBSD map of Vicky bluff lherzolite (T2VB3A) showing the mean orientation of the enstatite grains. The aggregate of opx seems to be made of grains with unrelated orientation, possibly hinting at a deformation-induced aggregation (i.e. metamorphic differentiation). This sample was cut in what appeared to be the XZ plane. Determination of the fabrics required the investigation of azimuths coincidences between phases.

was difficult, probably reflecting the linear nature of the deformation (stretching) and the proximity of sheath folds. Consequently, the sample presented here have a strong uncertainty and the spatial coincidence of the crystallographic axes of the different minerals will be needed to infer the most likely fabric combinations.

In the lherzolitic sample T2VB3A, the most likely fabrics of opx, cpx, olivine would be [001](100), [001](100) and [001](010) respectively as the maximum points of the axis share a similar azimuth (Fig.4.15-A). It is important to note that for this sample, (1) the maximum points of the fabric do not correspond to the structural framework and is not aligned with the N130 direction and (2) a shift of the crystallographic axes point maxima and between the pyroxenes olivine of $\sim 20^\circ$ degrees is observed. Sample 17T4EA, another lherzolite, shows similar fabrics for opx, olivine but a different [001](010) fabric for cpx. Additionally, it allows the identification of a [001](010) fabric for amphibole. EBSD mapping reveals similar deformation markers as those visible in thin section in both opx and olivine (Fig.4.15-B) and show a limited internal deformation for cpx.

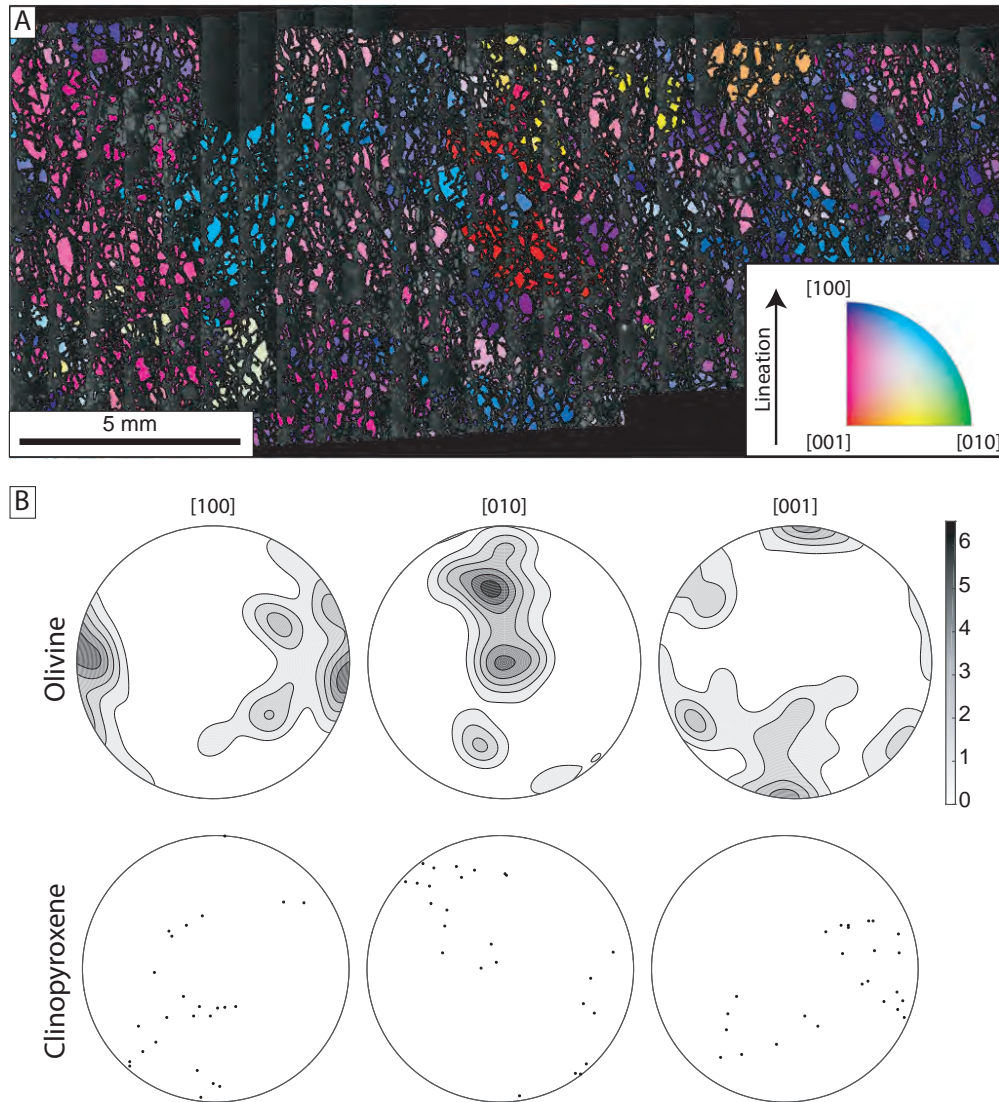


Fig.4.16: (A) Inverse pole-figure map of Vicky Bluff dunite (17T4AA) showing the crystallographic direction of the olivine grains with respect to the lineation direction. The large grain-size and the strong preferred orientation are clearly visible; (B) CPO of olivine and cpx in the corresponding sample.

In the Vicky Bluff dunite (Fig.4.16-A and Fig.4.16-B) the olivine [100] axis is aligned with the N130 direction which correspond to the direction of the lineation in the surrounding massifs (Boudier et al., 1989). Considering the orientation of the cpx grains as well as the olivine point maxima, it can be hypothesized that the most likely fabrics are [100](010) and [001](010) for olivine and cpx respectively (Fig.4.16-B). However, the number of cpx grain being less than 100, the interpretation has to be taken with care.

Pyroxenite layers in clear contact with the host peridotite and the surrounding area were investigated. T2VB4B provides microstructural information on both the pyroxenite layer and the lherzolite host (Fig.4.17-A and Fig.4.17-B). The cpx fabric originated solely from the

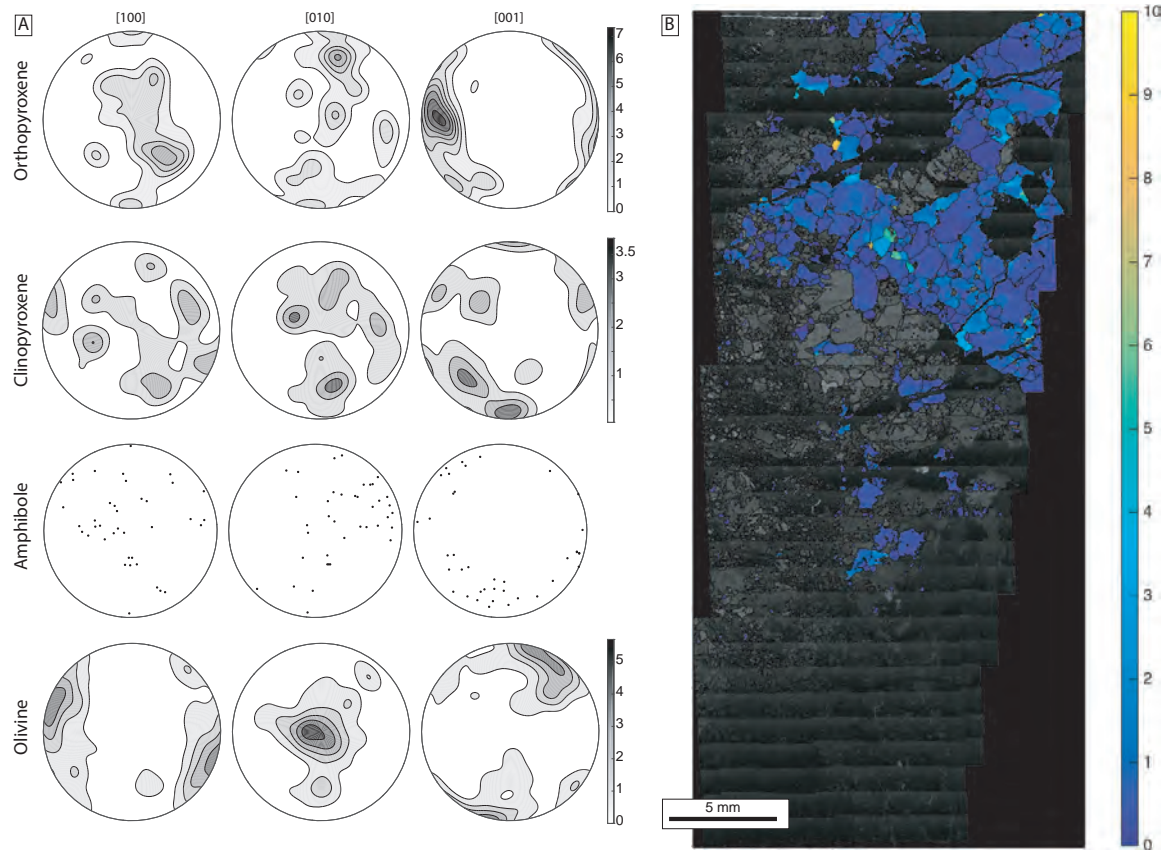


Fig.4.17: (A) CPO of opx, cpx, amphibole and olivine and (B) colour-coded EBSD map of Vicky Bluff lherzolite (T2VB4B) showing the misorientation to the mean orientation of the cpx grains. The limited internal deformation of the cpx is clearly visible as well as some equilibrated 120° contact between some cpx grains

pyroxenite layer and is random. In the lherzolite, olivine and opx have strong point maxima for [100] and [001] respectively. They both correspond to the lineation (N110 direction) making them the best candidates for a slip direction. Determination of the slip plane is more difficult as the foliation was unclear in the field. Considering the distribution of [100] and [010] of opx and olivine respectively as well as the eigenvalues suggesting a stronger point maximum component for opx [100] relative to opx [010], the most likely slip planes for opx and olivine are (100) and (010) respectively. A few amphibole grains allow the identification of a fabric mimicking that of the cpx, as observed in Corry peak (Fig.4.17-A).

Layered dunites

Two samples in the layered dunite locality were analysed: one harzburgite and one dunite both separated by 10m and a sharp contact.

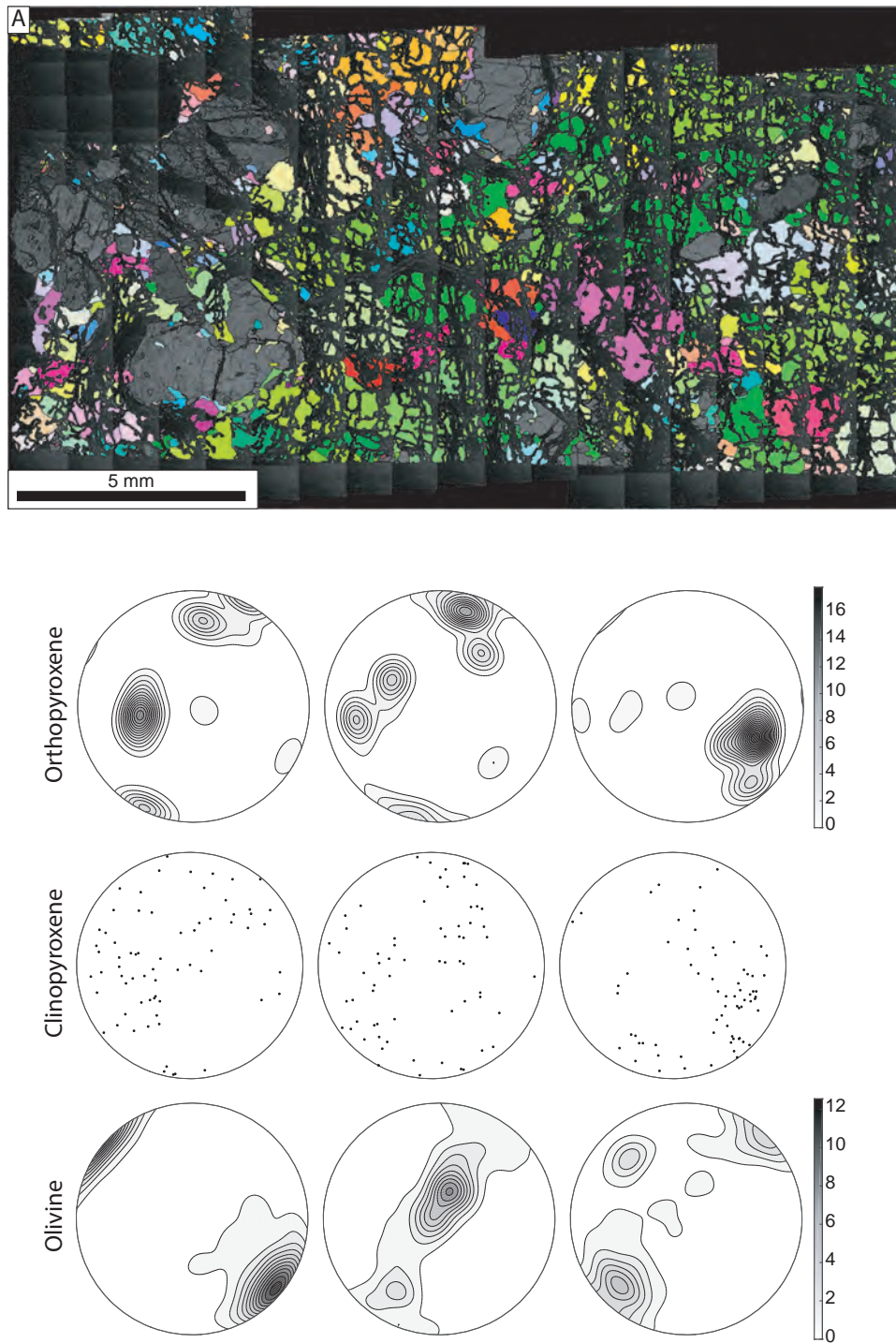


Fig.4.18: (A) Colour-coded EBSD map of the layered dunite harzburgite (TILD1A) showing the mean orientation of the olivine grains. The variability in grain size can be seen; (B) CPO of opx, cpx and olivine of the same analysis.

In the harzburgite (Fig.4.18-A), olivine fabric is consistent with a $[100](001)$. Olivine $[100]$ axis is aligned with the stretching direction, consistent with N140 (Fig.4.18-B). Opx, cpx and amphibole fabrics are difficult to interpret with certainty (Fig.4.18-B). Opx fabric display concentrations of $[100]$ and $[010]$ possibly fitting the foliation plane pole but its fabric remains too hazardous to determine.

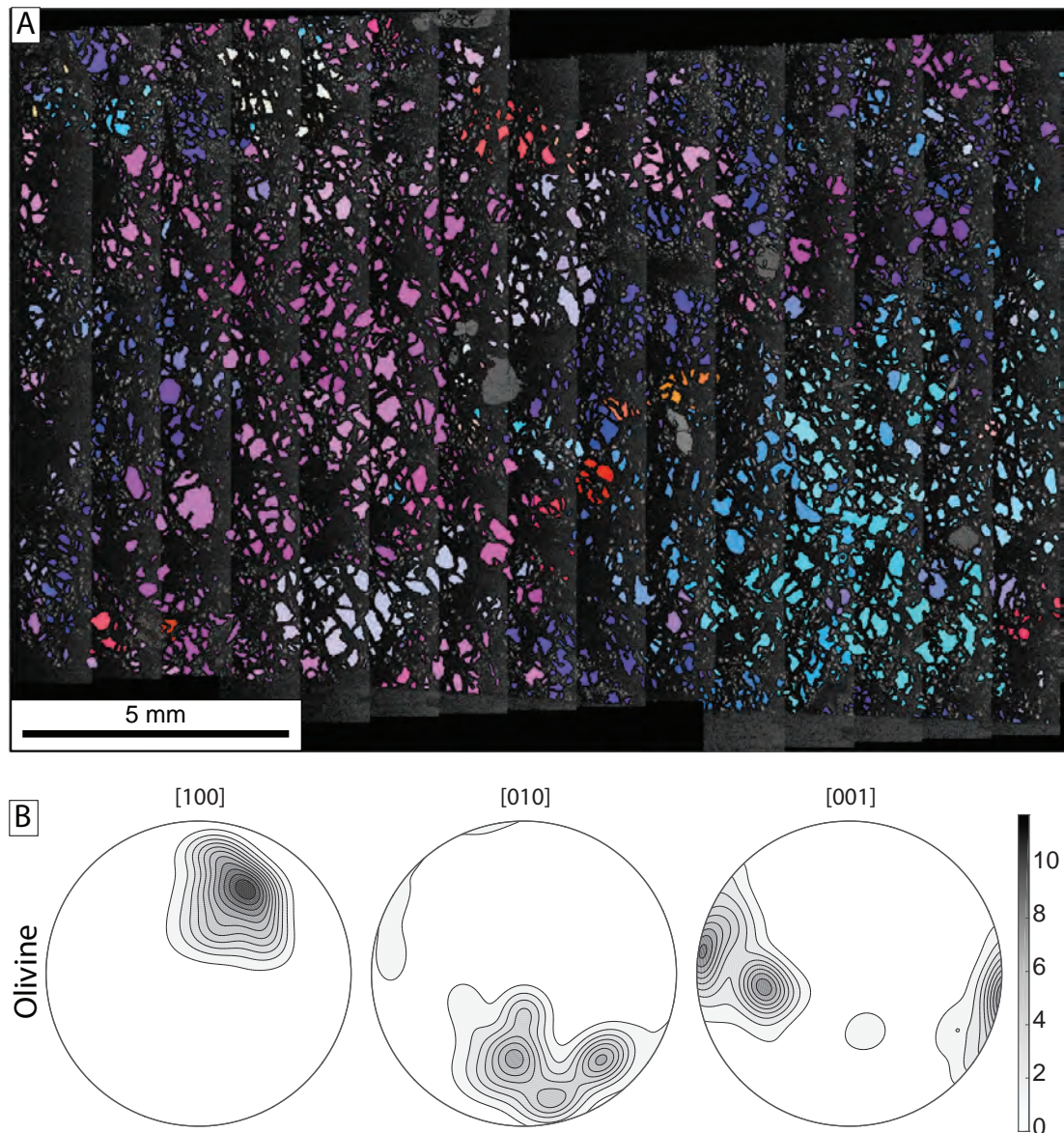


Fig.4.19: (A) Colour-coded EBSD map of dunite from the layered dunite locality (TILD2A) showing the mean orientation of the olivine grains. The large-grain size can be seen as well as the strong serpentinization; (B) CPO of olivine of the same analysis. It is important to note that the sample was cut vertical and a rotation was performed to bring the dataset in the same geographical reference frame than the neighbouring harzburgite to make comparison with the harzburgite fabric possible.

Dunite fabrics are not straight forward to interpret as the foliation was not visible in the field and the sample cut was simply made vertical. Rotation of the dunite orientation dataset assuming a foliation plane similar to the one in the neighbouring harzburgite does not yield a perfect fit with the harzburgite reference frame but suggest generally similar direction for the crystallographic axis. Assuming a Crystallographic axes [100], [010] and [001] for olivine in the dunite, are consistent with [001], [010] and [100] of the olivine in the harzburgite respectively (Fig.4.19 and Fig.4.20).

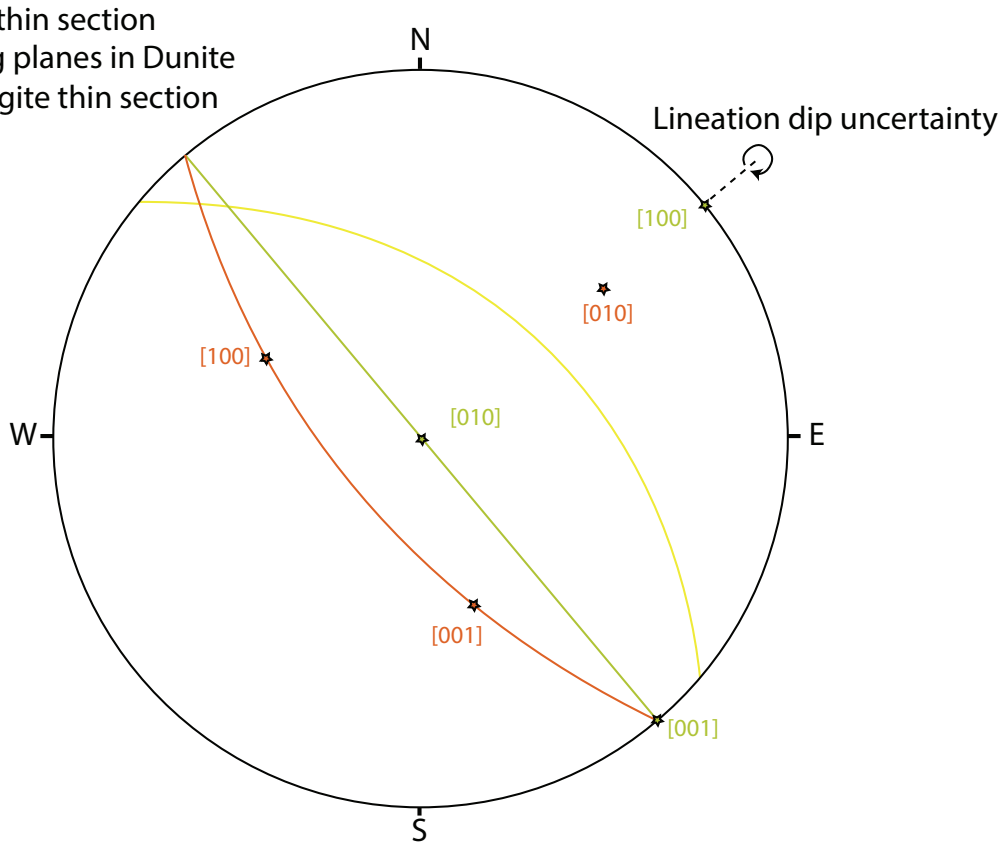


Fig.4.20: Stereonet depicting the direction of the point maximum of the olivine fabrics in the harzburgite (sample T1LD1A) in red and of a dunite (sample T1LD2A) in green. A representative measurement of the serpentine-rich plano-convex features in the dunites is pictured in yellow. The plane along which the harzburgite is cut is oriented N140 25W while the dunite sample was cut along a vertical plane containing the N140 direction. The harzburgite fabric being [100](001) and assuming a change in foliation dip of 25° in between the two samples, a rotation of the crystallographic axis along the lineation dip uncertainty axis would result in two possible fabric combination for the olivine: (1) [010](001) or (2) [001](010). As [010](001) has never been reported before ([010] is never the slip direction in olivine), a [001](010) fabric for the dunite olivine is the most likely.

Bear Creek

The Bear Creek locality hosts 5 different lithologies: lherzolite, finely-layered cumulates, massive pyroxenites, pegmatites and peridotitic enclaves. In this section the results in the stratigraphic order observed in the field are presented. As discussed before, the lineations were not observed in the Bear Creek locality. Consequently, the samples were cut in the plane normal to the foliation/layering containing the N130 direction. In order to provide reliable interpretations of the fabrics, the lineation component was, here also, analysed in the frame of spatial coincidence of the crystallographic axes between the phases.

Insight on the lherzolite microstructure is provided by samples T4BC2A and T4BC3A (Fig.4.21). Both samples display a common [001](010) fabric for cpx and either a [001](010) or [001](0kl) for opx. Olivine has an A-type fabric in sample T4BC2A and a B-type fabric in T4BC3A (Fig.4.21-A and Fig.4.21-C). Amphibole, when present, has a fabric mimicking that of cpx (Fig.4.21-A). The obliquity of the fabric relative to the structural reference frame is difficult to interpret as a well-defined lineation is lacking.

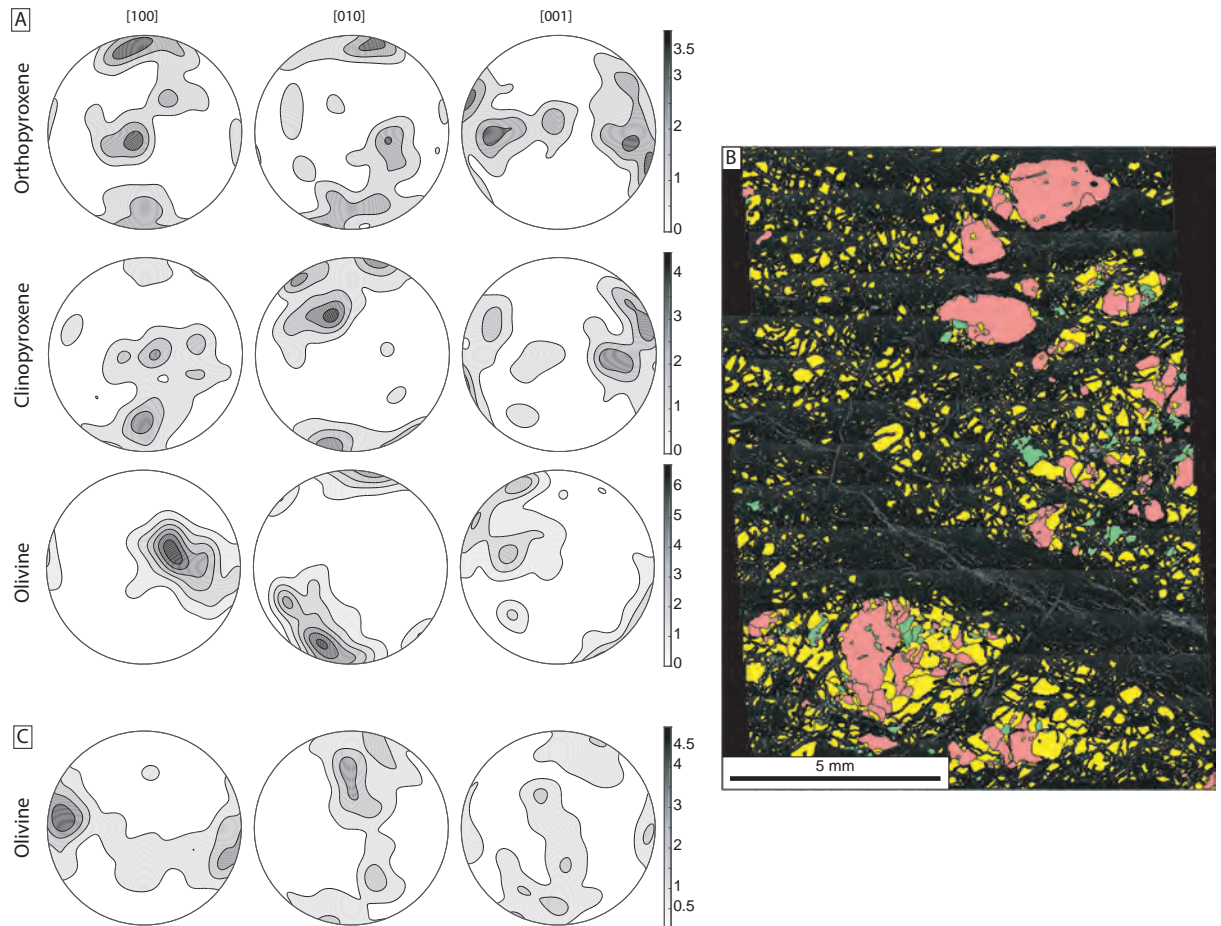


Fig.4.21: (A) CPO of opx, cpx, and olivine and (B) colour-coded EBSD map of Bear Creek lherzolite (T4BC3A) showing the phase distribution. Cpx is pictured in green, opx in red, amphibole in blue and olivine in yellow. (C) CPO of olivine from sample T4BC2A, showing a pattern different from that of sample T4BC3A.

Finely layered cumulates were investigated with samples T3BC1A, T4BC8A, T3BC3A and 01T12A. They present consistent microstructural data (Fig.4.22); cpx displays a [001] (010) fabric with an S-type shape (*sensu* Helmstaedt et al., 1972, Fig.4.22-A). In the majority of the cpx fabrics, weak clusters of [100] are also found next to the foliation pole. The opx fabric has a [001] axis cluster within the girdle aligned with the stretching direction, and has

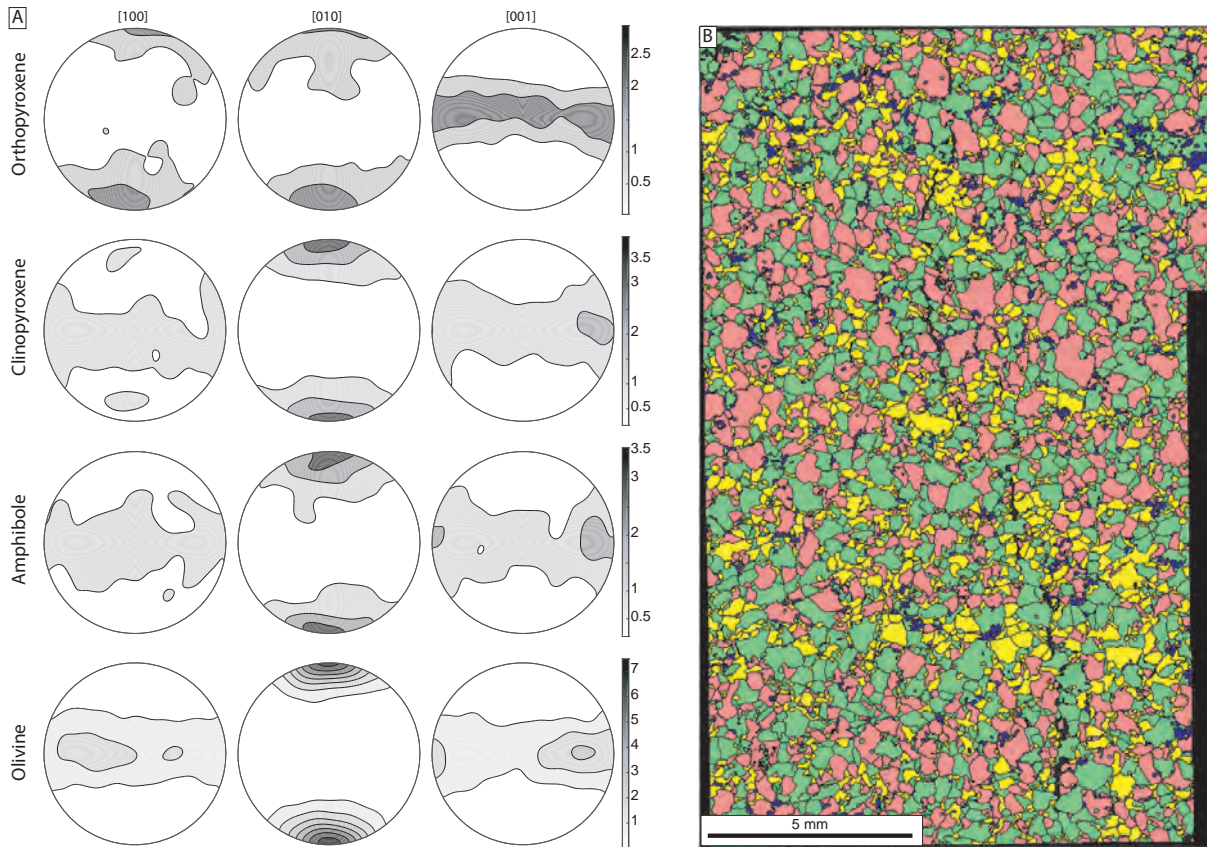


Fig.4.22: (A) CPO of opx, cpx, amphibole and olivine and (B) colour-coded EBSD map of a Bear Creek finely layered cumulate (T3BC1A) showing the phase distribution. Cpx is pictured in green, opx in red, amphibole in blue and olivine in yellow. The small and heterogeneous grain size is visible as well as the curvilinear grain boundaries.

a weak concentration of both [100] and [010] next to the foliation pole (Fig.4.22-A). Olivine has a dominant [001](010) fabric with a strong foliation component and clusters of greater concentration within the [001] girdle aligned with the lineation direction. When amphibole is present, it displays a fabric similar to that of cpx.

The fabric of massive pyroxenites was investigated through samples T3BC4A and T4BC4A (Fig.4.23). Both samples have twinned cpx and all-measurement pole-figures had to be used. In sample T3BC4A, the fabric of cpx is [001](010), with an important girdle component on the foliation plane (i.e. S-type, Fig.4.23-A). Interstitial olivine yields a similar [001](010) fabric, assuming a lineation at N130 as in the other Bear Creek samples. Sample T4BC4A shows a similar fabric for cpx, with a similar girdle component, but displays a concentration of [100] axes along the foliation pole that is most likely related to the large twinned cpx. The number of amphibole grains in sample T4BC4A is large enough to reveal a fabric similar to that of the cpx.

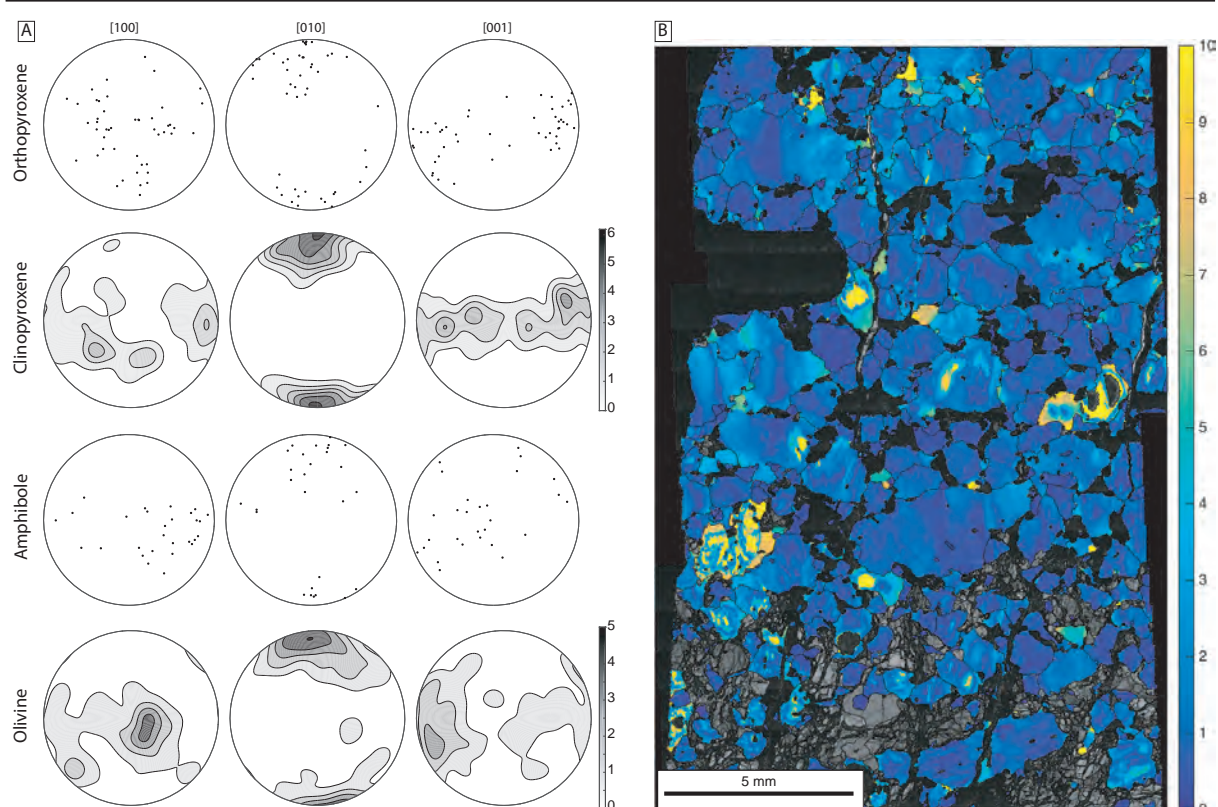


Fig.4.23: (A) CPO of opx, cpx, amphibole and olivine and (B) colour-coded EBSD map of a Bear Creek fine-grained massive pyroxenite (T3BC4A) showing the misorientation to the mean grain orientation for cpx. The larger grain size and the lattice misorientation are visible as well as the equilibrated triple junctions.

The microstructure of the pegmatites is accessible through sample 03T16A, located structurally above the top of the Bear Creek cross-section. As the sample was not oriented and only cpx has enough grains to determine a fabric, no absolute determination of fabrics is possible. However, the observation of cpx and amphibole fabric shape is still possible. Cpx CPO is made up of point maxima with no visible girdle, suggesting that the pegmatites are likely to have a fabric shape similar to an SL-type fabric (Fig.4.24). As in others lithologies, amphibole fabric is similar to that of cpx.

Peridotitic enclaves were investigated using sample T4BC6A (Fig.4.25). The microstructure of the host lherzolite is consistent with [100](010) and [001](100) fabrics for olivine and opx respectively (Fig.4.25-A). The fabric of the cpx forming the pyroxenite layer is consistent with that of the host lherzolite and would result in an S-type [001](010) fabric (Fig.4.25-B).

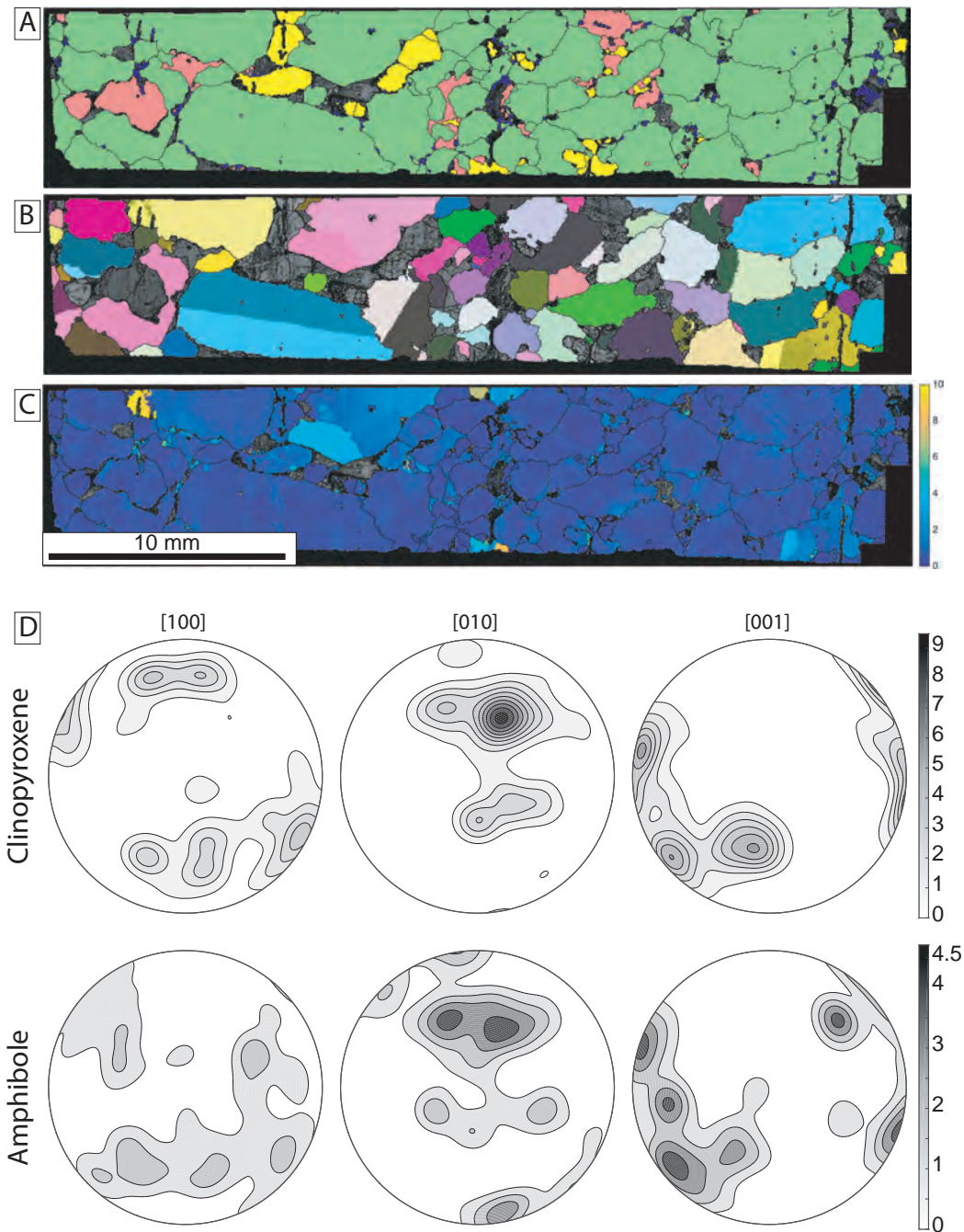


Fig.4.24: (A) colour-coded EBSD map of a Bear Creek fine-grained pegmatite (03T16A) showing the phase distribution. Cpx is pictured in green, opx in red, amphibole in blue and olivine in yellow; (B) Inverse pole-figure for cpx showing the numerous twins; (C) colour-coded EBSD map of the misorientation to the mean orientation of the grain, showing internally equilibrated grains; (D) CPO of cpx and amphibole from the same sample. The thin section was cut randomly as the structural reference frame was not observed.

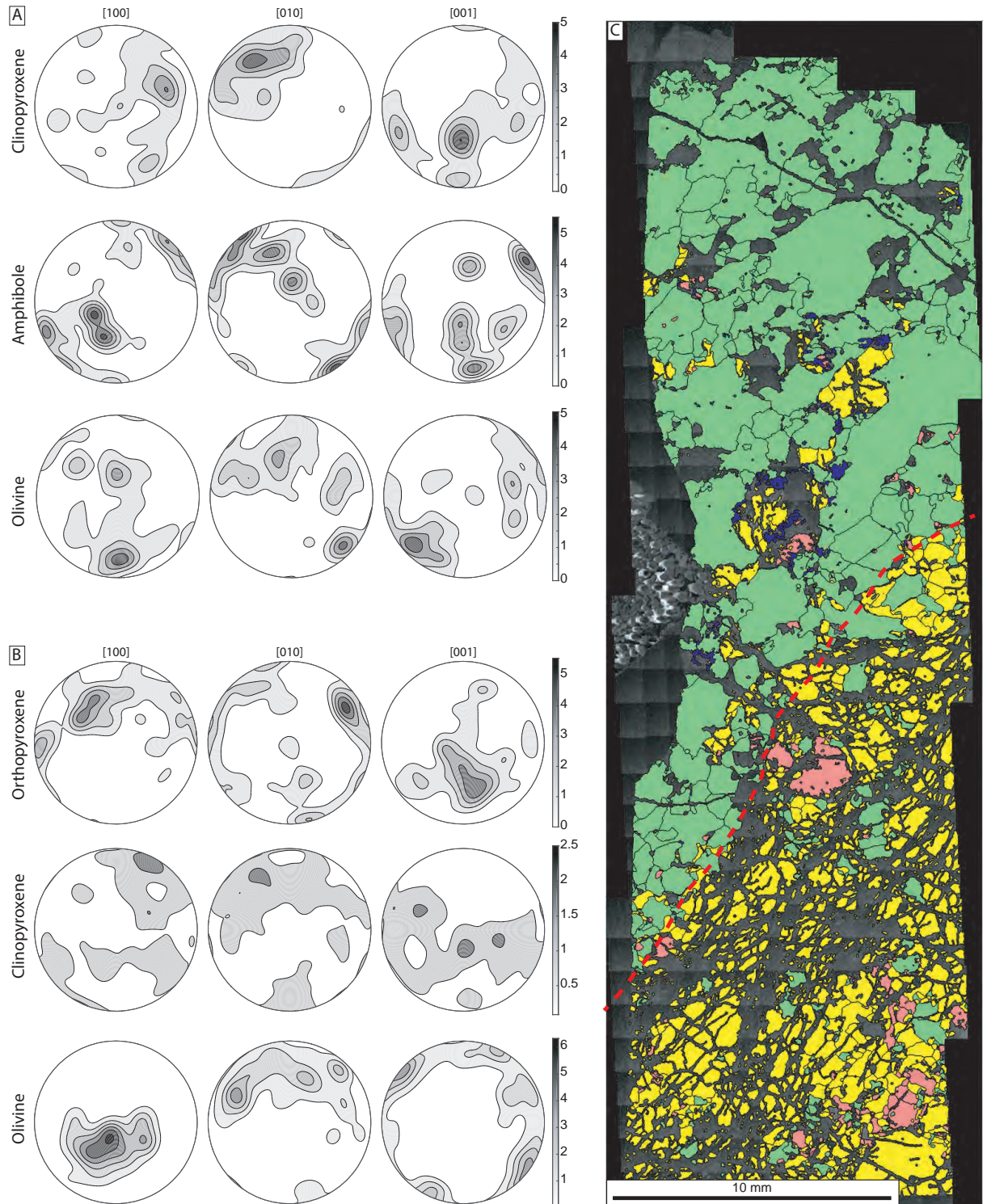


Fig.4.25: CPO and microstructure of a pyroxenite-bearing peridotite (T4BC6A). (A) CPO of cpx, amphibole and olivine from the pyroxenite layer (above the red line in (C)); (B) CPO of opx, cpx and olivine in the lherzolite section and (C) colour-coded EBSD map showing the phase distribution in the sample. Cpx is pictured in green, opx in red, amphibole in blue and olivine in yellow. Thin section was crafted in a random plane.

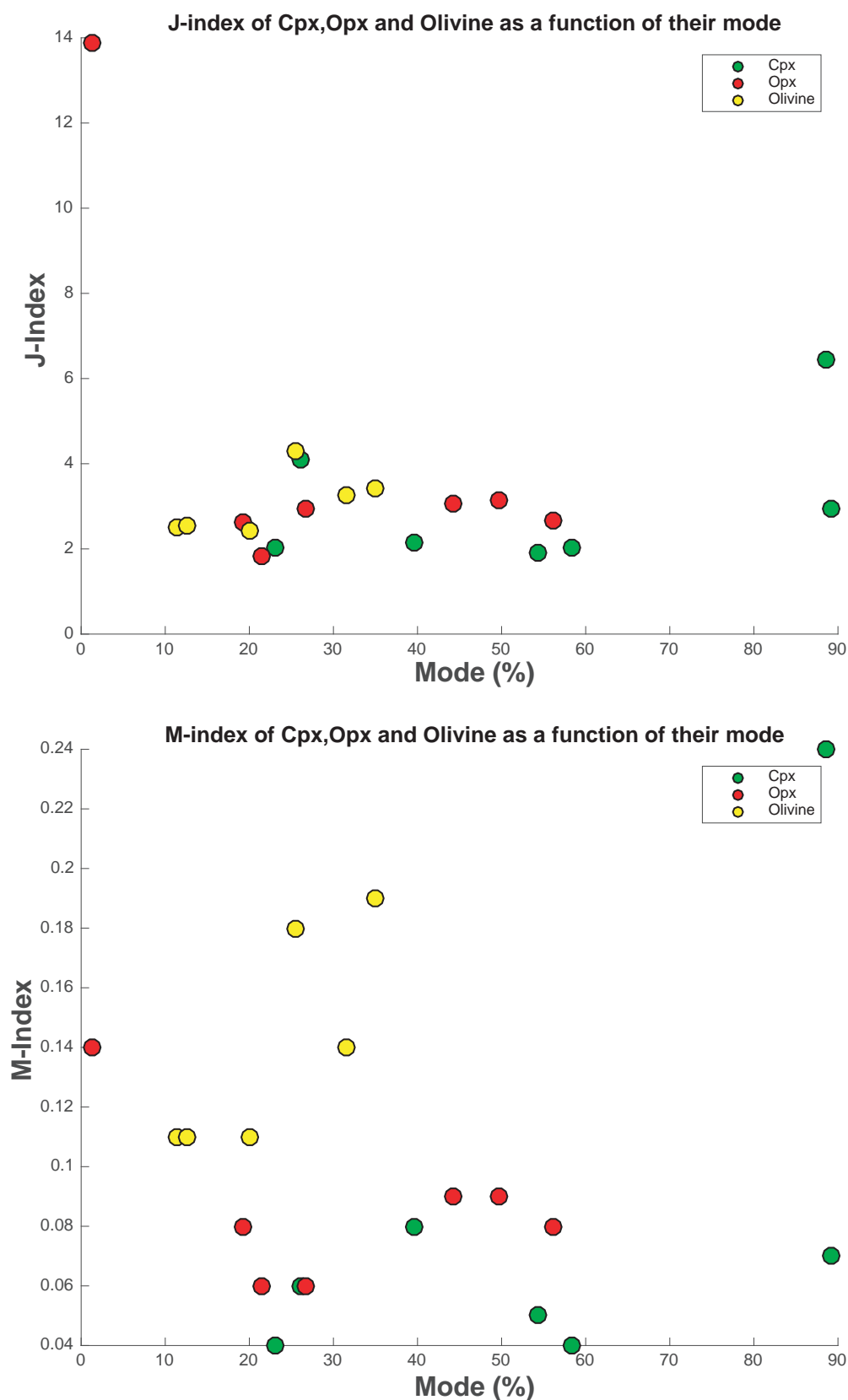


Fig.4.26: J- and M-indices of cpx, opx and olivine of the Bear Creek pyroxenite samples as a function of their relative abundance, derived from their respective EBSD analysis. Only finely layered pyroxenite and massive pyroxenite samples with an ODF calculated after one-point-per-grain data were considered here.

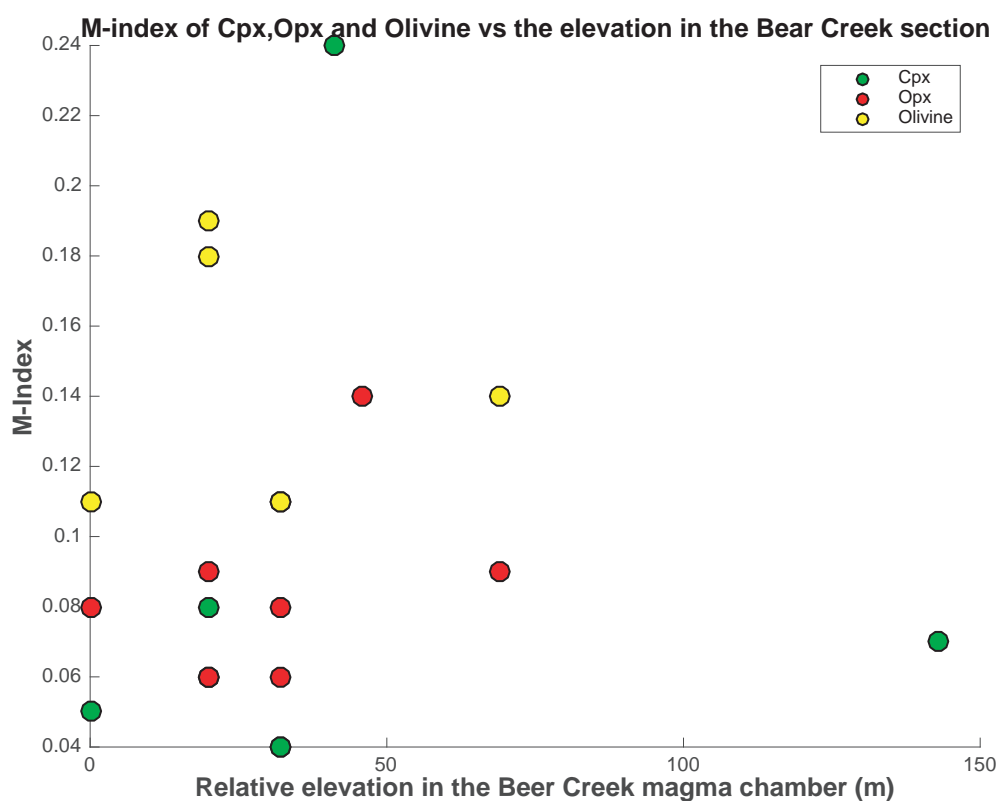
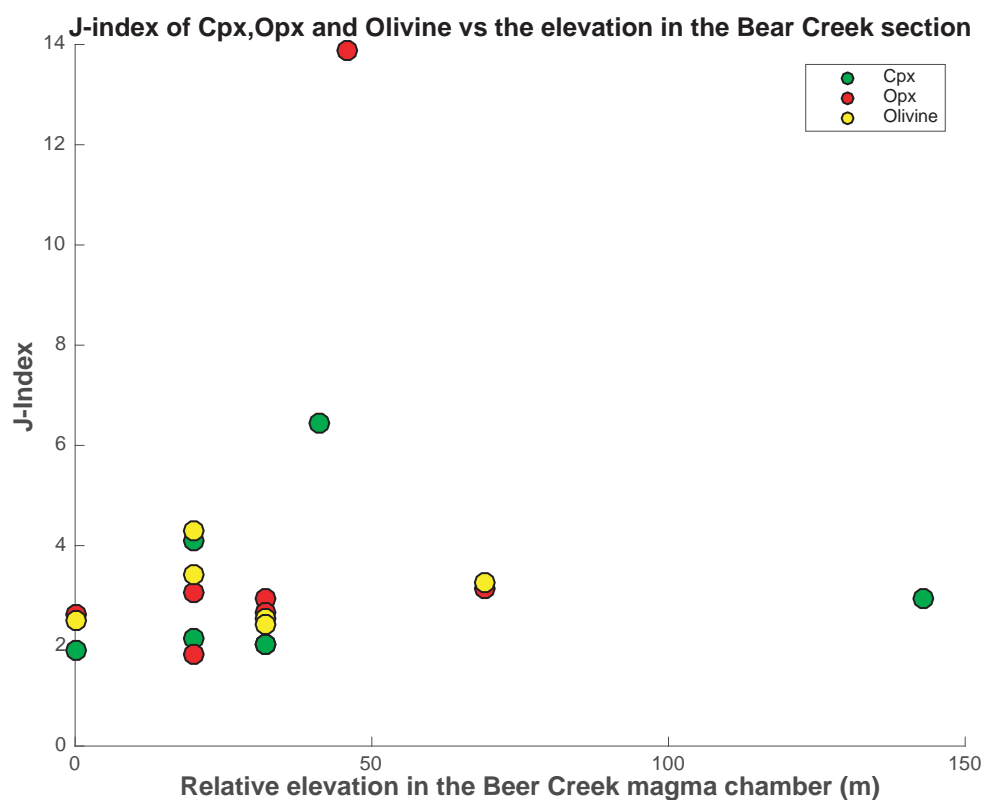


Fig.4.27: J- and M-indices of cpx, opx and olivine of the Bear Creek pyroxenite samples as a function of their structural height relative to sample T3BC1A. Only finely layered pyroxenite and massive pyroxenite samples with an ODF calculated from one-point-per-grain data were considered here.

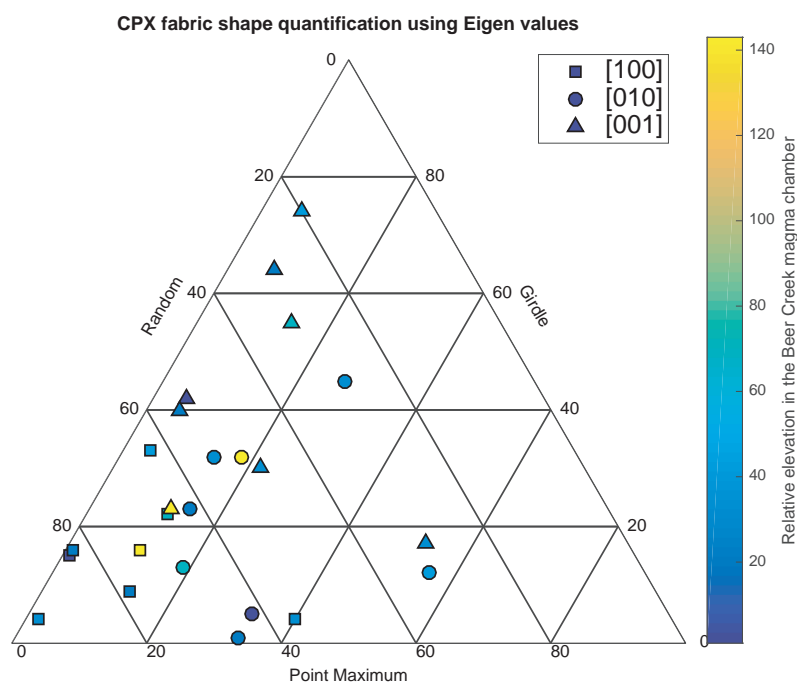


Fig.4.28: Eigenvalues of the 3 crystallographic directions of cpx from the Bear Creek pyroxenite samples. The colour code represents the structural height relative to sample T3BC1A. Only finely layered pyroxenite and massive pyroxenite samples with an ODF calculated from one-point-per-grain data were considered here.

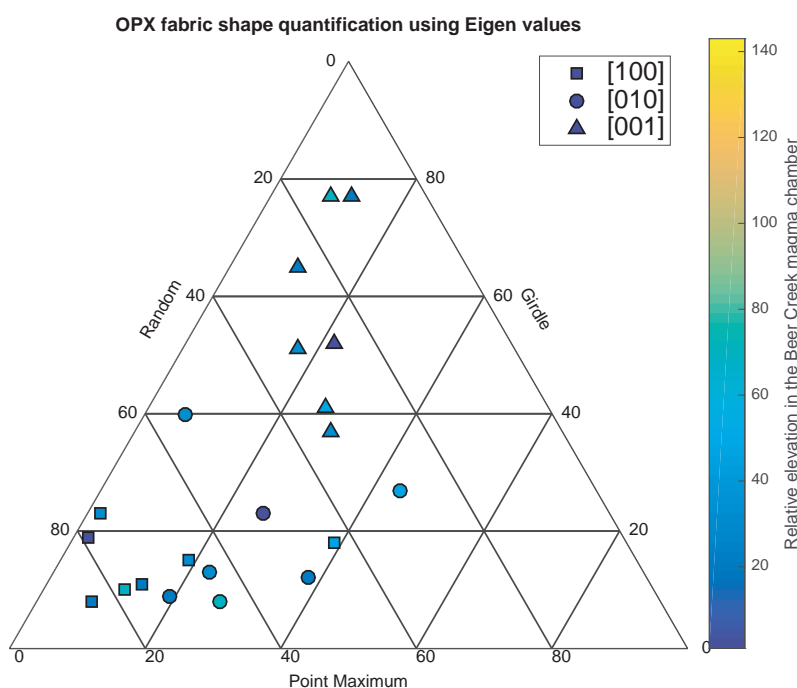


Fig.4.29: Eigenvalues of the 3 crystallographic directions of opx from the Bear Creek pyroxenite samples. The colour code represents the structural height relative to sample T3BC1A. Only finely layered pyroxenite and massive pyroxenite samples with an ODF calculated after one-point-per-grain data were considered here.

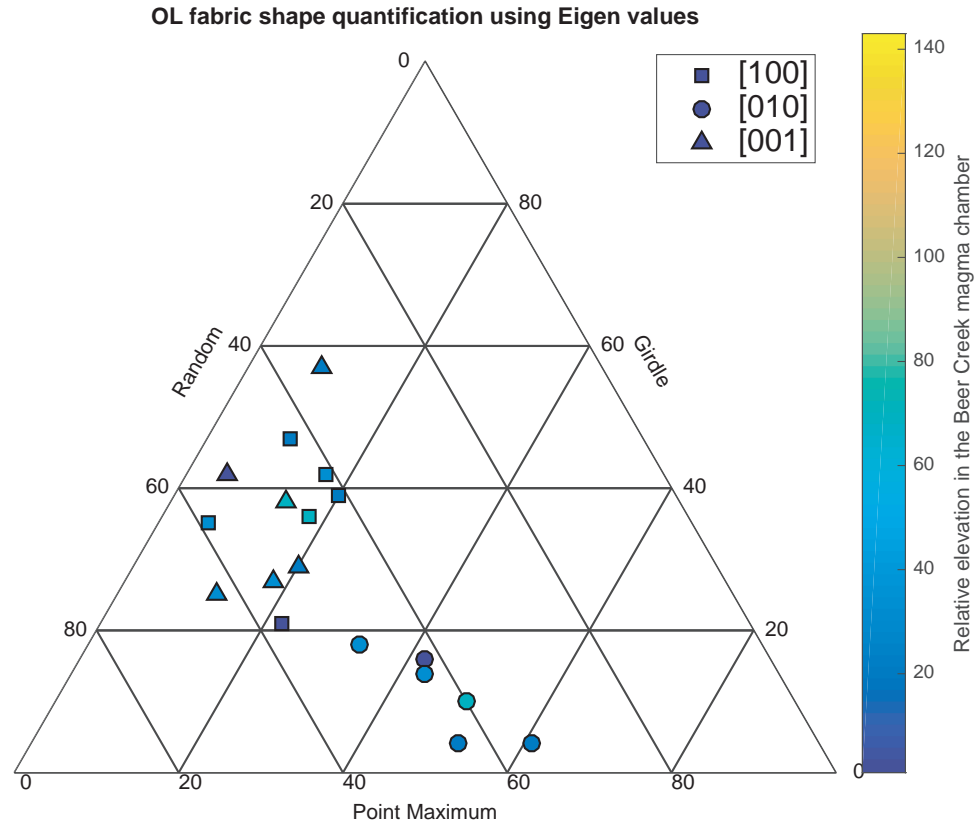


Fig.4.30: Eigenvalues of the 3 crystallographic directions of olivine from the Bear Creek pyroxenite samples. The colour code represents the structural height relative to sample T3BC1A. Only finely layered pyroxenite and massive pyroxenite samples with an ODF calculated after one-point-per-grain data were considered here.

The evolution of the textural indices (i.e. J- and M-indexes) for cpx, opx and olivine as a function of their mineral mode (Fig.4.26) and of their relative height in the section (Fig.4.27) was investigated. The elevation 0 was arbitrarily set at the elevation of sample T3BC1A, below which lherzolite crops out. The J-indices of the 3 phases do not correlate with elevation and remain stable despite the modal variations (Fig.4.26, Fig.4.27). M-indices do not correlate with either the mineral mode or the relative elevation. However, closer investigation reveals a consistently higher M-index for olivine than pyroxenes regardless of position or mode (Fig.4.26 and Fig.4.27).

The quantification of the fabric shapes of cpx, opx and olivine can allow evaluation of the possible contribution of gravity-driven processes to the microstructure of magmatic rocks in such a shallow setting. To investigate that aspect, eigenvalues of opx, cpx and olivine were computed for each crystallographic axis of interest using their orientation density function.

The eigenvalues were then normalized and plotted on a ternary diagram (Fig.4.28, Fig.4.29 and Fig.4.30). The shapes of the opx fabrics for [100] and [010] axes have similar eigenvalues and are close to the random end member (Fig.4.29). Opx [001] clearly shows a stronger point maximum and girdle component than the other axes but does not correlate with the position in the section. Quantification of the cpx fabric shape suggests that the [001] axis is mostly a mix between girdle and random components, [010] would be a mix between point maxima and random components, while [100] is mostly random (Fig.4.28). Again, no correlation with the relative elevation is visible. For olivine, eigenvalues suggest a similar contribution of the random component for each axis considered. Olivine [010] is consistent with a larger contribution of the point-maximum component for [010], while [100] and [001] are both closer to the girdle component (Fig.4.30).

4.6 - Conditions of deformation of the Trinity rocks

This section addresses the integration of field observations with textural and microstructural data, revealing the deformation history of the Trinity ophiolite at the four sampling sites. The implications of the deformation episodes and the related conditions are then considered in the context of the Trinity ophiolite and the Bear Creek magma chamber.

Corry Peak

Corry Peak is the location to examine the deformation conditions of the lowermost part of the mantle section was visited. In Corry Peak, 3 lithologies were sampled and analysed: lherzolite, dunite and pyroxenite veins embedded in the dunitic body.

In Corry Peak lherzolite, olivine CPO is consistent with a E-type fabric (i.e. [100] (001)). The E-type was previously observed in several different contexts and its origin is still debated. It could be indicative of (1) deformation at high stress and temperatures ~900°C (Michibayashi and Oohara, 2013); (2) high-temperature deformation with a high melt content (Tommasi et al., 2006) or (3) at low temperature during the mechanical weakening of a pre-existing anisotropy (Michibayashi and Mainprice, 2004). In this case, the equilibrated texture of the rock is not compatible with a high stress and low temperature deformation but is compatible with both other scenario. Recent study addressing the origin

of Trinity plagioclase-bearing lherzolite hypothetise it to be related to melt percolation and refertilisation (Dygert et al., 2016). This scenario is consistent with the presence of a E-type fabric for the olivine in the lherzolite.

In Corry peak dunites, the fabric of the cpx forming the pyroxenite layer in sample T5CP2A shows a [001](010) pattern that is characteristic of the deformation of cpx in high-temperature conditions (e.g. Amiguet, 2009; Bascou et al., 2002; Raterron et al., 1994). The shape of the fabric also indicates a contribution of both pure and simple shear to the deformation regime (Helmstaedt et al., 1972; Zhang et al., 2006). For olivine, an E-type (i.e. [100](001)) and a D-type fabric (i.e. [100]{0kl}) are found. Considering that the texture of sample T5CP2A suggests an annealing of the rock and the lack of further significant deformation, the E-type fabric of olivine is consistent in this case with deformation in a high temperature and possibly melt-rich environment. This interpretation is also consistent with the field observations in the neighbouring outcrop of Vicky bluff, which displays evidence of melt/rock interactions.

D-type fabric has been observed in several environments and could be indicative of (1) deformation at low/moderate stress and temperatures $\sim 900^{\circ}\text{C}$ (Michibayashi and Oohara, 2013); (2) deformation at low temperatures (750°C) under high-stress conditions such as in a lithospheric shear zones (Park and Jung, 2017) or (3) in similar conditions as A-type fabric (i.e. high temperature, low stress and low water content) but in a deformation regime dominated by simple shear, forcing the dislocations to move along [100] on both (010) and (001). In sample 17T25EA, the texture of the rock suggests annealing and therefore implies that the temperature remained high during a long enough time after the deformation event for annealing to operate. Consequently, the development of a D-type fabric at low temperature can be ruled out in that case. The origin of the D-type fabric is consistent with a high temperature, low stress environment where deformation by pure shear is dominant. This type of fabric is also consistent with a well-defined lineation and a foliation difficult to observe.

It can still be argued that the E- and D-type fabrics of olivine may have originated at low temperature, and that annealing took place afterward by a temperature increase possibly due to melt percolation or to an approach of the peridotite solidus induced by decompression. However, the close spatial coincidence of the maxima of the cpx fabric, indicative of high-

temperature deformation, make a high-temperature origin for the olivine fabrics a more likely scenario.

On the basis of the textural observations and EBSD data, the Corry Peak peridotites and pyroxenites are consistent with:

(1) A common-high temperature deformation episode (olivine and pyroxene fabrics) followed by an annealing episode affecting both lherzolites and dunites.

(2) Possible deformation of the dunites and plagioclase bearing lherzolites in the presence of melt.

Vicky Bluff

The Vicky Bluff outcrop is rich in melt-rock interaction features. In this locality, dunites may have crystallized through the interaction between a melt and a host peridotite. In this context, microstructural evidence may reveal the timing and conditions at which these interactions occurred.

In the Vicky Bluff lherzolite, the texture suggests that both recrystallization and annealing took place, thus indicating evolution in a high-temperature environment with low deformation before exhumation. Olivine and opx have constant [100](010) and [001](100) fabrics, respectively. Cpx shows two different fabrics, [001](010) and [001](100). The cpx [001](010) pattern, in this case a SL-fabric (*sensu* Helmstaedt et al., 1972), is characteristic of deformation in a high-temperature environment. [001](100) in cpx has been shown to appear in the upper mantle when temperature drops below 1000°C but still remains above 900°C (Raterron et al., 1994). The high-temperature evidence of the cpx fabrics is consistent with the microstructure of opx and olivine and the slip system potentially activated to form the fabric observed (Nicolas and Christensen, 1987). Field observations, the lower temperature suggested by the [001](100) fabric and the textural characteristics of cpx could also be understood as the result of a refertilization process of the host peridotite as seen in other massifs such as Ronda (e.g. Lenoir et al, 2001).

In the dunite, despite the poorly constrained structural reference frame, interpretation of the microstructure of olivine may be hypothesized using the rare cpx grains defining preferred direction for the crystallographic axis. As in the lherzolite, an [100](010) olivine fabric appears along with the [001](010) pattern for cpx, indicating both high-temperature and low-stress deformation conditions (Carter and Avé Lallemant, 1970; Nicolas and Christensen, 1987).

The Vicky Bluff pyroxenites give insights on their relationship/crystallization timing relative to the host rocks. Interpretation of the fabrics is again possible because of the spatial coincidence of the crystallographic axes. The host olivine displays a clear [100](010) fabric suggesting a high-temperature, low-stress environment. Both pyroxenes show a similar [001](100) fabric, although the cpx one is much weaker. This fabric in opx is consistent with the [100](010) olivine. [001](100) in cpx may indicate a lower-temperature deformation episode, between 900 and 1000°C, as observed in the lherzolites. As the point maxima of the minerals in the lherzolite and the pyroxenite are spatially consistent, the fabrics are inconsistent with a scenario where pyroxenites crosscut the lherzolite randomly in a late stage of the massif's history and do not experience any deformation. The pyroxenites thus are likely to have crystallized before the high-temperature deformation episode and therefore could represent a layering possibly concordant to that of the host peridotite. The equilibrated texture of the rock is a further indication that the pyroxenites experienced, to some extent (i.e. the conditions of activation of [001](100) for cpx), a history similar to that of the host lherzolite.

The Vicky Bluff mineral fabrics, texture and field observations are compatible with:

- (1) Emplacement of the pyroxenite layers before the end of high-temperature (i.e. >900°C, cpx fabric) plastic flow of the host-rock
- (2) An annealing episode re-equilibrating the textures possibly as in the annealing episode of Corry peak and possibly linked to a refertilization process.

The layered dunites are inferred to represent the second shallowest location sampled after the Bear Creek site. At this locality, two major lithologies were observed (harzburgite and dunite) and show evidence of possible complex melt/rock interactions.

In the harzburgite, a [100](001) olivine fabric (i.e. E-type fabric, Jung and Karato, 2001) is visible. E-type fabrics are commonly observed in various environments: (1) during the mechanical weakening of a pre-existing anisotropy at low temperature (Michibayashi and Mainprice, 2004); (2) at ~900°C with an important stress in shear zones (Michibayashi and Oohara, 2013); (3) at high temperature and high melt content (Tommasi et al., 2006) or (4) at high temperature, low stress and moderate water content (Katayama et al., 2004). Opx displays a [001](hk0) fabric. This peculiar fabric was reported by Jung et al. (2010) but not related to a particular deformation environment. All of the aforementioned scenarios hinted by the olivine microstructure are possible and could each be clues to a different deformation history that may or may not include the cooling of the domain and an annealing episode possibly linked to melt/rock interactions.

As seen previously, discussion of the fabric of olivine in the dunites is not straightforward because of the lack of a complete structural reference frame, the strong serpentinization and the almost monomineralic nature of the rock. Plotting the dunite orientation dataset in that of the neighbouring harzburgite assuming an error on the lineation dipping angle allows to narrow the interpretations of the olivine fabric in the dunite to two possibilities: (1) [010](100) or (2) [001](010). In both cases, a change in slip direction is observed. So far, as summarised by Michibayashi and Oohara (2013), no olivine fabric with [010] clustering next to the stretching direction has been reported. However a [001](010) fabric (i.e. B-Type fabric) is more commonly found and is a more likely outcome in nature.

Studies of settings with similar harzburgite-dunite associations have concluded that the dunites could represent conduits in which the transport of melt occurred (e.g. Braun and Kelemen, 2002; Quick, 1982). This suggests, in addition to the field observations, that including melt in the interpretations of the microstructure is critical. EBSD data reveal a change in the petrofabric of olivine between the harzburgite and the dunite. Assuming constant P-T conditions, such a change can be attributed to either (1) an increase in stress

and/or water content (i.e. a transition from E-type to C/B-type fabric, Katayama et al., 2004) or (2) deformation in the presence of melt pockets (Kohlstedt and Holtzman, 2009; Qi et al., 2018). While local variation in water content could be possible, no evidence of shear zones that could corroborate an increase in stress was observed thus making the presence of melt the most likely cause of the change in the petrofabric.

In Fig.4.20, the plano-convex features observed in the dunites does not seem to correlate with the crystallographic preferred orientation of the olivine thus suggesting these planes are not correlated to the plastic flow episode and could represent later fractures that happened during the serpentinisation of the massif.

The microstructure and field data from the harzburgites and dunites from the layered dunite locality are consistent with:

(1) Percolation of a melt and reaction with the host rock to form dunites before or during deformation at high temperature and low stress (E-type fabric and B-type fabric in the harzburgite and dunite respectively) of the harzburgites and of the dunites with melt pockets, possibly at the same time.

(2) Annealing and equilibration of the textures.

Bear Creek

The Bear Creek magma chamber, as described by Ceuleneer and Le Sueur (2008), may represent the intrusion of a boninitic melt into the oceanic lithosphere at shallow depth. This cumulate sequence offers a valuable opportunity to observe the state of the microstructure in a magmatic environment (i.e. in a “crystal mush”).

Field observations such as cross-bedding, enclaves and magmatic mineralogical and chemical trends (Ceuleneer and Le Sueur, 2008) suggest that the Bear Creek locality originated as an active magma chamber and therefore it is reasonable to expect it hosted large quantities of melt. Pegmatite segregations around enclaves may be clues to such an environment, as they could represent a very rapid expulsion of trapped melt during the impact of the falling enclave on the bottom of the magma chamber. Thin-section and field

observations of the Bear Creek cumulates tend to indicate that solid-state deformation was limited and that magmatic deformation is the most likely process to have occurred, if any. Pyroxenes, except for coarse-grained samples, do not show any deformation markers and only a few olivine grains display kink bands. This would suggest a very limited high-temperature deformation event mostly accommodated by olivine.

In the finely layered cumulates, the S-type fabric of cpx suggests pure shear at high temperature. Olivine and opx also show a dominance of 010-fibre fabrics and 100/010-fibre fabrics respectively as supported by the eigenvalues which indicate a well-defined foliation plane and a subtler lineation. The occurrence of S-type cpx is consistent with several scenarios where the 010-fibre and B-type fabric occurs in olivine. At high temperature, axial compression or transpression can form 010-fibre (i.e. Tommasi et al., 1999). Transition between A- and B-type fabric are also likely to result in 010-fibre when slip direction change over between [100] and [001], this includes deformation with interstitial melt, change of pressure or both (e.g. Holzmann et al., 2003; Vauchez et al., 2005; Mainprice et al., 2005). As described earlier in this chapter, B-type olivine has been observed in multiple high-temperature scenarios: (1) at low stress and high water content; (2) at high stress with moderate water content (Jung and Karato, 2001; Katayama et al., 2004) or (3) at low stress in the presence of melt pockets (Kohlstedt and Holtzman, 2009). Considering the case of fractional crystallisation in a magma chamber, olivine-rich lithologies would appear early in the sequence, concentrating incompatible components such as hydroxide in the melt. While the possibility of a high amount of water (as H) in the olivine triggering a B-type fabric cannot be excluded by the present study, a stress-driven B-type fabric for olivine is also unlikely as it is not supported by the textures of the samples collected. However, since the presence of interstitial melt in the cumulate was highly likely and is supported by the nature of the locality, it can be suggested that the B-type olivine found in the finely layered cumulates originated from magmatic deformation in the presence of melt pockets. The undeformed aspects both in the field and in thin section of the finely layered cumulates suggest that the commonly found 010-fibre fabric for opx and olivine and the S-type fabric of cpx are not the result of plastic deformation but rather of magmatic processes.

In previous studies of layered intrusion and cumulate suites, strong foliations and weak lineations were observed in the field, in thin sections and in anisotropy of magnetic susceptibility (i.e. AMS). AMS can be considered as a first order proxy for EBSD data as

the result is a function of the crystallographic preferred orientation (Biedermann et al., 2014). The strong planar component and weak lineation were attributed to crystal settling and compaction. It is realistic to consider that the Bear Creek finely-layered cumulates experienced the same processes (e.g. Boorman et al., 2004; Feinberg et al., 2006; Higgins, 1998, 2015). Results and fabrics are also consistent with previously reported fabrics of layered gabbroic intrusion in the crustal section of Oman (Benn and Allard, 1989).

If compaction is the main process in play, the lineation/stretching direction marked by the weak clustering of olivine, cpx and opx [001] axes along the N130 direction can be seen as the result of other phenomena: (1) a switch from pure shear to hyperbolic magma flow within the chamber resulting in a change of the deformation regime and creating a point maximum in the fabrics (Higgins, 2015); (2) the accommodation of local stress resulting from gravitational instability as hinted by the cross-bedding observed in the field; (3) the effect of the regional stress field stretching materials towards N130. The latter effect implies a much stronger contribution of compaction to the microstructure, relative to the local stress field, and possibly a rapid cooling of the chamber to escape plastic deformation. While each scenario and their combinations are possible and none can be discarded, the systematic coincidence between the olivine, cpx and opx [001] axes and the regional N130 stretching direction suggests the regional stress field is the simplest way to explain the [001] clusters. The weak concentration of the clusters is also an indication of the greater relative importance of the compaction process on the cumulate microstructure.

The lherzolite microstructures are clearly different from those of the layered cumulates and suggest a record of a stronger deformation. They have an SL-type fabric for cpx, suggesting deformation at high temperature, and a combination of pure and simple shear (Bascou et al., 2002; Helmstaedt et al., 1972). Olivine has an A-type fabric in sample T4BC2A and a B-type fabric in sample T4BC3A, which is located closer to the contact with the layered cumulates. Olivine CPO in the Bear Creek layered cumulates is almost exclusively B-type and was interpreted in this chapter as a result of deformation in the presence of interstitial melt. In the field, the lherzolites crop out structurally below the cumulates and are a reasonable candidate to represent the host rock that was intruded by a boninitic melt (Ceuleneer and Le Sueur, 2008). The change in slip direction of the olivine in sample T4BC3A could also be explained by shearing in the presence of melt as it is located less than 2m away from the layered cumulates and could have acted as pathway for melt.

The sampled peridotitic enclave provides information about a pyroxenite layer and the lherzolite in which it is embedded. Both sub-lithologies have consistent petrofabrics suggesting they recorded a common deformation event. The olivine fabric in the peridotite is A-type; opx has a [001](100) and cpx a [001](010) fabric in the pyroxenite layer. This combination is classically found in upper-mantle rocks and could indicate deformation in a high-temperature, low-stress and melt-free environment, which contrasts with the girdle-dominated fabrics of the cumulates. The lack of relationship between olivine and opx CPO and the structural framework, coupled with the similarity of the microstructure to mantle-derived material from the Trinity region is consistent with the idea of this lithology being the host rock into which a boninitic melt intruded. The possibility of a Christmas tree-like type intrusion (as seen in other contexts, e.g. Rocchi et al., 2002) is also unlikely as the fabrics of the enclave are randomly orientated relative to the basal lherzolite and the general structural frame of the area. The relative freshness of the enclaves compared with the serpentinized basal lherzolite may reflect the shielding of the enclaves from later fluid percolation by the then-crystallized cumulates.

Massive pyroxenites have fabrics similar to those of the finely layered cumulates but differ in having a coarser grain size, greater shape factor and an almost monomineralic composition. The origin and nature of a sample bearing this microstructure is unclear without additional geochemical data as: (1) they could represent melt segregates following the finely layered cumulates in the fractional crystallization sequence as suggested by the lower magnesium number of the cpx (Ceuleneer and Le Sueur, 2008) or (2) as seen in the field, they could also be the finer-grained fraction of the pegmatites that are seen intruding the finely layered cumulates along the compositional layering. Understanding the nature of this lithology is important to understand the dynamics of crystallization in the Bear Creek locality and the development of fabrics.

Sample T4BC4, a massive pyroxenite, shows a twinned macrocryst of cpx; the texture of the surrounding cpx grains suggests that the macrocryst is being replaced by static recrystallization of the surrounding cpx grains. This texture can be interpreted as the result of an interaction between a melt and the finely layered cumulates that can host cpx macrocrysts (see sample T3BC3). This would make sample T4BC4 a pegmatite and not a massive pyroxenite, and brings into question the very nature of the massive pyroxenite lithology that were sampled.

In sample 02T117-1, a sharp contact between the finely-layered cumulates and pegmatite is visible (Fig.4.31): on both sides of the sample, the two fabrics belong to the one found in the Bear creek finely-layered cumulates and massive pyroxenites and the respective textures are typical of the massive pyroxenites and finely-layered cumulates.

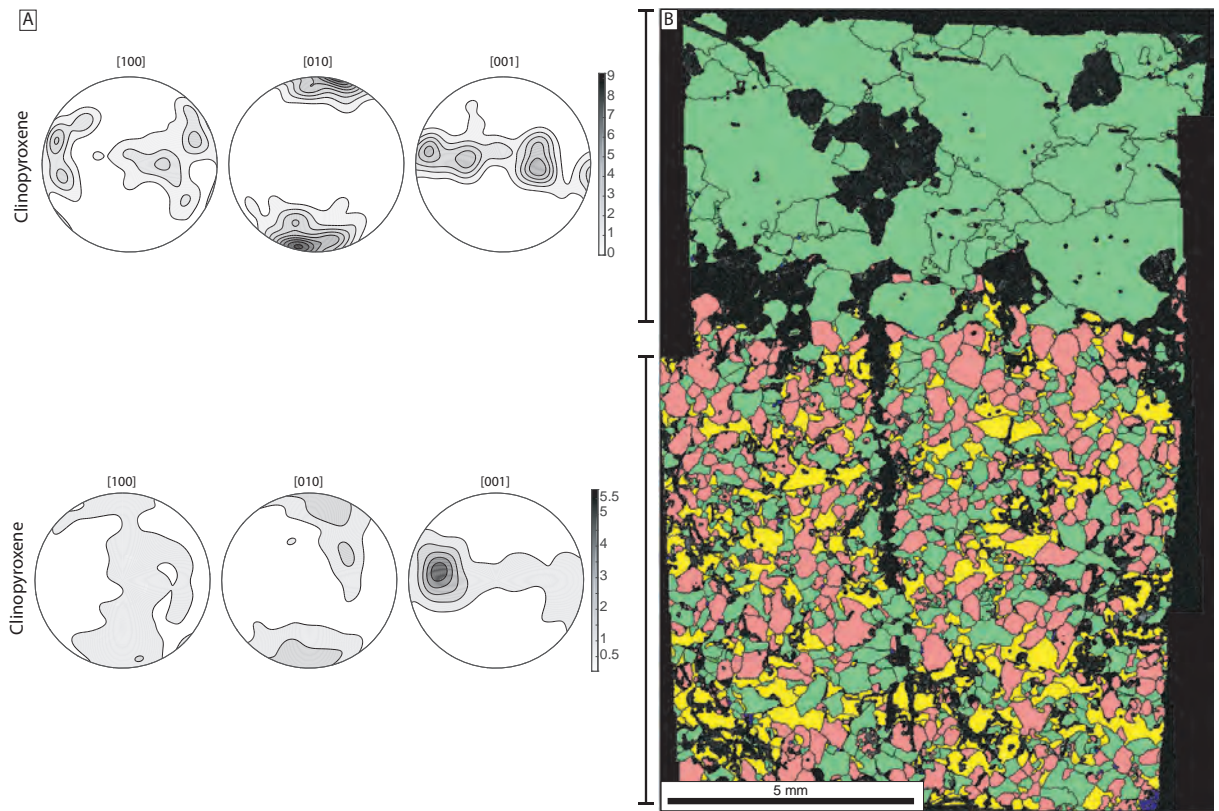


Fig.4.31: Pole-figures and phase map of sample 02T117-1. (A) pole-figure of cpx each corresponding to either the coarse and finer grained part; (B) Phase map showing the microstructure of the sample and the sharp change of microstructure. Cpx is pictured in green, opx in red, amphibole in blue and olivine in yellow. Thin section was cut perpendicular to the foliation and was not oriented relative to the north.

Considering the above, one can consider that at least some of the samples labelled as massive pyroxenite could instead be the finer-grained portion of the pegmatite segregations as, from a microstructure and field point of view, both lithologies can be very similar. A question comes now to mind: is there any massive pyroxenite or is there only finer-grained portions of pegmatite segregations? The existence of a massive pyroxenite lithology *sensu* Ceuleneer and Le Sueur (2008) cannot be discarded completely, because of the peridotitic enclaves found within it, and the chemical trends that were reported. Discriminating the two lithologies would require a more extensive survey of the locality including more samples, a specific mapping strategy as well as a geochemical analysis of the sample and is beyond the scope of this current study.

In these two lithologies, the development of the mineral fabrics may be a function of their nature. In both cases, a mechanical origin for the fabric can be discarded due to the field observations, leaving growth features or magmatic processes as remaining possibilities. Cumulate massive pyroxenite fabrics may also result from the processes at play in the finely layered cumulates. Their different textures may reflect the grain growth competition in an environment favourable for the crystallization of a single phase: nucleation of few grains would occur and their growth would continue as long as the neighbouring grains allow it. In this case, and in contrast to that of the finely layered cumulates, the lack of a viscosity contrast would hinder accommodation of the weak local stress, and could explain the moderate lattice misorientation in large cpx. In the case of the fine-grained fraction of a pegmatite, their rapid crystallization and the suggested melt/rock interaction, tend to indicate that the origin of the fabric lies in the crystal growth processes. The presence of cpx in the intruded finely-layered cumulates is a factor favourable to the rapid epitaxial crystallization of new grains of cpx. This process would result in similarly oriented material and therefore in a fabric similar to that of the host rock.

In the light of all the above, interpreting the fabrics of samples labelled as massive pyroxenites, and relating them to conditions of deformation, is hazardous as they could reflect the fabric of the surrounding rock. Consequently, no link is drawn between the finer-grained fraction of the pegmatitic outburst and massive pyroxenites and potential conditions of deformation.

The [001](010) fabric of the olivine-rich level in the massive pyroxenites and the change to an clearer orthorhombic symmetry suggest that they recorded plastic deformation. In a similar fashion than in the finely layered cumulate, the B-type fabric of olivine is best understood as deformation in the presence of interstitial melt.

The microstructure of the coarser-grained part of the pegmatite is difficult to interpret as a structural reference is missing and the small number of grains prevents comparison of fabrics of different phases. In addition, because the grain size is very coarse, and cpx shows clear twinning, the pole-figure of cpx is tricky to interpret, leaving the internal deformation as the only reliable parameter. In cpx, twinning can occur during deformation at low temperature in mylonites (Avé Lallemant, 1978). In this case, the cpx twins are more likely to be growth

twins, as suggested by Ceuleneer and Le Sueur (2008). Only moderate lattice deformation is visible in the cpx, opx and olivine grains, so it is consistent with the field observations, to conclude that the pegmatite was emplaced in a later stage and did not record deformation.

In summary, the field and microstructural data from the Bear Creek are consistent with:

(1) The intrusion of a large batch of melt into a lherzolite that was deformed at high temperature and low stress.

(2) Crystallization of finely layered cumulates followed by massive pyroxenites at high temperature, and incorporation of peridotitic enclaves during that process. Contemporaneous to the crystallization, the mineral fabrics were formed by a combination of compaction and a weak contribution from the regional stress most likely in the presence of interstitial melt. Also happening at the same time, peridotitic enclaves falling from the magma chamber roof and the compaction process are likely to have triggered coarser- and finer-grained pegmatitic outbursts during the fractional crystallization process. These particular outbursts should be located preferentially along the compositional layering or would surround the peridotitic enclaves.

(3) Later intrusions of pegmatitic melts resulted in secondary pegmatitic outbursts that cross-cut the basal lherzolites and crystallized also coarser and finer-grained pegmatites.

4.7 - The case of opx

In the four localities studied, opx microstructure did not provide as much information about the deformation condition as the olivine and cpx. This is mostly due to the more limited number of studies about its deformational behaviour with the consequence that few fabrics that have been reported.

In mantle xenoliths, opx fabric is generally [001](100) or random (Christensen and Lundquist, 1982; Nicolas and Christensen, 1987). [001](010) fabric was also reported in both experimental and natural samples and related to either (1) a strain rate greater than 40% (Ross and Nielsen, 1978) or (2) an important Al₂O₃ content (Manthilake et al., 2013). In Beni Boussera, Frets et al. (2012) concluded that [001](010) and [001](100) were activated

in pyroxenites that evolved under lithospheric-mantle conditions. Two other fabrics were reported by Jung et al. (2010) and were associated with deformation in a relatively opx-rich environment: [010](100) and [001](hk0) (i.e. BC- and ABC-types respectively). In Trinity, [001](hk0) and [001](100) are the most common opx fabrics. They are associated, with a few exceptions, to B-type and A-type olivine fabrics. As mentioned previously, B-type olivine in Trinity is most likely the result of deformation at high temperature and low stress in presence of an interstitial melt. Considering the dramatic effect that melt can have on the olivine fabrics (Kohlstedt and Holtzman, 2009), it is possible to hypothesise that an interstitial melt may also affect the deformational behaviour of opx and possibly trigger a [001](hk0) fabric. [001](hk0) could also represent a transition between AC- and BC-type fabrics during a change in dominant slip system that should, in both cases, occur at high temperatures. Further experimental work is needed to verify this hypothesis.

4.8 - The case of amphibole

In all studied sites, amphibole can be found but usually in small quantities. Amphibole CPO systematically mimics the cpx CPO. This observation, along with the textural association of amphibole with cpx suggests an epitaxial growth of the amphibole on cpx pre-existing grains. The fabrics suggest that amphibole grew after cpx in every lithology, even including the Bear Creek pegmatites, which are already relatively late in the magmatic history of the massif.

Such results are consistent with a metamorphic origin for the amphibole that may be related to the retrograde metamorphism during cooling of the massifs. This would indicate that no more plastic deformation occurred while in the amphibole plastic deformation field as another fabric would be expected.

4.9 - What did the microstructure reveal about the geology of the Trinity ophiolite?

This study of the microstructures of plagioclase lherzolite, lherzolite, harzburgite, dunite and cumulates from Trinity provides valuable information on the story these rocks experienced and recorded. The sites located in the mantle section (i.e. Corry Peak, Vicky Bluff and possibly the Layered Dunites) record an episode of solid-state flow, mostly at high

temperature in the presence of melt during and after deformation. The stretching direction inferred from the petrofabrics is similar (i.e. N130) in all the localities. All the above is consistent with the popular consensus that Trinity represents a fossil spreading ridge preserved from recycling thanks to early obduction (e.g. Boudier and Nicolas, 1985). Annealing suggests that static recovery took over from shearing after the plastic deformation event, maybe hinting at a different way to accommodate deformation in the later stages of the massifs evolution (i.e. localised shearing).

The intrusion of a boninitic melt within the Trinity lherzolite and its fractional crystallization produced the Bear Creek cumulates. They show microstructures and features similar to those of other well-known layered intrusions. The Bear Creek cumulates were later intruded by pegmatitic melts. The relative lack of plastic deformation in the Bear Creek cumulates and the lack of signs of deformation in the field suggest that the intrusion occurred later in the massif's history and post-date the main plastic-deformation event.

The data and interpretations presented are consistent with the geodynamic scenario proposed for the Trinity ophiolite which includes:

(1) The formation of the mantle material (i.e. in Corry peak, Vicky Bluff, and Layered Dunites) at a slow-spreading ridge.

(2) Percolation of that domain by melt and formation of melt-rock reaction features (i.e. in Corry peak, Vicky Bluff, and Layered Dunites). This most likely happened while deformation was undergoing.

(3) Later intrusion of the oceanic lithosphere by an arc-related magma in a non-neutral regional stress field leading to the formation of plutons with strong cumulate fingerprint (i.e. in Bear Creek).

(4) Cooling of the massif, preservation of the structures in every localities thanks to obduction

4.10 - Trinity and Cabo Ortegal: microstructural links and the deformation of pyroxenes

The primary motivation to study the Trinity pyroxenitic cumulates was to perform a comparison with the Cabo Ortegal pyroxenites. Both massifs host similar clinopyroxene-rich lithologies that crystallized from intrusions of boninitic melt (Ceuleneer and Le Sueur, 2008; Tilhac et al., 2016). Mineralogically, Cabo Ortegal and Trinity pyroxenites are similar. Forsterite is found in both locations. Cpx and opx both best fit with a diopside and enstatite crystallographic structure and chemistry.

The Cabo Ortegal pyroxenites differ from Trinity's on two major points:

(1) They crystallised at a pressure >1.2 GPa while Trinity pyroxenites crystallised at shallower depths (~ 0.1 GPa). As a consequence, the Cabo Ortegal pyroxenites formed, at least partially, by melt-rock interaction but also via cumulate processes (Tilhac et al., 2016).

(2) Cabo Ortegal pyroxenites experienced both prograde and retrograde metamorphism and a strong deformation, related to a delamination episode followed by entrainment and exhumation of the rocks in a subduction channel while Trinity cumulates were preserved from plastic deformation.

Based on the above, Trinity clinopyroxenes-rich cumulates can be good candidates for a “pre-deformation protolith” for the Cabo Ortegal pyroxenites. Affirmation of this requires the assumption that the Cabo Ortegal pyroxenites, which crystallised via cumulate processes, were affected by compaction as in the Trinity cumulates. If this assumption is correct, pyroxenites would crystallise with a pre-existing CPO characterised by [010] (and [100] for opx) perpendicular to the magmatic layering and a random distribution along the layering plane of [001] and [100] ([001] only, in the case of an opx with [100] along the magmatic layering plane). In the upper mantle, the [001](010) pattern will typically arise for cpx and [001](100) / [001](010) for opx. One can hypothesise that the pre-existing magmatic fabrics are likely to facilitate the development of such fabrics. However, it cannot be considered as a required parameter for this activation as opx and cpx in peridotite present similar fabrics and do not show any evidence of compaction.

Summary of Chapter 4

*Samples from **four localities** in the **Trinity ophiolite**, California, USA, were collected and representative samples for each lithology identified were studied using **EBSD**.*

*Mineral fabrics of the **mantle section** of the ophiolite are consistent with deformation in a **high-temperature environment** and in the presence of **interstitial melt** for some lithologies. The textures indicate that deformation ceased before an **annealing episode** occurred.*

*The **crustal section** of the Trinity ophiolite (the mafic-ultramafic intrusions) shows **textures and fabrics very distinctive from that of the mantle section**. **Compaction and crystal settling** controlled the crystallographic preferred orientations of the minerals in the **Bear Creek magmatic chamber**.*

*The data are consistent with a scenario in which **the Trinity complex** originated at an **oceanic spreading centre (likely back-arc)**, was **deformed and intruded by a boninitic melt** while **deformation was still active**. Deformation subsequently ceased, and **annealing** of the textures and **obduction of the ophiolite** took place.*

Chapter 5:
The Seismic Properties of
Layered Pyroxenite Media

5.1 - The problem of interpreting seismic data

Previous chapters discussed examples of how plastic deformation of minerals and flow in the presence of melt can result in a crystallographic preferred orientation (CPO). Consideration of the elastic properties of single crystals of each mineral constituting the upper mantle demonstrates that a concentration of the crystallographic axes (i.e. strong CPO) in one direction will create a fast and a slow velocity direction for the seismic waves (Fig.2.7, Ismail and Mainprice, 1998; Mainprice et al., 2013; Nicolas and Christensen, 1987). Using seismic tomography and other seismic inversions it is possible to determine the orientation of the fast-velocity direction for the different seismic waves and, by testing likely hypotheses, estimate and map the direction of mantle flow (e.g. work of Tanimoto and Anderson (1984), Fig.5.1). Amongst the hypotheses, the volumetric dominance of olivine in the upper mantle makes its CPO the most likely cause for large-scale seismic anisotropy (Raitt et al., 1969) leaving the effect of pyroxenes on seismic signals poorly investigated. Consequently, in regions where pyroxenites are potentially modally significant, (DeBari and Coleman, 1989; Girardeau et al., 1989; Khan et al., 1989; Khan et al., 1993; Garrido et al., 2007; Almqvist et al., 2013; O'Reilly and Griffin, 2013; Tilhac et al., 2016; Henry et al., 2017; Tilhac et al., 2017) seismic interpretations may not reflect the geological reality.

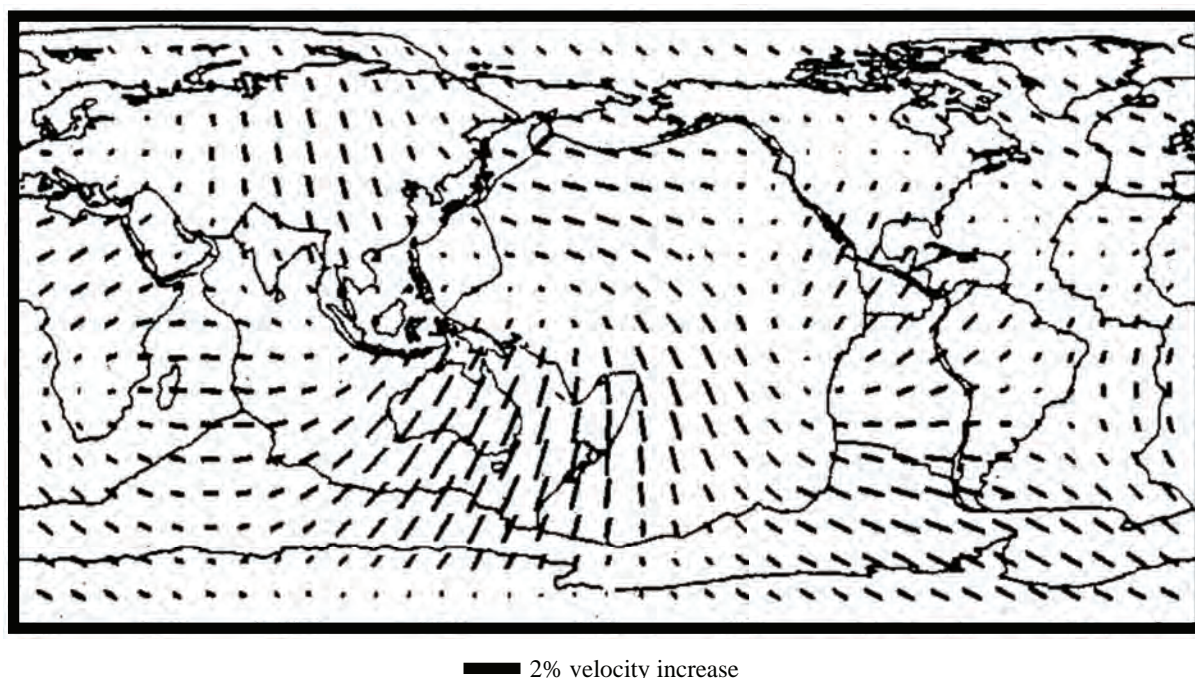


Fig.5.1: Mantle anisotropy between 200 and 400 km as calculated by Tanimoto and Anderson (1984). Lines are parallel to the fast direction of the Rayleigh waves, which are assumed to parallel the [100] olivine axis, thus providing an approximate direction of solid state flow in the mantle.

In the “subduction factory”, a large volume of crystallized melts or melt cumulates (i.e. pyroxenites) that did not make it to the surface, could be expected in the root of a volcanic arc, and eventually in the mantle wedge if recycling is operating. Pyroxenites in arc roots are one of the missing puzzle pieces required to understand the mass transfer and mass balance during continental growth and plate convergence magmatism (e.g. Jagoutz and Kelemen, 2015). Estimating their amounts is critical to fully understand how the plate building mechanism works.

Because of their great potential in recording magmatic processes, pyroxenes have been under the geochemical spotlight for decades but few studies have addressed their influence on seismic signals (Christensen and Lundquist, 1982; Wagner et al., 2006; Soustelle and Tommasi, 2010). Additionally, only the scenario of homogeneously distributed pyroxenes has been considered, while compelling geological evidence from studies of mantle-derived xenoliths and orogenic peridotite massifs in particular, indicates that pyroxene concentrations mostly occur as layers. This leaves unexplored, the fingerprint of such layering on the large-scale seismic properties of the upper mantle, the aim of this work.

Below, details are given for modelling the seismicity of pyroxenite-rich domains in order to identify criteria that could be indicative of a layered pyroxenite domain. Then the effect of such heterogeneities on the seismic signal received, is discussed

In this chapter, the following fundamental concepts will be developed:

- (1) What is the seismic fingerprint for a Herbeira-like domain and what difference does it make to the identifiable parameters typical of a standard supra-subduction upper mantle?
- (2) To what degree does pyroxene CPO changes the seismic signal of a domain?
- (3) To what extent does modal composition affect seismic properties in a layered medium?

5.2 - What is the link between EBSD and seismic waves?

Since the advent of EBSD in Earth Sciences, easy collection of large microstructural datasets has been greatly facilitated, and modelling of seismic properties is now more accessible. Mainprice et al. (2011) have transferred the Careware project into Matlab, first developed in Fortran (i.e. Mainprice, 1990). This program models the seismic properties of a rock using its mineral CPOs and a set of experimentally determined physical properties for each phase (i.e. elastic tensors and density). The philosophy of the method is to first combine, for each phase, an orientation density function (directly extracted from the EBSD datasets) with an experimental elastic tensor describing the elastic properties of that phase, to calculate the elastic properties of the given mineral in the medium of interest. Getting the elastic properties of the whole medium is achieved by adding the individual elastic tensor of each mineral forming the medium and weighting them with a user-defined mode. The seismic properties are finally calculated thanks to the resulting elastic tensor and density of the whole medium and is plotted using the MTEX toolbox.

This protocol has been used for decades in the community but has some evident limitations: (1) experimentally defined tensors may not represent accurately the sample in terms of chemistry or pressure/temperature; (2) accurate extrapolation of the tensor to the required P/T field is difficult because of the rarity of the derivatives in the literature and (3) the homogenisation of the tensors assumes a homogeneous spread and no structural features like layering can be taken into account.

Concerning the effect of such structures on the resulting seismic properties, the pioneering work of Backus (1962) showed that the observed anisotropy of a thinly layered isotropic medium can be accounted for by the layering itself. In other words, the structure of the rock can modify the seismic properties and it has to be taken into account when modelling a layered medium.

An accurate model of a layered pyroxenite-rich domain therefore requires the user to adapt the protocol of Mainprice et al. (2011) to include the structural features. Because olivine and pyroxenes are anisotropic minerals, their combination into a layer will result in an overall anisotropic layer. Using Backus' averaging technique on a pyroxenite / dunite complex is

impossible as this averaging method requires stacks of isotropic layers. Consequently, the calculus of Schoenberg and Muir (1989), who extended the Backus averaging to a thinly-layered anisotropic medium is needed. The validity of the method has been discussed and compared to other models by Carcione et al. (2012) who concluded that the theory performs very well. This averaging technique still presents limitations and assumes continuous, alternating and parallel layering. This assumption, even if not entirely accurate when it comes to layered pyroxenite massif, is a good first-order approximation and fits the reality of the field better than the assumption of a homogeneous medium.

5.3 - The philosophy of the modelling

In this work, a way to model the seismic properties of a layered medium has been developed. In this section, I describe the protocol and explain how and why each step is done. The code itself was designed to handle media comprised of opx, cpx and olivine. However, it can be modified to fit other contexts and rocks as long as the medium of interest is layered and that the correct elastic tensors are used. All functions are provided in the electronic appendices. Below is a description of how the modelling is realised:

Elastic tensor correction

For the sake of accuracy, the first operation to be performed is a correction of the elastic tensor and the density of cpx, opx and olivine according to a value of pressure and temperature specified by the user. At the temperature and pressure of the shallow upper mantle, the elastic tensor and density of olivine cpx and opx are only slightly modified relative to the room temperature and pressure values (Silver et al., 1999). Therefore, this operation was classically neglected by studies modelling the seismic properties of the uppermost part of the mantle. However, when going into deeper and hotter conditions, this correction becomes non-negligible (Mainprice et al., 2013). Correction of the elastic properties C_{ij} at a given P and T is performed following the equation of Mainprice (2007):

$$C_{ij}(P,T) = C_{ij}(P_o T_o) + (dC_{ij}/dP).\Delta P + 1/2(d^2 C_{ij}/dP^2).\Delta P^2 \\ + (dC_{ij}/dT).\Delta T + (d^2 C_{ij}/dPdT). \Delta P. \Delta T$$

where $C_{ij}(P_o, T_o)$ is the elastic tensor of the mineral at room pressure and temperature, dC_{ij}/dP and d^2C_{ij}/dP^2 the first and second order pressure derivative respectively, dC_{ij}/dT the first order temperature derivative, $d^2C_{ij}/dPdT$ the cross-pressure and temperature derivative, ΔP and ΔT the pressure and temperature variation relative to P_o and T_o . Unfortunately, not all of these derivatives have not been measured for each mineral studied. Therefore, olivine and opx have been corrected with the first-order pressure and temperature derivatives as well as with the second-order pressure derivative. Experimental values for cpx are rarer and only the first-order pressure and temperature derivatives were used.

Density correction

The seismic velocities being dependent on the density, this also has to be corrected. The following equation from Mainprice (2007) was used to make corrections according to the pressure and temperature specified by the user:

$$\rho(P, T) = \rho_o \{ (1 + (K'/K) \cdot (P - P_o))^{1/K'} [1 - \alpha_{av} (T - T_o)] \}$$

where ρ_o is the density at room temperature, K the bulk modulus, K' the pressure derivative of K , α_{av} the average value of the thermal expansion coefficient, P_o and T_o the room pressure and temperature respectively.

ODF calculations

Once the tensor has been corrected, ODF are calculated for each mineral. Contrary to the ODF noted in the previous chapters, a Dirichlet Kernel is used instead of a de la Vallée Poussin kernel as it is the one most adapted to model elasticity. A band width of 4 was chosen in order to best reflect the elastic properties, rather than the band-width of 2, which is better for thermal conductivity. For seismic properties it is important to account for the rock volume; therefore all the EBSD measurements were used in the calculation and not the 1-point-per-grain ODFs.

Definition of the different media

To model a layered medium, it is necessary to define the properties of each layer. A given layer will be defined by an elastic tensor and its density. If the mineral distribution within a layer does not show any structure, the averaging method described by Mainprice (1990) can be used. Beside CPO, the proportion of each layer is also specified at that point. Figure 5.3 represents a sketch of the model.

Calculation of the layered medium elastic tensor and seismic properties

The elastic tensor of a homogeneous equivalent medium to a layered medium made of dunite and pyroxenites is then calculated. The Schoenberg and Muir (1989) calculus achieves this by using the elastic tensors of the two media that were computed previously. The calculus will simulate the effect of a series of planar discontinuities on the elastic properties of the medium. This step returns an elastic tensor and a density that can then be used to calculate seismic properties with the dedicated tools in MTex. The assumptions behind this calculus are that (1) the frequency of the layering is smaller than the wavelength of the seismic wave travelling through and (2) the layers are continuous and, in this case, parallel to each other (Fig.5.2). This method, like the Backus averaging (Backus, 1962), is only dependent on the elastic constants, the density and the relative proportions of the layers, meaning that the actual thickness of the layers does not play a role as long as all the conditions are satisfied. Seismic properties are then computed following Mainprice et al. 2011 method and using the density and elastic tensor calculated before.

5.4 - A Herbeira-like model

The Herbeira massif of the Cabo Ortegal Complex, North-western Spain, contains one of the greatest volumes of exposed pyroxenites reported in a mantle-derived terrane. It preserves a section approximately 600m thick in which pyroxenite layers alternate with dunite in an otherwise harzburgitic mantle. This massif originated in the root of a volcanic arc before its subduction and following exhumation (Girardeau et al., 1989; Girardeau et al., 1990; Gil Ibarguchi et al., 1990; Ábalos et al., 2003; Puelles et al., 2012; Tilhac et al., 2016; Tilhac et al., 2017). The pyroxenite mineralogy is dominated by clinopyroxene and orthopyroxene with

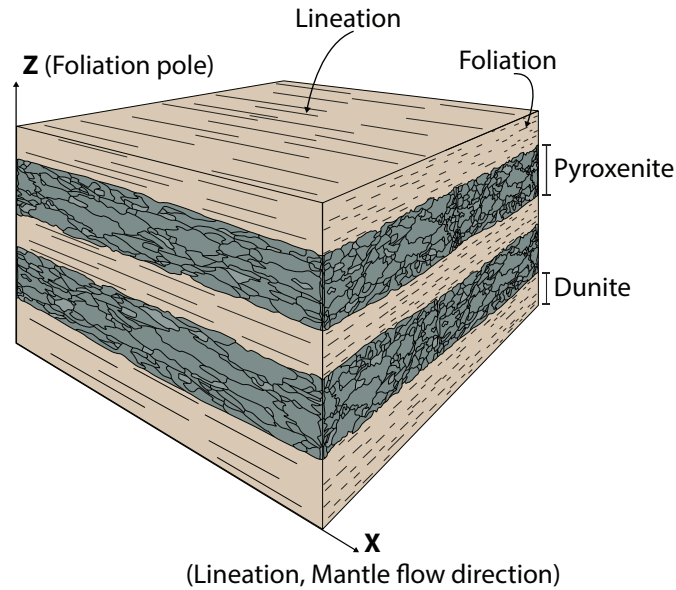


Fig.5.2: Representation of the geometrical and compositional parameters used for computation. Layered pyroxenites and dunites are shown with respect to the structural framework. The X direction of the model corresponds to the lineation (i.e. the flow direction), and the Z direction coincides with the pole of the foliation plane. The Y direction is normal to both X and Z, corresponding to the strike of the arc front in a subduction context.

minor olivine, and variable amounts of amphibole; the latter is mostly related to sub-solidus reactions. Based on the data from this well-characterised set of pyroxenites (Tilhac et al., 2016; Henry et al., 2017; Tilhac et al., 2017; Tilhac, 2017), the elastic tensor and density of the pyroxenite layers were computed using a representative CPO for each phase (sample 602C and 702A for opx and cpx respectively, see Fig.5.3) and following the protocol described by Mainprice et al. (2011).

The Cabo Ortegal dunites are heavily serpentinized, so for the of this study, the dunite layers are modelled as pure olivine exhibiting the CPO of peridotite xenoliths from the supra-subduction Avacha volcano, Kamchatka (Soustelle and Tommasi, 2010). They display a widespread A-type olivine pattern (Fig.5.3) and represent an analogue for the properties of the dunite-forming olivine from Herbeira before their complex tectono-metamorphic history (Jamaa, 1988), when intrusive melts crystallized the pyroxenites in an arc root environment (Tilhac et al., 2017). The relative proportions of the two layers were set at 60% dunite and 40% pyroxenite by volume, with pyroxenite layers defined as an 80:20 mixture of clinopyroxene and orthopyroxene. These ratios are consistent with field observations from the Cabo Ortegal Complex (Girardeau et al., 1989; Tilhac et al., 2016), as well as with those of selected other exposed sub-arc mantle terranes (e.g., Tonsina, Alaska, DeBari and Coleman,

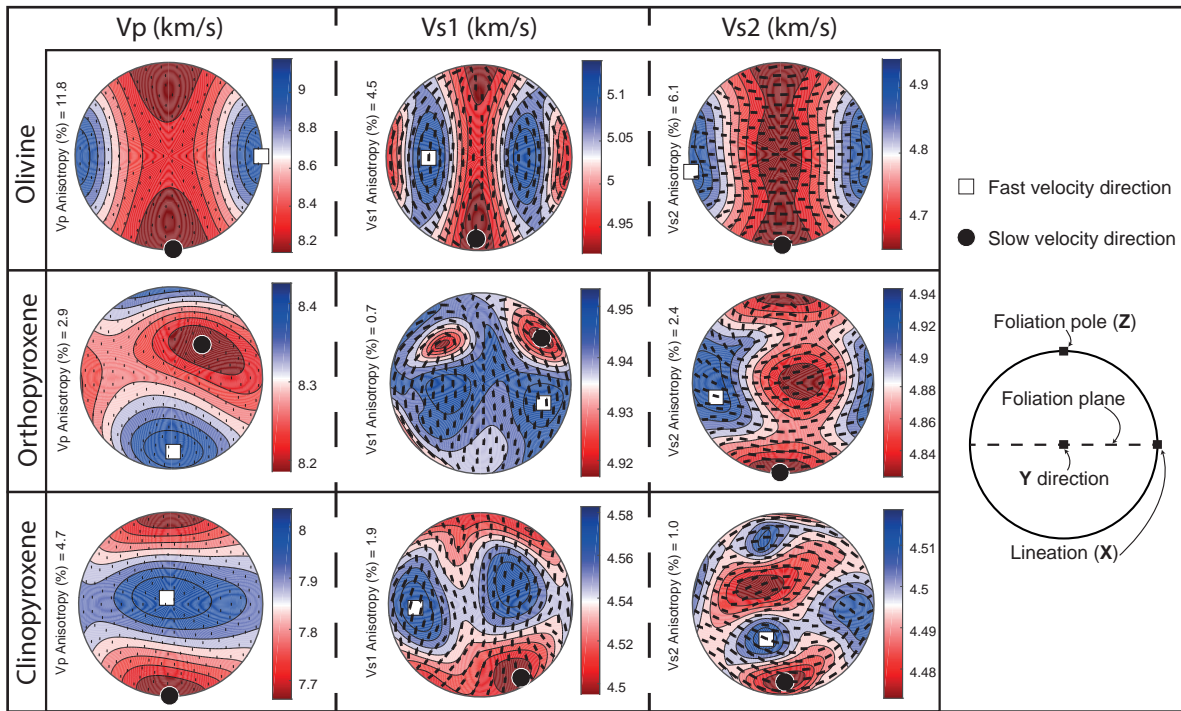


Fig.5.3: Vp, Vs1 and Vs2 waves speed (km/s) of the olivine, cpx and opx used in the models, plotted on a upper-hemisphere, equal area stereographic projection. The white square indicates the direction of maximum velocity while the black circle indicates the direction of minimum velocity. Olivine properties were extracted from Soustelle and Tommasi (2010). Seismic properties of cpx and opx were calculated using the protocol of Mainprice et al. (2011). Representative fabrics of the Herbeira pyroxenites were chosen from Henry et al. (2017) (sample 602C and 702A for opx and cpx respectively). Tensors have been corrected to 1000°C and 1GPa.

1989). For consistency, and where possible, the elastic tensors and density of each phase have been extrapolated (Mainprice, 2007) to realistic conditions of temperature (1000°C) and pressure (1 GPa) corresponding to the thermobarometric parameters calculated for Cabo Ortegal pyroxenites (Girardeau and Gil Ibarguchi, 1991; Tilhac et al., 2016; Henry et al., 2017).

The results of the simulation are shown in Fig.5.4. The maximum anisotropy of Vp, AVs, Vs1 and Vs2 for the layered model reach 8.4%, 5.8%, 3.6% and 4.1%, respectively. To reveal the impact of the presence of layered pyroxenites in an otherwise harzburgitic upper mantle, we have subtracted the calculated model from a homogeneous reference material. For that purpose, we used the seismic properties of a series of supra-subduction harzburgites calculated from xenoliths from the Avacha volcano, Kamchatka (Fig.5.4, Soustelle and Tommasi, 2010).

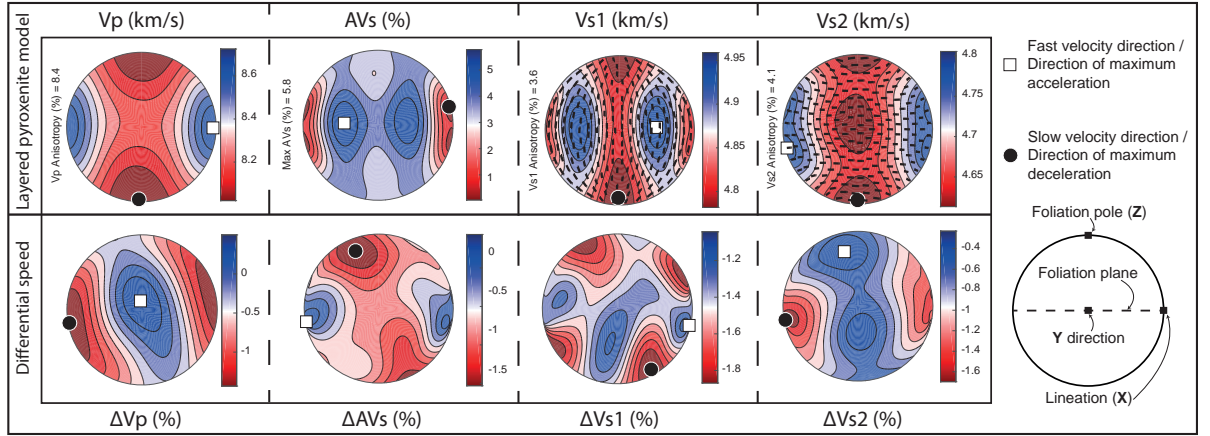


Fig.5.4: Results of the seismic experiments for the layered pyroxenite model and comparison of the result with a reference supra-subduction harzburgite. Seismic-wave velocities are plotted on an upper hemisphere, equal-area projection. Top row: Vp, AVs, Vs1 and Vs2 of the layered model relative to the structural reference. The fastest and slowest velocity directions are indicated by a white square and a black circle, respectively. Wave velocity values are in km/s. P- and S-wave polarisation planes are indicated with black dashes. Bottom row: Differential plots comparing a reference supra-subduction harzburgite with the layered pyroxenite model. The differential for Vp, Vs1 and Vs2 is a percentage defined as $\Delta V = 100 \cdot (V_{\text{model}} - V_{\text{reference}}) / (V_{\text{reference}})$. As AVs is already normalised by definition, $\Delta AVs = AVs_{\text{model}} - AVs_{\text{reference}}$. White squares and black circles show the directions of maximum acceleration and maximum deceleration, respectively.

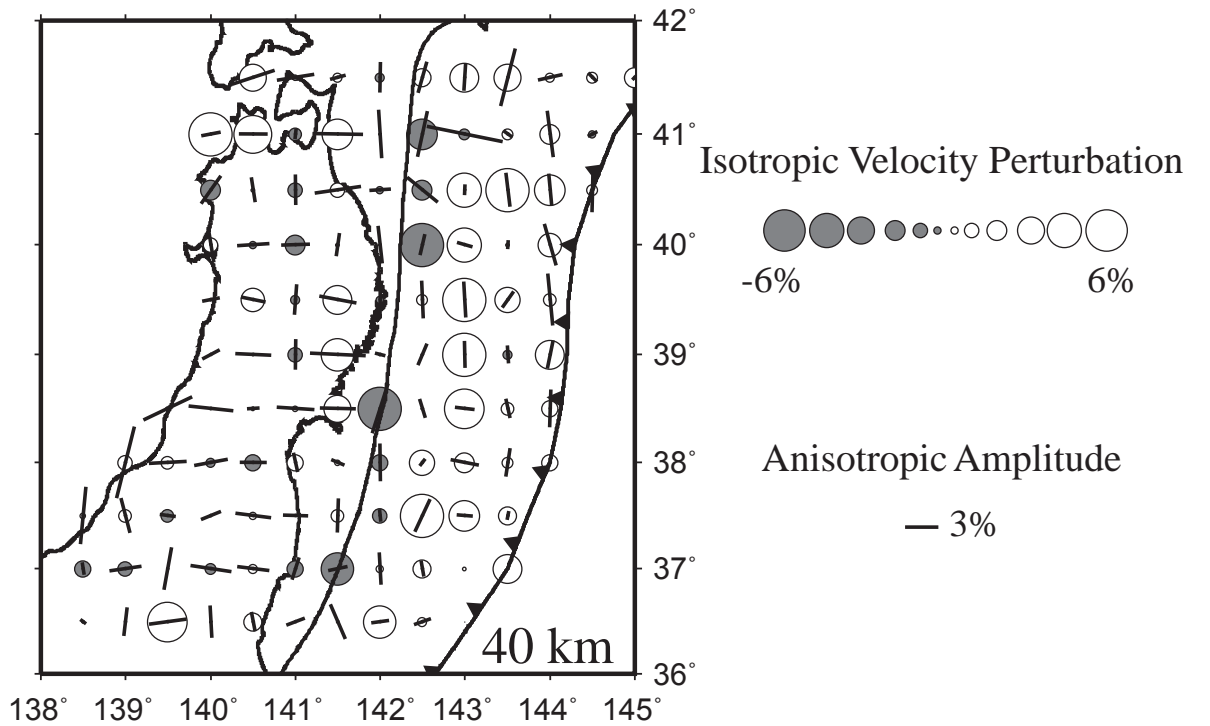


Fig.5.5: Tomographic inversion of P-waves showing the change in fast velocity direction below the volcanic arc of Honshu, Japan at moho depth. The change in direction can be coupled with a decrease in the maximum anisotropy. From Wang and Zhao, 2010.

Along the volcanic front of subduction zones, down in the mantle wedge, a switch of P-wave Fast-Velocity Direction (FVD) from trench-normal (X direction, Fig.5.2, Fig.5.3 , Fig.5.4 and Fig.5.6) to trench- parallel (Y direction, Fig.5.2, Fig.5.3, Fig.5.4 and Fig.5.6) is documented in seismic databases (e.g. Kneller et al., 2005; Wang and Zhao, 2008; Wang and Zhao, 2010 and Fig.5.5). This switch has been traditionally attributed to a change in dominant slip direction in olivine from [100] in the back arc to [001] in the forearc (Jung and Karato, 2001). In addition to a diminution of the maximum anisotropy for P-waves, the model suggests that a decrease in the P-wave velocity in the lineation (i.e. X) direction, as well as a P-wave velocity increase perpendicular to the lineation in the foliation plane (Y direction) can be expected if there are sufficient pyroxenite layers present within the upper mantle peridotite. In this model, the Y direction corresponds to the strike of the arc front, and abundant layered

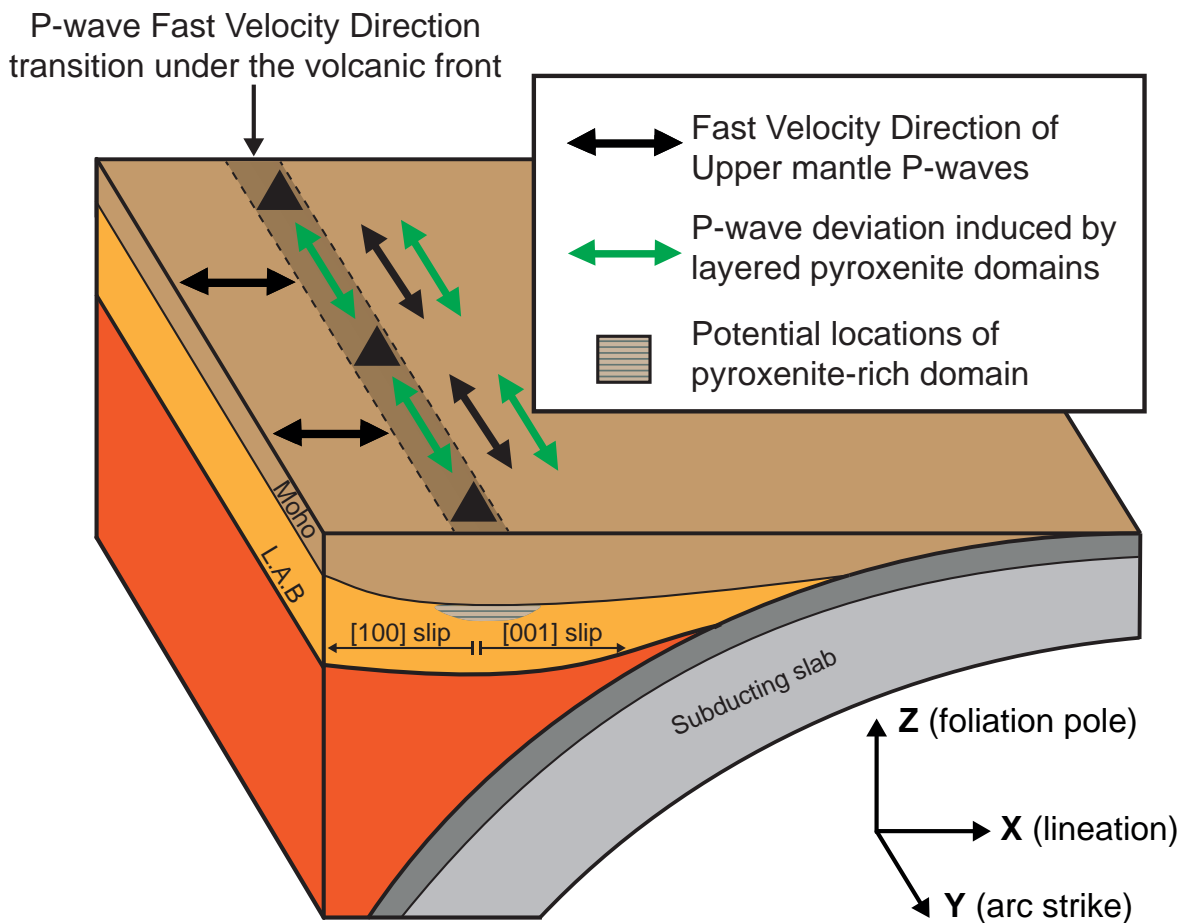


Fig.5.6: Schematic representation of the arc front of a subduction zone, illustrating the effect of pyroxenite layering on the FVD for P waves. The volcanic front coincides with the FVD between trench normal and trench parallel domains, previously solely attributed to the change in olivine slip direction from [100] to [001]. Layered pyroxenites, which are expected to occur in large volumes in the lithospheric arc root (hatched), could significantly contribute to the FVD switch by accelerating waves in the Y direction (green arrows).

pyroxenites occur either in the lithospheric arc root or in the recycled mantle wedge below. The results suggest that layered pyroxenites are responsible for this FVD switch by increasing P-wave velocity parallel to the arc. Large volcanic fronts (Rudnick, 2005) can extend laterally for 200 km. Mantle pyroxenitic layering similar to that of Herbeira along this front, would delay seismic waves travelling perpendicular to the arc strike by more than 0.4 sec, which is measurable.

A velocity drop in every direction is shown for S1 shear waves as well as a complex deviation that does not fit the structural reference frame (Fig.5.4). S2-wave velocity is modelled as decreasing strongly parallel to the lineation (X direction; Fig.5.4). Computation of the differential of AVs indicates a conservation of S-wave anisotropy along the lineation and a decrease in other directions; the direction of maximum deceleration is located near the foliation pole. As a large thickness of layered pyroxenites is most likely produced parallel to the Y and ultimately X directions, pyroxenite-rich domains are not likely to affect body

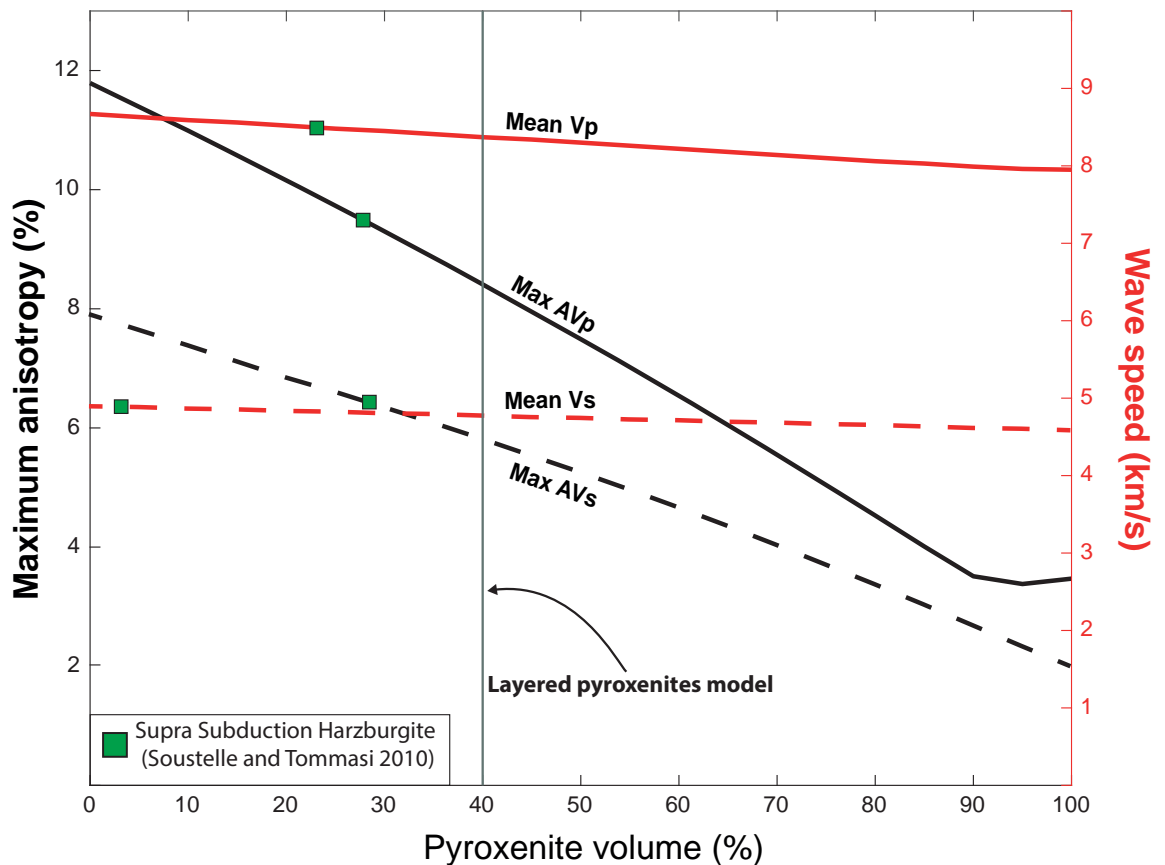


Fig.5.7: Maximum anisotropy and mean speed for P- (solid lines) and S-waves (dashed lines) as functions of the pyroxenite/dunite ratio, assuming constant fabrics throughout the whole compositional spectrum. Green squares mark the values of the reference model for each parameter.

waves in a measurable way, so that AVs is not the most appropriate parameter to identify the presence of layered pyroxenites.

Multiple iterations of this modelling also demonstrate that the mean velocity for P- and S-waves would remain nearly constant for any relative proportion of pyroxenites and dunites while the anisotropy of both P and S waves increases with the proportion of dunite (Fig.5.7). This result suggests that mean wave velocities cannot reliably identify domains of layered pyroxenites, although the anisotropy can. The elastic tensor of a volume with a similar rock-type mix was also computed, but assuming randomly distributed (rather than layered) minerals. The resulting tensor yields very similar seismic properties to that obtained using the Schoenberg and Muir (1989) calculus (Fig.5.7). This indicates that the tensor averaging method of Mainprice et al. (2011) provides a very good first approximation to the seismic properties of a layered pyroxenite-rich domain in the upper mantle.

Seismic signals can be used to identify some of the most important lithological heterogeneities in the upper mantle. This this could be done by tracking: (1) drops in the maximum P- and S-wave anisotropy and (2) anomalous surface-wave delays in both P- and S2-waves. This result suggests that layered pyroxenitic volumes of sufficient dimension may be seismically recognisable in the mantle; this may lead to the identification of paleo-subduction domains infiltrated by mantle fluids, provide a better understanding of the highly debated mass balance of the subduction factory, and pave the way for geophysical observations to help quantify the equally debated contribution of pyroxene-rich lithologies to the genesis of mantle-derived magmas.

5.5 - Testing different fabrics

Mineral CPO, deformational state and seismic properties are linked together and add a layer of complexity when interpreting seismic data. In nature, a variety of textures and CPO intensities for all minerals has been reported, therefore producing different seismic responses. Consequently, restricting the effect of pyroxenites only to the model of Herbeira in its current deformational stage is not a complete approach for more general interpretations. Two more models have to be made:

(1) an “undeformed” model simulating the properties of pyroxenites with only magmatic features, unaffected by plastic deformation (Fig.5.8).

(2) a “poorly oriented” model to simulate pyroxenites crystallizing without magmatic-derived fabrics (Fig.5.9).

As discussed in Chapter 4, the Trinity pyroxenites could be potential “pre-deformation protoliths” to the Cabo Ortegal pyroxenites. Performing modelling using the CPOs of Trinity pyroxenites will give insights on the impact of pyroxenite deformation in a subduction environment on the bulk seismic properties. A model was computed using pyroxenes CPO from sample T3BC4A, a massive pyroxenite with a texture comparable to that of

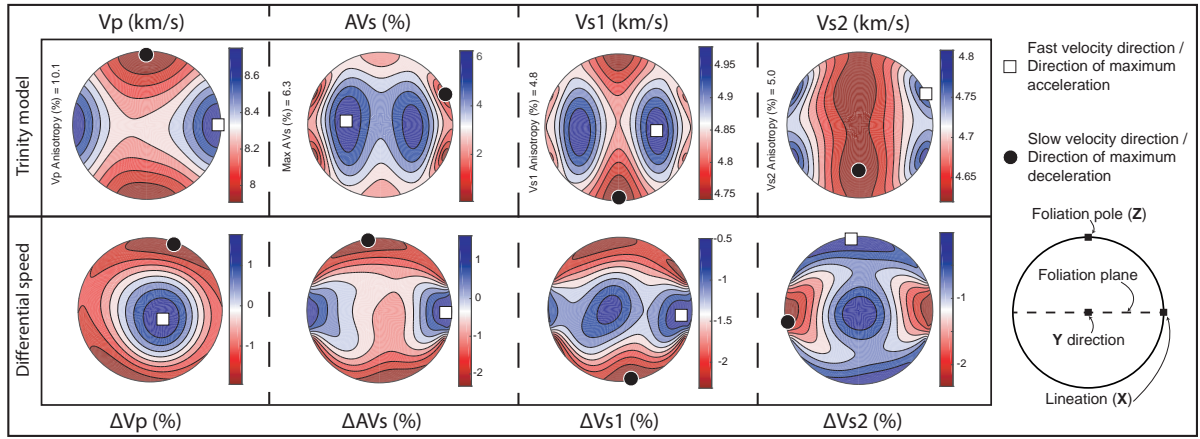


Fig.5.8: Results of the seismic calculations for the Trinity layered model and comparison of the result with a reference supra-subduction harzburgite. Legend is similar to that of Fig.5.4.

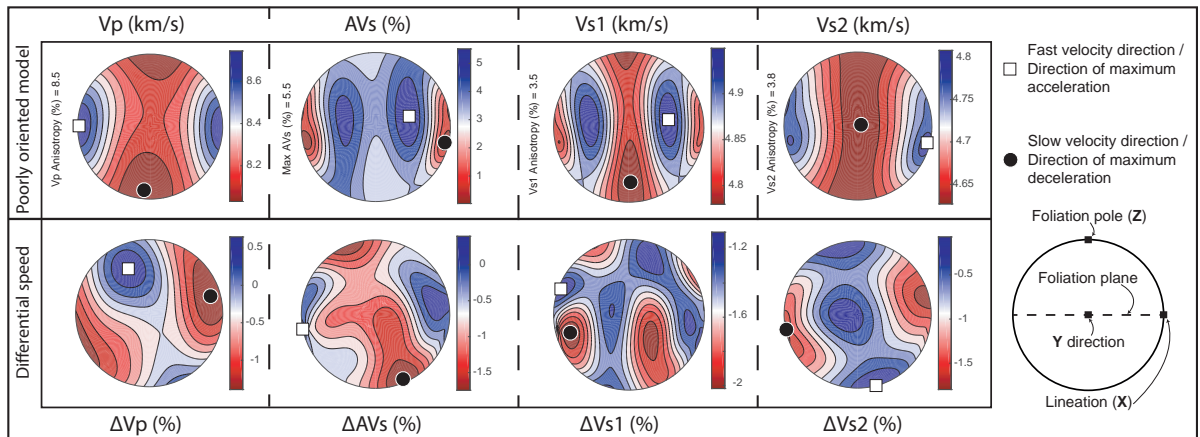


Fig.5.9: Results of the seismic calculations for the poorly-oriented layered model and comparison of the result with a reference supra-subduction harzburgite. Legend is similar to that of Fig.5.4.

a granoblastic sample from the Cabo Ortegal. Results are presented in Fig.5.8. Having pyroxenites with the fabric of Trinity pyroxenites instead of that of Herbeira increases the maximum anisotropy of both Vp and AVs. The deviations to the reference model are similar to that observed in the Herbeira model and appear in greater amplitude for Vp, AVs and Vs2. Contrary to the Herbeira model, the Vs1 deviations fit the structural framework and a clear decrease in the direction vertical to the layering is visible.

For the “poorly oriented” model, cpx and opx fabrics were extracted from *type-1* pyroxenite CO-100 that crystallised following replacive melt-rock interaction and does not show any cumulate trend (Tilhac et al., 2016). The maximum seismic wave anisotropies are similar to that of the Herbeira model. Deviations similar to that of Herbeira are seen for AVs, Vs1 and Vs2. Vp, on the other hand, is slowed along the lineation and is accelerated approximatively in the foliation pole direction with a magnitude similar to that of Herbeira (Fig.5.9).

Combining the three models gives a better constraint on the effect that layered pyroxenites can have on the seismic signal:

(1) P-waves velocity would change at the percentage scale. The deviations will be normal to the flow direction for plastically deformed pyroxenites and pyroxenites that experienced compaction.

(2) AVs will be reduced in the foliation pole direction and accelerated in the lineation direction regardless of the deformational state of the pyroxenite.

(3) Vs1 will be slowed regardless of the pyroxenite CPO; the signal deviations fit the structural reference frame only in the case of a Trinity fabric (i.e. important reduction along the foliation pole direction).

(4) Vs2 has a consistent deviation relative to layered pyroxenite and is slowed with a stronger velocity drop along the lineation direction regardless of the CPO.

5.6 - Testing different abundances

The modelling protocol used in this study requires as inputs only (1) the modal fraction and (2) the mineral fabrics of each phase.

In the previous example, fixed modal compositions were used, based on the example of the Herbeira massif. Another way to work with the data could be to consider pyroxenite fabrics as constant throughout the whole compositional spectrum. This assumption is consistent with the fabrics obtained in the Cabo Ortegal and Trinity pyroxenites (i.e. where no relationship between fabrics and modal abundance was found) but clashes with other results suggesting that the modal abundance of the phases may control the fabric of that phase or other phases (e.g. Jung et al., 2010; Soustelle and Manthilake, 2017).

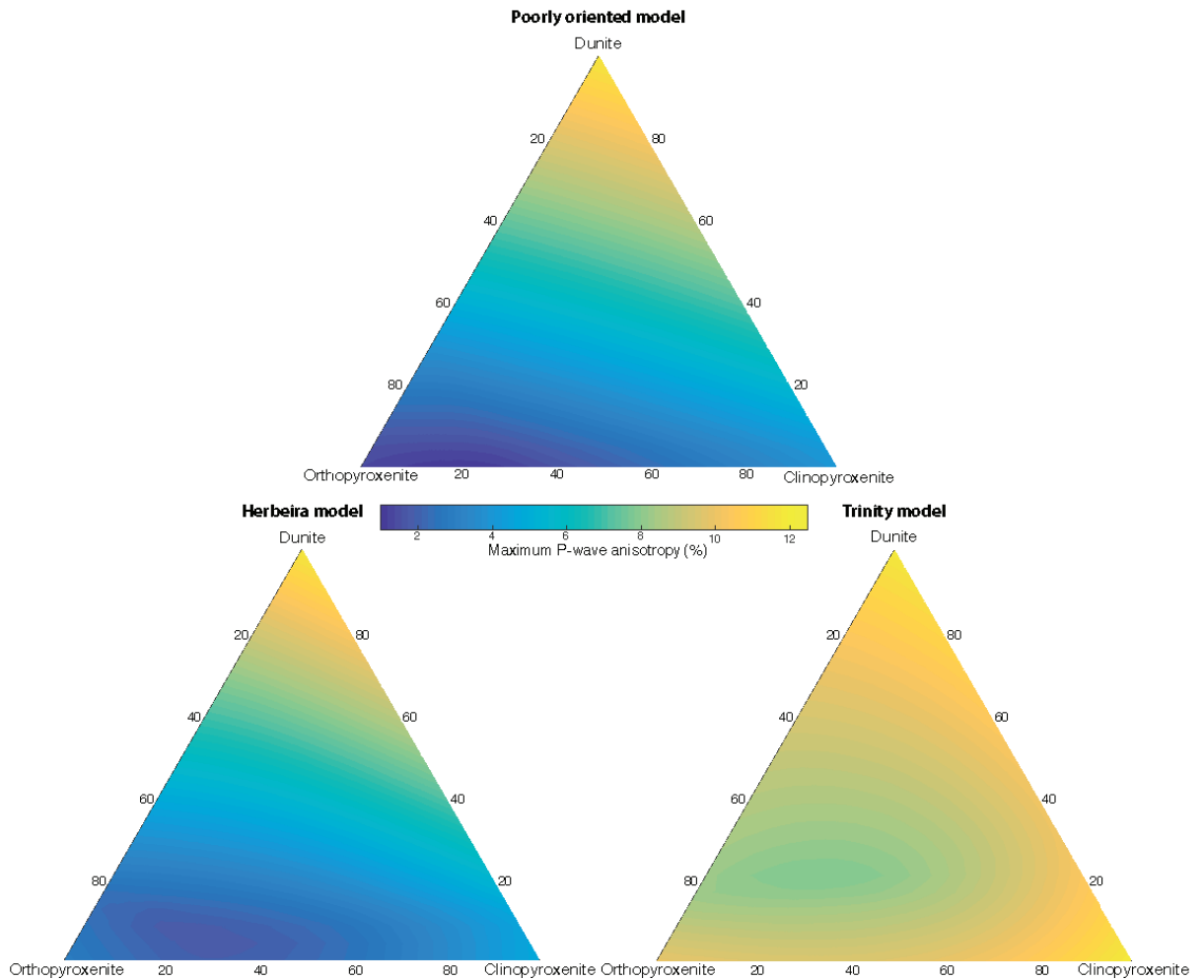


Fig.5.10: Ternary diagram in the Dunite-Clinopyroxenite-Orthopyroxenite system showing the maximum P-wave anisotropy as a function of the modal composition and the fabric used as input. The colour-scale is common to the three models.

Assuming this working hypothesis to be acceptable in the case of a pyroxenite layered medium, the code can be modified to calculate the seismic properties of a layered cake at any position in the compositional spectrum.

For each case described previously (i.e. Herbeira, Trinity and the poorly oriented models), a series of 231 models was computed, covering the entire compositional spectrum. The maximum anisotropy of the P-waves as well as that of S-waves was extracted for each model. The data were plotted on a ternary diagram using the TERNPLOT package developed for Matlab by Carl Sandrock.

Fig.5.10 shows the results of the simulation for the maximum P-wave anisotropy. In the Herbeira and poorly-oriented models, the dunite content clearly conditions the maximum anisotropy of P waves. The cpx content in the pyroxenite layers seems to increase the

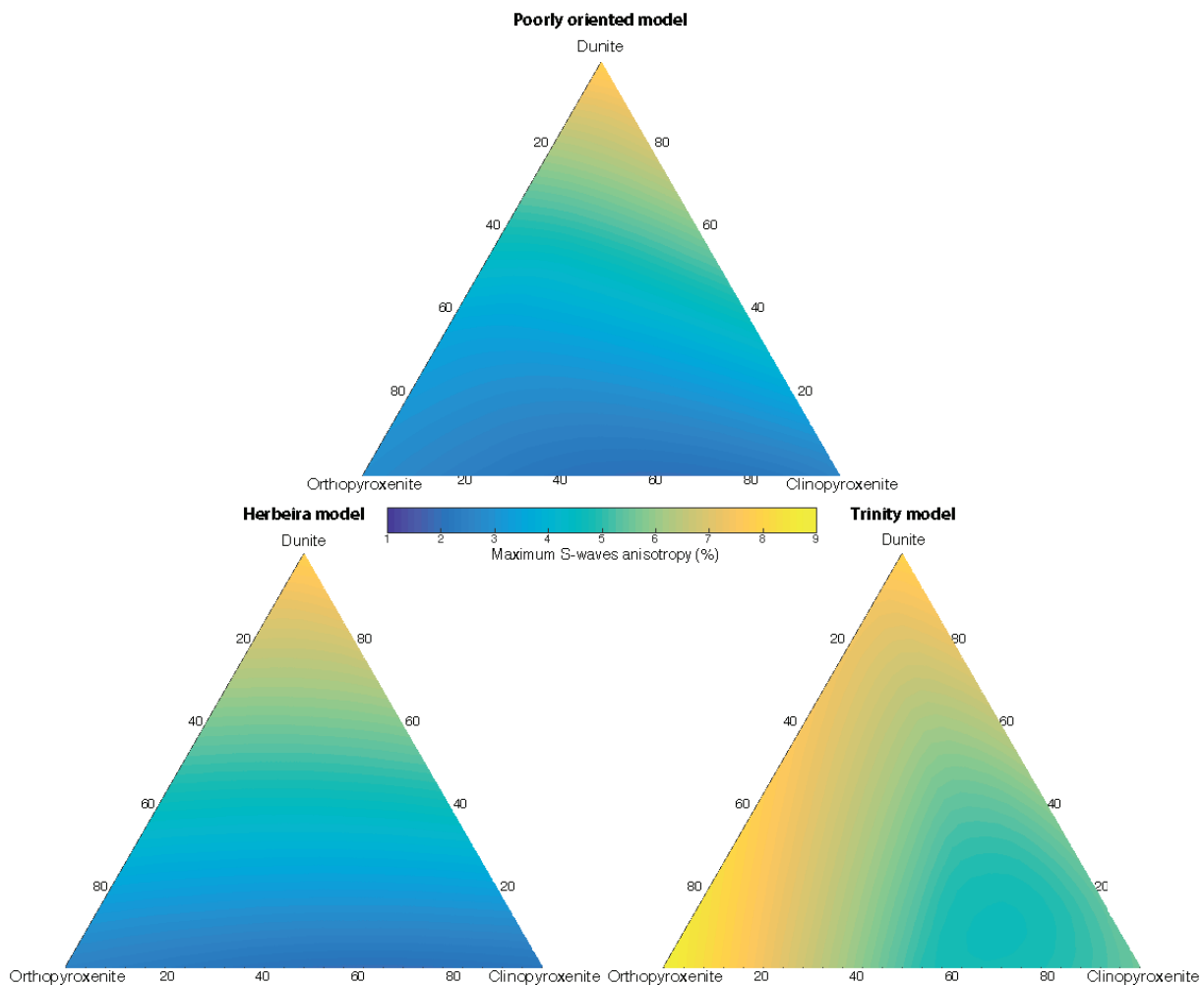


Fig.5.11: Ternary diagram in the Dunite-Clinopyroxenite-Orthopyroxenite system showing the maximum S-wave anisotropy (i.e. AVs) as a function of the modal composition and the fabric used as input. The colour-scale is common to the three models.

maximum anisotropy in both cases and the opx content appears to be correlated with a weaker anisotropy. In the case of Trinity, the maximum anisotropy value is more homogeneous across the compositional spectrum and is consistently higher than 8%. Similar maximum anisotropies are reached at 100% dunite or 100% clinopyroxenite.

AVs display similar trends for the Herbeira and poorly-oriented models and suggest that higher AVs are found with higher dunite content (Fig.5.11). In the case of Trinity, the variation range of AVs throughout the models is narrower and the maximum is reached in the orthopyroxenites and the minimum in the clinopyroxenites.

These models show that the pyroxene fabrics and their relative abundance will have an influence on the bulk rock seismic properties. Interestingly, the Herbeira pyroxenites and “poorly oriented” models result in very similar trends and maximum values, suggesting that plastically deformed pyroxenites or randomly crystallized pyroxenites will have similar seismic responses. According to these models, layered pyroxenites bearing a magmatic fabric similar to that of Trinity pyroxenites will result in greater bulk rock anisotropy for both P- and S-waves whatever the composition.

Summary of Chapter 5

A mechanism to model anisotropic layered media using EBSD data was explored and tested.

The seismic signature of a Herbeira-like domain is close to that of a regular supra- subduction harzburgite but will induce signal deviation only in the anisotropic spectrum.

Different fabrics for the pyroxenites were tested. A poorly oriented pyroxenite will yield seismic properties similar to those of a plastically deformed pyroxenite. Stronger anisotropies for P- and S-waves are found with fabrics resulting from compaction.

The effects due to different relative abundances of pyroxenites and dunite was also tested. This revealed very similar variations for both plastically deformed and poorly-oriented pyroxenites. For a similar composition, compaction-related fabrics will yield the most highly anisotropic seismic properties.

Chapter 6:

Integrated Discussions and Perspectives

In this study, the microstructures of mantle-derived pyroxenites in two contrasted settings were determined. Here the main results are integrated and discuss in a broader context.

Chapter 3 addressed the pyroxenite-rich massif of Herbeira, Cabo Ortegal. The data are consistent with a deformation event in a mantle wedge followed by introduction into a subduction channel. The interpretations suggest that the pyroxenites were plastically deformed, most likely by slip along [001](100) for opx and along [001]{110} and/or [001](100) for cpx. It was concluded that the pyroxenite microstructures preserve the high-temperature history ($>1000^{\circ}\text{C}$) of the samples, as there is no sign of lower-temperature deformation overprint. Cabo Ortegal pyroxenites could therefore be representative of deformed pyroxenites in a relatively shallow mantle wedge (i.e. <1.2 GPa, Tilhac et al., 2016).

Chapter 4 reported on microstructures of pyroxenites from different units of the Trinity Ophiolite. In Trinity, pyroxenites from the outcrops of mantle rocks have similar microstructural behaviour to that of Cabo Ortegal. Most fabrics can be either random or [001](100) for opx, [001]{110} and/or [001](100) for cpx. This would indicate that deformation at a spreading centre (likely back-arc in the case of Trinity) and in a mantle wedge could result in similar fabrics in pyroxenites. Pyroxenites in the cumulates from a mafic-ultramafic intrusion comprising part of the crustal section of the ophiolite show different fabrics, characterized by a strong planar component and a poorly developed lineation. It is concluded that these particular fabrics were acquired by a combination of crystal settling and compaction with a moderate overprint of plastic deformation, if any.

6.1 - On the relative stability of the pyroxenite fabrics

Results from Chapter 3 and 4 suggest that in a shallow upper mantle, pyroxenite fabrics could be similar across a variety of geodynamic contexts (e.g. mantle wedge settings for Cabo Ortegal and slow spreading back-arc basin for Trinity). Fabrics significantly differ from the above only in the case of cumulate pyroxenites forming by crystal settling / compaction, with a weak contribution of sub-solidus deformation (i.e. a strong planar to linear ratio would appear).

In addition, the analysis show that for Cabo Ortegal and Trinity pyroxenites, the fabrics and operating slip systems appear to be unrelated to the mineral mode and to the rock texture. That relative independence of the fabrics from the modal composition within a pyroxenite layer may make pyroxenite a reliable proxy for deformation conditions (i.e. temperature, pressure or water content) and would contrast with peridotite fabrics, which have been shown to be affected by the mineral mode (e.g. Soustelle and Manthilake, 2017).

6.2 - On the development of fabrics in pyroxenites

The interpretations presented in this work allow the inference of two scenarios for the development of pyroxenite fabrics during a deformation event:

(1) Pyroxenites are cumulates and/or experienced compaction: the fabric strength will be reduced over time until a typical plastically-deformed fabric arises. During this process, the fabrics would tend to evolve from girdle to point maximum. This whole process corresponds to the overprinting of the original magmatic fabric by a fabric induced by plastic deformation.

(2) Pyroxenites are replacive and/or did not experience compaction: the fabric is likely to start as poorly oriented and will evolve towards a plastically-deformed fabric. Therefore, strength of the fabric would increase but in a lesser magnitude than in the previous scenario.

In both scenarios, different starting points will converge to a similar state. In nature, as material is more likely to be deformed with increasing time, the plastically-deformed state should largely dominate.

However, a complete understanding of the development of fabrics in pyroxenites requires the characterisation of every possible magmatic fabrics end-members. Besides a planar fabric, a purely linear fabric could be achieved by the injection of a magma in a sill where crystal settling would not be operating because of the limited thickness of the sill. As magmatic fabric are controlled by shape preferred orientation of the minerals (e.g. Launeau, 2004), a linear magmatic fabric should show a strong concentration of the [001] of both cpx and opx (i.e. the elongation direction of a euhedral crystal) aligned with the magmatic flow. This would have similar implications in terms of fabric development in pyroxenites as, [001] is the slip

direction in most cases during plastic deformation. Further investigations of magmatic fabrics in pyroxenites are required to have a complete view of the initial state spectrum.

6.3 - On pyroxenites and shear instabilities

Previous studies showed that the presence of compositional heterogeneities is very likely to facilitate the nucleation of shear instabilities in the upper mantle (e.g. De Bresser et al., 1998; De Bresser et al., 2000; Chen et al., 2001).

In the Cabo Ortegal pyroxenites, the stronger viscosity of the pyroxenite layers relative to the host rock indirectly affects the localisation of deformation. Conversely, in contexts where the viscosity contrast is reversed, pyroxenite layers would nucleate shearing (e.g. Toy et al., 2010). Consequently, the presence of significant amount of pyroxenites in the upper mantle should be taken into account when analysing how shear operates.

Therefore, a pyroxenite-rich, heterogeneous upper mantle is likely to trigger the nucleation of shear zones, favouring subsequent fluid percolation (e.g. *type3* pyroxenites in Cabo Ortegal).

6.4 - On the seismic signature of layered pyroxenites

In chapter 5, that the seismic signature of a pyroxenite-rich domain is demonstrated to be a direct function of the mineral fabrics and consequently is an indirect function of the deformation history. Given that a plastically-deformed fabric is likely to be the most common one in Earth's upper mantle at any given time, the Herbeira model seismic properties may be considered as a robust and representative way to characterise the seismic properties of a pyroxenite-rich domain.

As the microstructure of a pyroxenite-rich domain will evolve with deformation (and time), a change in seismic signature with time could be predicted.

In supra-subduction zones, if delamination and/or mechanical erosion of the arc root are operative, pyroxenite-rich domains are likely to be entrained into asthenosphere from the arc

root, and subsequently experience changes in fabrics that reflect the increasing deformation caused by their introduction into the asthenospheric flow. Assuming a scenario where a melt intrudes a volcanic arc root, crystallises pyroxenites and the arc root is delaminated, the contribution of the pyroxenites to the seismic properties can be integrated over time for two different outcomes:

(1) After crystallization, a stronger anisotropic signature (i.e. Trinity model) would arise under the volcanic arc. During delamination and over time, the contribution would tend towards less anisotropy (Herbeira model). This scenario, corresponding to the progressive deformation of compacted pyroxenites, would imply less and less anisotropic contribution from the pyroxenites to the seismic signal in the mantle wedge along the flow direction.

(2) A weakly anisotropic contribution (i.e. the poorly oriented model) would evolve towards the plastically-deformed model. In this scenario, corresponding to the progressive deformation of replacive or non-compacted pyroxenite, the contribution to the bulk anisotropy would increase slightly following the evolution of the system.

The results of the models are consistent with the positive correlation between the maximum anisotropy and the CPO strength but are counter-intuitive in terms of the deformation-strength relationship. On one side, Trinity pyroxenite microstructures suggest a relatively undeformed material (at least in the solid-state) and that an initial magmatic fabric results in a very strong CPO and therefore strong seismic anisotropy. On the other side, the Herbeira pyroxenites display a strongly deformed texture but no magmatic fabric which results in a lower maximum seismic anisotropy. Assuming that Trinity represents a possible initial state before high solid-state deformation (i.e. Cabo Ortegal pyroxenites) the previously made observations suggest that deformation of pyroxenites may reduce their bulk seismic anisotropy because of the randomisation of the well-defined magmatic fabric during deformation. This phenomenon can be explained by several factors:

(1) In the case of cpx, the complex crystal symmetry leads to the activation of several slip systems that will eventually lead to poorly-oriented fabrics and a low bulk anisotropy.

(2) The most common fabric of plastically deformed opx (i.e. $[001](100)$) does not cause

strong anisotropy. In opx, [001] and [100] have similar wave speeds, and their concentration would induce maximum points having almost similar wave speeds and therefore a rather weak anisotropy. Stronger anisotropy for opx can be reached by concentration of the [010] axis (as in the Trinity model). The difference in the contribution of the opx to the seismic anisotropy between the Cabo Ortegal and Trinity opx can be explained solely by this observation.

(3) For both pyroxenes, the high-temperature deformation mechanisms involve the dynamic recrystallization of strained grains by subgrain rotation and the creation of new grains with a different orientation to their parents; rolling of grains in the matrix will result in a less strongly concentrated ODF on the pole-figure and lead to lower J- and M-indexes in plastically-deformed samples.

6.5 - Further perspectives

This work is a step toward the understanding of the rheology of pyroxenite-rich mantle lithologies and their physical properties. Better constraints on the origin and impact of pyroxenites in the mantle will require further work, including in the following directions.

The collection of microstructural data for other deformed pyroxenites in different geodynamic contexts (e.g. intraplate magmatism or in other ophiolites) would be important if the environment of deformation happens to be the major factor controlling the deformational behaviour of pyroxenites.

A difficulty in studying pyroxenites is that, unlike olivine, pyroxenes have not attracted much interest from experimentalists and geophysicist. More studies on activation of pyroxene slip systems and fabrics as functions of temperature, pressure and water content would be useful to accurately relate microstructural observations to an environment of deformation.

In Cabo Ortegal and Trinity, pyroxenites may contain interstitial melt (amphibole 1 in Cabo Ortegal and the compaction mechanism in Trinity). To model the seismic properties accurately, the effect of that melt needs to be taken into account in the calculation, perhaps using another equivalent medium theory (see Mainprice, 2007). To do that, the geometry of the melt pockets and their volume must be determined. Furthermore, the seismic models

presented here consider only the case of horizontal layering. However, other intrusion geometries (i.e. dykes) can be investigated using the same protocol.

In Trinity, more field work would be required to get the most accurate structural framework possible. This would settle any possible uncertainty on the interpretation of the petrofabrics. A closer investigation of the Bear Creek cumulates with a special emphasis on the pegmatitic segregations and their textural evolution might result in distinctive criteria to differentiate the finer-grained fraction of pegmatitic outbursts from the cumulate massive pyroxenites

Chapter 7:

General Conclusions

The overarching aim of this study is to provide a robust characterisation of the microstructures of pyroxenites and the consequences for their petrophysical properties. In order to understand their textural evolution, natural samples from two contrasting geodynamic contexts were studied.

To achieve the goals of the project, a protocol for processing Electron Back-Scattered Diffraction data was developed using the MTEX toolbox available for Matlab. The script architecture is documented along with the philosophical framework for the processing. The script itself and an example of use are provided.

The resultant new knowledge for microstructures of plastically deformed pyroxenites from the *Cabo Ortegal* provide new data to constrain the geological history of the massif. The new evidence shows that that pyroxenites recorded high-temperature deformation and were preserved from further overprint.

In Cabo Ortegal, the abundance of layered pyroxenites provides a good example for exploring the importance of heterogeneities on the bulk rheology of the mantle. The results showed that the presence of pyroxenites can indirectly localize shearing and subsequently create preferred pathways for fluid percolation.

In the Trinity ophiolite, the microstructures of peridotites and pyroxenites from the mantle section provide robust constraints on the conditions of deformation of the massif. The Trinity mantle section is characterised by high-temperature plastic deformation, generally in the presence of melt. This is consistent with the spectacular melt/rock interaction features visible in the field. The crustal section of the ophiolite allows the investigation of a pre-deformation texture of pyroxenite. The microstructures of the Bear Creek cumulates are described and related to compaction and crystal settling, in contrast to the plastically-deformed pyroxenites of the Cabo Ortegal.

Using MTEX and Matlab, the observational and microstructural data from the two localities enabled modelling of the seismic properties of a pyroxenite-rich domain. A new protocol was created by integrating an equivalent-medium theory with a widely used modelling technique. The models showed that a layered pyroxenite-rich domain in the upper mantle will produce

a distinctive signal deviation in seismic anisotropy relative to a typical supra-subduction material. To have a broader approach to the problem, pyroxenite-rich domains were modelled using fabrics from plastically deformed pyroxenites, undeformed pyroxenites and poorly oriented pyroxenites, to examine the effect of the relative abundance of different types of pyroxenite and host (dunite) rock. We found that a plastically-deformed pyroxenite yields results similar to those for a poorly-oriented pyroxenite while an undeformed pyroxenite results in relatively stronger anisotropy of seismic wave speeds.

References

- Ábalos, B., Azcarrage, J., Gil Ibarguchi, J. I., Mendia, M. S., and Santos Zalduegui, J. S., 1996, Flow Stress, strain rate and effective viscosity evaluation in a high-pressure metamorphic nappe (Cabo Ortegal, Spain): *Journal of Metamorphic Geology*, **v. 14**, no. 2, p. 227-248.
- Ábalos, B., Fountain, D. M., Ibarguchi, J. I. G., and Puelles, P., 2011, Eclogite as a seismic marker in subduction channels: Seismic velocities, anisotropy, and petrofabric of Cabo Ortegal eclogite tectonites (Spain): *Geological Society of America Bulletin*, **v. 123**, no. 3-4, p. 439-456.
- Ábalos, B., Puelles, P., and Gil Ibarguchi, J. I., 2003, Structural assemblage of high-pressure mantle and crustal rocks in a subduction channel (Cabo Ortegal, NW Spain): *Tectonics*, **v. 22**, no. 2, p. 1006.
- Abily, B., and Ceuleneer, G., 2013, The dunitic mantle-crust transition zone in the Oman ophiolite: Residue of melt-rock interaction, cumulates from high-MgO melts, or both?: *Geology*, **v. 41**, no. 1, p. 67-70.
- Achenbach, K. L., Cheadle, M. J., Faul, U., Kelemen, P., and Swapp, S., 2011, Lattice-preferred orientation and microstructure of peridotites from ODP Hole 1274A (15°39'N), Mid-Atlantic Ridge: Testing models of mantle upwelling and tectonic exhumation: *Earth and Planetary Science Letters*, **v. 301**, no. 1-2, p. 199-212.
- Agee, C. B., 1993, Petrology of the Mantle Transition Zone: *Annual Review of Earth and Planetary Sciences*, **v. 21**, no. 1, p. 19-41.
- Albert, R., Arenas, R., Gerdes, A., Sánchez Martínez, S., Fernández-Suárez, J., and Fuenlabrada, J. M., 2014, Provenance of the Variscan Upper Allochthon (Cabo Ortegal Complex, NW Iberian Massif): *Gondwana Research*, **v. 28**, no. 4, p. 1434-1448.
- Allègre, C. J., and Turcotte, D. L., 1986, Implications of a two-component marble-cake mantle: *Nature*, **v. 323**, no. 6084, p. 123-127.
- Almqvist, B. S. G., Burg, J. P., Berger, J., and Burlini, L., 2013, Seismic properties of the Kohistan oceanic arc root: Insights from laboratory measurements and thermodynamic modeling: *Geochemistry, Geophysics, Geosystems*, **v. 14**, no. 6, p. 1819-1841.
- Amiguet, E., 2009, Déformation expérimentale de diopside dans les conditions de pression et température du manteau supérieur [PhD: Université des Sciences et Technologies de Lille].

- Amiguet, E., Cordier, P., and Raterron, P., 2010, Deformation of diopside single crystals at mantle pressure. TEM characterization of dislocation microstructures: *European Journal of Mineralogy*, **v. 22**, no. 2, p. 181-187.
- Arenas, R., Díez Fernández, R., Sánchez Martínez, S., Gerdes, A., Fernández-Suárez, J., and Albert, R., 2014, Two-stage collision: Exploring the birth of Pangea in the Variscan terranes: *Gondwana Research*, **v. 25**, no. 2, p. 756-763.
- Avé Lallemant, H. G., 1978, Experimental deformation of diopside and websterite: *Tectonophysics*, **v. 48**, no. 1–2, p. 1-27.
- Bachmann, F., Hielscher, R., Jupp, P. E., Pantleon, W., Schaeben, H., and Wegert, E., 2010a, Inferential statistics of electron backscatter diffraction data from within individual crystalline grains: *Journal of Applied Crystallography*, **v. 43**, no. 6, p. 1338-1355.
- Bachmann, F., Hielscher, R., and Schaeben, H., 2010b, Texture Analysis with MTEX – Free and Open Source Software Toolbox: *Solid State Phenomena*, **v. 160**, p. 63-68.
- , 2011, Grain detection from 2d and 3d EBSD data—Specification of the MTEX algorithm: *Ultramicroscopy*, **v. 111**, no. 12, p. 1720-1733.
- Backus, G. E., 1962, Long-wave elastic anisotropy produced by horizontal layering: *Journal of Geophysical Research*, **v. 67**, no. 11, p. 4427-4440.
- Bascou, J., Tommasi, A., and Mainprice, D., 2002, Plastic deformation and development of clinopyroxene lattice preferred orientations in eclogites: *Journal of Structural Geology*, **v. 24**, no. 8, p. 1357-1368.
- Beaumont, C., Ellis, S., and Pfiffner, A., 1999, Dynamics of sediment subduction-accretion at convergent margins: Short-term modes, long-term deformation, and tectonic implications: *Journal of Geophysical Research: Solid Earth*, **v. 104**, no. B8, p. 17573-17601.
- Benn, K., and Allard, B., 1989, Preferred Mineral Orientations Related to Magmatic Flow in Ophiolite Layered Gabbros: *Journal of Petrology*, **v. 30**, no. 4, p. 925-946.
- Berger, A., and Stünitz, H., 1996, Deformation mechanisms and reaction of hornblende: examples from the Bergell tonalite (Central Alps): *Tectonophysics*, **v. 257**, no. 2–4, p. 149-174.
- Biedermann, A. R., Pettke, T., Reusser, E., and Hirt, A. M., 2014, Anisotropy of magnetic susceptibility in natural olivine single crystals: *Geochemistry, Geophysics, Geosystems*, **v. 15**, no. 7, p. 3051-3065.

- Biermann, C., and Van Roermund, H. L. M., 1983, Defect structures in naturally deformed clinoamphiboles—a TEM study: *Tectonophysics*, **v. 95**, no. 3–4, p. 267-278.
- Bodinier, J. L., Guiraud, M., Fabriés, J., Dostal, J., and Dupuy, C., 1987, Petrogenesis of layered pyroxenites from the Lherz, Freychinède and Prades ultramafic bodies (Ariège, French Pyrénées): *Geochimica et Cosmochimica Acta*, **v. 51**, no. 2, p. 279-290.
- Boorman, S., Boudreau, A., and Kruger, F. J., 2004, The Lower Zone–Critical Zone Transition of the Bushveld Complex: a Quantitative Textural Study: *Journal of Petrology*, **v. 45**, no. 6, p. 1209-1235.
- Bouchez, J. L., Lister, G. S., and Nicolas, A., 1983, Fabric asymmetry and shear sense in movement zones: *Geologische Rundschau*, **v. 72**, no. 2, p. 401-419.
- Boudier, F., Le Sueur, E., and Nicolas, A., 1989, Structure of an atypical ophiolite: The Trinity complex, eastern Klamath Mountains, California: *Geological Society of America Bulletin*, **v. 101**, no. 6, p. 820-833.
- Boudier, F., and Nicolas, A., 1985, Harzburgite and lherzolite subtypes in ophiolitic and oceanic environments: *Earth and Planetary Science Letters*, **v. 76**, no. 1–2, p. 84-92.
- Braun, M. G., and Kelemen, P. B., 2002, Dunite distribution in the Oman Ophiolite: Implications for melt flux through porous dunite conduits: *Geochemistry, Geophysics, Geosystems*, **v. 3**, no. 11, p. 1-21.
- Brouxel, M., and Lapierre, H., 1988, Geochemical study of an early Paleozoic island-arc-back-arc basin system. Part 1: The Trinity Ophiolite (northern California): *Geological Society of America Bulletin*, **v. 100**, no. 7, p. 1111-1119.
- Brouxel, M., Lapierre, H., Michard, A., and Albarède, F., 1988, Geochemical study of an early Paleozoic island-arc-back-arc basin system. Part 2: Eastern Klamath, early to middle Paleozoic island-arc volcanic rocks (northern California): *Geological Society of America Bulletin*, **v. 100**, no. 7, p. 1120-1130.
- Bunge, H. J., 1982, Texture analysis in materials science: mathematical methods, Elsevier.
- Carcione, J. M., Picotti, S., Cavallini, F., and Santos, J. E., 2012, Numerical test of the Schoenberg-Muir theory: *Geophysics*, **v. 77**, no. 2, p. C27-C35.
- Carter, N. L., and Avé Lallemant, H. G., 1970, High Temperature Flow of Dunite and Peridotite: *Geological Society of America Bulletin*, **v. 81**, no. 8, p. 2181-2202.

- Ceuleneer, G., and Le Sueur, E., 2008, The Trinity ophiolite (California): the strange association of fertile mantle peridotite with ultra-depleted crustal cumulates: *Bulletin de la Societe Geologique de France*, **v. 179**, no. 5, p. 503-518.
- Chen, S., O'Reilly, S. Y., Zhou, X., Griffin, W. L., Zhang, G., Sun, M., Feng, J., and Zhang, M., 2001, Thermal and petrological structure of the lithosphere beneath Hannuoba, Sino-Korean Craton, China: evidence from xenoliths: *Lithos*, **v. 56**, no. 4, p. 267-301.
- Christensen, N. I., and Lundquist, S. M., 1982, Pyroxene orientation within the upper mantle: *Geological Society of America Bulletin*, **v. 93**, no. 4, p. 279-288.
- Couvy, H., Frost, D. J., Heidelbach, F., Nyilas, K., Ungár, T., Mackwell, S., and Cordier, P., 2004, Shear deformation experiments of forsterite at 11 GPa - 1400°C in the multianvil apparatus: *European Journal of Mineralogy*, **v. 16**, no. 6, p. 877-889.
- De Bresser, J., Ter Heege, J., and Spiers, C., 2000, Grain size reduction by dynamic recrystallization: can it result in major rheological weakening?: *International Journal of Earth Sciences*, **v. 90**, no. 1, p. 28-45.
- De Bresser, J. H. P., Peach, C. J., Reijs, J. P. J., and Spiers, C. J., 1998, On dynamic recrystallization during solid state flow: Effects of stress and temperature: *Geophysical Research Letters*, **v. 25**, no. 18, p. 3457-3460.
- DeBari, S. M., and Coleman, R. G., 1989, Examination of the deep levels of an island arc: Evidence from the Tonsina Ultramafic-Mafic Assemblage, Tonsina, Alaska: *Journal of Geophysical Research: Solid Earth*, **v. 94**, no. B4, p. 4373-4391.
- Díaz Aspiroz, M., Lloyd, G. E., and Fernández, C., 2007, Development of lattice preferred orientation in clinoamphiboles deformed under low-pressure metamorphic conditions. A SEM/EBSD study of metabasites from the Aracena metamorphic belt (SW Spain): *Journal of Structural Geology*, **v. 29**, no. 4, p. 629-645.
- Dollinger, G., and Blacic, J. D., 1975, Deformation mechanisms in experimentally and naturally deformed amphiboles: *Earth and Planetary Science Letters*, **v. 26**, no. 3, p. 409-416.
- Downes, H., 2007, Origin and significance of spinel and garnet pyroxenites in the shallow lithospheric mantle: Ultramafic massifs in orogenic belts in Western Europe and NW Africa: *Lithos*, **v. 99**, no. 1-2, p. 1-24.

- Dygert, N., Liang, Y., and Kelemen, P. B., 2016, Formation of Plagioclase Lherzolite and Associated Dunite–Harzburgite–Lherzolite Sequences by Multiple Episodes of Melt Percolation and Melt–Rock Reaction: an Example from the Trinity Ophiolite, California, USA: *Journal of Petrology*, **v. 57**, no. 4, p. 815-838.
- Feinberg, J. M., Wenk, H.-R., Scott, G. R., and Renne, P. R., 2006, Preferred orientation and anisotropy of seismic and magnetic properties in gabbro-norites from the Bushveld layered intrusion: *Tectonophysics*, **v. 420**, no. 3-4, p. 345-356.
- Frets, E., Tommasi, A., Garrido, C. J., Padrón-Navarta, J. A., Amri, I., and Targuisti, K., 2012, Deformation processes and rheology of pyroxenites under lithospheric mantle conditions: *Journal of Structural Geology*, **v. 39**, no. 0, p. 138-157.
- Garrido, C. J., Bodinier, J.-L., Dhuime, B., Bosch, D., Chanefo, I., Bruguier, O., Hussain, S. S., Dawood, H., and Burg, J.-P., 2007, Origin of the island arc Moho transition zone via melt-rock reaction and its implications for intracrustal differentiation of island arcs: Evidence from the Jijal complex (Kohistan complex, northern Pakistan): *Geology*, **v. 35**, no. 8, p. 683.
- Gerya, T. V., and Stöckhert, B., 2002, Exhumation rates of high pressure metamorphic rocks in subduction channels: The effect of Rheology: *Geophysical Research Letters*, **v. 29**, no. 8, p. 102-101-102-104.
- Gerya, T. V., Stöckhert, B., and Perchuk, A. L., 2002, Exhumation of high-pressure metamorphic rocks in a subduction channel: A numerical simulation: *Tectonics*, **v. 21**, no. 6, p. 1056.
- Getsinger, A. J., and Hirth, G., 2014, Amphibole fabric formation during diffusion creep and the rheology of shear zones: *Geology*, **v. 42**, no. 6, p. 535-538.
- Gil Ibarguchi, J. I., Mendia, M., Girardeau, J., and Peucat, J. J., 1990, Petrology of eclogites and clinopyroxene-garnet metabasites from the Cabo Ortegal Complex (northwestern Spain): *Lithos*, **v. 25**, no. 1–3, p. 133-162.
- Girardeau, J., and Gil Ibarguchi, J. I., 1991, Pyroxenite-Rich Peridotites of the Cabo Ortegal Complex (Northwestern Spain): Evidence for Large-Scale Upper-Mantle Heterogeneity: *Journal of Petrology*, **v. Special_Volume**, no. 2, p. 135-154.
- Girardeau, J., Gil Ibarguchi, J. I., and Ben Jamaa, N., 1990, Les peridotites et pyroxenites du complexe catazonal du Cabo Ortegal.
- Girardeau, J., Ibarguchi, J. I. G., and Jamaa, N. B., 1989, Evidence for a Heterogeneous Upper Mantle in the Cabo Ortegal Complex, Spain: *Science*, **v. 245**, no. 4923, p. 1231-1233.

- Girardeau, J., and Mercier, J. C. C., 1988, Petrology and texture of the ultramafic rocks of the Xigaze ophiolite (Tibet): constraints for mantle structure beneath slow-spreading ridges: *Tectonophysics*, **v. 147**, no. 1–2, p. 33-58.
- Gruau, G., Lecuyer, C., Bernard-Griffiths, J., and Morin, N., 1991, Origin and Petrogenesis of the Trinity Ophiolite Complex (California): New Constraints from REE and Nd Isotope Data: *Journal of Petrology*, **v. Special_Volume**, no. 2, p. 229-242.
- Hamilton, W., 1969, Mesozoic California and the Underflow of Pacific Mantle: *Geological Society of America Bulletin*, **v. 80**, no. 12, p. 2409-2430.
- Helffrich, G. R., and Wood, B. J., 2001, The Earth's mantle: *Nature*, **v. 412**, no. 6846, p. 501-507.
- Helmstaedt, H., Anderson, O. L., and Gavasci, A. T., 1972, Petrofabric studies of eclogite, spinel-Websterite, and spinel-lherzolite Xenoliths from kimberlite-bearing breccia pipes in southeastern Utah and northeastern Arizona: *Journal of Geophysical Research*, **v. 77**, no. 23, p. 4350-4365.
- Henry, H., Tilhac, R., Griffin, W. L., O'Reilly, S. Y., Satsukawa, T., Kaczmarek, M.-A., Grégoire, M., and Ceuleneer, G., 2017, Deformation of mantle pyroxenites provides clues to geodynamic processes in subduction zones: Case study of the Cabo Ortegal Complex, Spain: *Earth and Planetary Science Letters*, **v. 472**, p. 174-185.
- Higgins, M. D., 1998, Origin of Anorthosite by Textural Coarsening: Quantitative Measurements of a Natural Sequence of Textural Development: *Journal of Petrology*, **v. 39**, no. 7, p. 1307-1323.
- , 2015, Quantitative Textural Analysis of Rocks in Layered Mafic Intrusions, in Charlier, B., Namur, O., Latypov, R., and Tegner, C., eds., *Layered Intrusions*: Dordrecht, Springer Netherlands, p. 153-181.
- Holtzman, B., Kohlstedt, D., Zimmerman, M., Heidelbach, F., Hiraga, T., and Hustoft, J., 2003, Melt segregation and strain partitioning: implications for seismic anisotropy and mantle flow: *Science*, **v. 301**, no. 5637, p. 1227-1230.
- Irwin, W. P., 1966, Geology of the Klamath Mountains province: *Geology of northern California: California Division of Mines and Geology Bulletin*, **v. 190**, p. 19-38.
- Irwin, W. P., and Mankinen, E. A., 1998, Rotational and accretionary evolution of the Klamath Mountains, California and Oregon, from Devonian to present time, The Survey.
- Ismail, W. B., and Mainprice, D., 1998, An olivine fabric database: an overview of upper mantle fabrics and seismic anisotropy: *Tectonophysics*, **v. 296**, no. 1–2, p. 145-157.

- Jacobsen, S. B., Quick, J. E., and Wasserburg, G. J., 1984, A Nd and Sr isotopic study of the Trinity peridotite; implications for mantle evolution: *Earth and Planetary Science Letters*, **v. 68**, no. 3, p. 361-378.
- Jagoutz, O., and Kelemen, P. B., 2015, Role of Arc Processes in the Formation of Continental Crust: *Annual Review of Earth and Planetary Sciences*, **v. 43**, no. 1, p. 363-404.
- Jamaa, N. B., 1988, Les peridotites de bay-of-islands (terre neuve) et de cap ortegal (espagne): approche petro-structurale.
- Jung, H., and Karato, S. I., 2001, Water-Induced Fabric Transitions in Olivine: *Science*, **v. 293**, no. 5534, p. 1460-1463.
- Jung, H., Mo, W., and Green, H. W., 2009, Upper mantle seismic anisotropy resulting from pressure-induced slip transition in olivine: *Nature Geosci*, **v. 2**, no. 1, p. 73-77.
- Jung, H., Park, M., Jung, S., and Lee, J., 2010, Lattice preferred orientation, water content, and seismic anisotropy of orthopyroxene: *Journal of Earth Science*, **v. 21**, no. 5, p. 555-568.
- Karato, S.-I., and Li, P., 1992, Diffusion creep in perovskite: implications for the rheology of the lower mantle: *Science*, **v. 255**, no. 5049, p. 1238-1240.
- Katayama, I., Jung, H., and Karato, S.-i., 2004, New type of olivine fabric from deformation experiments at modest water content and low stress: *Geology*, **v. 32**, no. 12, p. 1045.
- Khan, M. A., Jan, M. Q., and Weaver, B. L., 1993, Evolution of the lower arc crust in Kohistan, N. Pakistan: temporal arc magmatism through early, mature and intra-arc rift stages: *Geological Society, London, Special Publications*, **v. 74**, no. 1, p. 123-138.
- Khan, M. A., Jan, M. Q., Windley, B. F., Tarney, J., and Thirlwall, M. F., 1989, The Chilas Mafic-Ultramafic Igneous Complex; The root of the Kohistan Island Arc in the Himalaya of northern Pakistan: *Geological Society of America Special Papers*, **v. 232**, p. 75-94.
- Kirby, S. H., and Kronenberg, A. K., 1984, Deformation of clinopyroxenite: Evidence for a transition in flow mechanisms and semibrittle behavior: *Journal of Geophysical Research: Solid Earth*, **v. 89**, no. B5, p. 3177-3192.
- Kneller, E. A., van Keken, P. E., Karato, S.-i., and Park, J., 2005, B-type olivine fabric in the mantle wedge: Insights from high-resolution non-Newtonian subduction zone models: *Earth and Planetary Science Letters*, **v. 237**, no. 3-4, p. 781-797.
- Ko, B., and Jung, H., 2015, Crystal preferred orientation of an amphibole experimentally deformed by simple shear: *Nature Communication*, **v. 6**.

- Kohlstedt, D. L., and Holtzman, B. K., 2009, Shearing Melt Out of the Earth: An Experimentalist's Perspective on the Influence of Deformation on Melt Extraction: *Annual Review of Earth and Planetary Sciences*, **v. 37**, no. 1, p. 561-593.
- Kornprobst, J., 1969, High temperature, high pressure alpine-type peridotite and associated pyroxenites (with or without garnet) from Beni Bouchera (Morocco): *Contributions to Mineralogy and Petrology*, **v. 23**, no. 4, p. 283-322.
- Lambart, S., Laporte, D., Provost, A., and Schiano, P., 2012, Fate of Pyroxenite-derived Melts in the Peridotitic Mantle: Thermodynamic and Experimental Constraints: *Journal of Petrology*, **v. 53**, no. 3, p. 451-476.
- Lanphere, M. A., Irwin, W. P., and Hotz, P. E., 1968, Isotopic Age of the Nevadan Orogeny and Older Plutonic and Metamorphic Events in the Klamath Mountains, California: *Geological Society of America Bulletin*, **v. 79**, no. 8, p. 1027-1052.
- Launeau, P., 2004, Evidence of magmatic flow by 2-D image analysis of 3-D shape preferred orientation distributions: *Bulletin de la Société Géologique de France*, **v. 175**, no. 4, p. 331-350.
- Le Sueur, E., Boudier, F., Cannat, M., Ceuleneer, G., and Nicolas, A., 1984, The Trinity mafic-ultramafic complex: first results of the structural study of an untypical ophiolite: *Ophioliti*, **v. 9**, p. 487-498.
- Lenoir, X., Garrido, C. J., Bodinier, J.-L., Dautria, J.-M., and Gervilla, F., 2001, The Recrystallization Front of the Ronda Peridotite: Evidence for Melting and Thermal Erosion of Subcontinental Lithospheric Mantle beneath the Alboran Basin: *Journal of Petrology*, **v. 42**, no. 1, p. 141-158.
- Lindsley-Griffin, N., 1977, The Trinity ophiolite, Klamath Mountains, California: *Oregon Department of Geology and Mineral Industries Bulletin*, **v. 95**, p. 107-120.
- Lipman, P. W., 1964, Structure and origin of an ultramafic pluton in the Klamath Mountains, California: *American Journal of Science*, **v. 262**, no. 2, p. 199-222.
- Llana-Fúnez, S., Marcos, A., Galán, G., and Fernández, F. J., 2004, Tectonic thinning of a crust slice at high pressure and high temperature by ductile-slab breakoff (Cabo Ortegal Complex, northwest Spain): *Geology*, **v. 32**, no. 5, p. 453.
- Mainprice, D., 1990, A FORTRAN program to calculate seismic anisotropy from the lattice preferred orientation of minerals: *Computers & Geosciences*, **v. 16**, no. 3, p. 385-393.
- Mainprice, D., 2007, Seismic anisotropy of the deep Earth from a mineral and rock physics perspective, *Treatise in Geophysics-Volume 2 Mineral Physics*, p. 437-492.

- Mainprice, D., Bachmann, F., Hielscher, R., and Schaeben, H., 2015, Descriptive tools for the analysis of texture projects with large datasets using MTEX: strength, symmetry and components: *Geological Society, London, Special Publications*, **v. 409**, no. 1, p. 251-271.
- Mainprice, D., Barruol, G., and Ismaïl, W. B., 2013, The Seismic Anisotropy of the Earth's Mantle: from Single Crystal to Polycrystal, *Earth's Deep Interior: Mineral Physics and Tomography From the Atomic to the Global Scale*, American Geophysical Union, p. 237-264.
- Mainprice, D., Hielscher, R., and Schaeben, H., 2011, Calculating anisotropic physical properties from texture data using the MTEX open-source package: *Geological Society, London, Special Publications*, **v. 360**, no. 1, p. 175-192.
- Mainprice, D., Tommasi, A., Couvy, H., Cordier, P., and Frost, D. J., 2005, Pressure sensitivity of olivine slip systems and seismic anisotropy of Earth's upper mantle: *Nature*, **v. 433**, no. 7027, p. 731-733.
- Mankinen, E. A., Lindsley-Griffin, N., and Griffin, J. R., 2002, Concordant paleolatitudes for Neoproterozoic ophiolitic rocks of the Trinity Complex, Klamath Mountains, California: *Journal of Geophysical Research: Solid Earth*, **v. 107**, no. B10, p. EPM 11-11-EPM 11-18.
- Manthilake, M. A. G. M., Miyajima, N., Heidelbach, F., Soustelle, V., and Frost, D. J., 2013, The effect of aluminum and water on the development of deformation fabrics of orthopyroxene: *Contributions to Mineralogy and Petrology*, **v. 165**, no. 3, p. 495-505.
- Martínez Catalán, J. R., Arenas, R., Abati, J., Martínez, S. S., García, F. D., Suárez, J. F., Cuadra, P. G., Castiñeiras, P., Barreiro, J. G., Montes, A. D., Clavijo, E. G., Pascual, F. J. R., Andonaegui, P., Jeffries, T. E., Alcock, J. E., Fernández, R. D., and Carmona, A. L., 2009, A rootless suture and the loss of the roots of a mountain chain: The Variscan belt of NW Iberia: *Comptes Rendus Geoscience*, **v. 341**, no. 2-3, p. 114-126.
- Martínez Catalán, J. R., Arenas, R., Díaz García, F., Rubio Pascual, F. J., Abati, J., and Marquínez, J., 1996, Variscan exhumation of a subducted Paleozoic continental margin: The basal units of the Ordenes Complex, Galicia, NW Spain: *Tectonics*, **v. 15**, no. 1, p. 106-121.
- Matzen, A. K., Wood, B. J., Baker, M. B., and Stolper, E. M., 2017, The roles of pyroxenite and peridotite in the mantle sources of oceanic basalts: *Nature Geoscience*, **v. 10**, no. 7, p. 530-535.

- Mercier, J.-C. C., and Nicolas, A., 1975, Textures and Fabrics of Upper-Mantle Peridotites as Illustrated by Xenoliths from Basalts: *Journal of Petrology*, **v. 16**, no. 2, p. 454-487.
- Michibayashi, K., and Mainprice, D., 2004, The Role of Pre-existing Mechanical Anisotropy on Shear Zone Development within Oceanic Mantle Lithosphere: an Example from the Oman Ophiolite: *Journal of Petrology*, **v. 45**, no. 2, p. 405-414.
- Michibayashi, K., and Oohara, T., 2013, Olivine fabric evolution in a hydrated ductile shear zone at the Moho Transition Zone, Oman Ophiolite: *Earth and Planetary Science Letters*, **v. 377-378**, p. 299-310.
- Miyazaki, T., Sueyoshi, K., and Hiraga, T., 2013, Olivine crystals align during diffusion creep of Earth's upper mantle: *Nature*, **v. 502**, no. 7471, p. 321-326.
- Morimoto, N., 1988, Nomenclature of Pyroxenes: *Mineralogy and Petrology*, **v. 39**, no. 1, p. 55-76.
- Müntener, O., and Ulmer, P., 2006, Experimentally derived high-pressure cumulates from hydrous arc magmas and consequences for the seismic velocity structure of lower arc crust: *Geophysical Research Letters*, **v. 33**, no. 21.
- Muramoto, M., Michibayashi, K., Ando, J. I., and Kagi, H., 2011, Rheological contrast between garnet and clinopyroxene in the mantle wedge: An example from Higashi-akaishi peridotite mass, SW Japan: *Physics of the Earth and Planetary Interiors*, **v. 184**, no. 1-2, p. 14-33.
- Nakajima, J., Shimizu, J., Hori, S., and Hasegawa, A., 2006, Shear-wave splitting beneath the southwestern Kurile arc and northeastern Japan arc: A new insight into mantle return flow: *Geophysical Research Letters*, **v. 33**, no. 5, p. L05305.
- Nicolas, A., and Christensen, N. I., 1987, Formation of Anisotropy in Upper Mantle Peridotites - A Review: *Composition, structure and dynamics of the lithosphere-asthenosphere system*, p. 111-123.
- O'Reilly, S. Y., and Griffin, W. L., 2013, Moho vs crust-mantle boundary: Evolution of an idea: *Tectonophysics*, **v. 609**, no. 0, p. 535-546.
- Ohuchi, T., Kawazoe, T., Nishihara, Y., Nishiyama, N., and Irifune, T., 2011, High pressure and temperature fabric transitions in olivine and variations in upper mantle seismic anisotropy: *Earth and Planetary Science Letters*, **v. 304**, no. 1-2, p. 55-63.
- Ordóñez Casado, B., Gebauer, D., Schäfer, H. J., Ibarguchi, J. I. G., and Peucat, J. J., 2001, A single Devonian subduction event for the HP/HT metamorphism of the Cabo Ortegal complex within the Iberian Massif: *Tectonophysics*, **v. 332**, no. 3, p. 359-385.

- Ordóñez-Casado, B., Gebauer, D., Schäfer, H., Gil Ibarguchi, J., and Peucat, J., 1996, A single subduction event at ca. 392 Ma for the ultramafic-mafic HP/HT rocks of the Cabo Ortegal Complex: *Geogaceta*, **v. 20**, no. 2, p. 489-490.
- Park, M., and Jung, H., 2017, Microstructural evolution of the Yugu peridotites in the Gyeonggi Massif, Korea: Implications for olivine fabric transition in mantle shear zones: *Tectonophysics*, **v. 709**, p. 55-68.
- Passchier, C. W., and Trouw, R. A., 1996, *Microtectonics*, Springer.
- Peucat, J. J., Bernard-Griffiths, J., Ibarguchi, J. I. G., Dallmeyer, R. D., Menot, R. P., Cornichet, J., and De Leon, M. I. P., 1990, Geochemical and geochronological cross section of the deep Variscan crust: The Cabo Ortegal high-pressure nappe (northwestern Spain): *Tectonophysics*, **v. 177**, no. 1–3, p. 263-292.
- Prior, D. J., Boyle, A. P., Brenker, F., Cheadle, M. C., Day, A., Lopez, G., Peruzzi, L., Potts, G., Reddy, S., Spiess, R., Timms, N. E., Trimby, P., Wheeler, J., and Zetterstrom, L., 1999, The application of electron backscatter diffraction and orientation contrast imaging in the SEM to textural problems in rocks: *American Mineralogist*, **v. 84**, no. 11-12, p. 1741-1759.
- Puelles, P., Ábalos, B., and Gil Ibarguchi, J. I., 2009, Transposed high-pressure granulite fabrics (Cabo Ortegal, NW Spain): Implications on the scales of deformation localization: *Journal of Structural Geology*, **v. 31**, no. 8, p. 776-790.
- Puelles, P., Gil Ibarguchi, J. I., Beranoaguirre, A., and Ábalos, B., 2012, Mantle wedge deformation recorded by high-temperature peridotite fabric superposition and hydrous retrogression (Limo massif, Cabo Ortegal, NW Spain): *International Journal of Earth Sciences*, **v. 101**, no. 7, p. 1835-1853.
- Qi, C., Hansen, L. N., Wallis, D., Holtzman, B. K., and Kohlstedt, D. L., 2018, Crystallographic Preferred Orientation of Olivine in Sheared Partially Molten Rocks: The Source of the “a-c Switch”: *Geochemistry, Geophysics, Geosystems*.
- Quick, J. E., 1981, Petrology and petrogenesis of the Trinity peridotite, An upper mantle diapir in the eastern Klamath Mountains, northern California: *Journal of Geophysical Research: Solid Earth*, **v. 86**, no. B12, p. 11837-11863.
- , 1982, The origin and significance of large, tabular dunite bodies in the Trinity peridotite, northern California: *Contributions to Mineralogy and Petrology*, **v. 78**, no. 4, p. 413-422.

- Raith, R. W., Shor, G. G., Francis, T. J. G., and Morris, G. B., 1969, Anisotropy of the Pacific upper mantle: *Journal of Geophysical Research*, **v. 74**, no. 12, p. 3095-3109.
- Raterron, P., Doukhan, N., Jaoul, O., and Doukhan, J. C., 1994, High temperature deformation of diopside IV: predominance of {110} glide above 1000°C: *Physics of the Earth and Planetary Interiors*, **v. 82**, no. 3, p. 209-222.
- Rocchi, S., Westerman, D. S., Dini, A., Innocenti, F., and Tonarini, S., 2002, Two-stage growth of laccoliths at Elba Island, Italy: *Geology*, **v. 30**, no. 11, p. 983-986.
- Rooney, T. P., Riecker, R. E., and Gavasci, A. T., 1975, Hornblende deformation features: *Geology*, **v. 3**, no. 7, p. 364-366.
- Ross, J. V., and Nielsen, K. C., 1978, High-temperature flow of wet polycrystalline enstatite: *Tectonophysics*, **v. 44**, no. 1-4, p. 233-261.
- Rudnick, R. L., 2005, The crust, Gulf Professional Publishing.
- Satsukawa, T., Griffin, W. L., Piazzolo, S., and O'Reilly, S. Y., 2015, Messengers from the deep: Fossil wadsleyite-chromite microstructures from the Mantle Transition Zone: *Sci Rep*, **v. 5**, p. 16484.
- Satsukawa, T., and Michibayashi, K., 2009, Determination of slip system in olivine based on crystallographic preferred orientation and subgrain-rotation axis: examples from Ichinomegata peridotite xenoliths, Oga peninsula, Akita prefecture: *Geological Society of Japan*.
- Schmandt, B., Jacobsen, S. D., Becker, T. W., Liu, Z., and Dueker, K. G., 2014, Dehydration melting at the top of the lower mantle: *Science*, **v. 344**, no. 6189, p. 1265-1268.
- Schoenberg, M., and Muir, F., 1989, A calculus for finely layered anisotropic media: *Geophysics*, **v. 54**, no. 5, p. 581-589.
- Silver, P., Mainprice, D., Ismail, W. B., Tommasi, A., and Barruol, G., 1999, Mantle structural geology from seismic anisotropy: *Spec. Publ. Geochem. Soc*, **v. 6**, p. 79-103.
- Simpson, C., and Schmid, S. M., 1983, An evaluation of criteria to deduce the sense of movement in sheared rocks: *Geological Society of America Bulletin*, **v. 94**, no. 11, p. 1281-1288.
- Skemer, P., and Karato, S.-i., 2008, Sheared lherzolite xenoliths revisited: *Journal of Geophysical Research: Solid Earth*, **v. 113**, no. B7, p. B07205.
- Skemer, P., Katayama, I., Jiang, Z., and Karato, S.-i., 2005, The misorientation index: Development of a new method for calculating the strength of lattice-preferred orientation: *Tectonophysics*, **v. 411**, no. 1-4, p. 157-167.

- Sobolev, A. V., Hofmann, A. W., Sobolev, S. V., and Nikogosian, I. K., 2005, An olivine-free mantle source of Hawaiian shield basalts: *Nature*, **v. 434**, p. 590.
- Soustelle, V., and Manthilake, G., 2017, Deformation of olivine-orthopyroxene aggregates at high pressure and temperature: Implications for the seismic properties of the asthenosphere: *Tectonophysics*, **v. 694**, p. 385-399.
- Soustelle, V., and Tommasi, A., 2010, Seismic properties of the supra-subduction mantle: Constraints from peridotite xenoliths from the Avacha volcano, southern Kamchatka: *Geophysical Research Letters*, **v. 37**, no. 13, p. 1944-8007.
- Soustelle, V., Tommasi, A., Demouchy, S., and Ionov, D. A., 2010, Deformation and Fluid–Rock Interaction in the Supra-subduction Mantle: Microstructures and Water Contents in Peridotite Xenoliths from the Avacha Volcano, Kamchatka: *Journal of Petrology*, **v. 51**, no. 1-2, p. 363-394.
- Stampfli, G. M., and Borel, G. D., 2002, A plate tectonic model for the Paleozoic and Mesozoic constrained by dynamic plate boundaries and restored synthetic oceanic isochrons: *Earth and Planetary Science Letters*, **v. 196**, no. 1–2, p. 17-33.
- Starkey, J., 1968, The geometry of kink bands in crystals - a simple model: *Contributions to Mineralogy and Petrology*, **v. 19**, no. 2, p. 133-141.
- Tanimoto, T., and Anderson, D. L., 1984, Mapping convection in the mantle: *Geophysical Research Letters*, **v. 11**, no. 4, p. 287-290.
- Tilhac, R., 2017, Petrology and geochemistry of pyroxenites from the Cabo Ortegal Complex, Spain.: *Macquarie University*, p. 230.
- Tilhac, R., Ceuleneer, G., Griffin, W. L., O'Reilly, S. Y., Pearson, N. J., Benoit, M., Henry, H., Girardeau, J., and Grégoire, M., 2016, Primitive Arc Magmatism and Delamination: Petrology and Geochemistry of Pyroxenites from the Cabo Ortegal Complex, Spain: *Journal of Petrology*, **v. 57**, no. 10, p. 1921-1954.
- Tilhac, R., Grégoire, M., O'Reilly, S. Y., Griffin, W. L., Henry, H., and Ceuleneer, G., 2017, Sources and timing of pyroxenite formation in the sub-arc mantle: Case study of the Cabo Ortegal Complex, Spain: *Earth and Planetary Science Letters*, **v. 474**, p. 490-502.
- Tommasi, A., Tikoff, B., and Vauchez, A., 1999, Upper mantle tectonics: three-dimensional deformation, olivine crystallographic fabrics and seismic properties: *Earth and Planetary Science Letters*, **v. 168**, no. 1, p. 173-186.

- Tommasi, A., Vauchez, A., Godard, M., and Belley, F., 2006, Deformation and melt transport in a highly depleted peridotite massif from the Canadian Cordillera: Implications to seismic anisotropy above subduction zones: *Earth and Planetary Science Letters*, **v. 252**, no. 3-4, p. 245-259.
- Toy, V. G., Newman, J., Lamb, W., and Tikoff, B., 2010, The Role of Pyroxenites in Formation of Shear Instabilities in the Mantle: Evidence from an Ultramafic Ultramylonite, Twin Sisters Massif, Washington: *Journal of Petrology*, **v. 51**, no. 1-2, p. 55-80.
- Uyeda, S., and Kanamori, H., 1979, Back-arc opening and the mode of subduction: *Journal of Geophysical Research: Solid Earth*, **v. 84**, no. B3, p. 1049-1061.
- Van Calsteren, P. W. C., 1978, Geochemistry of the polymetamorphic mafic-ultramafic complex at Cabo Ortegal (NW Spain): *Lithos*, **v. 11**, no. 1, p. 61-72.
- Van Calsteren, P. W. C., Boelrijk, N. A. I. M., Hebeda, E. H., Priem, H. N. A., Den Tex, E., Verdurmen, E. A. T., and Verschure, R. H., 1979, Isotopic dating of older elements (including the Cabo Ortegal mafic-ultramafic complex) in the Hercynian orogen of NW Spain: Manifestations of a presumed Early Paleozoic mantle-plume: *Chemical Geology*, **v. 24**, no. 1-2, p. 35-56.
- Vaquero, P. V., and Fernández, F., 1996, Edad de enfriamiento U/Pb en rutilos del Gneis de Chímparra (Cabo Ortegal, NO de España): *Geogaceta*, **v. 20**, p. 475-478.
- Vauchez, A., Dineur, F., and Rudnick, R., 2005, Microstructure, texture and seismic anisotropy of the lithospheric mantle above a mantle plume: Insights from the Labait volcano xenoliths (Tanzania): *Earth and Planetary Science Letters*, **v. 232**, no. 3-4, p. 295-314.
- Vogel, D. E., 1967, Petrology of an eclogite- and pyrigarnite-bearing polymetamorphic rock complex at Cabo Ortegal, NW Spain: Leyden.
- Wagner, L. S., Beck, S., Zandt, G., and Ducea, M. N., 2006, Depleted lithosphere, cold, trapped asthenosphere, and frozen melt puddles above the flat slab in central Chile and Argentina: *Earth and Planetary Science Letters*, **v. 245**, no. 1, p. 289-301.
- Wallin, E. T., Coleman, D. S., Lindsley-Griffin, N., and Potter, A. W., 1995, Silurian plutonism in the Trinity terrane (Neoproterozoic and Ordovician), Klamath Mountains, California, United States: *Tectonics*, **v. 14**, no. 4, p. 1007-1013.

- Wallin, E. T., and Metcalf, Rodney V., 1998, Supra Subduction Zone Ophiolite Formed in an Extensional Forearc: Trinity Terrane, Klamath Mountains, California: *The Journal of Geology*, **v. 106**, no. 5, p. 591-608.
- Wang, J., and Zhao, D., 2008, P-wave anisotropic tomography beneath Northeast Japan: *Physics of the Earth and Planetary Interiors*, **v. 170**, no. 1–2, p. 115-133.
- , 2010, Mapping P-wave anisotropy of the Honshu arc from Japan Trench to the back-arc: *Journal of Asian Earth Sciences*, **v. 39**, no. 5, p. 396-407.
- Weil, A. B., Gutiérrez-Alonso, G., Johnston, S. T., and Pastor-Galán, D., 2013, Kinematic constraints on buckling a lithospheric-scale orocline along the northern margin of Gondwana: A geologic synthesis: *Tectonophysics*, **v. 582**, no. 0, p. 25-49.
- Wright, S. I., Nowell, M. M., and Field, D. P., 2011, A Review of Strain Analysis Using Electron Backscatter Diffraction: *Microscopy and Microanalysis*, **v. 17**, no. 3, p. 316-329.
- Xiong, Q., Henry, H., Griffin, W. L., Zheng, J.-P., Satsukawa, T., Pearson, N. J., and O'Reilly, S. Y., 2017, High- and low-Cr chromitite and dunite in a Tibetan ophiolite: evolution from mature subduction system to incipient forearc in the Neo-Tethyan Ocean: *Contributions to Mineralogy and Petrology*, **v. 172**, no. 6.
- Zhang, J., Greenii, H., and Bozhilov, K., 2006, Rheology of omphacite at high temperature and pressure and significance of its lattice preferred orientations: *Earth and Planetary Science Letters*, **v. 246**, no. 3-4, p. 432-443.

